

ANGLE-RESOLVED
CATHODOLUMINESCENCE NANOSCOPY

Cover image: [electron beam].

Ph.D. Thesis University of Amsterdam, May 2014
Angle-resolved Cathodoluminescence Nanoscopy
Toon Coenen

ISBN XXX-XX-XXXXX-XX-X

A digital version of this thesis can be downloaded from <http://www.amolf.nl>.

ANGLE-RESOLVED CATHODOLUMINESCENCE NANOSCOPY

Hoekafhankelijke Kathodeluminescentienanoscopie

(met een samenvatting in het Nederlands)

ACADEMISCH PROEFSCHRIFT

ter verkrijging van de graad van doctor
aan de Universiteit van Amsterdam
op gezag van de Rector Magnificus
prof. dr. D.C. van den Boom
ten overstaan van een door het college voor promoties
ingestelde commissie,
in het openbaar te verdedigen in de Agnietenkapel
op donderdag 15 mei 2014 te 10:00 uur

door

Toon Coenen

geboren te Hilversum, Nederland

Promotiecommissie

Promotor: Prof. dr. A. Polman

Overige Leden: Prof. dr. J. W. M. Frenken
Prof. dr. F. J. García de Abajo
Prof. dr. M. S. Golden
Prof. dr. T. Gregorkiewicz
Prof. dr. L. Novotny

Faculteit der Natuurwetenschappen, Wiskunde en Informatica

This work is part of the research program of the 'Stichting voor Fundamenteel Onderzoek der Materie' (FOM), which is financially supported by the 'Nederlandse organisatie voor Wetenschappelijk Onderzoek' (NWO). It is also funded by NanoNextNL, a nanotechnology program funded by the Dutch ministry of economic affairs.

Contents

1	Introduction	11
1.1	Microscopy	11
1.2	Nanophotonics: managing light on the nanoscale	13
1.3	Nanoantennas	14
1.4	Resolving optical properties on the nanoscale	15
1.5	Outline of this thesis	17
2	Spectroscopy with fast free electrons	19
2.1	Electron beam excitation	19
2.1.1	Coherent excitation	20
2.1.2	Incoherent excitation	22
2.2	Angle-resolved cathodoluminescence imaging spectroscopy	24
2.2.1	Spectral imaging	25
2.2.2	Measuring angular emission profiles	27
2.3	Mirror alignment	28
2.4	Measuring in k -space with a pinhole scanner	30
2.5	Electron energy-loss spectroscopy	31
3	Angle-resolved cathodoluminescence imaging spectroscopy	35
3.1	Introduction	35
3.2	Fourier microscopy with a paraboloid mirror	36
3.3	Angular pattern of transition radiation	38
3.4	Conclusions	40
4	Directional emission from plasmonic Yagi-Uda antennas probed by angle-resolved cathodoluminescence spectroscopy	41
4.1	Introduction	41
4.2	Sample fabrication	43
4.3	Single-particle response	43
4.4	Spectral imaging of a Yagi-Uda antenna	44

4.5	Antenna radiation patterns	45
4.6	Coupled electrical dipole model	49
4.7	Comparison between experiment and theory	51
4.8	Conclusions	52
5	Deep-subwavelength spatial characterization of angular emission from single-crystal Au plasmonic ridge nanoantennas	53
5.1	Introduction	53
5.2	Antenna fabrication	55
5.3	Direct imaging of Fabry-Pérot modes	55
5.4	Resonance evolution and modal dispersion	57
5.5	Boundary-element-method modeling	59
5.6	Reflection coefficients	60
5.7	Ridge angular patterns	61
5.8	Theoretical model for angular patterns	63
5.9	Conclusions	65
5.10	Methods	66
6	Polarization-sensitive cathodoluminescence Fourier microscopy	67
6.1	Introduction	67
6.2	Sample and experimental setup	69
6.3	Polarization-filtered angular patterns	70
6.4	Enhancing polarization contrast	76
6.5	Emission polarization reconstruction	78
6.6	Conclusions	80
7	A planar parabolic antenna	83
7.1	Introduction	83
7.2	Sample fabrication	85
7.3	CL imaging of elliptical cavity plasmon modes	85
7.4	Resonance model for ellipses	87
7.5	Conclusions	91
7.6	Supplementary information	91
7.6.1	Supplementary figures	91
7.6.2	Calculation of effective coupling volume	93
8	Directional emission from a single plasmonic scatterer	95
8.1	Introduction	95
8.2	Cathodoluminescence spectra	97
8.3	Directional scattering	98
8.4	Multipolar decomposition	100
8.5	Guidelines for strong directionality	105
8.6	Conclusions	106
8.7	Methods	106

9	Optical properties of individual plasmonic holes probed with local electron beam excitation	107
9.1	Introduction	107
9.2	Sample fabrication	108
9.3	Spectral response measurements	109
9.4	CL signal decay away from the hole	110
9.5	Simulation results	112
9.6	Angular response	115
9.7	Conclusions	119
10	Variable modal excitation efficiency in plasmonic dolmens through nanoscale electron beam positioning	121
10.1	Introduction	121
10.2	Dolmen geometry and fabrication	123
10.3	Single nanorods and dimers	124
10.4	Inter-particle coupling in the dolmen	128
10.5	Size-dependent optical response	131
10.6	Variable modal excitation efficiency	133
10.7	Varying intrinsic coupling strength	134
10.8	Conclusions	135
10.9	Supplementary information	136
10.9.1	Sample fabrication on TEM membranes	136
10.9.2	EELS and CL experiments	137
10.9.3	FDTD simulations	138
10.9.4	Hybridization schemes for dimer and dolmen	140
10.9.5	Discriminating longitudinal dimer modes	141
11	Deep-subwavelength imaging of the modal dispersion of light	143
11.1	Introduction	143
11.2	Imaging delocalized photonic crystal modes	145
11.3	Momentum spectroscopy in photonic crystals	147
11.4	Localized mode in an H1 photonic crystal cavity	147
11.5	Localized modes in an L3 cavity	149
11.6	Spatial resolution estimate	151
11.7	Conclusions	154
11.8	Methods	154
11.9	Supplementary information	155
12	Resonant modes of single silicon nanocavities excited by electron irradiation	157
12.1	Introduction	157
12.2	Sample fabrication	158
12.3	Imaging Mie modes in silicon cylinders	159
12.4	Numerical modeling	161

Contents

12.5 Mode evolution as a function of particle diameter	162
12.6 Analytical disc model	164
12.7 Angular patterns	166
12.8 Nature of lowest-order mode	168
12.9 Conclusions	169
12.10 Methods	170
References	173
Summary	189
List of publications	193

1

Introduction

1.1 Microscopy

Beyond what the naked eye can see there exists a fascinating microscopic hidden world. Biological cells, for example, are composed of tiny nanoscale structures which determine their biological function. Electrical integrated circuits which form the basis for modern-day technology like computers and communication technology are built up from nanoscale circuit elements. Materials in general, have atomic structure on the Ångstrom scale and possess grain structure, roughness, faceting *etc.* on a mesoscopic scale which determine their properties. In order to understand such structures, devices, or materials it is of great importance to study their constituent building blocks.

To study this microscopic world we make use of microscopes. The word microscopy originates from the Greek words μικρός (mikros) meaning “small” and σκοπεῖν (skopein) which means “to see”. The field of microscopy was initiated more than 350 years ago, when Robert Hooke and Antoni van Leeuwenhoek started to employ optical microscopes to reveal microscopic features of cells, muscle fibers, bacteria, and other microbiological structures with a level of detail that had never been observed before [1, 2]. Since then microscopy has become a cornerstone of biological and physical sciences.

Vice versa, the development in microscopy over the years has enabled significant advances in technology, materials science, and biology. For example, the last decades a revolution has taken place in the electrical integrated circuit industry where circuit elements have shrunk into the nanoscale regime, starting a new era of nanotechnology. This would not have been possible without significant advances in the field of microscopy which, during this period, moved into the realm of “nanoscopy”, *i.e.* microscopy on the nanoscale. Currently there are three main branches of microscopy:

- Optical microscopy
- Electron microscopy
- Scanning probe microscopy

in which light, electrons, and nanoscale tips are used for image formation, respectively. Examples of advanced optical microscopy (OM) techniques are stimulated emission depletion microscopy (STED) [3, 4], photoactivatable localization microscopy (PALM) [5], and stochastic optical reconstruction microscopy (STORM) [6]. Common electron microscopy techniques are scanning electron microscopy (SEM), (scanning) transmission electron microscopy (TEM, STEM) and low-energy electron microscopy (LEEM) [7]. Combined with (scanning) transmission electron microscopy one can perform electron energy-loss spectroscopy (EELS). Examples of scanning probe techniques that employ nanoscale tips are atomic force microscopy (AFM) [8, 9] and scanning tunneling microscopy (STM) [8, 10].

Several techniques combine elements from the three microscopy branches. In tip-enhanced Raman scattering (TERS) [11, 12] and near-field scanning optical microscopy (NSOM) [13–19] one combines elements from optical microscopy with scanning probe microscopy. Also STM can be combined with optical microscopy where the STM tip acts as a local light source [20, 21]. In photoemission electron microscopy (PEEM) [22–24] the sample is irradiated with light after which the photoelectrons are collected and imaged using electron optics. PEEM is often combined with LEEM in a single microscope system [7]. Conversely, in cathodoluminescence spectroscopy (CL) and energy dispersive x-ray spectroscopy (EDS) one uses an electron beam as excitation source after which the visible/infrared (CL) and x-ray (EDS) photons are collected.

An overview of microscopy techniques is given in Table 1.1 together with the type of probe/signal that is used and an approximate in-plane spatial resolution range. The table also shows whether the technique is sensitive to geometry, composition, and/or the electrical/optical properties of a structure. Each technique has specific demands on the sample preparation, environment, fluorescent labeling, conductivity *etc.* which can limit its applicability. We note that this table is just meant to give a concise overview of the most common techniques, and does not include all existing microscopy techniques.

The resolution of optical microscopy techniques has been improved significantly although the superresolution techniques usually require special fluorescent labeling. In many biological systems this labeling can be done with great accuracy enabling nanoscale resolving power in such systems. The optical techniques are particularly sensitive to the optical properties. The electron microscopy techniques are fast, reliable, and have a high in-plane spatial resolution (down to 80 pm for TEM). Advances in tomography and holography have enabled 3D image reconstruction on the atomic scale [25]. For TEM imaging the sample requirements are stringent as one requires very thin electron-transparent membranes. Nevertheless,

1.2 Nanophotonics: managing light on the nanoscale

Technique	Probe	Signal	Resolution	Geometry	Composition	Electronic Properties	Optical properties
OM	Light	Light	$\lambda/2$	+	+/-	-	+
STED	Light	Light	2 – 100 nm	+	+/-	-	+
PALM/STORM	Light	Light	20 – 100 nm	+	+/-	-	+
CL	Electrons	Light	5 – 1000 nm	+	+/-	-	+
SEM	Electrons	Electrons	1 – 5 nm	+	+/-	-	-
TEM/STEM	Electrons	Electrons	80 pm – 1 nm	+	+/-	-	-
STEM EELS	Electrons	Electrons	0.1 – 10 nm	+	+	-	+/-
LEEM / PEEM	Elec. / Light	Electrons	1 – 10 nm	+	+/-	+	+/-
EDS	Electrons	X-rays	40 – 1000 nm	+	+	-	-
AFM	AFM tip	Tip deflection	0.1 – 1 nm	+	-	-	-
STM	STM tip	Current / Light	0.1 – 1 nm	+	+/-	+	+/-
TERS	TERS tip	Light	2 – 200 nm	+	+/-	-	-
NSOM	NSOM tip	Light	5 – 200 nm	+	+/-	-	+

Table 1.1: Overview of microscopy techniques. We indicate what probe is used and what signal is measured for each technique and what the typical in-plane spatial resolution is. In the last four columns we show to what properties the technique is most sensitive. Green (+) means that the technique in general can be used to determine that property. Yellow (+/-) means that the technique can be used to determine such properties in some cases and red (-) means that it in general cannot be used for measuring these properties.

the electron microscopy techniques are versatile and in principle can be sensitive to many properties depending on the excitation/detection mode. The scanning probe techniques often heavily rely on the tip geometry which can be hard to control. On the other hand scanning probe techniques can have atomic-scale in-plane resolution and unparalleled out-of-plane sub-atomic resolution. Furthermore they are very surface-sensitive making it a method of choice in surface science.

1.2 Nanophotonics: managing light on the nanoscale

Since 1970, the size of circuit components in electronic integrated circuits has shrunk at an exponential rate. As predicted by Moore's law [26], the number of transistors per unit area has doubled every 18 months. In the last decade, the field of photonics has seen a similar trend where optical/photonic components are developed and miniaturized with the aim to generate, detect, guide, or switch light at the nanoscale. This branch of optics/photonics is often referred to as nanophotonics.

Light is sensitive to many properties of matter and hence is very useful for many sensing and imaging applications. Furthermore, light can be used to transmit large amounts of information at large speeds with low losses, potentially leading to faster computation and communication applications. Moreover, the quantum nature

of light could be utilized to switch and interrogate Qbits enabling quantum computation which could lead to an exponential increase in computation speed for some types of calculations [27, 28]. Implementing optical sensing or computing schemes on the nanoscale and integrating those with electrical circuits on a single chip would allow for faster and more efficient devices in which many functions can be performed in parallel.

Because the wavelength of light in the visible and near-infrared spectral regime is relatively large it is not trivial to shrink optical components to the level of current electrical integrated circuits. However, by using strongly polarizable nanostructured metallic and high-index dielectric materials the wavelength can be shrunk by more than an order of magnitude and light can be confined to nanoscale volumes. The basic building block or “elementary particle” in nanophotonics is the nanoantenna.

1.3 Nanoantennas

Nanoantennas can form an interface between the near and far field [29]. In reception mode they can collect light from an area larger than its geometrical cross section and funnel it towards a local receiver. In transmission mode a nanoantenna can enhance and direct the emission from a local transmitter. This local transmitter/receiver can be a fluorescent molecule, quantum dot, or nanodiamond for instance. A schematic of these processes is shown in Fig. 1.1. Nanoantennas are often composed of metals like gold, silver, or aluminium that support plasmonic resonances. Recently, high-index dielectric/semiconductor nanostructures have attracted attention as efficient antennas as well [30, 31]. In both cases the structures support optical resonances in the visible/near-infrared spectral regime with scattering cross sections much larger than their geometrical cross sections. The resonance wavelengths can be tuned by varying shape and size [32]. Many of the nanoantenna design concepts originate from radio-frequency/microwave regime antenna designs [33–35], scaled down appropriately taking into account material dispersion effects, to function in the spectral region of interest.

Nanoantennas are promising for a large variety of applications. Their light harvesting and light directing properties can be used in anti-reflection coatings and light trapping in solar cells [30, 36], spontaneous emission control [13, 37–40], nanoscale sensing [41–49], low-threshold steam generation [50, 51], color filters in camera chips [52, 53], and targeted medicine [54–56]. The strong field enhancements that can be attained in nanoantennas are also very suitable for surface-enhanced Raman scattering [57, 58] and nonlinear effects [59–61], to mention a few examples. Due to their nanoscale nature, characterization of the optical nanoantenna properties poses a challenge in itself.

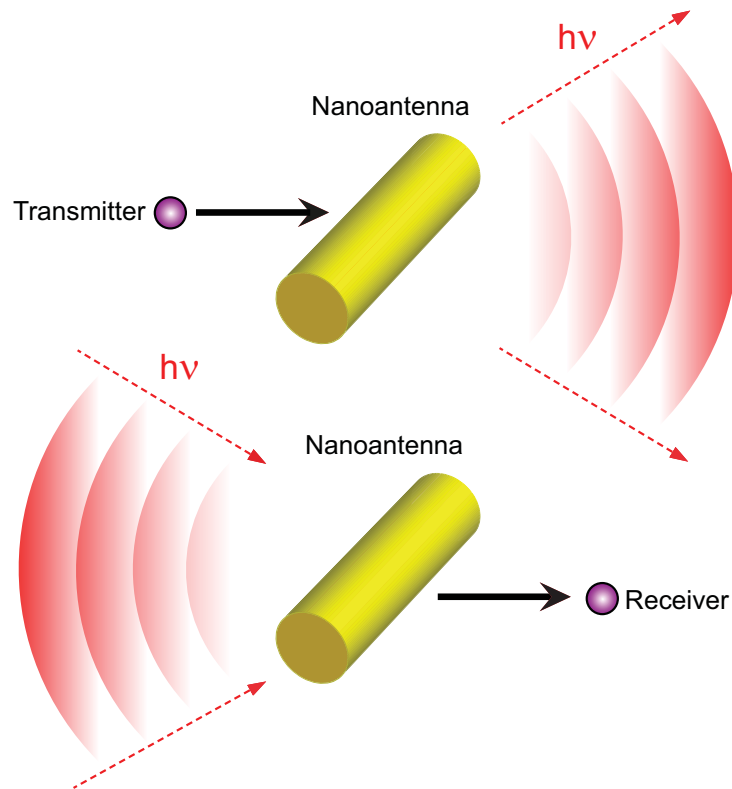


Figure 1.1: Schematic of a nanoantenna in reception and transmission mode. Nanoantennas form an interface between the near and far field. In transmission mode the nanoantenna represented by the yellow bar can enhance and direct the emission from a local transmitter (purple circle). In reception mode it can collect light from an area larger than its geometrical cross section and funnel it to a local receiver.

1.4 Resolving optical properties on the nanoscale

Conventional optical microscopy is limited in resolution by the diffraction limit. Abbe's law of diffraction states that two points that are spaced less than $d = \lambda_0/(2NA)$, where λ_0 is the free space wavelength and NA is the numerical aperture of the microscope, cannot be resolved by the microscope. This makes conventional optical microscopy unsuited for studies at the true nanoscale. To illustrate this, Fig. 1.2(a) shows a transmission electron micrograph of an optical antenna composed of a single 125 nm long gold rod on a Si_3N_4 membrane. The plasmon resonance of this rod occurs at $\lambda_0 = 750$ nm (see Fig. 10.6). The optical wavelength is drawn to scale together with the corresponding diffraction-limited spot (red circle in (a)). Clearly the antenna falls well within this spot so optical microscopy is inadequate for spatial characterization of the optical properties of such a small structure.

A solution to this problem is to use a beam of fast electrons to probe opti-

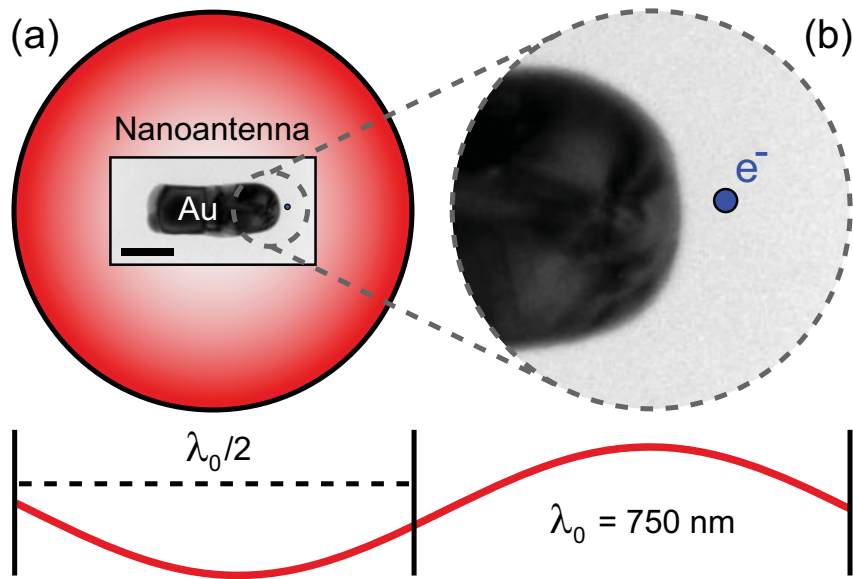


Figure 1.2: (a) Bright-field transmission electron micrograph of a 125 nm long gold rod on a Si₃N₄ membrane, which acts as nanoantenna and is resonant at $\lambda_0 = 750$ nm. Scale bar is 50 nm. The overlaid red circle represents a diffraction-limited spot for $\lambda_0 = 750$ nm and an NA = 1. The small blue dot represents a 5 nm electron beam (to scale). (b) Magnified image of area enclosed by the gray dashed circle in (a).

cal properties at the nanoscale [62, 63]. Using electrons as an optical excitation source has two main advantages. First, the excitation resolution can be very high, as typical electron microscopes can focus and position an electron beam at 1 – 10 nm spatial resolution (see Table 1.1). For comparison a blue circle representing a 5 nm spot is shown in Fig. 1.2(a). Because the spot is very small compared to the antenna we have blown up part of the electron micrograph to better visualize the size (Fig. 1.2(b)). Second, since the measurements are performed in an electron microscope environment the full electron microscopy toolbox can be used to correlate nanoscale geometrical features with the optical response. Two electron spectroscopy techniques that have gained significant interest for optical studies at the nanoscale are:

- **Cathodoluminescence (CL) Spectroscopy** where the electron induced light emission is collected and measured. CL spectroscopy is usually performed in a SEM although it is also possible to perform measurements in a TEM [64, 65].
- **Electron Energy-Loss Spectroscopy (EELS)** where the loss of electron energy is used for spatial characterization of materials. These measurements are usually performed in a TEM.

In this thesis we develop novel CL spectroscopy tools and use them to investigate optical antennas and other nanophotonics structures. A comparison with EELS is also made.

1.5 Outline of this thesis

In this thesis we present a new experimental technique; angle-resolved cathodoluminescence (CL) imaging spectroscopy (ARCIS) that combines the superior spatial resolution of electron microscopy with the optical sensitivity of optical microscopy. Chapters 2 and 3 give a detailed technical description of the technique. To demonstrate its versatility and applicability to nanophotonics, ARCIS is applied to several types of metallic and dielectric nanostructures most of which function as nanoantennas. These are described in chapters 4-12.

In **Chapter 2** electron-material interactions are discussed, where we distinguish between coherent and incoherent interactions. Subsequently the ARCIS technique is introduced and the experimental configuration is discussed in detail. Furthermore the electron energy-loss spectroscopy setup used in Chapter 10 is described.

Chapter 3 describes the angle-resolved spectroscopy configuration of ARCIS and the corresponding data correction procedures. The technique is calibrated by studying the angle-resolved radiation pattern of a known source of radiation: transition radiation from a single-crystalline gold substrate

In **Chapter 4** we use ARCIS to study the optical properties an array of five gold nanoparticles which acts as a subwavelength optical Yagi-Uda antenna. We demonstrate that the antenna array is strongly directional and that the directionality can be controlled by selectively driving one of the antenna elements. The angular response of the array antenna is modeled using a coupled dipole model which takes into account interparticle coupling and interaction with the substrate.

In **Chapter 5** we focus on the optical properties of gold plasmonic ridge antennas of different length which act as traveling wave antennas. The reflective end facets of the ridge antenna cause standing wave modes on the ridge and fringe patterns in the angular profile which can be visualized with ARCIS. From the data we extract a dispersion relation for the guided ridge plasmon mode.

Chapter 6 introduces polarization-sensitive Fourier microscopy as further extension of the ARCIS technique. We analyze the angular and polarization distribution for transition radiation from a gold surface and from a gold ridge antenna and compare these with the theoretical distributions. We demonstrate that it is possible to reconstruct the emission polarization without *a priori* knowledge of the source.

In **Chapter 7** we use ARCIS to characterize elliptical arena cavities that are milled into a gold substrate. We image the plasmon modes inside the cavities and find that the resonance spectrum is solely determined by the major axis length and the reflection phase pickup at the cavity boundaries. Finally we demonstrate that these elliptical cavities act as parabolic antennas and hence can show a remarkably strong directionality.

Chapter 8 describes how a single plasmonic scatterer can act as directional scatterer. Using ARCIS, we find that the angular response of the nanoparticle strongly depends on excitation position and that this can be used to beam light in a well-defined direction. The beaming is caused by interference between

in-plane and out-of-plane multipole components. Using a combination of full-wave simulations and analytical point-scattering theory we determine the relative contribution of different multipoles.

In **Chapter 9** we study the spectral and angular properties of nanoscale holes in a gold film. We find a striking complementarity in the directionality of the emission compared to the nanoparticles studied in Chapter 8. The data are compared to full-wave simulations and a simple analytical model in order to understand the ARCIS results.

In **Chapter 10** we use EELS and CL measurements to gain more insight into the near-field coupling in composite plasmonic “dolmen” antennas. We demonstrate that by controlling the position of the electron beam the degree of coupling to different modes of the system can be precisely controlled. The EELS and CL measurements were performed on the same structures enabling a direct comparison between the two. We find that in some cases EELS and CL yield very similar information, while in other cases there are distinct differences due to the modal scattering efficiencies.

In **Chapter 11** we study the optical modes in 2D silicon nitride photonic crystal membranes using ARCIS. We image delocalized modes in 2D hexagonal crystals and localized modes in photonic crystal cavities. Using momentum spectroscopy we visualize the spatially-resolved dispersion in the crystal.

Finally, in **Chapter 12** we study the resonant behavior of silicon nanodiscs using ARCIS. We measure resonance spectra and determine the corresponding field profiles for different disc diameters. Using the angular emission profiles we resolve the electric and magnetic nature of the disc resonances, and elucidate their directional properties.

Overall, this thesis introduces angle-resolved cathodoluminescence imaging spectroscopy (ARCIS) as a novel microscopy technique to resolve optical properties at the nanoscale. By combining elements from electron and optical microscopy we are able to resolve optical phenomena that are impossible to elucidate with other techniques.

2

Spectroscopy with fast free electrons

Electron beam spectroscopies provide a powerful platform for studying a wide variety of nanophotonic structures like nanoantennas, nanocavities, and photonic crystals. In this Chapter we describe in detail which processes occur when a fast electron beam interacts with a sample. Furthermore we discuss the experimental techniques that are used throughout this thesis. In particular we describe angle-resolved cathodoluminescence imaging spectroscopy and electron energy-loss spectroscopy. Both techniques rely on a beam of energetic free electrons as excitation source but use different detection mechanisms.

2.1 Electron beam excitation

When a beam of energetic fast electrons (0.1 keV – 300 keV of energy per electron) hits a sample a multitude of processes can occur. The interaction with the sample leads to the generation of low-energy secondary electrons (SEs) and more energetic backscattered electrons (BSEs) which provide information about the surface topology and composition of the sample and hence can be used for microscopy. Electrons that are transmitted either directly or indirectly can be used for microscopy as well. Because electrons have a restmass their de Broglie wavelength is orders of magnitude smaller than the wavelength for photons at the same energy. For a 2 eV electron the corresponding wavelength is 0.86 nm whereas for a photon it is 620 nm. At 300 keV an electron travels at $0.8c$ and relativistic effects must be taken

into account; The de Broglie wavelength then is 2 pm. Even though state-of-the-art electron microscopes still operate far away from the electron wave diffraction limit, an imaging resolution of 80 pm has been demonstrated which means that structure and composition of materials can be studied on the atomic scale [66–68].

Besides the electron signals, a broad spectrum of electromagnetic radiation ranging from x-rays to the mid-IR is generated through a variety of incoherent and coherent processes which will be discussed below. The electromagnetic radiation that is generated in the visible/NIR regime of the spectrum is usually referred to as cathodoluminescence (CL) as the radiation is generated by cathode rays (fast electrons). For an historical overview on the discovery of cathode rays and CL we refer the reader to Ref. [69]. Figure 2.1 shows an overview of signals that can be measured when a material is irradiated by energetic electrons, together with the corresponding characterization techniques.

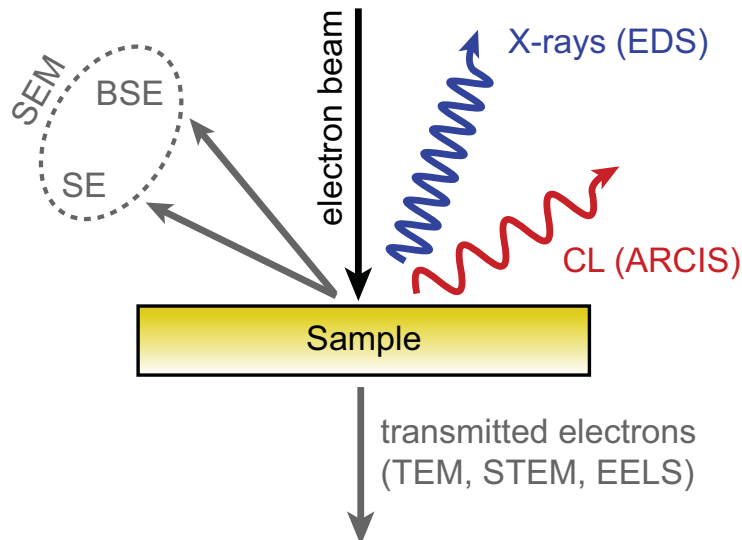


Figure 2.1: Schematic showing some of the processes that occur when an energetic beam of electrons impinges on a sample. These processes are used for different characterization techniques as indicated in the schematic.

2.1.1 Coherent excitation

An electron moving at a constant velocity through space is accompanied by evanescent electromagnetic fields that extend away from the electron and cannot couple to propagating radiation [63]. When the electron interacts with matter these fields can be coherently transferred and sometimes converted to free-space radiation. An example of such a process is transition radiation (TR) generation, where an electron passes through an interface between two media with different refractive indices. The electron transition through the interface polarizes electrons near the interface, inducing an effective vertical dipole moment. Because the electron transition is

very fast the TR spectrum is broad band. Furthermore, the interaction is highly localized in space which means there is a broad distribution in available momenta. This allows direct excitation of guided waves that have an in-plane momentum larger than that of a free-space light at the same frequency, such as surface plasmon polaritons (SPPs) on the interface between a plasmonic metal and a dielectric. A schematic of TR and SPP excitation for an Au substrate is shown in Fig. 2.2(a).

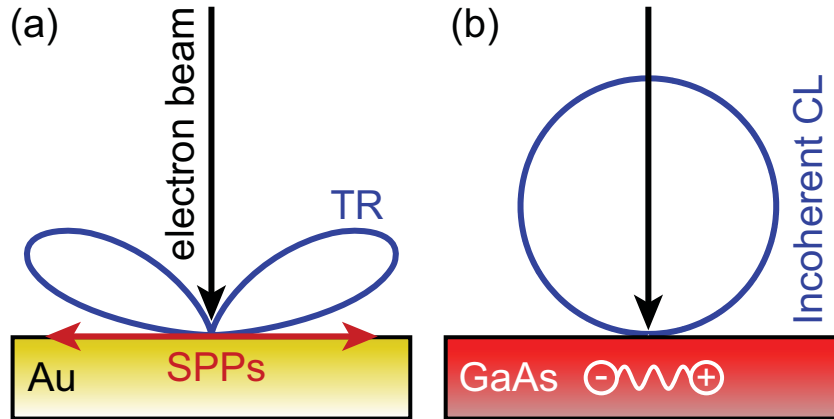


Figure 2.2: (a) Excitation of a gold substrate where transition radiation and SPPs are generated. The blue curve represents the radiation pattern for TR which is similar to that of a vertical point dipole source on a gold substrate (for a detailed description of how this pattern is calculated see Section 3.3). (b) Schematic of electron beam excitation of gallium arsenide where radiative electron hole pair recombination lead to a strong incoherent CL component. Due to the randomized emission inside of the substrate the emission pattern usually resembles a Lambertian emission distribution.

A second example of coherent excitation is Cherenkov radiation where the electron travels faster than the speed of light in the medium, which means that the electron dispersion lies above the light line in the medium and the evanescent fields transform into radiating fields at an angle that is determined by the velocity of the the electron relative to the speed of light in the medium. It has been proposed that this type of radiation can be utilized for efficient heralded single-photon generation of a particular color, if one lets the electrons move parallel to a 1D waveguide [70].

The probability of an electron losing energy through these coherent processes can be related to the induced vertical electric field acting back on the electron. The electron is sensitive only to the vertical electric field component because that is the only way in which the electron can decelerate and perform work, *i.e.* transfer energy to a structure. Because of energy conservation the electron can loose energy to a structure. However, if an external field is supplied such as an ultrafast laser pulse for example, the electrons can also gain quanta of energy [71–74]. Because of this E_z sensitivity the electrons often couple to vertical electric dipole modes and guided modes with transverse magnetic (TM) character like the single-interface SPP mode in Fig. 2.2. This is markedly different from plane waves where the electric field

oscillates transverse to the propagation direction leading to a preferential coupling to xy -components for normal incidence.

It has been shown theoretically that for z -invariant structures there exists a rigorous connection between the electron energy-loss (EEL) probability and the z -projection of local density of optical states (LDOS) integrated along the electron trajectory [63, 75]. Also for structures that do not have a z -invariant geometry there can be qualitative agreement between the z -projection of the integrated LDOS and the EEL signal although this is not always the case, as is described in Ref. [76]. The EEL probability takes into account non-radiative as well as radiative processes whereas the CL probability contains information only about the radiative processes. This means that modes that are dark, *i.e.* that do not couple to far field radiation, as bulk plasmons for example, do show up in the EEL but not in the CL signal. Making quantitative predictions about the LDOS based on the EEL/CL probability is not straightforward and one should be cautious in doing so. As the electron beam is not affected by xy LDOS components, optical modes with strong in-plane fields such as dipolar dimer modes which exhibit strong hotspots in the dimer gap do not appear as such in EEL/CL maps [76–79]. Nevertheless, using coherent electron beam excitation one can obtain useful insights into the local optical response of nanostructures for a broad wavelength range simultaneously. By using a pulsed electron source in conjunction with a femtosecond laser one can also study the time dynamics of light-electron interactions in nanostructures which is also referred to as 4D electron microscopy (2 spatial dimensions, energy, and time) [72, 74, 80–82]. Furthermore, by rotating a sample one can perform tomography and holography on nanomaterials which can be used to obtain structural and chemical information in 3D [25]. Most recently, EELS and CL tomography have been developed demonstrating yet another form of 4D electron microscopy, as these techniques provide 3D spatial information on the local optical properties for a broad range of energies [83–85].

2.1.2 Incoherent excitation

Besides the coherent processes electrons can also excite incoherent transitions in a material. In particular one can drive high-energy core transitions which can be detected using EELS (see Section 2.5) or energy-dispersive x-ray spectroscopy (EDS). These transitions provide a unique fingerprint for local elemental analysis in electron microscopy. Incoherent light emission in the visible/near-infrared regime can also occur through band-edge electron-hole recombination in bulk/nanostructured semiconductors [86, 87] and quantum-confined structures [65, 88], intra- $4f$ transitions in rare-earth ions, defect luminescence in materials [89, 90] *etc.* This incoherent emission has been used in the past in cathode-ray-tube (CRT) televisions, and is still used in geology to identify and characterize minerals [91]. Furthermore, phosphor screens are used routinely in electron microscopes to convert electron signals into optical signals as these are easier to detect using standard silicon cameras or photomultiplier

tubes. It is important to note that the cathodoluminescence spectrum does not necessarily match the photoluminescence spectrum of a material because the relatively large momentum of the electrons allows for the excitation of transitions which are momentum-forbidden for light. Also, the cross sections for electron impact excitation generally differ from those for optical excitation. Nevertheless incoherent CL spectroscopy provides a powerful platform for locally studying the material properties. Figure 2.3 shows spectra that we have measured on $\text{SiO}_2:\text{Er}^{3+}$, InP, GaAs, SiO_2 , $\text{YAG}:\text{Ce}^{3+}$, CdS, InGaN, ZnO, and GaN respectively. The strong emission peaks that are observed are due to one or more of the incoherent processes mentioned above.

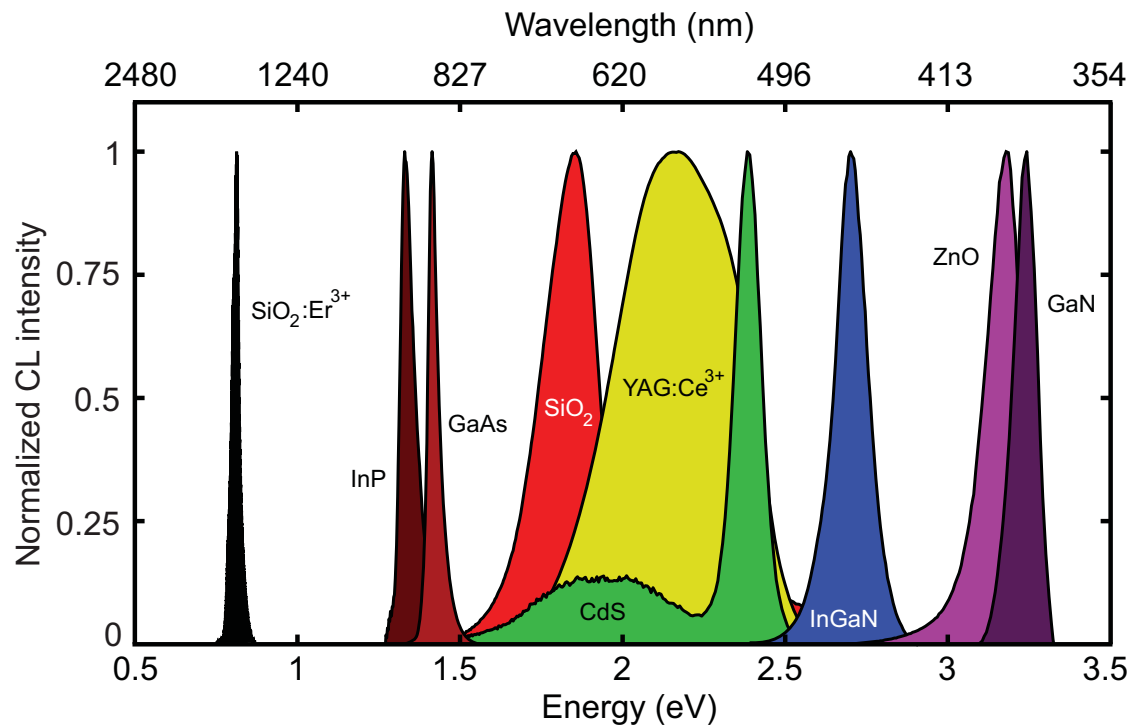


Figure 2.3: Normalized CL spectra (5 – 30 keV electrons) for a variety of dielectric and semiconductor materials. The $\text{SiO}_2:\text{Er}^{3+}$, GaAs, SiO_2 , $\text{YAG}:\text{Ce}^{3+}$, and GaN emission was measured on bulk/planar materials. The other spectra were measured on nanomaterials: InP (nanowire grown with the vapor-liquid-solid method), CdS (colloidal platelet), InGaN (quantum well embedded in GaN), and ZnO (nanoparticle powder).

Because an electron beam can be tightly focused precise lateral characterization of materials is possible. By changing the electron energy one can also alter the penetration depth enabling materials characterization in 3D. Incoherent emission is generally oriented randomly inside the material and as result it is emitted approximately in a Lambertian emission distribution [92, 93]. A schematic of this process is shown in Fig. 2.2(b) for GaAs which is a strongly luminescent material due to its direct bandgap. Note that there is also TR radiation generation for GaAs but its

intensity is very small compared to the incoherent band edge luminescence. The excitation of incoherent radiation can be very efficient because one energetic electron can easily create multiple photons as it creates a cascade of excitation events. In fact, incoherent luminescence is usually excited more efficiently by the cloud of slow secondary electrons rather than the primary beam. As a result the incoherent radiation often is much stronger than the coherent radiation from the same structure. This puts restrictions on the substrates that can be used if one is interested in coherent signals. For instance, SiO₂ which is a standard substrate for many optical experiments, exhibits very strong defect luminescence under electron beam irradiance [89] (see Fig. 2.3) making it impractical for coherent CL spectroscopy. Finally, it should be noted that in some cases the incoherent CL is bleached. This can be particularly severe for organic compounds which often decompose under electron irradiation.

2.2 Angle-resolved cathodoluminescence imaging spectroscopy

In this section we will discuss the angle-resolved cathodoluminescence imaging spectroscopy (ARCIS) setup that is used throughout this thesis. The main component of the setup is a FEI XL-30 Schottky field emission gun (SFEG) scanning electron microscope (SEM) (see Fig. 2.4(a)). The SEM is equipped with a specially designed micromanipulation stage that carries an off-axis aluminum paraboloid mirror (0.1 parabola coefficient, 0.5 mm focal distance, 1.46π sr acceptance angle, 10 nm RMS roughness, and $\lambda/2$ curve accuracy)(Fig. 2.4(b,c)). Directly above its focal point, this paraboloid has a 600- μm -diameter hole through which the electron beam can reach the sample. The size of the hole is a tradeoff between loss in acceptance angle and a larger field of view in the electron microscope as the hole size is increased. The mirror collects the generated CL and redirects it out of the SEM through a glass vacuum flange into an enclosed optics box (the black box in Fig. 2.4(a)). The nanomanipulation stage allows proper focusing of the paraboloid by using four piezoelectric stepper motors connected to a titanium leaf spring system (visible in Fig. 2.4(b)). This system provides translational degrees of freedom (x , y over a range of ~ 1 mm with an accuracy of ~ 500 nm) as well as control over mirror tilt and yaw ($\sim 10^\circ$ range with an accuracy of $\sim 0.1^\circ$). Vertical alignment of the sample with the mirror focus is achieved by varying the SEM stage height. The alignment procedure is discussed in more detail in Section 2.3. The micropositioning system was designed by Iliya Cerjak and Hans Zeijlemaker at AMOLF.

Figure 2.4(d) shows a schematic of the CL setup. For spectral imaging purposes, the CL that is collected by the paraboloid is focused onto a 600- μm -diameter-core multimode fiber using an achromatic lens. This fiber diameter gives the system an effective focal area of $20 \times 20 \mu\text{m}^2$. Outside this area the the CL-emission is not efficiently collected by the fiber. The fiber is connected to a spectrometer (PI Acton SP2300i) with a liquid-nitrogen-cooled (LN) silicon CCD array (Princeton In-

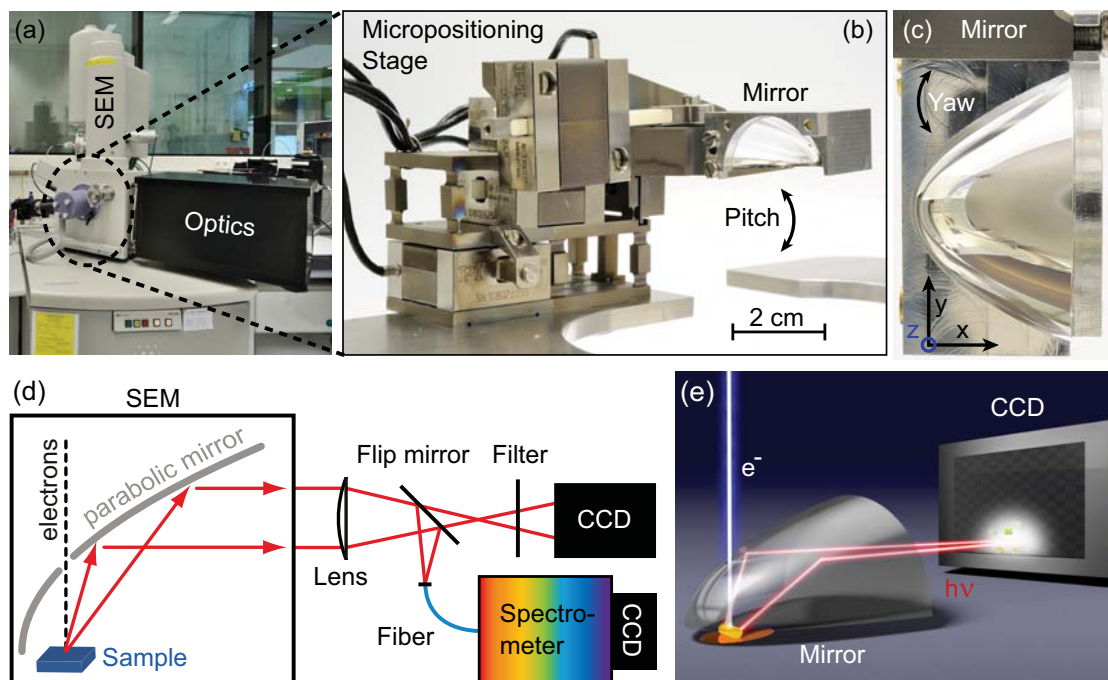


Figure 2.4: (a) Photograph of FEI XL-30 SFEI with CL optics box attached. (b) Inside the chamber a piezoelectric mirror positioning system is mounted which can be used to position a parabolic mirror in four dimensions (x, y , pitch, and yaw). (c) Photograph taken from the bottom of the mirror. (d) Schematic overview of the setup showing the different detection schemes. (e) Graphical representation of angle-resolved detection of CL on a 2D CCD array (image by Tremani). (Design in (b) by Iliya Cerjak and Hans Zeijlemaker, Pictures (a-c) by Henk-Jan Boluijt)

struments, Spec-10 100F/LN, 1340×100 pixels) which is used for spectral analysis of the CL emission. For all spectral measurements shown throughout this Thesis we have used hardware binning of the CCD pixels for a better signal-to-noise ratio (SNR) (100 times in the vertical direction and 4 times in the horizontal direction yielding an effective imaging array of 335×1 pixels). A spectrometer with a 1×1024 pixel LN-cooled InGaAs array for measurements in the infrared (1000 – 1800 nm) (PI OMA V) is also available for CL experiments in the near-infrared. Data taken with this IR system are not reported in this thesis.

2.2.1 Spectral imaging

By raster-scanning the tightly focused electron beam in 2D we can build up a 3D datacube by collecting a spectrum at each excitation position. At each position we can also collect the secondary electron signal so we can simultaneously collect a SEM image so that CL features can be correlated with geometrical features. We should note that the SEM images that are collected during CL sessions are of lower quality than for a regular sample inspection in a SEM, due to the presence of the parabolic mirror. First, the mirror prevents the sample from reaching the optimum

distance from the pole piece for imaging (sample can only get to 13 mm whereas 5 mm is optimal). This, and the disturbing effect of the large metallic mirror in between pole piece and sample precludes the use of the ultra-high resolution immersion mode in which a large magnetic field is applied to the sample to direct electrons towards the through-the-lens electron detector. Second, the metallic mirror also perturbs the focusing fields of the electromagnetic lenses, reducing the imaging resolution. Third, the mirror blocks a large part of the secondary electrons preventing them from reaching the detector, thereby greatly reducing the SE signal. In fact, due to the geometry of our SEM the SE detector is behind the parabolic mirror (on the closed side of the mirror) which is suboptimal. The collection efficiency could be enhanced by having the SE detector on the open side of the mirror. These issues reduce the SE imaging resolution to $\sim 5 - 10$ nm which is good enough for many optical studies. Even though only a fraction of the SEs are collected, the SNR in the images is still good enough because we typically use a beam current of ~ 1 nA which is 10 – 100 times higher than for regular SEM imaging.

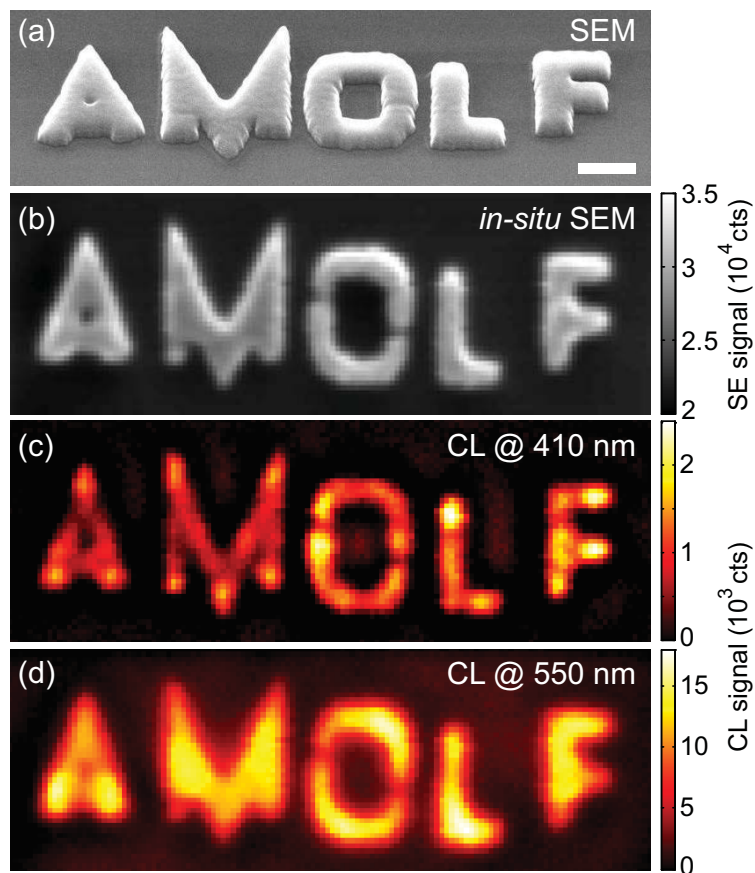


Figure 2.5: (a) High-resolution scanning electron micrograph of an AMOLF logo etched into a 100 nm thick Si layer on a 300 nm box layer of SiO₂, taken at a 52° stage tilt (scale bar corresponds to 250 nm). (b) Secondary electron signal collected during CL acquisition. 2D CL excitation maps of the structure at (c) $\lambda_0 = 410$ nm and (d) 550 nm integrated over a 20 nm bandwidth.

In order reliably scan a structure we use a drift-correction algorithm which compares SEM images of an area with a clear geometrical feature to correct for the effects of beam- and sample drift *in situ*. To minimize charging effects it is important to use a reasonably conductive substrate (metals, semiconductors, or thin insulators layers with conductive substrate). Electron-transparent Si_3N_4 or amorphous carbon TEM membranes have been employed successfully as well.

An example of a 2D spectral imaging measurement is shown in Fig. 2.5(c,d) for free space wavelengths of 410 and 550 nm respectively, together with a scanning electron micrograph of the structure taken at high resolution (a) and the SE image that was collected simultaneously during the CL scan (b). The structure on which the measurement was performed was an AMOLF logo etched into a 100 nm thick silicon device layer of an SOI wafer with reactive-ion etching (same fabrication procedure as described in Section 12.2). Because the feature size in Si characters is on the scale of the wavelength in silicon, optical resonances exist in this logo which can be visualized with CL imaging. The scanning pixel size in this measurement was $20 \text{ nm} \times 20 \text{ nm}$ and we used an integration time of 0.2 s/pixel at an 1 nA beam current. The total measurement time was 20 minutes for this scan. The background signal from the underlying oxide layer and silicon substrate were subtracted to visualize the modes in the logo. The excitation distributions clearly depend on wavelength which is expected for such resonant structures as will be discussed in Chapter 12.

2.2.2 Measuring angular emission profiles

Besides the spectral response knowledge of the angular emission profile of a nanostructure provides key information about the optical modes and band structure of a nanomaterial. The 2D lateral intensity profile of the parallel beam emanating from the paraboloid mirror is a direct measure of the angular emission. We measure the beam profile by directing it to a 2D Peltier-cooled (-70°C) back-illuminated CCD array (Princeton Instruments, PIXIS 1024B with a 1024×1024 pixel CCD chip). A schematic illustration of this type measurement is shown in Fig. 2.4(e). The achromatic lens is defocused to ensure that the beam fills the CCD array (demagnification factor of 2). This collection geometry is similar to “Fourier imaging”, also known as “conoscopic imaging”, or “defocused imaging” in microscopy [94, 95]. Such Fourier imaging consists of imaging the back-aperture of a microscope objective that contains the full wave vector information of emitted light onto a CCD. For this setup, the equivalent interpretation is that each point on the paraboloid is associated with a unique emission angle which can be described by a zenithal angle θ running from 0° to 90° (where $\theta = 0^\circ$ is normal to the surface) and an azimuthal angle ϕ running from 0° to 360° (where the paraboloid vertex is at $\phi = 180^\circ$). If the mirror is well-focused, each point in the CCD image corresponds to a single point on the paraboloid and as a result we can directly convert a CCD image to a radiation pattern for the upper hemisphere. Because of the mirror curvature the amount of solid angle collected per CCD pixel is not constant and the data points in θ and ϕ are not equally spaced. We use a triangular interpolation routine to

obtain an equidistant data set in θ and ϕ space, and we correct the data for the coordinate transformation to obtain emitted power per steradian (for details about the conversion from CCD image to angular pattern see Chapter 3). For the angular measurements we usually use 4×4 hardware binning of the CCD pixels for an improved SNR. For spectral selectivity 40 nm band pass color filters are used, which represents a good trade-off between spectral resolution and signal level. We use an electric flip mirror to switch between the spectral and angular functionalities of the CL setup.

In the beam path space is reserved for other optical components such as polarizers. Polarization sensitive angle-resolved CL is discussed in detail in Chapter 6. A commercial version of our ARCIS system has been developed recently by DELMIC B.V. A full description and a 3D movie of that system can be found at www.delmic.com/products/sparc/.

2.3 Mirror alignment

Accurate alignment of the parabolic mirror is key for efficient CL spectroscopy. The piezodriven micropositioning system allows accurate positioning of the mirror such that the electron beam hits the sample exactly in the mirror focus. If the mirror is aligned properly, the beam emanating from the mirror should have a semicircular shape similar to that of the mirror end facet. However, if there is a misalignment in x , y , or z (see coordinate system in Fig. 2.4(c)) the beam pattern is distorted in a way characteristic for that misalignment. Using raytracing calculations one can calculate what type of pattern should be expected for a given misalignment [96]. Figure 2.6 shows the effect of a misalignment in x , y , and z on the beam profile, both measured and calculated using raytracing. The pattern for the fully aligned mirror is shown in the top left image of Fig. 2.6. The measured images are taken without the lens flipped in, *i.e.* without demagnification, because in this configuration misalignments can be recognized and corrected more easily.

While the raytracing program uses absolute displacements in x , y , and z with respect to the ideal mirror focus position, the piezomotors do not give position feedback so do not provide absolute values for the mirror position. Actual misalignments for x and y in the experiment were derived by matching the raytracing pattern to the measured pattern for a given misalignment, and are given in each set of images (misalignment values are given relative to the mirror focus position). The SEM stage does have absolute position feedback so for z the measured stage positions are used as input for the raytracing program. Overall there is good agreement between the raytracing and the measured patterns, both in the pattern shape and asymmetry. The differences are explained by imperfections in the mirror due to the diamond turning fabrication process (clearly visible as radial distortions in the measured images), and small differences in pitch and yaw angle, which are assumed to be zero in the raytracing program and the experiment.

During the mirror alignment we can recognize the distorted patterns and move

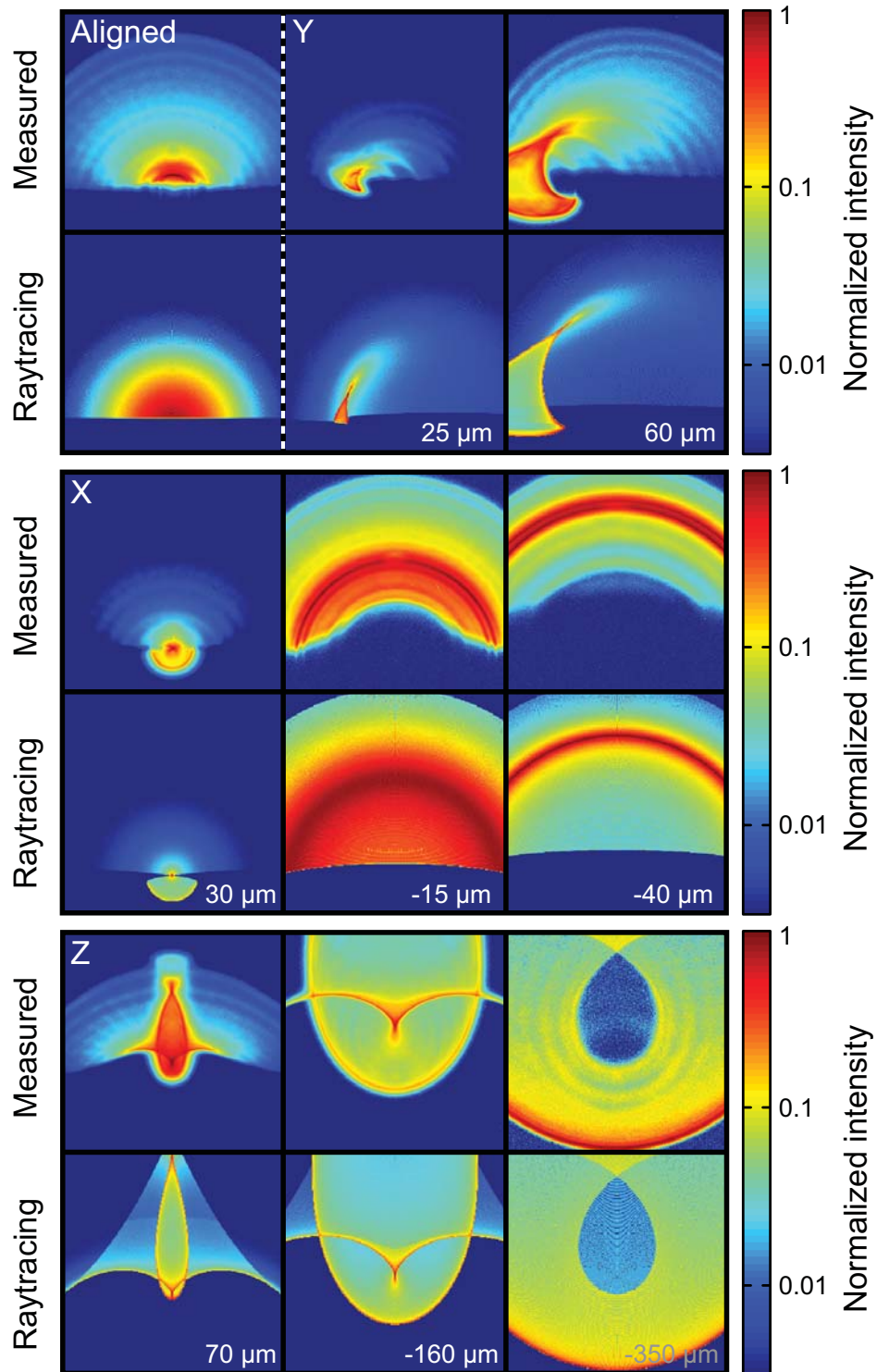


Figure 2.6: 2D CCD images when properly aligned (top row left) and for various misalignments in y (top row right) x (second row) and z (bottom row). Under each measured image the corresponding raytracing image is shown. For x and y the absolute misalignment is estimated by matching the raytracing images to the measurements. Absolute position values from the SEM stage were used for z .

the piezomotors accordingly to achieve a fully aligned system (see Fig. 2.6). For an experienced user this alignment procedure is straightforward and can be finished easily within 15 minutes, even if the initial misalignment varies due to non-reproducibility of mounting the piezosystem in the SEM. A next step is to automate the alignment procedure, which was beyond the scope of this project.

2.4 Measuring in k -space with a pinhole scanner

In the angular collection scheme as shown in Fig. 2.4 we have good angular precision but the wavelength selectivity is determined by the spectral filters which in our case have a bandwidth of 40 nm. For many nanophotonic systems, such as those supporting plasmonic resonances, this is not a problem because the spectral features are usually quite broad. However, to study high- Q cavities or periodic/apertic photonic crystals with a complex dispersion relation, it would be desirable to have much higher spectral resolution (ideally down to ~ 1 nm). Using spectral bandpass filters is impractical for this purpose. Therefore we have

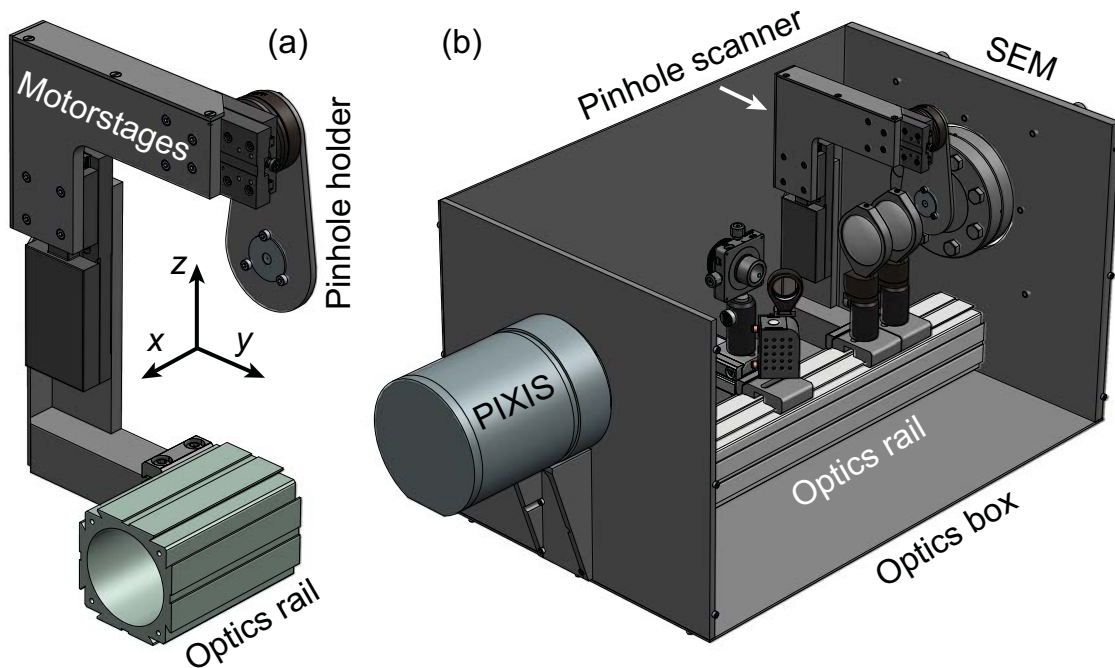


Figure 2.7: (a) Pinhole scanner design. The position of the motor stages and pinhole are indicated. For reference we have included the coordinate system. The scanner is clamped to the optics rail which is aligned with the optical axis of the parabolic mirror. (b) Implementation of the pinhole scanner in the optics box. The position of the SEM is indicated (also see Fig. 2.4(a) to see how the optics box is attached to the SEM). In this image the PIXIS 2D camera has been moved to the outside of the box to create more space for additional optics. (Images and design by Iliya Cerjak)

designed a complementary detection system similar to the system developed by Yamamoto *et al.* [97, 98]. It is based on a 2D pinhole scanner which acts as a filter in momentum-space. By choosing the pinhole size one can find the ideal tradeoff between signal level and angular resolution. Pinholes with 100, 150, and 500 μm diameter can be used. If we include the demagnification factor the collection area of a 4×4 binned CCD pixel of the 2D PIXIS camera is equivalent to a pinhole with a diameter of 117 μm . The smallest pinhole size thus roughly corresponds to one binned CCD pixel. After the pinhole one can use the spectrometer to measure the momentum-filtered spectrum with 1 nm spectral resolution for a broad wavelength range determined by the type of diffraction grating that is used in the spectrometer. In combination with the ability to very precisely locally excite a structure this allows for a new way of CL characterization. Although this measurement technique in principle is much slower than the angle-resolved detection scheme as described in Section 2.2, in many cases the measurement time can be significantly reduced by taking advantage of symmetries in the structure.

A schematic drawing of the pinhole scanner is shown in Fig. 2.7(a). Fig. 2.7(b) shows how the scanner is implemented in the optics box which is attached to the SEM (see Fig. 2.4(a)). The pinhole scanner that we have designed can be inserted and removed mechanically from the beam path so one can easily switch between different measurement configurations. The pinhole movement is controlled by two motorized translation stages which allows pinhole scanning in the xz -plane with a minimum stepsize of 0.05 μm (bidirectional repeatability = 1.6 μm and a backlash < 6 μm). This is more than sufficient for precise angular measurements as these require a typical stepsize of $\geq 50 \mu\text{m}$. The pinhole holder is large enough such that the rest of the beam is always blocked. The scanner geometry was designed by Iliya Cerjak. The pinhole scanning and camera data collection are synchronized through a software program developed by Sander van de Haar and Sjoerd Wouda, all at AMOLF.

2.5 Electron energy-loss spectroscopy

As described in Section 2.1 EELS is a technique that is complementary to CL. We have performed EELS experiments (Chapter 10) in a 300 keV aberration-corrected FEI Titan transmission electron microscope (Fig. 2.8(a)) located at the Nanocharacterization Laboratory at Stanford University (CA, USA). This TEM is equipped with an electron monochromator and Gatan EEL spectrometer in which electrons of different energies are separated by a magnetic field and subsequently imaged by a camera (Fig. 2.8(b)). The EELS measurements are performed in scanning transmission electron microscopy (STEM) mode where the electrons are focused to a spot of ~ 1 nm. During the EELS acquisition one can simultaneously collect a STEM image using the annular dark field detector (ADF) as the EELS spectrometer only collects electrons close to the beam normal.

With EELS one can study core transitions to spatially resolve the atomic com-

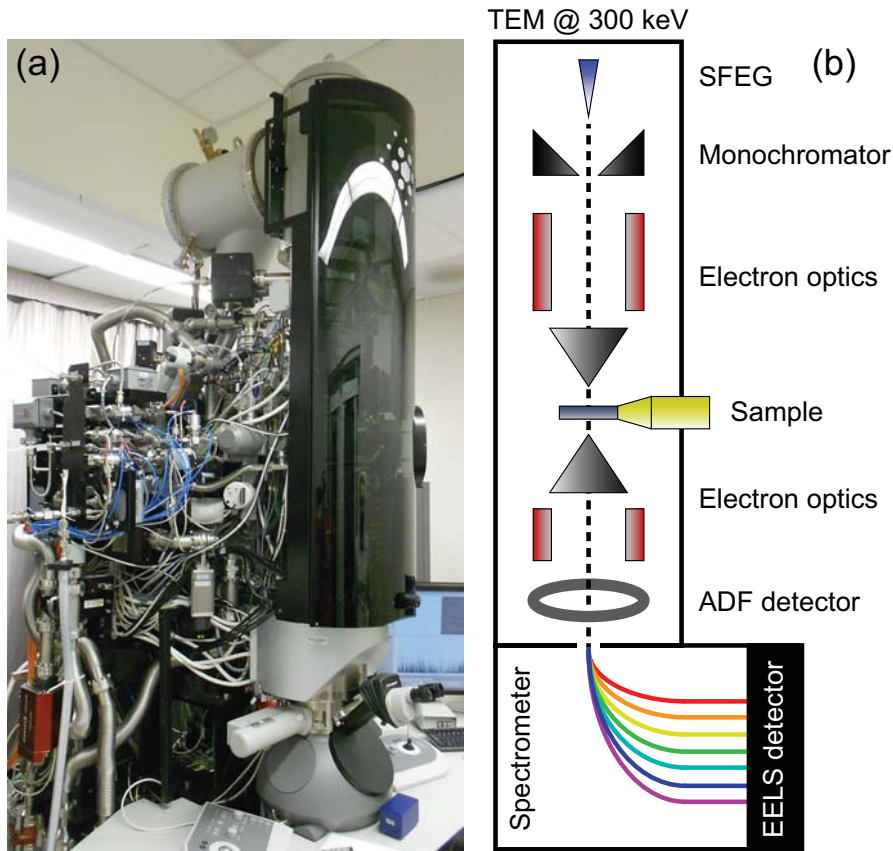


Figure 2.8: (a) Photograph of FEI Titan TEM at Stanford University (b) Schematic of the EELS setup. After interaction with the sample the electrons are separated in energy by a magnetic field. Subsequently the electron signal is converted to an optical signal by a phosphor screen and detected by a CCD camera.

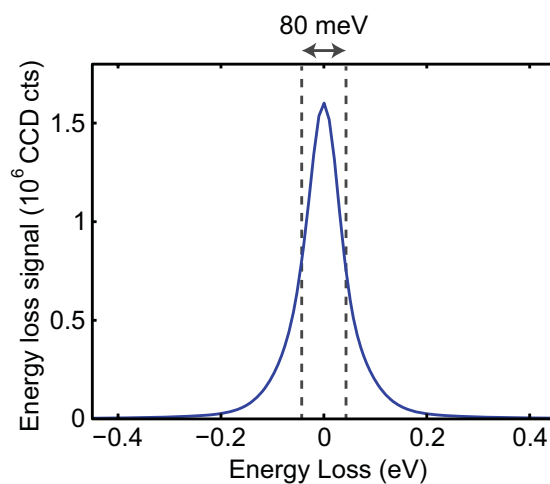


Figure 2.9: EELS spectrum showing zero-loss peak measured through a punctured membrane (vacuum) for 300 keV electron energy. The FWHM is indicated by the gray dashed lines (80 meV).

position of a structure [99]. The extreme sensitivity of this technique is apparent from the fact that atomic defects in graphene [100] or specific atom columns in crystals can be resolved for instance [101]. Usually these transitions involve high energies (typically > 100 eV) and as result the corresponding loss peaks are well separated from the primary beam energy and can be resolved quite easily. However, for EELS measurements in the visible/NIR spectral regime the energy-loss features are very close to the “zero-loss” peak (ZLP) of the primary beam. It is thus essential to minimize the energy width of the primary beam. State-of-the-art TEMs have efficient monochromators which allow for a very narrow energy distribution of the electrons in the beam. One can measure this distribution by measuring an EELS spectrum through a punctured TEM membrane (through vacuum). Such a measurement is shown in Fig. 2.9 for 300 keV electrons, measured using the Stanford TEM. Because there are no sample interactions only the zero-loss peak corresponding to the unperturbed primary beam is observed. In general, samples prepared for TEM are so thin that a large fraction of the electrons are transmitted without interacting with the sample and hence this ZLP is always clearly present in any EELS measurement. In this case we find a full-width half-maximum (FWHM) for the ZLP of 80 meV which is only 2.7×10^{-7} of the average electron energy, and good enough for resolving spectral features on the tail of the ZLP in the spectral region of interest.

3

Angle-resolved cathodoluminescence imaging spectroscopy

In this Chapter we present a cathodoluminescence spectroscopy technique which combines deep subwavelength excitation resolution with angle-resolved detection capabilities. The cathodoluminescence emission is collected by a paraboloid mirror and is projected onto a 2D CCD array. The azimuthal and polar emission pattern is directly deduced from the image. As proof of principle, we use the technique to measure the angular distribution of transition radiation from a single crystalline gold surface under 30 keV electron irradiation. We find that the experiment matches very well with theory, illustrating the potential of this technique for the characterization of nanophotonic structures.

3.1 Introduction

In nanophotonics, the research field concerned with the manipulation of light at the nanoscale, basic building blocks like waveguides [15], nanoantennas [29], and nanocavities [102], often have subwavelength geometrical features. Optical phenomena in these structures cannot be resolved with far-field optical microscopy due to Abbe's law of diffraction that provides a limit to the smallest distance over which individual objects can be distinguished. Several spatially resolved spectroscopy techniques have been developed to reach a resolution

below that limit, including scanning near-field optical microscopy (SNOM) [94], stimulated emission depletion (STED) microscopy [3], photoactivatable localization microscopy (PALM) [5], and stochastic optical reconstruction microscopy (STORM) [6].

Alternatively, cathodoluminescence (CL) imaging spectroscopy is a technique that has a high spatial resolution as well, as it uses an electron beam as an excitation source. In CL spectroscopy, a focused electron beam is raster scanned over a sample. The electron beam effectively acts as a supercontinuum light source that excites the sample according to the local density of optical states (LDOS) [63, 103]. Previous work has shown that CL imaging spectroscopy is a powerful technique for probing (nano)photonic environments. In particular, in the field of plasmonics, where large spatial variations in the LDOS can occur on deep subwavelength length scales, CL spectroscopy has proven to be an important characterization technique [64, 102, 104].

So far, the CL technique was limited to measuring spectral response as a function of excitation position, and no information about the total angular distribution of the CL emission could be collected. Yamamoto and coworkers developed a technique by which the angular distribution of CL was measured by translating a pinhole in front of a CCD camera, thus collecting point-by-point angular data [97, 98]. In this Chapter, we present a further advanced experimental technique to resolve the angular distribution of the CL emission. We demonstrate the technique by measuring transition radiation (TR) for a single crystal gold substrate.

3.2 Fourier microscopy with a paraboloid mirror

In our CL system we measure the angular profile by projecting the beam emanating from the paraboloid mirror onto a 2D CCD camera (see Fig. 2.4 for setup configuration). Figures 3.1(a) and (b) show how each pixel in the 2D CCD image is mapped onto angles θ and ϕ , calculated using the known geometrical properties of the paraboloid and the experimental settings:

$$d_{eff} = d_{pix} n_{mag} b \quad (3.1a)$$

$$y = y_{pix} d_{eff} \quad (3.1b)$$

$$z = z_{pix} d_{eff} + d_{foc} \quad (3.1c)$$

$$r = \sqrt{y^2 + z^2} \quad (3.1d)$$

$$x = ar^2 - \frac{1}{4a} \quad (3.1e)$$

$$\theta = \cos^{-1} \left(\frac{z}{\sqrt{x^2 + r^2}} \right) \quad (3.1f)$$

$$\phi = \tan^{-1} \left(\frac{y}{x} \right) \quad (3.1g)$$

where d_{eff} is the effective pixel size which can be calculated from the hardware binning setting in the CCD array b , the individual CCD pixel size d_{pix} (13 μm), and the demagnification factor of the image by the achromatic lens n_{mag} which corresponds to 2.01 in this case. y_{pix} and z_{pix} are the CCD pixel numbers in the y and z direction respectively, from which the x and z distance from the virtual paraboloid apex can be calculated. Note that one needs to add the focal length of the off-axis paraboloid d_{foc} (0.5 mm) to get the correct z -distance from the apex. Using y and z we can find x , where a is the parabola coefficient (1/10). The solid angle covered per pixel (Ω) which is used to correct the data to photon flux per unit of solid angle is given by

$$\Omega = d_{eff}^2 \frac{2ar^2 - x}{(x^2 + r^2)^{3/2}} \quad (3.2)$$

Here we take the assumption that the pixels are small enough that we can locally regard the mirror surface flat so that we neglect the curvature of the mirror within the projected area of one CCD pixel [98]. Figure 3.1(c) shows Ω for our mirror geometry. Integrating over all pixels that fall within the beam gives a total acceptance angle of 1.46π sr, equivalent to a NA = 0.96 for a microscope objective. Taking only the half space on the closed side of the mirror (see Fig. 2.4(c-e)), the collected solid angle is 0.96π sr, *i.e.*, 96% of the radiation; the remaining 4% leaves through the small opening between mirror and sample. Since we have the ability to rotate the sample by 180° , we can almost entirely reconstruct the emission pattern for the upper hemisphere, corresponding to an effective NA of 0.999.

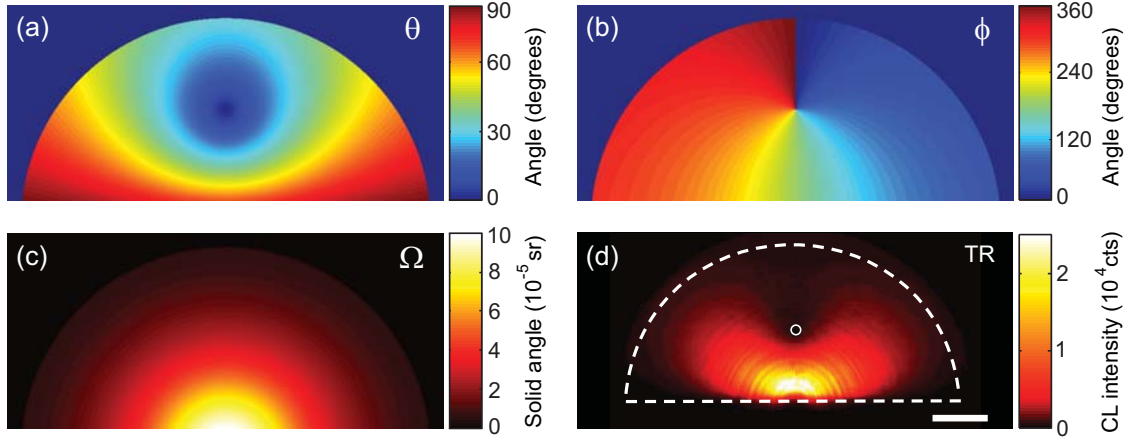


Figure 3.1: Maps relating pixel position in the CCD image to (a) polar angle θ , (b) azimuthal angle ϕ , and (c) the solid angle per pixel, allowing conversion to an absolute radiation pattern. (d) CCD image showing the measured transition radiation from a single-crystalline gold sample. The white dashed line indicates the mirror contour, and the white circle indicates the position of the hole in the mirror. The scale bar is 2 mm which corresponds to 154 CCD pixels.

3.3 Angular pattern of transition radiation

When an electron passes through an interface between two dielectric environments, it induces a dipole moment on the surface which radiates into the far field which is known as (TR). The TR angular pattern is very similar to that of a vertical point dipole on a surface [103]. To test the angle-resolving capabilities of the setup, we measured the TR emission from a polished single-crystalline Au (100) surface irradiated with 30 keV electrons over the full spectral band of the CCD. A CCD image is recorded with a collection time of only 10 s. For each measurement, we collected an additional image with the electron beam blanked as a reference. Subsequently, this signal was subtracted from the TR-measurement to remove dark counts from the CCD and signal originating from other sources than the sample.

Figure 3.1(d) shows a CCD image obtained using the method described above. The semicircular shape of the paraboloid end face can clearly be recognized. The dark concentric rings in the image are caused by radial imperfections in the mirror which are inherent to the diamond turning fabrication process of the mirror. Also, the hole in the mirror is visible close to the center of the beam. The area around the hole corresponds to emission angles that are almost normal to the surface. This area is relatively dark, while other parts corresponding to more grazing angles appear to be brighter (see Fig. 3.1(a)). This particular pattern in the CCD image points towards a toroidally shaped emission pattern as predicted for transition radiation.

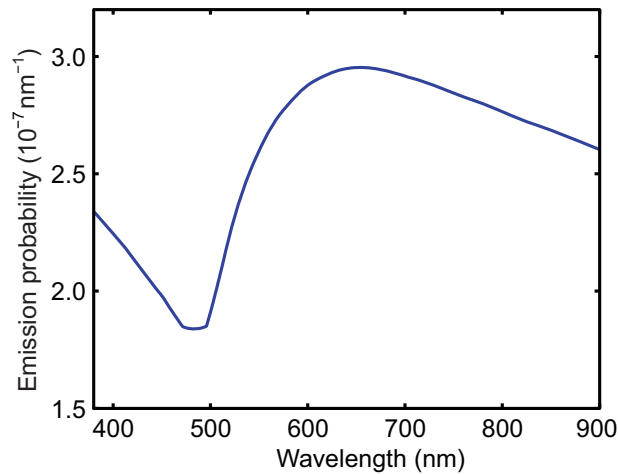


Figure 3.2: TR emission probability per incoming 30 keV electron per nm bandwidth as a function of wavelength for the entire upper hemisphere calculated for a gold substrate.

Figure 3.2 shows the probability of exciting a TR photon on a gold surface integrated over the entire upper hemisphere, which was calculated using the theory described in Ref. [63] and tabulated optical constants [105]. Broadband emission is expected in the 350 – 950 nm spectral band, with a dip around 500 nm which is related to the plasmon resonance frequency in gold. Integrating the probability

of TR emission from 350 to 950 nm, we find a generation rate of 10^{-4} photons per incident electron. In this experiment, a current of 12 nA was used which should then generate 8×10^6 photons s^{-1} . Taking into account the acceptance angle of the mirror, known reflection losses in the optics, and the quantum efficiency of the CCD camera, we expect $\sim 4 \times 10^6$ photons s^{-1} to be detected by the CCD camera. Integrating over all pixels in Fig. 3.1(d), we find a collection rate of 3.9×10^6 photons s^{-1} ; similar to the calculated value. This indicates that the angle-resolved CL technique provides an accurate absolute measurement of the emitted radiation intensity.

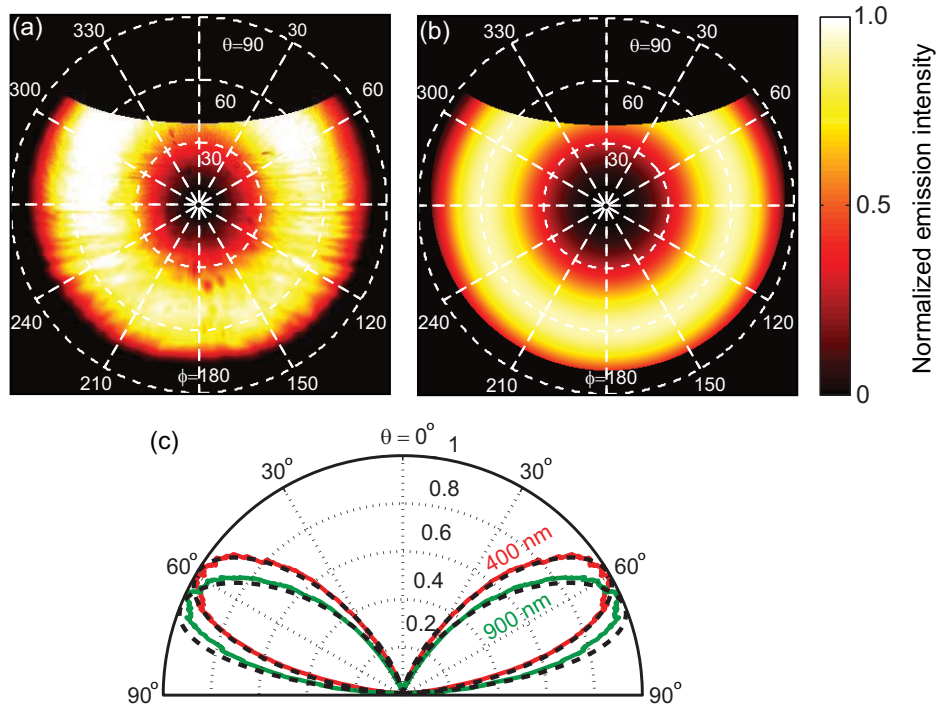


Figure 3.3: Angle-resolved cathodoluminescence emission patterns of the transition radiation for single-crystalline Au (30 keV e^-). (a) Normalized measured emission pattern collected without color filter showing the total emission intensity as a function of emission angles θ and ϕ . (b) Normalized calculated emission pattern for the same spectral range as in (a). (c) Emission pattern integrated over ϕ for transition radiation at $\lambda_0 = 400$ and 900 nm (solid lines) and theory (dashed lines).

To investigate the directionality of the emission in more detail, the CCD image in Fig. 3.1(d) was converted into a radiation pattern using the conversion maps shown in Figs. 3.1(a-c). The data were interpolated to yield points that are equally spaced in θ and ϕ . Figure 3.3(a) shows the angular distribution of TR emission mapped onto a polar grid where the radius represents polar angle θ , and the polar plot angle represents azimuthal angle ϕ . Fig. 3.3(b) shows the calculated angular distribution for 30 keV electron beam excitation integrated over the spectral sensitivity band of the CCD camera (350 – 1000 nm). Data for angles that are not col-

lected by the mirror are set to zero (black). CL emission close to the surface normal (around $\theta = 0^\circ$) is not collected because of the hole in the mirror. Radiation emitted almost grazing to the surface ($\theta > 85^\circ$) is also not collected because of the small space between mirror and sample (0.5 mm). The largest loss in acceptance angle, clearly visible in the upper part of Figs. 3.3(a) and (b), corresponds to the open part of the paraboloid (see Fig. 2.4(b)). The experiment clearly shows a toroidal emission pattern, in good agreement with calculation. Indeed, the radiation pattern is very similar to that of a vertically oriented point dipole located close to a reflective surface [94].

Next, we investigate the wavelength dependence of the angular radiation pattern. Band pass filters (40 nm) were placed in the beam path with center wavelengths λ_0 ranging from 400 nm to 900 nm in steps of 50 nm, and emission patterns were measured at each wavelength. For these measurements, an integration time of 120 s was used to enable accurate measurements at 900 nm where the sensitivity of the CCD detector is lowest. To accurately compare experiment and theory, the emission patterns were integrated over azimuthal angle ϕ . Data in the range $\phi = 150^\circ$ - 210° were not taken into account as this corresponds to the section where the aberrations in the mirror are largest (see Fig. 3.3(a)). Figure 3.3(c) shows the normalized CL intensity as function of θ for λ_0 400 nm and 900 nm together with theoretically predicted emission patterns. We find excellent agreement between experiment and theory. The overall shape of the lobes is well reproduced, and the small difference in lobe orientation between these wavelengths (peak emission around $\theta = 60^\circ$ for 400 nm and around $\theta = 70^\circ$ for 900 nm) is clearly observed.

3.4 Conclusions

In conclusion, we have presented an experimental technique for angle-resolved cathodoluminescence spectroscopy. We determined the angular distribution of transition radiation from a single crystal gold substrate and found that the experimental results agree very well with theory. A photon count rate in the order of 10^6 photons s^{-1} is observed, corresponding closely to the calculated value. The mirror collection geometry corresponds to an effective NA = 0.96. Combining the angle resolved capabilities with the high spatial excitation resolution of electron microscopy makes this cathodoluminescence technique an interesting tool for studying a wealth of optical phenomena in a wide variety of photonic nanostructures.

4

Directional emission from plasmonic Yagi-Uda antennas probed by angle-resolved cathodoluminescence spectroscopy

Optical nanoantennas mediate optical coupling between single emitters and the far field, making both light emission and reception more effective. Probing the response of a nanoantenna as a function of position requires accurate positioning of a subwavelength sized emitter with known orientation. In this Chapter we use a high-energy electron beam as a broad band point dipole source of visible radiation, to study the emission properties of a Yagi-Uda antenna composed of a linear array of Au nanoparticles. We show angle-resolved emission spectra for different wavelengths and find evidence for directional emission of light that depends strongly on where the antenna is excited. We demonstrate that the experimental results can be explained by a coupled point dipole model which includes the effect of the dielectric substrate.

4.1 Introduction

Plasmonic nanoantennas have gained great interest because of their ability to enhance and redirect light emission from single emitters [29]. Promising applications include spectroscopy [106, 107], single-photon sources, single photon ab-

sorption [108], and light harvesting [109]. A wide variety of different optical antenna geometries have been studied, ranging from single metal nanoparticles [13, 110, 111] to dimers with narrow gaps [38] and more complex multi-element structures [39, 112].

A particularly well-known antenna for radio waves is the Yagi-Uda antenna [33]. Classical Yagi-Uda antennas consist of a single feed element which is actively driven by electrical current and which is surrounded by parasitic resonant scattering elements that couple through dipole-dipole coupling. The collective coherent scattering of the antenna elements can result in a highly directional emitter or receiver [33, 113]. The Yagi-Uda antenna design can be scaled down in size for visible wavelength operation by using metallic nanoparticles, which have a localized surface plasmon resonance, as proposed in Refs. [113–116].

Similar to their radio wave counterparts it has been shown recently that such plasmonic arrays act as efficient nanoscale receiving antennas for light due to dipole-dipole coupling [117, 118]. Confocal microscopy measurements have shown that they have the ability to concentrate an incident light beam at a well-defined wavelength-dependent position on the antenna array [114]. Conversely, it has been shown that metal particle arrays can also be used to direct light into a well-defined wavelength-dependent direction, provided one manages to position a single emitter on a single antenna element [39]. On the basis of these reports, it is anticipated that designed plasmonic and metamaterial clusters can be used to fully control directionality, polarization, and emission rate of single quantum sources.

Optical antenna properties are often probed by using far-field optical microscopy techniques. By their very nature, however, nanoantennas have features much smaller than the wavelength of light making it impossible to spatially resolve their emission properties with free space optics. Several techniques have been developed recently to address this problem. It has been shown that chemically functionalized quantum dots positioned close to an antenna can be effective local probes [39], although controlling the position, quantity, and quality of the quantum dots can be challenging. Nitrogen vacancy centers (NV centers) in nanodiamonds have also been used successfully as local excitation sources of plasmon antennas. Single nanocrystals including NV centers can be positioned at will in nanoantenna geometries using atomic force microscopy tips to position either the NV centers or metal antenna constituents on a substrate [119, 120]. However, it is challenging to obtain full 2D control using this method.

In scanning near field optical microscopy (SNOM) one does have the ability to raster scan the excitation over the antenna [121, 122]. However, for efficient excitation the tip has to be in close proximity to the antenna, thereby perturbing the dielectric environment and thus affecting the experiment. To obtain further insight in the directional behavior of Yagi-Uda antennas, an alternative technique is required, which enables measurements of the angle-resolved response at any desired wavelength and excitation position on a single nanoantenna.

In this Chapter we use a 30 keV electron beam focused to a nanoscale spot

to excite plasmonic Yagi-Uda antennas with a spatial resolution of ~ 10 nm. We collect the antenna radiation (cathodoluminescence, CL) using a paraboloid mirror integrated in an electron microscope and determine the angle-resolved radiation spectrum, as a function of excitation position. We find evidence for directional photon emission that depends strongly on the excitation position and demonstrate that the experimental results are explained by an analytical point dipole model. The experiment illustrates the potential of angle-resolved CL measurements for the characterization of a wide array of photonic nanostructures.

4.2 Sample fabrication

We fabricated gold nanoparticle antenna arrays consisting of five cylindrical nanoparticles on a crystalline silicon substrate using electron beam lithography and liftoff. We used a 350 nm thick layer of ZEP520A as positive resist for electron beam lithography with a Raith E-line system. After exposure and development, a gold layer was deposited using thermal physical vapor deposition. After lift-off in *n*-methylpyrrolidone (NMP) at 65 °C for 3 h, we obtain gold nanoparticles on silicon with a diameter of 98 nm, a height of 70 nm, and a center-to-center distance of 135 nm. This geometry results in a total length of 638 nm which is roughly equal to one visible wavelength. Figures 4.1(a,b) show a scanning electron micrograph and a schematic representation of the antenna array under investigation.

4.3 Single-particle response

A 30 keV electron beam passes through a hole in a parabolic mirror and irradiates a 10 nm spot on the sample, thereby producing CL emission. The collected CL either can be focused onto a fiber which is connected to a spectrometer (bottom right) or is sent to a 2D CCD array (top right). Defocused arrangement allows us to retrieve angular information (see Chapters 2 and 3 for details).

To find the response of an individual particle, we collect the CL emission as function of excitation position (10×10 nm pixel size) for an isolated particle with the same dimensions as the particles in the array. In Fig. 4.1(c) the CL emission spectrum integrated over all excitation positions on the particle is shown. The data were corrected for the wavelength-dependent system response using the transition radiation of a single crystal Au sample [103]. Furthermore the background radiation due to the silicon substrate was subtracted. The spectrum shows one strong peak at 577 nm which we attribute to a dipolar localized surface plasmon resonance along the vertical axis of the cylindrical particle. Note that the resonance is at much shorter wavelength than for similar particles on a silicon substrate under optical excitation [123], which we attribute to the fact that the electron beam excites these particles along their vertical axis.

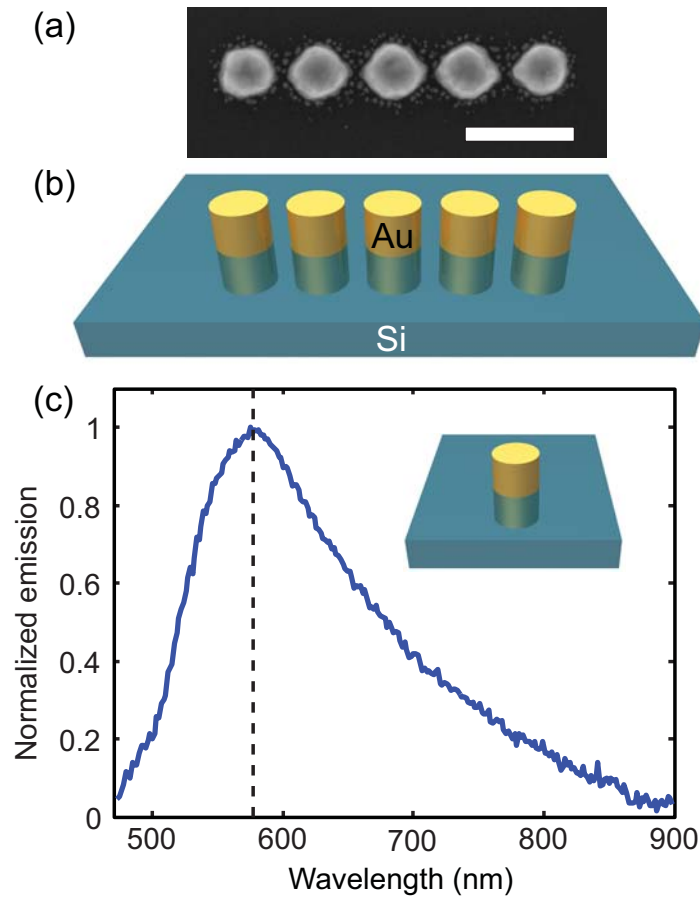


Figure 4.1: (a) Scanning electron micrograph of a plasmonic Yagi-Uda antenna of gold particles (diameter 98 nm, height 70 nm, on Si). Scale bar represents 200 nm. (b) Schematic of the antenna. (c) Normalized CL-emission spectrum as function of wavelength for a single nanoparticle with similar dimensions to the particles in the array. The peak corresponds to 2×10^4 counts/s at 1 nA per 1.7 nm bandwidth.

4.4 Spectral imaging of a Yagi-Uda antenna

To study the spectral response of the antenna, we raster scan the electron beam (1 nA current) over the nanoantenna in 10 nm steps with a dwell time of 0.1 s per pixel and collect an entire visible spectrum at each position. Figure 4.2(a-c) shows the CL intensity as a function of e-beam position for center wavelengths of 500, 600, and 750 nm integrated over a bandwidth of 10 nm. The data were corrected for the silicon background radiation. Evidently the individual particles can clearly be distinguished as excitation points that generate large cathodoluminescence signals in all images. Given the small particle size (~ 100 nm) compared to the wavelength, the images demonstrate the very high spatial resolution of the CL imaging technique. From the SEM image in Fig. 4.1(a) it is clear that all five particles have approximately the same size, which suggests that they will have similar polarizabilities. However in the images of Fig. 4.2 the outer particles are significantly brighter than the center

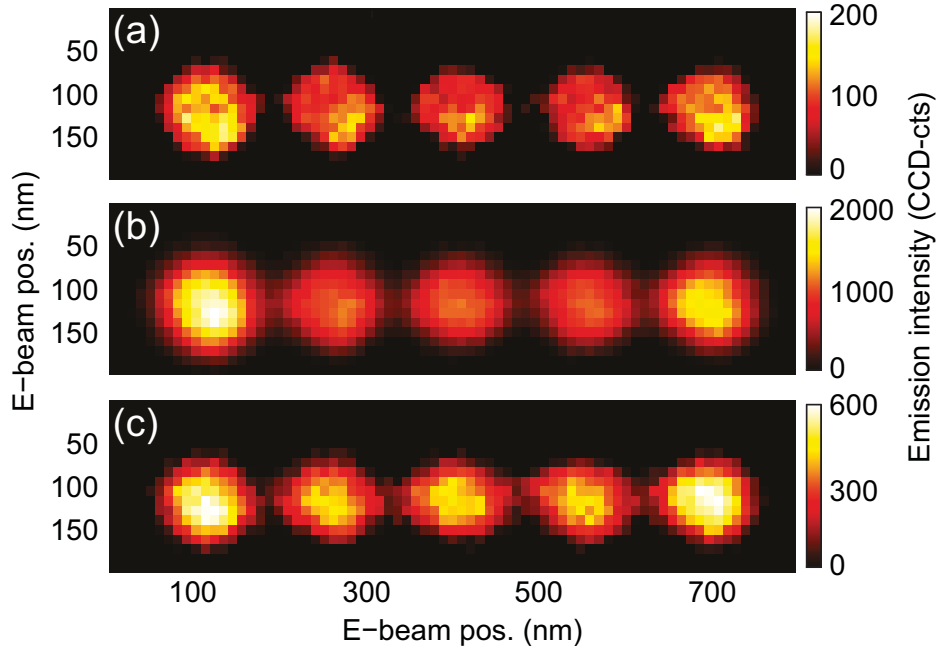


Figure 4.2: Spatially resolved excitation maps of the nanoantenna shown in Figure 4.1a, showing CL intensity as function of e-beam position for (a) 500 nm, (b) 600 nm, and (c) 750 nm detection wavelength integrated over a 10 nm bandwidth. Integration time per pixel is 0.1 s.

particles, with a relative contrast that is highest for $\lambda_0 = 600$ nm (emission is ~ 1.4 times stronger for outer particles). This observation indicates that coupling between the particles is important for the overall emission intensity that is generated upon local excitation.

4.5 Antenna radiation patterns

Next we turn to measuring the radiation pattern of a nanoantenna as a function of wavelength and excitation position, by using the angle-resolved CL collection. To this end, we measure the emission pattern of the antenna for wavelengths from 400 to 750 nm in steps of 50 nm using 40 nm bandpass color filters. To increase the signal-to-noise ratio, we used 2×2 hardware binning of the CCD pixels, increased the current to 10 nA, and extended the dwell time to 40 s. We excite each of the five particles in its center and collect a radiation pattern for each of the excitation positions. To eliminate background signal, we subtract a reference measurement from a bare silicon substrate collected using the same color filter and dwell time.

The result of such a measurement for excitation of the outer left particle (see sketch, Fig. 4.3(a)) collected at $\lambda_0 = 500$ nm is shown in Fig. 4.3(b). The data are presented in a polar plot where the radius represents θ , the polar angle represents ϕ , and the color scale gives the normalized emission intensity. The measurement

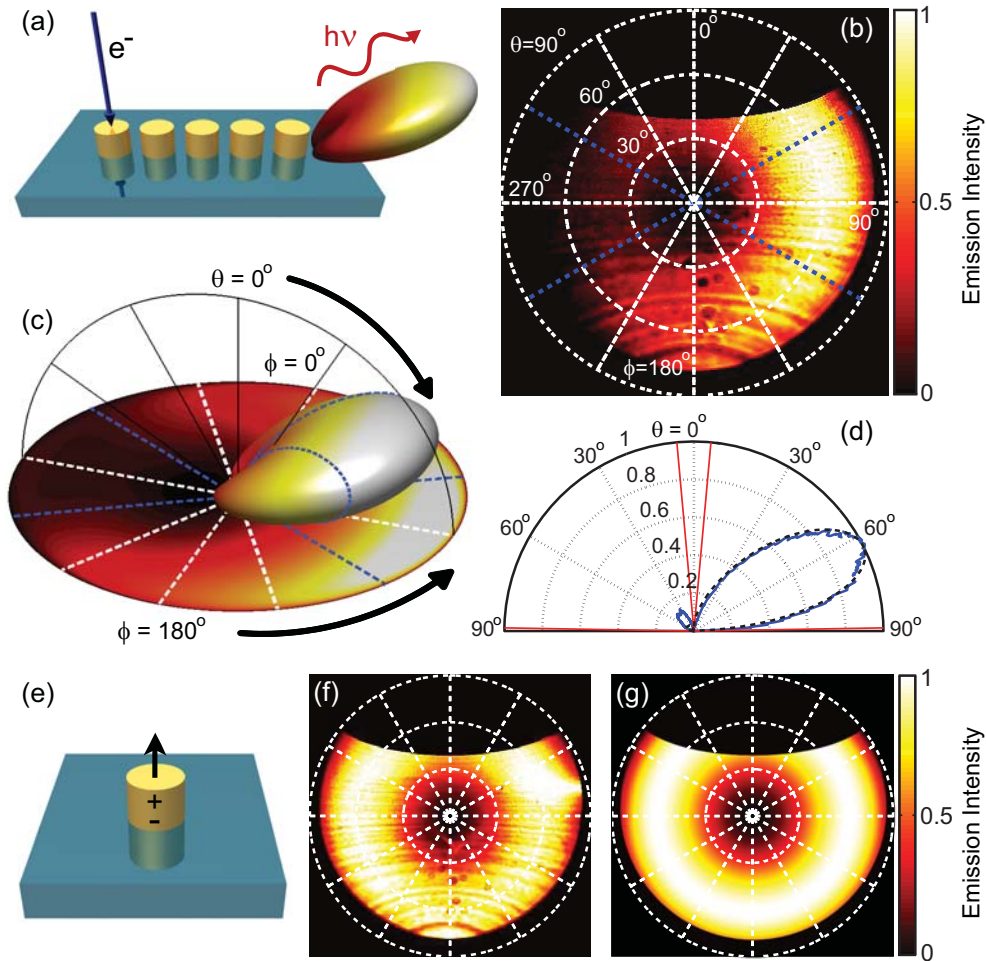


Figure 4.3: (a) Schematic of the excitation geometry. (b) CL emission intensity as a function of angle collected with a 40 nm band-pass filter centered at 500 nm, for excitation of the outer left particle. The blue dashed lines indicate the range of ϕ that is integrated to obtain the crosscut shown in (d). (c) 3D representation of theoretical radiation pattern for this excitation position and wavelength, together with a projection onto a 2D grid. Note that in this projection the spacing of θ is not equidistant like in (b). The blue lines again indicate integration limits for the crosscut. (d) Cross-cut through the angular data showing CL intensity as a function of θ (blue curve) together with theory (black dashed curve). The red lines indicate the range of θ that cannot be collected by the mirror. (e) Schematic of a single particle which is vertically polarized by the electron beam. (f) CL-emission intensity as a function of angle for a single nanoparticle integrated over all wavelengths (350 – 1000 nm). (g) Calculated emission pattern for a vertically oriented point dipole spaced 35 nm above a silicon substrate, emitting at 577 nm.

reveals that when the leftmost particle is excited, most cathodoluminescence is collected in a single lobe that points toward the right end of the antenna, *i.e.*, to the side away from the excitation point. The dark region that extends from $\phi = 300^\circ$ to $\phi = 60^\circ$ for $\theta > 40^\circ$ is due to the fact that we do not collect part of the radiation pattern due to the mirror geometry. Similarly, a small part of the radiation around

$\theta = 0^\circ$ is not collected due to the hole in the mirror that allows the electron beam to pass from the SEM pole piece to sample. To more clearly visualize the directionality of emission that is evident from the polar plot in Fig. 4.3(b), we extract a cross-cut of the data (blue curve) by integrating over ϕ from 60° to 120° and from 240° to 300° yielding CL intensity as function of θ only (Fig. 4.3(d)). This integration omits that part of the hemisphere where we do not collect emission due to the mirror geometry and the part where the aberrations in the mirror are largest (ϕ between 120° and 240°). The cross cut reveals a prominent lobe at $\theta = 60^\circ$, with a width of $\sim 20^\circ$ that is ~ 5 times stronger in intensity than the small lobe that extends to the left. For reference we show that the measured radiation pattern of a single nanoparticle is isotropic in ϕ (Fig. 4.3(f)) directly implying that the directionality is due to coupling between particles. Furthermore, the single particle data show that each single particle in the array is equivalent to a vertically oriented dipole above a silicon substrate when excited with the electron beam (see theory in Fig. 4.3(g)) [94].

Figure 4.4 extends the angle-resolved data set shown in Fig. 4.3 to different wavelengths and excitation positions. The top row in Fig. 4.4 shows the radiation patterns for $\lambda_0 = 500, 600,$ and 750 nm for excitation of the outer left, center, and outer right nanoparticle. The radiation pattern clearly depends strongly both on wavelength and on the position of the electron beam. As expected the emission pattern is roughly mirror symmetric for all wavelengths when the center particle is excited. For excitation of the outer particles, however, the emission is highly directional. Interestingly, the sign of the directionality reverses for increasing wavelength. For 500 and 600 nm the radiation is emitted along the particle array away from the excited particle while for 750 nm it is emitted in the opposite direction (on the side of the excited particle). To our knowledge this data set represents the first measurements in which the directionality of a multielement nanoantenna can be probed and changed at will by moving the excitation spot.

We now turn to the interpretation of our observation that the emission from an Au particle array that is excited at one of its ends is directional. Qualitatively, this switching behavior is well-known for Yagi-Uda arrays [39, 114, 115] and can be explained by the fact that the Yagi-Uda antenna is a traveling wave antenna with a radiation pattern that is the coherent sum of the radiation from each induced dipole in the chain [33, 113]. On one side of the cut-off frequency, the induced phase profile is well matched to forward propagating free photons, leading to beaming away from the excitation point. On the other side of cut-off, interference is destructive in the forward direction, leading to beaming in the backward direction. To interpret the directionality in more detail, we setup a quantitative model. Since the electron beam is azimuthally symmetric, it excites a vertical dipole with the same azimuthal symmetry (also called a $m = 0$ dipole in literature where m in that case is the azimuthal quantum number) in the directly excited nanoparticle on which the electron beam is located [64, 102]. This dipole induces dipole moments in the other particles, and the collective interference of light radiated by all five coherently coupled dipole moments gives rise to the collected radiation pattern. We note that the refractive index of the silicon substrate is high, so a major portion

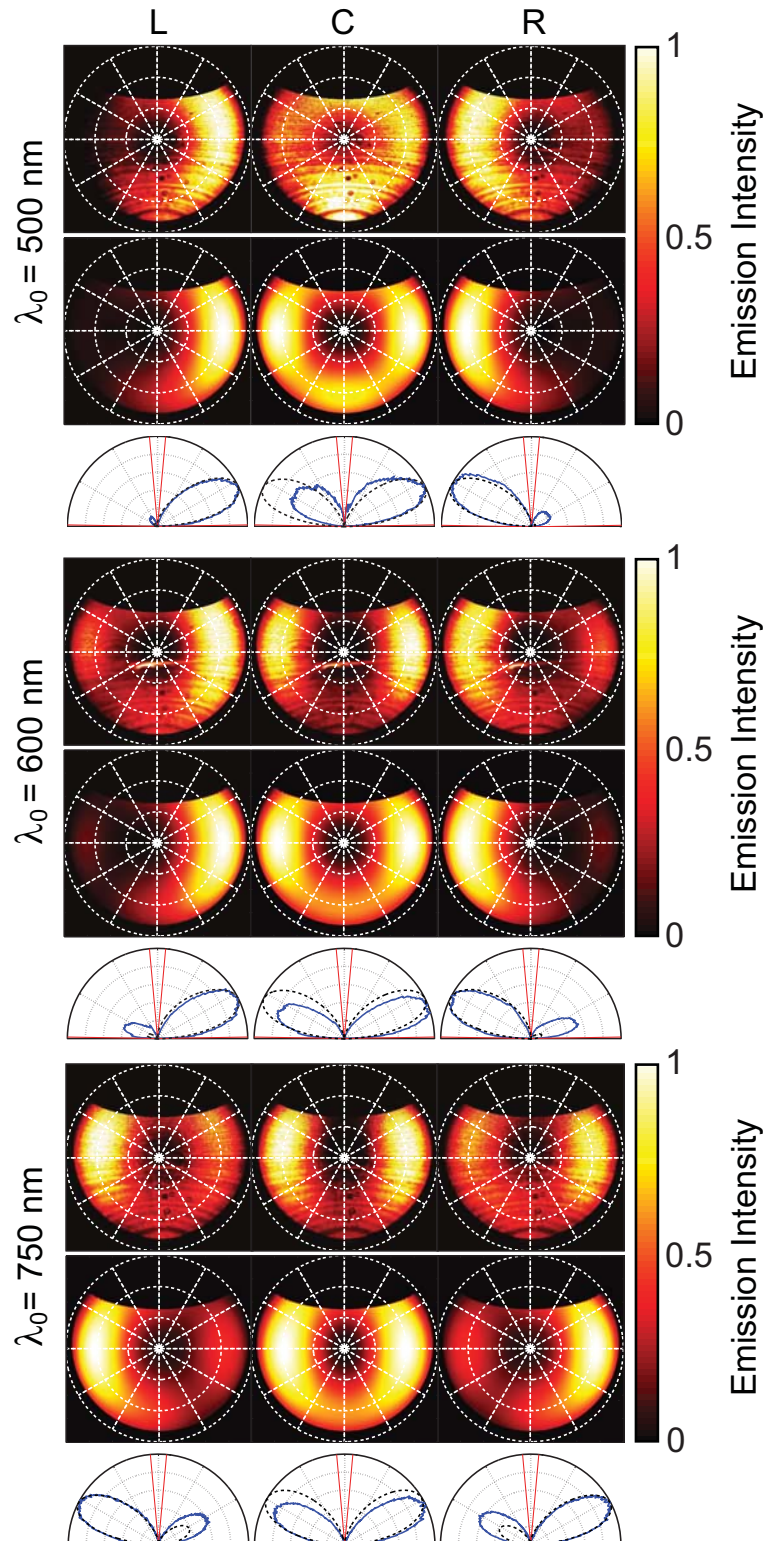


Figure 4.4: Measured angle-resolved emission patterns (top rows), calculated emission patterns (middle rows), and cross-cuts through both (bottom rows) for excitation of the outer left (L), center (C), and outer right (R) particle shown for $\lambda_0 = 500, 600,$ and 750 nm, respectively.

of the light is scattered into the substrate ($\sim 90\%$) where it cannot be detected. On the other hand the substrate also significantly enhances the LDOS at the position of the dipole, increasing the excitation probability. Hence a significant CL signal is still expected.

4.6 Coupled electrical dipole model

To take into account the coherent coupling, far-field interference, and the influence of the substrate, we setup an analytical point dipole model [114]. In this model, each particle is described as a point dipole that has a dipole moment $\mathbf{p} = \alpha\mathbf{E}$ in response to a driving field \mathbf{E} , where the polarizability α contains the plasmon resonance. In a complex array of N particles, the dipole moment induced in particle m is due to the field that is directly induced by the driving E_{in} and the field that is radiated by each other dipole in the array. This realization leads to the following set of equations

$$p_m = \alpha[E_{in} + \sum_{\substack{n=1 \\ n \neq m}}^N G(r_m, r_n)p_n] \quad (4.1)$$

that can be self-consistently solved to find the induced dipole moment p_m in each particle. In this equation, the Green dyadic $G(r, r')$ quantifies the field at position r due to a dipole located at position r' . Provided one uses the electrodynamic expression for the field of a dipole for $G(r, r')$, and correctly implements radiation damping in the polarizability α , this formalism describes scattering to all scattering orders and with correct handling of retardation, interference, and energy balance. In this work, particles are placed at the interface between vacuum and a high index substrate, which strongly influences the radiation. We have successfully implemented this asymmetric environment in a point scattering model, by replacing the Green dyadic of free space

$$G(r, r') = (k^2 + \nabla\nabla) \frac{e^{ik|r-r'|}}{|r-r'|} \quad (4.2)$$

that is ordinarily used [124, 125] in Eq. 4.1 with the Green function for a dielectric interface. We implemented the Green function for a dielectric interface as listed in Ref. [94] (chapter 10) but transformed to cylindrical coordinates, to be optimally equipped to deal with poles that are encountered when performing the required integral over parallel wave vector via contour integration [126]. Once the induced dipole moments are found with aid of $G(r, r')$, we construct the far-field radiation pattern by coherent addition of the far field of each dipole, making use of the asymptotic far-field approximations to $G(r, r')$, discussed in Ref. [94] section 10.6. For the above-mentioned procedure to result in a self-consistent energy-conserving theory, the polarizability also needs to be amended. It is well-known that if one starts with the electrostatic polarizability of, for instance a plasmon

nanosphere in vacuum $\alpha_0 = 3V(\epsilon - 1)/(\epsilon + 2)$, one needs to add a dynamic correction (radiation damping) to the polarizability to properly take into account that scatterers lose energy by radiation into the far field [127]. This radiation correction takes the form

$$\frac{1}{\alpha} = \frac{1}{\alpha_0} - \frac{2\iota k^3}{3} \quad (4.3)$$

for particles in a homogeneous environment. The damping term $2\iota k^3/3$ is in fact derived from the local density of optical states, *i.e.*, from $\text{Im}\{G(r, r')\}$, that quantifies how much energy a dipole moment of given strength at position r radiates. By generalizing the radiation damping correction to

$$\frac{1}{\alpha} = \frac{1}{\alpha_0} - \iota \text{Im}\{G(r, r')\} \quad (4.4)$$

we obtain a self-consistent theory that satisfies the optical theorem also in the presence of an interface. The following facts should be noted. First, the radiation damping clearly depends on position relative to the interface in proportion to the LDOS defined by the interface. This fact was first realized in an experiment by Buchler *et al.* [128], who measured variations in line width in scattering spectra of a single plasmon sphere as a function of its distance to a mirror. Second, in the above equations, α , α_0 as well as $\text{Im}\{G(r, r')\}$ should all be interpreted as tensors. This tensorial nature is well appreciated for the static polarizability α_0 of anisotropic plasmon particles such as oblate or prolate metal nanoparticles. Interestingly, the orientation dependence of the LDOS that is enclosed in the tensor $\text{Im}\{G(r, r')\}$ implies that even spherical particles with an isotropic geometry specified in α_0 will have an anisotropic electrodynamic response α when brought in proximity to an interface [129]. To model the experiments presented in this work, we use a Lorentzian damped resonance line shape for the static polarizability

$$\alpha_0 = \frac{\omega_0^2}{\omega_0^2 - \omega^2 - \iota\omega\gamma} 4\pi a_0^3 \quad (4.5)$$

Here a_0 is the particle radius, ω_0 the resonance frequency of a single particle, and γ is the intrinsic time constant for material damping. We take the resonance frequency to correspond to the resonance measured by spectrally resolved CL of a single nanoparticle (577 nm, see Fig. 4.1(c)), and set the Ohmic damping rate, γ , to be $8.3 \times 10^{13} \text{ s}^{-1}$, appropriate for gold [130]. For the crystalline silicon substrate tabulated optical constants were used [130]. For E_{in} we use a vertically oriented dipole positioned in the center of one of the nanoparticles (35 nm above the substrate), to mimic the e-beam excitation.

4.7 Comparison between experiment and theory

We use the coupled dipole model to calculate the far-field emission pattern for each wavelength and excitation position. Figure 4.3(c) shows the calculated far field emission for excitation of the leftmost particle, at a wavelength of 500 nm. As in the data, the calculated emission pattern is strongly peaked in the direction away from the excitation point. We extract a cross section through angular integration over the same range as discussed before, which allows us to directly compare experiment and theory. The strong directionality observed in the data is well described by the point dipole model.

Figure 4.4 shows comparisons between theory and experiment for the three wavelengths studied and excitation positions. Overall, the agreement between theory and experiment is excellent for all wavelengths, as evidenced in both polar plots and the cross sections (Fig. 4.4, bottom row). Theory predicts a directional radiation pattern for excitation at the array ends, which for $\lambda_0 = 500$ and 600 nm occurs away from the excitation point, and swaps direction for $\lambda_0 = 700$ nm, exactly as in the experiment. Additionally, at $\lambda_0 = 500$ nm and for excitation of the center particle, the appearance of an extra lobe at $\phi = 180^\circ$ is predicted by the theory which also clearly is present in the data. Moreover, the coupled dipole model correctly predicts that in the angular range presented in Figs. 4.3 and 4.4, most of the radiation is emitted around $\theta = 60^\circ$ (for all three wavelengths in both forward and backward radiating cases). We note that, in contrast to the left/right asymmetry in the radiation pattern, the radiation angle of 60° relative to the surface normal is not dictated by coupling between particles. Indeed, also in the case of a single point dipole emitter 35 nm above a silicon substrate, theory dictates that most of the radiation is emitted around $\theta = 60^\circ$ (see Fig. 4.3(g)) [94]. It is clear from Figure 4.4 (bottom row) that not only the position but also the width of the main emission lobes agrees very well with the theory for both θ and ϕ . Slight discrepancies between theory and data are evident from inspection of the polar maps in Figure 4.4; for excitation of the center particle the measured radiation patterns are not completely symmetric. Furthermore the theory predicts that the radiation should be slightly more unidirectional. Apart from these minor discrepancies between theory and data, which we attribute to fabrication imperfections and the possible occurrence of multipole resonances, the theory reproduces all major features of the experiment. To quantify this agreement further, we calculate the ratio between forward (away from excitation point along the particle array) and backward (toward excitation point) scattered light for both theory and experiment and find that all the experimentally obtained ratios are within a factor 1.3 from the theoretical prediction. The largest experimentally observed ratio (5.3:1) was obtained for excitation of the outer left particle at $\lambda_0 = 500$ nm, whereas the smallest ratio (1:1.9) was found for excitation of the outer left particle at $\lambda_0 = 750$ nm. The theoretically calculated ratios are 6.7:1 and 1:2.3, respectively. Finally we note that the point dipole model can also be compared to the spatial distributions in Fig. 4.2. By integrating the emission over the angular range collected by the mirror, we obtain the total collected intensity for

a particular wavelength and as a function of the point of excitation. For 600 nm we find that according to theory the contrast in emitted intensity between the outer and center particles should be 1.5. This contrast is very similar to the brightness contrast between the outer and center particles observed in the spatial map of CL intensity in Fig. 4.2. We hence conclude that the CL imaging technique allows one to reliably determine the antenna directionality as well as the radiation strength of the individual dipole elements.

4.8 Conclusions

In conclusion we have used angle-resolved cathodoluminescence spectroscopy to probe both the spectral response and the angular emission of a linear particle array Yagi-Uda antenna upon localized excitation. The electron beam excitation allows one to locally drive the antenna with extremely high spatial resolution (~ 10 nm) and to probe the response for the entire visible range of the electromagnetic spectrum. The measurements show directional emission which strongly depends on which of the particles is excited and on the free space wavelength. The directionality is a consequence of coherent near-field and far-field interactions between different plasmon resonators in the array. The experimental results can be described accurately by using an analytical coupled dipole model which includes the effect of the silicon substrate. Our work establishes angle-resolved CL spectroscopy as a powerful technique to spatially and spectrally resolve the radiation strength and the directivity of single and composite emitter structures without any ensemble averaging; a unique advantage compared to other techniques.

5

Deep-subwavelength spatial characterization of angular emission from single-crystal Au plasmonic ridge nanoantennas

We use spatially and angle-resolved cathodoluminescence imaging spectroscopy to study the radiation mechanism of single plasmonic ridge antennas with lengths ranging from 100 to 2000 nm. We measure the antenna's standing wave resonances up to the fifth order and measure the dispersion of the strongly confined guided plasmon mode. Furthermore we measure the angular emission patterns and demonstrate that the shortest ridges can be modeled as a single point-dipole emitter oriented either upward ($m = 0$) or in-plane ($m = 1$). The far-field emission pattern for longer antennas ($m > 2$) is well described by two interfering in-plane point dipoles at the end facets, giving rise to a fringe pattern, where the number of fringes increases as the antenna becomes longer. Furthermore, we determine the antenna radiation pattern as a function of excitation position. By including the phase of the radiating dipoles into our simple dipole model, we completely reproduce this effect.

5.1 Introduction

Optical nanoantennas form an interface between localized nanoscale emitters and the far field. In transmission mode, they have the ability to direct and enhance ra-

diative emission. *Vice versa*, in reception mode, they can strongly confine incident free-space light into a nanoscale volume [29]. Plasmonic nanoantennas, in particular, have gained much interest recently because of their small footprint and strong interaction with light. Potential applications include enhanced light absorption in solar cells [36, 131], nanoscale photodetection [132], surface-enhanced spectroscopy for biosensing [133], and strong enhancement of nonlinear effects [59, 134]. Several antenna designs consisting of multiple components have been proposed in literature such as Yagi-Uda antennas composed of an array of coupled metal nanoparticles [39, 113, 114, 135] or bowtie antennas consisting of two closely spaced triangular nanoparticles [38]. Importantly, the individual building blocks of these more complex designs (metallic nanoparticles in various shapes and sizes) can act as antennas, as well [13, 110, 111]. Experimental characterization and physical understanding of these single components is of vital importance for designing more complex geometries but is difficult to obtain due to their nanoscale dimensions. An example of an elemental single-component antenna structure is the plasmonic ridge antenna [136]. In such a structure, surface plasmon polaritons (SPPs) are confined to a ridge that is carved in the surface of a metal substrate. In this antenna geometry, the two end facets of the ridge act as mirrors defining a cavity in which SPPs are resonantly confined, similar to the resonances observed in metallic nanowires [16, 137–140]. Due to their small size, these Fabry-Pérot cavities have a large free spectral range; the cavity quality factor Q is determined by the SPP propagation loss as well as the reflection losses at the end facets. One advantage of the ridge antenna is that it is monolithically attached to the metal substrate, making fabrication relatively simple. Moreover, nearly all of the antenna radiation is emitted into the upper hemisphere due to the highly reflective substrate, enabling efficient radiation collection.

Previously, we have studied the resonances of these ridge antennas using cathodoluminescence (CL) imaging spectroscopy [136]. Using a 30 keV electron beam as a point source to generate SPPs on the ridge, we measured standing SPP waves at well-defined wavelengths corresponding to the cavity resonances. While these measurements clearly indicate the presence of antenna resonances, they do not provide insight into the radiation mechanism of these antennas. Here we use the CL technique that is now expanded by two unique features to fully identify this mechanism. First, by using a piezoelectrical mirror stage, we are able to precisely position the mirror collecting the CL signal in such a way that its focus coincides with the ridge antenna, increasing the photon collection rate ~ 50 times compared to our previous work. With this enhanced signal, we resolve the spatial intensity distribution of the standing wave detection to an extent that the full dispersion of the SPP ridge plasmons can be accurately determined. Second, by using the new angle-resolved detection capability of the CL system, we are able to directly determine the far-field radiation pattern of the ridge antenna for every antenna resonance (see Chapters 2 and 3 for details on the experimental setup). By scanning the electron beam across the antenna, the radiation profiles are determined as a function of position with deep subwavelength precision. The high spatial resolu-

tion, sensitivity, and angular detection capabilities of our CL instrument enable characterization of the ridge antenna properties to an extent that is unrivalled by any other measurement technique.

5.2 Antenna fabrication

Ridge antennas were fabricated by inversely patterning a single-crystalline gold substrate using focused-ion-beam (FIB) milling. The ridge lengths were in the range of 100-2000 nm, varied in 100 nm increments. All ridges were 120 nm wide (width measured 65 nm above the substrate) and 130 nm high. Figure 5.1 shows a scanning electron micrograph of a 700 nm long ridge together with a schematic of the structure. The FIB-milled arena surrounding the antenna is made to have a gradually decreasing depth away from the antenna to prevent parasitic SPP reflections.

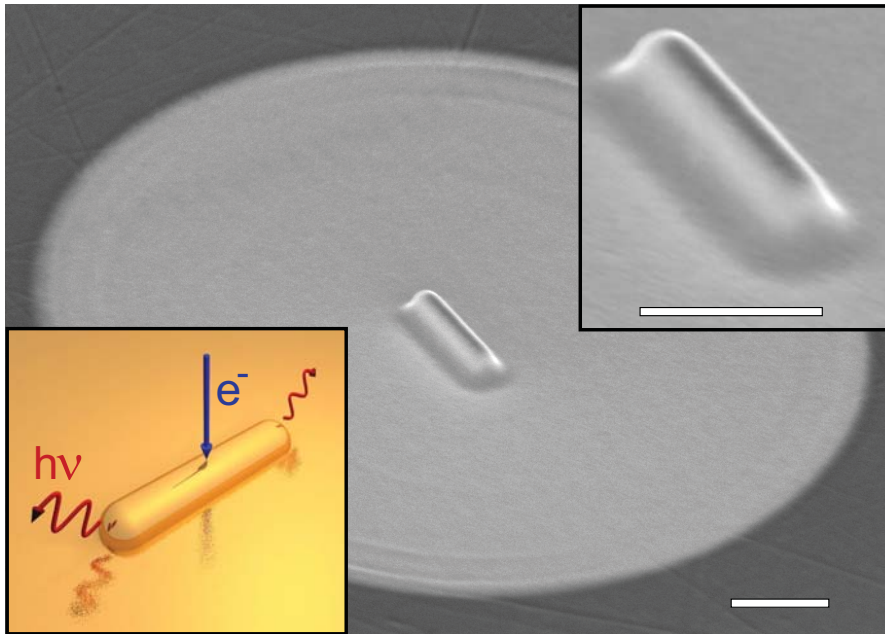


Figure 5.1: Scanning electron micrograph of a 700 nm long, 130 nm high, and 120 nm wide (measured at 65 nm height) antenna. Top right inset: Close-up of the structure. Bottom left inset: graphic showing the e-beam excitation of the ridge with subsequent photon emission from the end facets. Scale bars are 500 nm.

5.3 Direct imaging of Fabry-Pérot modes

To probe the cavity resonances, we scan a 30 keV electron beam in 10 nm steps over the center of each ridge and collect a CL spectrum for each position (for details see Methods). Figures 5.2(a-c) show the CL emission intensity as function of position

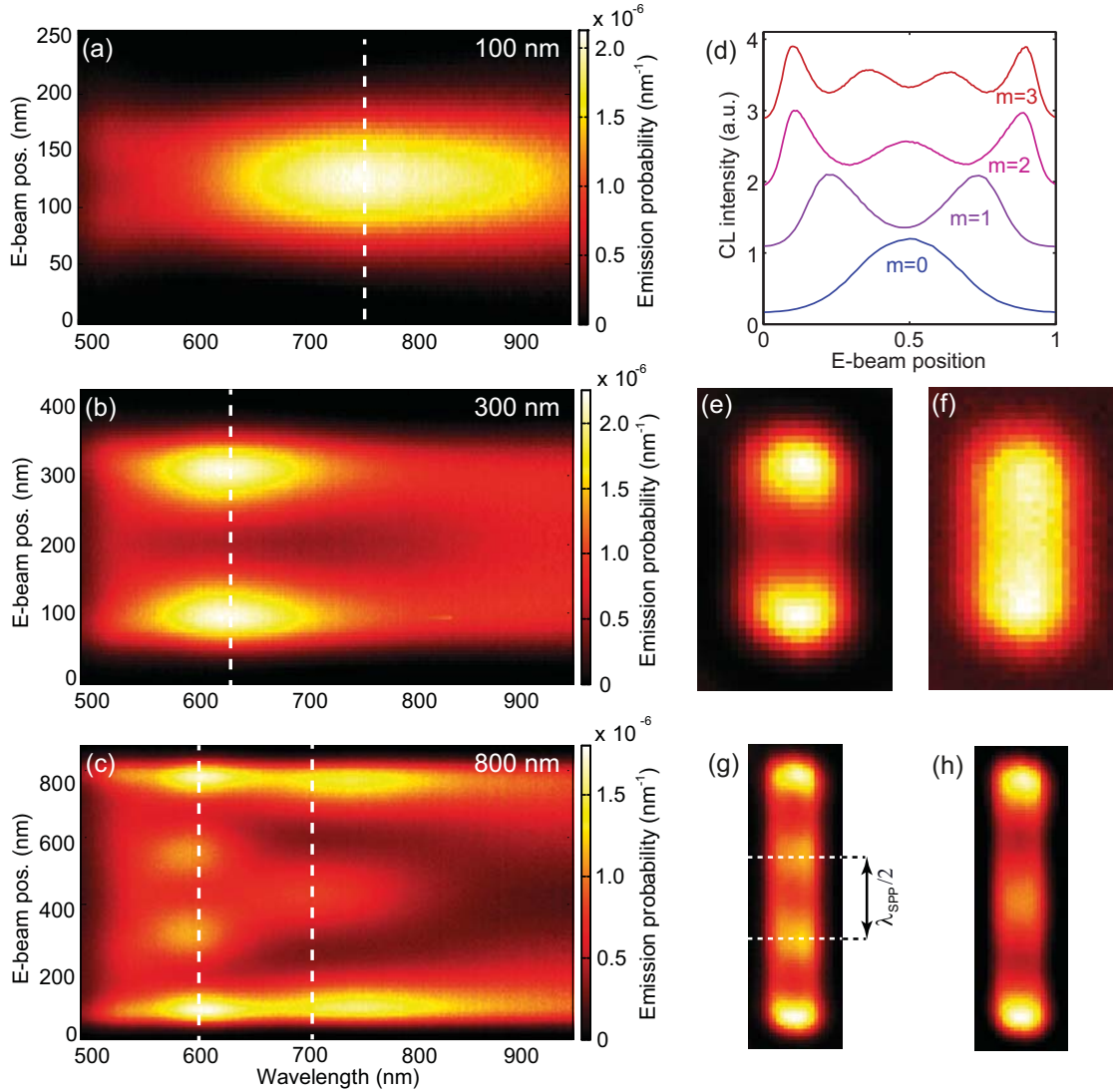


Figure 5.2: Experimental data: collected CL emission probability per incident electron as a function of position and wavelength, obtained by scanning the electron beam in 10 nm steps across a (a) 100 nm, (b) 300 nm, and (c) 800 nm long Au ridge antenna. (d) Cross cuts through the experimental data along the dashed lines are indicated in panels (a-c), showing the spatial resonance profiles for $m = 0-3$. The CL intensity has been normalized to 1, and the curves have been offset vertically for clarity. The horizontal scale has been normalized to the antenna length for each case. No data smoothing was used to obtain these curves. Spatially resolved 2D excitation maps of the 300 nm long antenna, showing resonant CL intensity as function of e-beam position for (e) $\lambda_0 = 625$ nm ($m = 1$) and (f) $\lambda_0 = 950$ nm ($m = 0$) integrated over a 10 nm bandwidth. (g) Excitation maps for the 800 nm long antenna for $\lambda_0 = 600$ nm ($m = 3$) and (h) $\lambda_0 = 700$ nm ($m = 2$). For the $m = 3$ resonance, the spacing between the two central antinodes corresponds to $\lambda_{SPP}/2$.

and wavelength for ridges with lengths of 100, 500, and 800 nm, respectively. The color scale represents the fraction of photons emitted per incident electron per unit

bandwidth. For the 100 nm long ridge, we observe a strong peak in CL emission in the center of the ridge around 750 nm free-space wavelength. The fact that this resonance is only excited efficiently in the center suggests that it has $m = 0$ (azimuthal) symmetry [64, 102] (also see Chapters 4 and 8).

For the 300 nm ridge, we observe strong CL emission near the end facets of the ridge, corresponding to a $m = 1$ “dipolar” resonance for which $\lambda_{SPP}/2$ fits into the resonator. Here λ_{SPP} is the SPP wavelength at a frequency corresponding to the free-space wavelength in the figure. For the 800 nm ridge, standing wave patterns are visible at $\lambda_0 = 700$ and 600 nm, with 3 and 4 antinodes, respectively, corresponding to a $m = 2$ “quadrupolar” resonance and a $m = 3$ “octupolar” resonance. Figure 5.2(d) shows the standing wave profile for these resonances, obtained by plotting the CL intensity of the data in Figs. 5.2(a-c) along the ridge length at the resonance wavelength. The resonance orders $m = 0, 1, 2,$ and 3 are indicated in the figure. It is interesting to note that the CL technique enables probing of the even-order resonances. This is not possible with optical excitation under normal incidence, for which excitation of even-order resonances is forbidden for symmetry reasons [16, 141]. In contrast, the point-like electron beam excitation is not restricted to odd-order resonances [142]. The high signal-to-noise ratio in the data of Fig. 5.2(d) reflects the high collection efficiency for this antenna geometry and the sensitivity of our CL system.

Next, 2D excitation maps are made by raster scanning the electron beam over the antenna in two dimensions. By using the resonance wavelengths identified from the line scans, we can plot the 2D spatial profiles of the resonances. Figure 5.2(e-h) shows 2D CL maps for the 300 and 800 nm long ridges at the resonance wavelengths integrated over 10 nm bandwidth. Figure 5.2(e) shows the $m = 1$ resonance at $\lambda_0 = 625$ nm for the 300 nm long ridge. This antenna possesses a $m = 0$ resonance as well at $\lambda_0 = 950$ nm, for which the spatial profile is plotted in Fig. 5.2(f). The $m = 0$ nature is clearly reflected in the uniform intensity observed across the entire antenna area. Figure 5.2(g,h) shows the $m = 3$ and $m = 2$ resonance spatial emission patterns and 600 and 700 nm, respectively. The spatial modulation of the emission intensity corresponding to the SPP standing wave pattern can clearly be distinguished.

5.4 Resonance evolution and modal dispersion

By summing all CL spectra from a line scan, we obtain an integrated CL spectrum showing all antenna resonances. Figure 5.3 shows such spectra for ridges with lengths from 100 to 1200 nm (we omit the longer ridges to reduce the number of curves, but we did measure their spectra). The resonance orders $m = 0-5$ are indicated in the figure. All resonances show a progressive red shift for increasing antenna length as expected. The visibility of the resonances decreases for longer antennas due to the increasing SPP propagation losses and the decreasing free spectral range. From the antinode spacing, the plasmon wavelength can be

deduced as this corresponds to $\lambda_{SPP}/2$ [137]. As the SPP experiences a phase shift upon reflection [142, 143], this analysis can only be performed on antennas with at least four antinodes ($m \geq 3$), such as in Fig. 5.2(g).

By using the standing wave profiles from multiple ridges for resonances with orders $m \geq 3$, we are able to reconstruct the complete dispersion curve for this plasmonic ridge antenna from 560 to 900 nm (1.4 – 2.2 eV). This result is shown in Fig. 5.4. For reference, we also show the light line in vacuum (black dashed line) and the dispersion curve for a SPP on a flat gold-vacuum interface (red curve), calculated using optical constants for single-crystal Au obtained with spectral ellipsometry. Figure 5.4 clearly shows that for the higher energies the measured dispersion strongly deviates from the planar SPP case and the light line; the largest effective modal index we find is $n_{SPP} = 1.22$ measured at $\lambda_0 = 575$ nm. This implies that the ridge waveguide mode cannot leak energy to SPPs on the substrate surrounding the ridge nor can it couple directly to far-field radiation. Therefore, we conclude that for these wavelengths most of the radiation is emitted from the antenna end facets, as is illustrated in the inset of Fig. 5.1. For larger wavelengths, the dispersion in Fig. 5.4 approaches the planar SPP dispersion and the light line, indicating that at these wavelengths antenna radiation during propagation may contribute to the losses, possibly leading to a reduction in the Q of the guided SPP mode. From

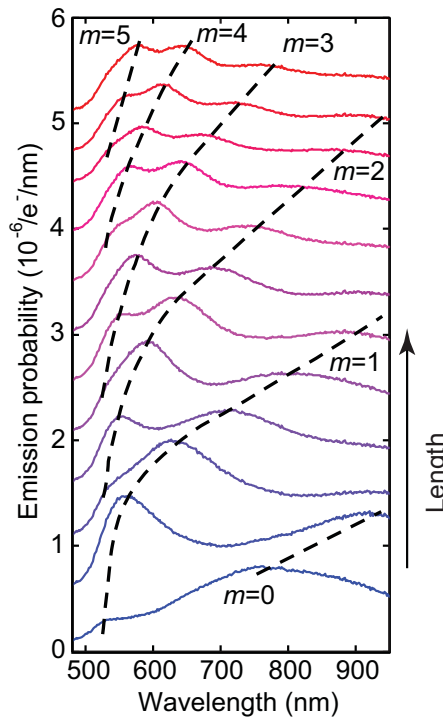


Figure 5.3: Integrated CL spectra for different ridge antennas with $L = 100$ - 1200 (100 nm steps). The spectra have been vertically offset for clarity. The evolution of the resonance orders is indicated by the black dashed curves.

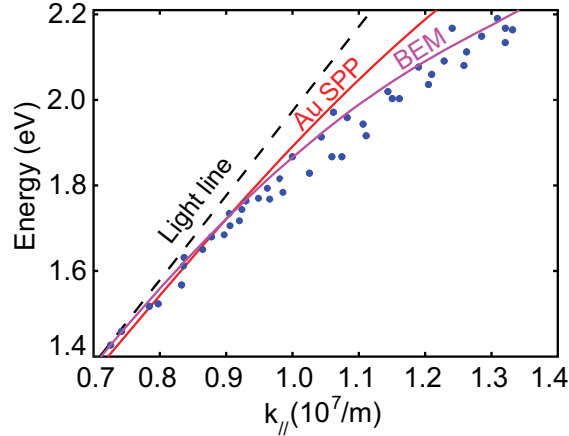


Figure 5.4: Experimental antenna dispersion (blue dots) derived from the standing wave patterns of ridges with $L = 700 - 2000$ nm and a BEM dispersion calculation (magenta curve) showing plasmon wave vector *versus* energy. For reference, the light line in vacuum (black dashed curve) and the dispersion curve for a SPP on a planar single-crystalline gold surface (red curve) are shown.

Fig. 5.2, it is clear that the end facets are relatively bright compared to the central antinodes which can be attributed to a locally enhanced coupling to plasmons. This makes it difficult to extract the complex plasmon wave vector and reflection coefficients using a Fabry-Pérot model [16, 142, 144] since this enhanced coupling is not taken into account.

5.5 Boundary-element-method modeling

To obtain further insight into the confinement, loss, and dispersion of the SPP modes, we perform electromagnetic calculations using the two-dimensional boundary-element method (BEM2D) [145, 146]. To obtain an exact representation of the geometry used in the experiment, we made a cross section of one of the ridge antennas using FIB (Figure 5.5(a)) and we subsequently parameterized the SEM profile for use in the BEM calculations. In the calculation, the waveguide is infinitely long, which means that effects from the end facets are not taken into account. We first calculate the induced near field on the ridge by a vertically oriented dipole located 10 nm above the ridge, mimicking the e-beam excitation, for wavelengths of 600 nm (Fig. 5.5(b)) and 900 nm (Fig. 5.5(c)). In both cases, the electric field intensity is clearly confined to the ridge. As expected, the modal electric field is more confined at 600 nm than at 900 nm. Using BEM, we can also calculate the ridge mode dispersion by calculating the local density of states (LDOS) 10 nm above the waveguide for different photon energies and mode wave vectors. Subsequently, we fit a Lorentzian line shape to the calculated LDOS *versus* wave vector for a given energy from which we derive the LDOS maxima to obtain a relation between wave vector and energy (see Fig. 5.4, magenta curve). The

calculated curve matches well with the experimentally determined dispersion data. From the width of the Lorentzian fits, we can determine the modal Q , from which we can extract the propagation length (L_{SPP}) of the waveguide mode [136]. We find for a free-space wavelength of 600 nm that $Q = 16$ ($L_{SPP} = 1.3 \mu\text{m}$) and for 800 nm $Q = 130$ ($L_{SPP} = 17 \mu\text{m}$). Using the same optical constants, we calculate propagation lengths for planar SPPs of 5.4 and 49 μm , respectively.

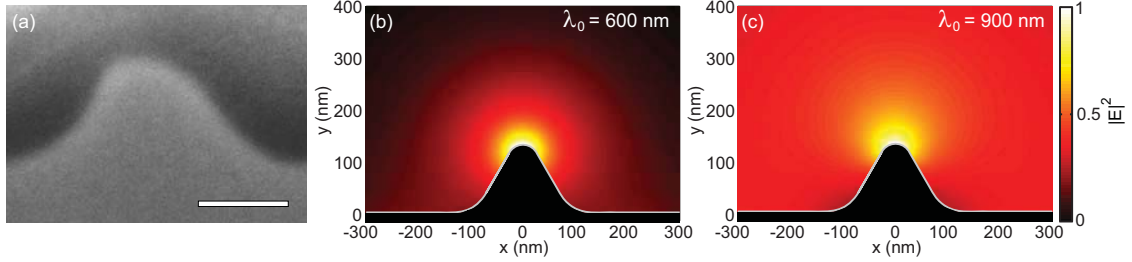


Figure 5.5: (a) SEM image taken of an antenna cross section made by FIB with a sample tilt of 52° (scale bar 100 nm). BEM calculation of the induced near field by a vertically oriented dipole positioned 10 nm above the ridge waveguide for (b) $\lambda_0 = 600 \text{ nm}$ at $k = 1.12 k_0$ and (c) $\lambda_0 = 900 \text{ nm}$ at $k = 1.002 k_0$. The ridge antenna geometry is indicated in black.

Since the waveguide propagation length is much shorter for higher energies than for lower energies, we conclude that the waveguide loss in the detected wavelength range is dominated by ohmic damping rather than radiative damping. While these BEM calculations are made for infinite ridges, and thus only take into account propagation losses, the measurements are performed on finite-length ridges where reflection losses of the cavity also play an important role. As a result, the experimental resonance Q will be lower than the modal Q . Indeed, the cavity Q for all resonances shown in Fig. 5.3 is estimated to be in the range of 2-10, significantly lower than the values calculated above. Moreover, the highest resonance Q values are found for the shorter wavelengths, opposite to the trend based purely on propagation loss. This is explained by the fact that for shorter wavelengths the cavity end facet is a better mirror due to the higher modal index of the plasmon mode.

5.6 Reflection coefficients

Using the complex plasmon wave vector calculated with BEM, we can estimate the complex reflection coefficient by applying a simple Fresnel reflection model. Here the reflection coefficient r is given by $(n_{SPP} - 1)/(n_{SPP} + 1)$, with n_{SPP} being the complex mode index k_{SPP}/k_0 [143]. If we do this for the 800 nm long ridge at $\lambda_0 = 600 \text{ nm}$ ($m = 3$ resonance), we find that $r = 0.086 + 0.0153i$. This shows that only a small fraction of the energy is reflected at the end facet and most of the energy is coupled to far-field radiation. From this coefficient, we can also directly find the phase pickup Φ as $r = |r|e^{i\Phi}$, which for this antenna corresponds

to 0.06π [143]. This is a relatively small phase shift compared to values reported in Refs. [16] and [142]. In those cases, the metal antennas were ultrathin (25 and 20 nm, respectively), leading to stronger plasmon confinement, higher ohmic losses, and a larger mode mismatch with free space resulting in a much larger phase pickup which cannot be accurately determined with a simple Fresnel model [143]. An alternative method to estimate Φ is by measuring the spacing between the outer antinode at the end facet and the neighboring antinode. This distance is affected by the phase pickup, but as is clear from Fig. 5.2(g), the spacing is very close to the spacing between the central antinodes, suggesting that there is only a minor phase pickup. In fact, if we calculate the phase pickup for the 800 nm ridge this way, we find a value of 0.02π , which is close to the value predicted by the Fresnel model.

5.7 Ridge angular patterns

Using the angle-resolved detection capabilities in our CL instrument, it is possible to determine the angular radiation profiles of the antenna for every excitation position on the antenna, that is, with deep subwavelength resolution. The CL emission is collected by the paraboloid mirror and imaged by a 2D CCD array from which we obtain the emission intensity as a function of polar (zenithal) angle θ and azimuthal angle ϕ (see Chapter 3). The measurements are made spectrally selective using 40 nm band-pass color filters. We determine the angular emission distribution for antennas with different lengths at wavelengths corresponding to the antenna resonances. In this way, the radiation patterns for different resonance orders can be systematically compared.

We scan the electron beam in 25 nm steps over the center of the ridge in a line and collect a radiation pattern at each position. The left column in Fig. 5.6 shows the angular distribution of CL emission for $m = 0, 1, 2, 3, 4$, and 5 obtained from 6 different antenna lengths (indicated in the figure). The depicted emission patterns were collected with the electron beam positioned on the central antinode for even-order resonances ($m = 0, 2, 4$) and on one of the two central antinodes for the odd-order resonances ($m = 1, 3, 5$). The antennas were oriented normal to the optical axis of the mirror. For the shortest antenna (100 nm), the radiation pattern clearly has a toroidal “doughnut” shape, consistent with the azimuthal symmetry associated with the $m = 0$ resonance [64, 102]. Since the ridge antenna is integrated with a conductive substrate, this resonance is distinct from the vertically oriented dipole resonance in a metallic nanoparticle on a dielectric substrate as described in Chapter 4 and 8, where charge separation occurs in the direction normal to the surface. Instead, it can be attributed to a “monopolar breathing type” resonance with a circularly symmetric charge distribution, as shown schematically in the bottom row of Fig. 5.6 [102]. In terms of a Fabry-Pérot resonator, it can be understood as being a “zero-length” cavity where the resonance condition is almost completely determined by the phase pickup upon reflection [147]. From the toroidally shaped emission pattern, it is clear that this resonance has an effective dipole moment

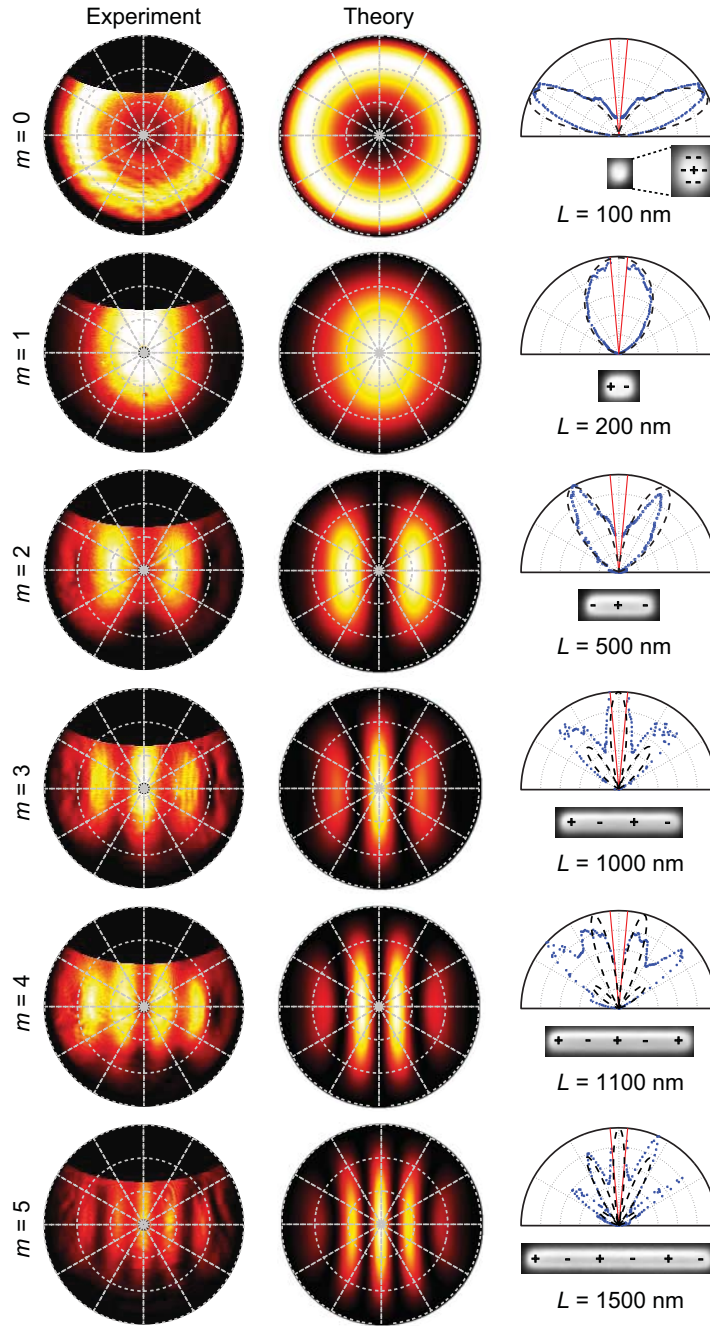


Figure 5.6: Measured angle-resolved emission patterns (left column row) and calculated emission patterns (second column). The antennas are oriented horizontally. The third row shows cross cuts through measurements (blue dots) and calculations (black dashed line) along $\phi = 90$ and 270° (see Fig. 3.3 for axis labels), showing emission patterns for $m = 0, 1, 2, 3, 4$, and 5 resonances, collected from ridges with different lengths (see SEM images in third column). In the SEM images, we have also indicated snapshots of the charge distributions corresponding to each resonance (we have enlarged the SEM image for the 100 nm long antenna to improve the visibility). From top to bottom, the measurements were collected at $\lambda_0 = 750, 550, 600, 650, 600$, and 650 nm. The angular range that is not collected by the mirror because of the hole is indicated by the red curves ($\theta < 5^\circ$).

normal to the substrate. In contrast, the emission pattern for the $m = 1$ resonance corresponds to that of a dipole oriented in the plane of the antenna, as indicated by the charge distribution in the right column. The radiation profile from this dipole can be interpreted as an out-of-plane toroid with its symmetry axis oriented along the antenna's major axis, distorted by presence of the reflective gold surface, which leads to one strong radiation lobe pointing toward the surface normal. The next resonance, $m = 2$, does not have a contribution normal to the surface but shows two off-normal emission lobes around $\theta = 30^\circ$. Subsequently, the $m = 3, 4$, and 5 resonances show three, four, and five lobes, respectively, where a central lobe pointing toward the normal is only observed for the odd-order resonances.

5.8 Theoretical model for angular patterns

To model the antenna radiation patterns, we distinguish between short and long antennas. The short 100 and 200 nm antennas were modeled by a single-point dipole source that is oriented either vertically ($m = 0$) or horizontally ($m = 1$) along the antenna axis. We construct the far-field radiation pattern making use of the asymptotic far-field approximations discussed in Ref. [94] (section 10.6). We placed the point dipole 65 nm above the Au surface, corresponding to half of the antenna height. Optical constants for single-crystal Au from spectral ellipsometry were used as input for the calculations. The second column in Fig. 5.6 shows the calculated angular radiation profiles. They show close resemblance to the measured profiles for the short antennas. To perform a quantitative comparison between experiment and theory, we plot the polar distribution of the CL emission intensity by taking a cross cut along $\phi = 90$ and 270° (along the length of the antenna). The measured and calculated data, plotted in the third column of Fig. 5.6, agree quite well.

For the longer antennas, the point-dipole approximation is not applicable, and the following model is developed. As described above, from the dispersion data it follows that, especially for shorter wavelengths, direct coupling of SPPs to the far field is weak and consequently the emission is mostly from the two end facets. This phenomenon has been observed experimentally by others, as well [17, 20, 148]. Taminiau *et al.* have suggested that these types of traveling wave antennas can be approximated as two radiating dipoles oriented along the long axis of the antenna located at the end facets, with their phase and amplitude fully determined by the SPP waves [144]. We take a similar approach where the phase and amplitude of the dipoles at the end facets is determined by the distance between the electron beam excitation position and the antenna ends. Subsequently we calculate the far-field radiation patterns of the two interfering dipoles for the relevant resonance wavelengths (see second and third row in Figure 5.6) by coherently adding the far field of both dipoles [94]. The measured emission direction and the number of lobes are quite well reproduced by this relatively simple model. From the model, we see that for $m = 2, 4$, with the end facet dipoles 180° out of phase, destructive interference occurs at $\theta = 0^\circ$. In contrast, for $m = 3, 5$, in-phase dipoles lead to constructive

interference in that direction. For the $m = 2$ resonance, good agreement between the calculated and measured angular patterns is observed. For the higher-order resonances, the number of radiation lobes as well as the orientation is well described by our model, while discrepancies are found in the exact amplitudes. This is partly due to the fact that we used a 40 nm detection bandwidth in the experiment while the calculations were performed at the resonance peak wavelength. From the Rayleigh-Carson reciprocity theorem, it follows that the even-order resonances cannot be excited with free-space light under normal incidence. In other words, if the antenna does not emit efficiently normal to the surface, it is also not possible to efficiently excite it along that direction. However, if excited under an angle, significant coupling to these even-order resonances is possible due to retardation effects, as is described in Ref. [16]. In our experiment, the electron beam acts as a vertically oriented point-dipole source which does allow strong coupling. Thus, by using the CL technique, we are able to efficiently probe the spectral and angular response of all of the different resonance orders in the antennas and directly see which resonances are difficult to access using optical far-field techniques.

To further test the far-field interference model, we investigate the radiation pattern for different excitation positions on the antenna. Our angle-resolved CL technique is a unique and ideal tool for this study, as it enables local excitation of the antenna mode with deep subwavelength spatial resolution for all wavelengths of interest. Figure 5.7 (top row) shows measured angular emission patterns for the $m = 2$ resonance of the 500 nm long antenna at $\lambda_0 = 600$ nm collected at three different excitation positions as indicated in the electron micrographs in the bottom row. When excited in the center, the dipoles are 180° out of phase, giving rise to the symmetric radiation pattern found before in Fig. 5.6. For excitation close to the end facets, the pattern is no longer symmetric and the radiation emission is stronger away from the excitation point, along the antenna. Moving the electron beam across the antenna changes the relative phase of the dipoles since SPPs have to travel different distances to reach the two end facets, resulting in asymmetric emission patterns.

For even-order resonances, one might expect that the dipoles are always 180° out of phase if excited in an antinode of the standing wave pattern. This is indeed the case for excitation at the central antinode, for which SPPs propagate an equal distance to both end facets and generate two oppositely oriented dipoles. If we would move the electron beam $\lambda_{SPP}/2$ to another antinode, the dipoles should again be 180° out of phase, resulting in a symmetric angular emission pattern. However, for this quadrupolar resonance, the last antinodes are slightly offset in space due to the phase shift upon reflection, leading to a different relative phase between the dipoles and an asymmetry in the emission pattern. The difference in end-facet brightness decreases fringe-visibility although in this case that effect is only minor. The second row in Fig. 5.7 shows the calculated emission patterns using the dipole model, and the third row again shows cross cuts through both the data and theory. The results are very similar to the measurement. The model predicts the same asymmetry as is observed in the measurement, and also, the magnitude

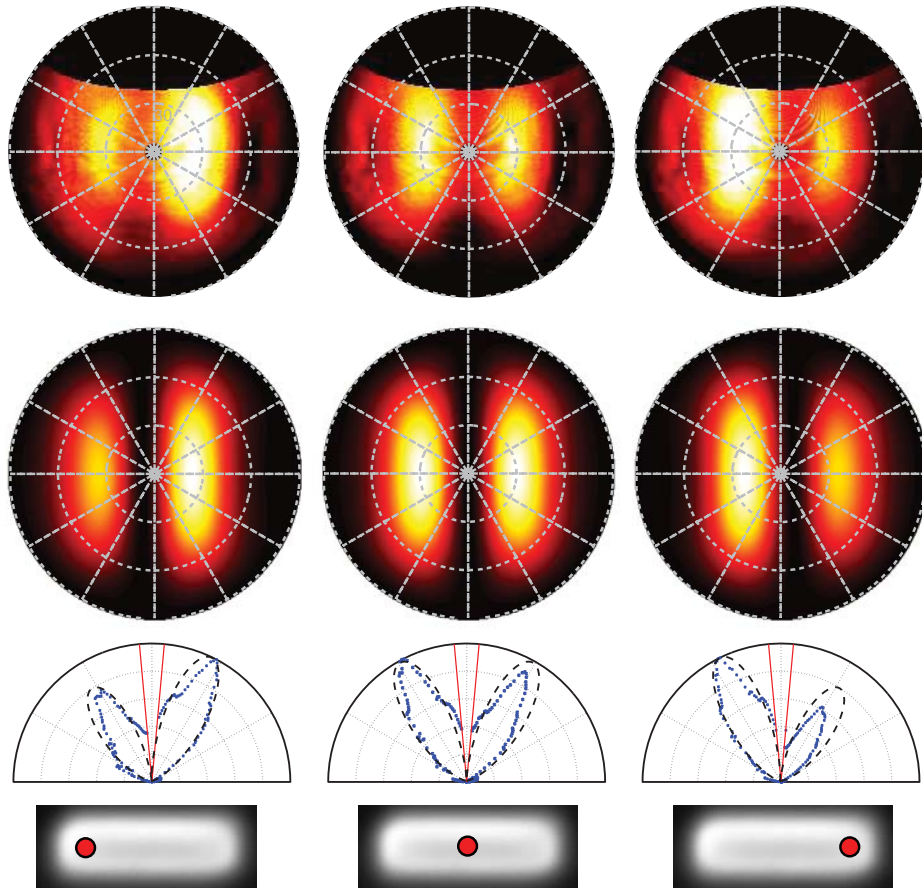


Figure 5.7: Measured angle-resolved emission patterns (top row), calculated emission patterns (second row), and cross cuts through both (third row) for excitation of the outer left, center, and outer right position of the 500 nm long ridge (see bottom row), collected at $\lambda_0 = 600$ nm.

of the lobes is predicted well.

5.9 Conclusions

In conclusion, we have resolved the resonances and radiation patterns for gold ridge surface plasmon polariton nanoantennas with deep subwavelength resolution. From the measured antinode spacing in the spatial maps of the antenna resonances, we determined the dispersion relation for the guided mode along the antenna; these results are in good agreement with boundary element method calculations. The resonance quality factor is in the range of 2 – 10 and is determined by ohmic damping within the metal and radiative losses at the end facets. The angular emission patterns for all resonance orders $m = 0 - 5$ were resolved using angle-resolved cathodoluminescence spectroscopy. The emission pattern for antennas shorter than 200 nm can be modeled as a single-point dipole source oriented ei-

ther in the normal direction (100 nm antenna) or in the planar direction (200 nm). Longer ridges act as traveling wave antennas with a radiation profile that is well described by two radiating dipoles placed at the end facets, with their relative phase determined by the antenna length and the wavelength. Using the unique spatially resolved capabilities of the CL technique, we were able to determine the antenna radiation pattern for different excitation positions. We find that changing the excitation position on the antenna changes the phase of the emitting end facet dipoles and thus influences the radiation pattern. This study shows how angle-resolved cathodoluminescence spectroscopy can be used to probe nanoantenna properties in great detail and with subwavelength precision. The fundamental insights obtained for this particular monolithic nanoantenna design can be used to design more complex coupled directional antenna structures with a tailored radiation profile.

5.10 Methods

Nanoantenna Fabrication. The ridges were fabricated with FIB using a FEI Helios dual beam system in a Czochralski grown single-crystalline gold pellet, which was mechanically polished to achieve sub-10 nm RMS roughness. To fabricate a sharply defined gold ridge, we used the lowest ion beam current of 1.5 pA and a short dwell time of 100 ns. The gradual change in depth of surrounding arena was achieved by slowly decreasing ion dose away from the antenna in a linear fashion. The cross section of the ridge was made by performing a cleaning cross section which prevents tapering. To ensure shape retention during milling, a layer of platinum was deposited using electron-beam-induced deposition (EBID).

Cathodoluminescence Experiments. For the line scans, a dwell time of 1 s was used, and for the spectral images, 0.5 s was used. For both, a current of 1 nA was used. We corrected the data for system response by measuring the transition radiation spectrum for gold and comparing that to theory [63, 103]. For the angle-resolved measurements, we used 15 s dwell time and a current of 10 nA to increase signal-to-noise ratio. Spectral sensitivity was achieved by filtering the CL beam with 40 nm band-pass color filters. To purely look at the resonance emission from the antennas, we subtract the transition radiation background. For both the spectroscopy and angular measurements, we use a spatial drift correction algorithm to correct for the effects of beam and sample drift.

6

Polarization-sensitive cathodoluminescence Fourier microscopy

Determining the emission polarization properties of subwavelength structures like optical nanoantennas, nanocavities and photonic crystals is important to understand their physical properties and to optimize their use in applications. In this Chapter we extend the angle-resolved cathodoluminescence imaging (ARCIS) technique with polarization-sensitive angular detection. As proof-of-principle, we experimentally probe the emission polarization properties of three orthogonal dipolar emitters of which the polarization is known and find excellent agreement between experiment and theory. We show how to predict the polarization-filtered pattern if the emission polarization is known. Furthermore, we calculate that by introducing a slit in the beam path the polarization contrast in cathodoluminescence spectroscopy can be strongly enhanced. Finally, we reconstruct the emission polarization from the experimental data and show that from these field patterns we can infer the orientation of the induced dipole moment.

6.1 Introduction

The degree of coupling between light and matter strongly depends on the polarization of the incoming electromagnetic field. For instance, a point-dipole emitter like

a dye-molecule, nitrogen vacancy center or quantum dot is most efficiently driven when the electric field of the light wave is aligned with its electric dipole axis [94, 149]. Moreover, in optically active (bio)molecules the handedness of the light can also influence the coupling strength. The ability to manipulate and probe the polarization state of light is key in many applications including lasers, flat screen televisions and video projectors. Also in the field of nanophotonics polarization plays an important role. The excitation efficiency of a localized surface plasmon resonance (LSPR) [150], Mie resonance [151], or guided mode [152] often is polarization dependent. For instance, one can access two orthogonally oriented dipole resonances in a rectangular hole surrounded by metal or in a metallic nanorod by choosing the incoming polarization either along or transverse to the long axis of the structure [153, 154]. *Vice versa*, when such a resonance is driven by an incident light wave or localized source, the far-field emission can also be strongly polarized in a way that is characteristic for the charge distribution associated with that resonance. Measuring the emission polarization can be used to deduce in which direction a structure is polarized.

In optical microscopy, the far-field emission pattern of molecules [95], nanoantennas [155] and coupled systems (where a localized emitter is coupled to an antenna) [39, 156] can be obtained by imaging the back focal plane of the microscope objective (Fourier microscopy). When performing Fourier microscopy on nanoantennas fed by fluorescent probes like quantum dots or dye molecules, the pump light can be separated from the fluorescence by using a color filter or dichroic mirror because the fluorescence is Stokes-shifted from the pump light. The bandwidth of these probes is limited however, so as an alternative, one can also measure optical scattering directly to study the scattering properties of the antenna. Although this method potentially gives broadband information on the scattering properties of a structure it is not possible to selectively separate the scattering from the pump light by means of a color filter. As a result the background signal from the excitation beam usually is relatively strong in such measurements, making it more difficult to see the angular distribution from the scattering object. It has been shown recently by Sersic *et al.* that this can be solved by using a dark-field excitation configuration like a prism (total internal reflection (TIR) mode) [155].

In the previous chapters, we have demonstrated that angle-resolved cathodoluminescence (CL) imaging spectroscopy (ARCIS) is a good alternative technique for studying the far-field emission properties of nanoantennas. In CL spectroscopy an energetic electron beam, focused into a nanoscale spot, is used as broadband excitation source. Because of its high excitation resolution (~ 10 nm) one can efficiently excite a single structure with a relatively low background signal, essentially making it a dark-field technique as well, where the optical scattering from a single antenna dominates the Fourier image. However, up until now it has not been possible to obtain the polarization of the emission for different emission angles. In this article we show how to deduce the emission polarization when using angle-resolved CL imaging, thereby adding an extra dimension to the technique. As proof-of-principle, we experimentally probe the emission polarization properties of three

orthogonal dipolar emitters of which the polarization is well-known and find excellent agreement between experiment and theory.

6.2 Sample and experimental setup

In this experiment we use a Czochralski grown single-crystal gold substrate with a polished surface. We study CL emission originating from an unstructured part of the sample as well as from a 300 nm long, 120 wide, and 130 nm high plasmonic ridge nanoantenna (for a more detailed description see Chapter 5), fabricated using focused-ion-beam (FIB) milling by inversely patterning the gold surface. A scanning electron micrograph of the structure is shown in Fig. 6.1(a). We use a 30 keV electron beam (1 nA beam current) from a scanning electron microscope (SEM) as a broadband nanoscale excitation source. The resulting CL emission is collected using an aluminum half-paraboloid mirror (effective NA of 1.46π sr) and directed towards a 2D 1024×1024 pixel imaging camera which measures the in-

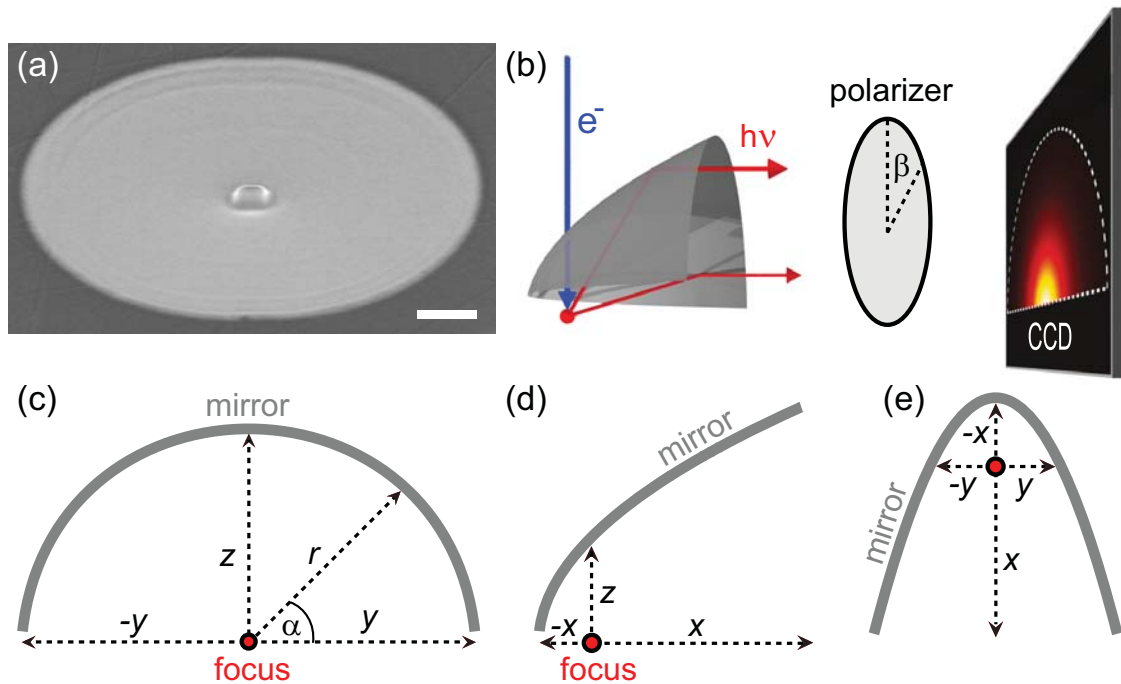


Figure 6.1: (a) Scanning electron micrograph of a 300 nm long ridge antenna taken at a 52° inclination of the microscope stage. The scale bar represents 500 nm (b) Schematic overview of the experimental setup. The electron beam (blue arrow) excites the sample generating CL (red arrows) which is collected by the paraboloid mirror and converted into a parallel beam. The beam goes through a linear polarizer set at an angle β and is projected onto a 2D CCD array. $\beta = 0^\circ$ corresponds to alignment of the polarizer with the z -axis. (c) Front view, (d) side view, and (e) top view perspective of the paraboloid mirror showing the coordinate system that is used. For clarity only the mirror contours are shown.

tensity profile of the beam (see Fig. 6.1(b)). From this profile the angular intensity distribution of the emission can be deduced (see Chapter 3). We place a linear polarizer fixed in a rotation mount in between the camera and the mirror, allowing detection of the angular CL emission pattern for different polarizer angles β . For wavelength selectivity we use 40 nm band pass color filters, that are placed in the beam path. In this Chapter we use the same cartesian coordinate system as defined in Fig. 2.4(c), where the x -dimension is aligned with the optical axis of the mirror, the z -dimension is parallel to the incoming electron beam and the y -dimension is transverse to the optical mirror axis. Figures 6.1(c-e) illustrate how the coordinate system is oriented with respect to the mirror.

6.3 Polarization-filtered angular patterns

When an electron passes through an interface between two dielectric environments, it induces a broadband transient dipole on the surface which radiates into the far field (transition radiation (TR)) [63, 103]. This dipole moment is oriented vertically with respect to the interface (z -direction, parallel to the electron beam) and the corresponding angular emission pattern has a characteristic toroidal “doughnut” shape (see Fig. 3.3). The toroid is bent upwards due to the reflective metal substrate. Figure 6.2(a) shows the calculated emission intensity for TR as function of zenithal angle θ and azimuthal angle ϕ . All radiation patterns shown in this Chapter are normalized to 1. The emission pattern was calculated for a free-space wavelength (λ_0) of 650 nm using the expressions for TR-emission [63] and tabulated permittivity values for the gold substrate [105]. The ridge antenna exhibits an in-plane dipolar resonance aligned with its long axis (in the xy -plane parallel to the surface) at $\lambda_0 = 650$ nm, which is most efficiently excited by the electron beam at the extremities of the ridge (see Figs. 5.2(b,e)). Figure 6.2(b) shows the emission pattern for an in-plane dipole calculated using asymptotic far-field expressions for a point dipole above a substrate [94]. In this case we have placed the dipole 65 nm (half of the antenna height) above the gold surface. The pattern now shows one emission lobe pointing towards the normal. By rotating the SEM sample stage with respect to the mirror in the xy -plane we can probe the emission polarization response for x - and y -oriented dipoles. Thus, by using both the unstructured substrate and ridge we have access to three orthogonal dipole orientations with known emission polarization which we can use to test the polarization sensitivity of our experimental setup.

Figures 6.2(c,d) show cross cuts through (a) and (b) along the blue dashed line ($\phi = 90 - 270^\circ$) yielding emission intensity as function of θ (blue solid curves) in which we have indicated the polarization direction $\hat{\mathbf{e}}$ (red arrows) for different emission directions $\hat{\mathbf{d}}$. The electric field orientation for (c) corresponds to that of a vertically oriented point dipole source [94] and to an in-plane point dipole for (d). It is clear that the vertical dipole is radially polarized (p-polarized) whereas for the in-plane dipole the emission polarization is aligned with the dipole moment

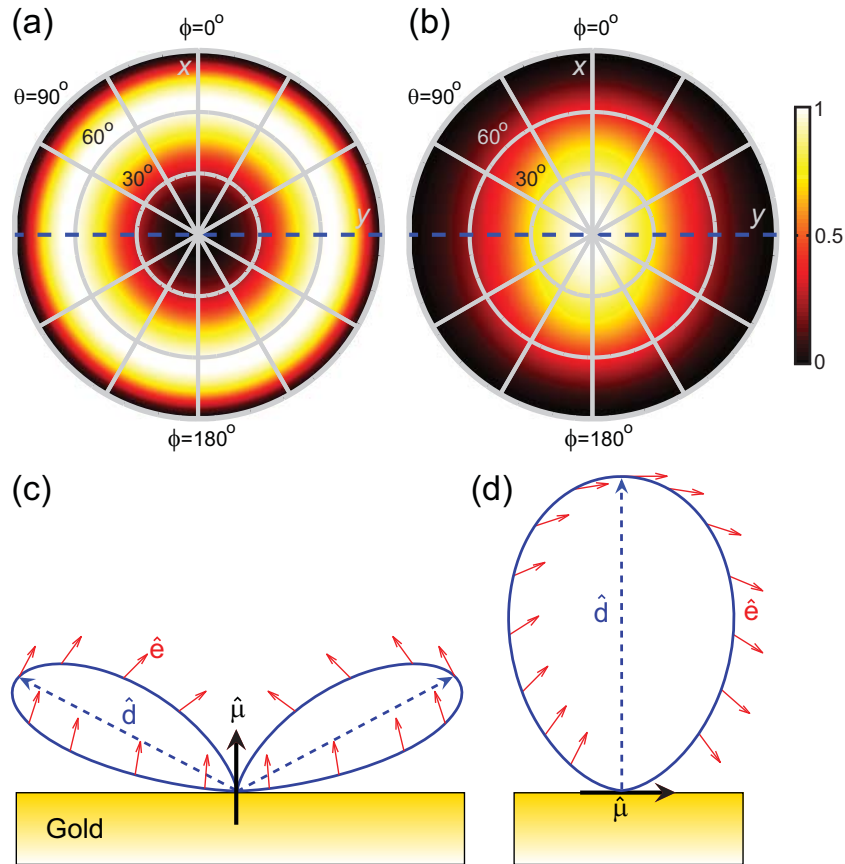


Figure 6.2: (a) Calculated normalized cathodoluminescence emission intensity as function of zenithal angle θ and azimuthal angle ϕ for TR on a gold substrate which is similar to the pattern for a vertically oriented dipole $\hat{\mu}$ (black arrow). (b) Calculated angular pattern for an in-plane point dipole like the ridge antenna, aligned along y . (c,d) Cross cuts through (a) and (b) along the blue dashed lines showing the angular patterns as function of θ . For each emission direction \hat{d} there is a corresponding electric field orientation \hat{e} which is indicated by the red arrows for a selection of emission directions.

In optical Fourier microscopy light is usually collected with a high quality microscope objective. Such an objective converts the light originating from a point source at the focal point to a plane wave propagating in the z -direction. Assuming that we have a ‘perfect’ objective (no aberrations and perfect transmission), calculating its effect on the dipole emission polarization is quite straightforward since all the electric field components are projected onto the xy -plane, transverse to the propagation direction. The resulting polarization-filtered angular pattern is a convolution of the far-field pattern and the polarization filtering after light collection. Figure 6.3 shows the angular emission intensity collected with a $NA = 0.96$ (same acceptance angle as the paraboloid) objective for z - and y -dipole orientations, respectively, when the polarizer is aligned with the x - or y -axis. The black ring around the pattern corresponds to grazing angles that are not collected by the

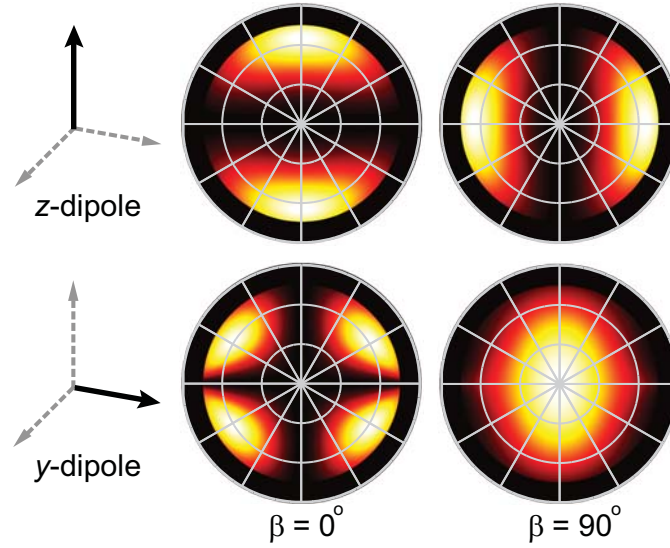


Figure 6.3: Calculated radiation patterns for a z - and y -dipole collected with a “perfect” optical microscope objective (NA = 0.96).

objective. For a z -dipole, the part of the emission toroid where the field is (partly) aligned with the polarizer is transmitted. Due to its azimuthally symmetric field distribution this pattern rotates along with the polarizer. For the y -dipole the dipole emission pattern is relatively well-preserved when the polarizer is aligned with the dipole-axis. However, for the cross-polarization the pattern is strongly altered and shows four off-normal lobes. For an x -dipole the result is the same but rotated by 90° .

To study the emission polarization for the three dipole orientations in our experimental setup, we excite the bare gold substrate and the ridge antenna and collect a polarization-filtered CCD-image for 120 seconds at $\lambda_0 = 650$ nm. For the ridge antenna we position the beam close to the end facet where the excitation probability of the in-plane dipole resonance is high (see Figs. 5.2(b,d,e)). We vary β from 0° to 170° in steps of 10° yielding 18 polarization-filtered angular patterns per dipole orientation. The two columns on the left of Fig. 6.4 show experimentally obtained angular emission patterns (CL emission intensity as function of zenithal angle θ and azimuthal angle ϕ) for $\beta = 0^\circ$ and $\beta = 90^\circ$ collected for all three orientations. As expected, the collected pattern depends strongly on polarization and dipole orientation. Furthermore, the observed patterns deviate strongly from the patterns collected without polarizer (see Figs. 3.3, 5.6 and 6.2(a,b)). For the x - and z -dipole the emission is strong along the centerline of the mirror (from $\phi=0^\circ$ to $\phi=180^\circ$), along the optical (x)-axis for $\beta = 0^\circ$, whereas for $\beta = 90^\circ$ the centerline is dark and we see two transverse lobes. It is clear that these patterns are profoundly different from the calculated Fourier images for the microscope objective in Fig. 6.3.

In our setup we collect the CL emission using a reflective aluminum paraboloid mirror which has a polarization response that strongly differs from a microscope

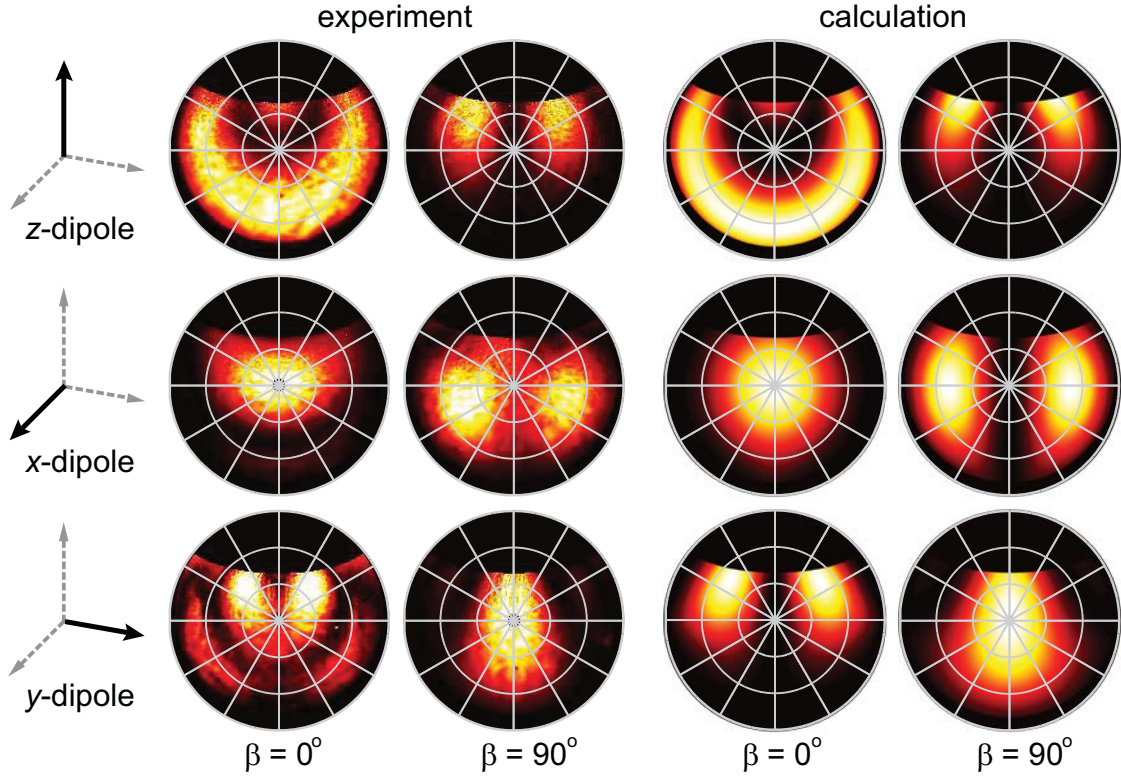


Figure 6.4: Experimental (first two columns) and calculated (last two columns) angular cathodoluminescence emission patterns for different dipole orientations and polarizer angles β measured at $\lambda_0 = 650$ nm (30 keV electrons). The black area around $\phi = 0^\circ$ is not collected by the mirror. The hole is located at $\theta = 0^\circ$ in the center of the polar plot.

objective. Because of the paraboloidal shape the emission polarization direction after reflection is significantly altered. Furthermore, since the permittivity of aluminum has a non-negligible imaginary part in the visible spectral range, the emission polarization can become ellipsoidal after reflection for some incoming electric field orientations. Thus, in order to fully understand the experimental results we have to calculate what effect the mirror has on the polarization for each emission angle. To calculate the polarization-filtered angular pattern for a particular polarizer angle and dipole orientation we take the following approach. We define an emission vector $\hat{\mathbf{d}}$ which specifies the emission direction for a combination of θ and ϕ (Eq. 6.1 (a)) which can be done by simply using spherical coordinates. For every emission direction, the electric field orientation $\hat{\mathbf{e}}$ for a dipole oriented along $\hat{\boldsymbol{\mu}}$ can be calculated, using the same asymptotic far-field expressions as used for Fig. 6.2. Note that the polarization direction is always perpendicular to the emission propagation direction ($\hat{\mathbf{d}} \cdot \hat{\mathbf{e}} = 0$).

$$\hat{\mathbf{d}} = [\sin\theta \cos\phi \quad \sin\theta \sin\phi \quad \cos\theta] \quad (6.1a)$$

$$\hat{\mathbf{c}} = [ar^2 \quad r \cos\alpha \quad r \sin\alpha] \quad (6.1b)$$

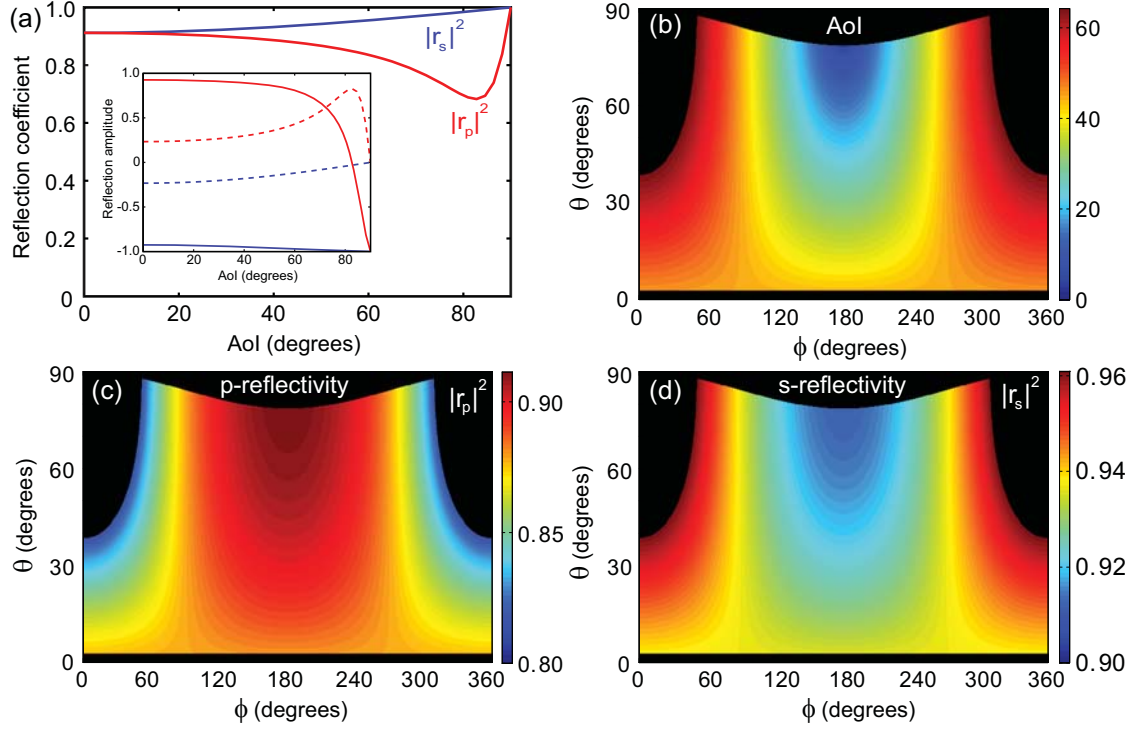


Figure 6.5: (a) Reflectivity as function of angle of incidence (AoI) for an aluminum surface at $\lambda_0 = 650$ nm calculated for s- and p-polarized light. The inset shows the real (solid curves) and imaginary (dashed curves) parts of the Fresnel reflection coefficients for s- and p-polarized light. (b) Angle of incidence on the mirror surface for all emission angles θ and ϕ collected by the mirror. Angles that are not collected are colored black. (c) Reflectivity of the mirror for p-polarized light and (d) s-polarized light.

To calculate the reflection properties we have to take into account the mirror geometry. The position of the paraboloid in cartesian space ($\vec{\mathbf{c}}$) can be parameterized in terms of r and α where $r = (y^2 + z^2)^{1/2}$, $\alpha = \cos^{-1}(y/r)$ and a is the parabola coefficient which is 0.1 for our paraboloid. The surface normal of the paraboloid can be attained by taking the cross product of the α - and r -gradient of $\vec{\mathbf{c}}$.

$$\vec{\mathbf{n}} = \nabla_{\alpha} \vec{\mathbf{c}} \times \nabla_r \vec{\mathbf{c}} \quad (6.2)$$

Expressions for the gradients can simply be attained by symbolic differentiation of Eq. 6.1(b). To calculate the reflection at the mirror surface we need to calculate the Fresnel reflection coefficients for s-polarized (r_s) and p-polarized (r_p) light for different angles of incidence (AoI). Figure 6.5(a) shows $|r_s|^2$ and $|r_p|^2$ as function of the AoI for $\lambda_0 = 650$ nm [149]. The real and imaginary parts of the reflection coefficients are shown in the inset of (a). It is clear that the reflectivity for s-polarized light is always higher than for p-polarized light. The angle of incidence on the mirror for a light ray emitted in a direction $\hat{\mathbf{d}}$ is given by $\text{AoI} = \cos^{-1}(\hat{\mathbf{d}} \cdot \hat{\mathbf{n}})$. Figure 6.5(b) shows the AoI for all combinations of θ and ϕ . In some parts of the mirror the light reflects

under quite a grazing angle (up to 63°). From Figs. 6.5(a,b) we can calculate r_s^2 and r_p^2 for each emission direction (Figs. 6.5(c,d)). The reflectivity is always higher than 0.8 for all collected emission angles and incoming polarizations.

By definition the s-polarization direction $\hat{\mathbf{s}}$ is given by $\hat{\mathbf{n}} \times \hat{\mathbf{d}}$ and the p-polarization direction $\hat{\mathbf{p}}$ is given by $\hat{\mathbf{d}} \times \hat{\mathbf{s}}$. Now we can decompose the incoming polarization into a p-polarized and s-polarized part by projecting $\hat{\mathbf{e}}$ onto $\hat{\mathbf{p}}$ and $\hat{\mathbf{s}}$. By multiplying the p-and s-components of the field with the appropriate Fresnel coefficients (see Fig. 6.5) we can calculate the electric field orientations after reflection. Note that we have to correct for the fact that the p-component of the field changes direction after reflection from the mirror in order to maintain orthogonality with the propagation direction. Since the paraboloid converts the light from a point source into a plane wave traveling along the x -direction the electric field only has y -and z -components after reflection. To find the electric field after the polarizer we have to multiply the field components with the Jones matrix for a linear polarizer.

$$\vec{\mathbf{E}}_{out} = \begin{bmatrix} E_y \\ E_z \end{bmatrix} \begin{bmatrix} \cos^2 \beta & \sin \beta \cos \beta \\ \sin \beta \cos \beta & \sin^2 \beta \end{bmatrix} \quad (6.3)$$

By multiplying $|\vec{\mathbf{E}}_{out}|^2$ with the characteristic angular intensity distribution for the dipole orientation under consideration (see Figs. 6.2(a,b)) we can compare our calculations to the experiment and explain the observations.

The third and fourth column in Fig. 6.4 show the calculated polarization-filtered angular emission distributions. For the z -oriented dipole the calculation agrees very well with the data. For the line $\phi = 0 - 180^\circ$ the emission is bright for $\beta = 0^\circ$ and dark for $\beta = 90^\circ$. The reflection of the radially polarized emission in the center of the mirror (along the x -axis at $y = 0$) only has p-character and after reflection the electric field only has a z -component. For $\beta = 0^\circ$ the field is fully transmitted whereas for 90° the field is blocked, explaining the bright and dark bands in the center. A similar explanation can be given for the x -dipole, where the reflection also only has p-character and the field after reflection is again oriented along z . The y -oriented dipole only has s-character in the center of the mirror (the field is aligned with y), and as a result we observe the opposite behavior: a dark band for $\beta = 0^\circ$ and a bright band for $\beta = 90^\circ$. The observed patterns are a convolution of the initial far-field intensity distribution (Fig. 6.2) with the emission polarization properties. The differences between the patterns for the different dipole orientations are due to both effects. It is clear that the calculation matches our experimental results better for the z -dipole than for the x -and y -dipole. We attribute this to the fact that the properties of the z -oriented transition dipole are very close to an analytical point dipole, whereas the antenna resonance has dipolar character but is not a pure point dipole due to the physical size and limited aspect ratio (2.5:1) of the antenna.

To illustrate that our approach works for other polarizer angles as well we show both the experimental and calculated patterns for the z -oriented dipole for $\beta = 0 - 150^\circ$ in steps of 30° (Fig. 6.6). The gradual change of the angular pattern when rotat-

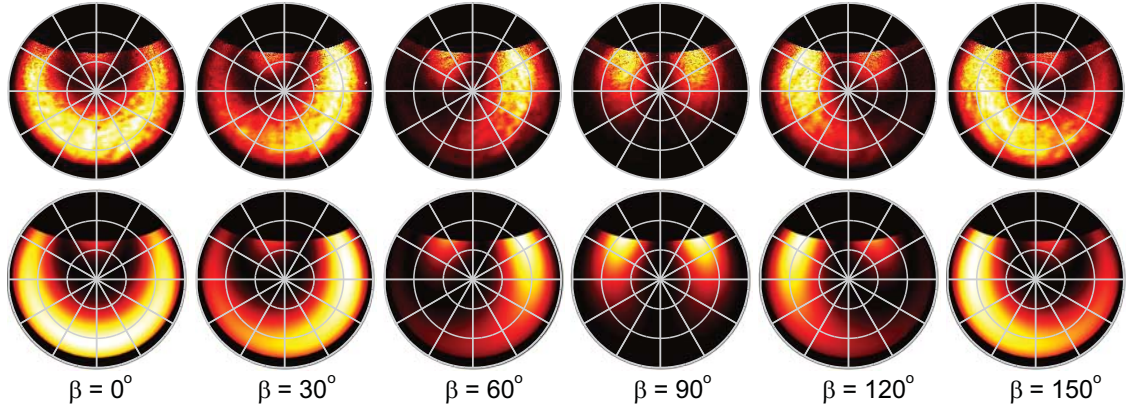


Figure 6.6: Experimental (top row) and calculated (bottom row) polarization-filtered angular cathodoluminescence emission patterns for transition radiation measured for different polarizer angles at $\lambda_0 = 650$ nm. Radiation patterns are shown for $\beta = 0^\circ, 30^\circ, 60^\circ, 90^\circ, 120^\circ$, and 150° respectively.

ing the polarizer is clearly visible in both the experiment and calculation, demonstrating the accuracy of our model.

6.4 Enhancing polarization contrast

When using a microscope objective for detection of emission originating from an in-plane dipole above a gold substrate, the total intensity integrated over all collected angles (obtained from Fig. 6.3) is ~ 30 times higher when the polarizer is aligned with the dipole axis than for the cross-polarized orientation. This means that when the collected optical scattering or fluorescence is sent to a spectrometer for spectral analysis one can clearly distinguish two dipole orientations by using a polarizer after light collection. Due to its azimuthally symmetric charge distribution there is no contrast for a z -dipole. As we have shown in the previous Section, the mirror strongly affects the detected polarization. We can calculate the polarization contrast for our experimental setup by integrating the emission patterns shown in Fig. 6.4. The polarization contrast for our detection geometry is significantly lower than for the objective. Interestingly the contrast for x and y differ slightly which is due to the fact that the paraboloid mirror is not azimuthally symmetric in its response like an objective. This is also the reason why the contrast for z is not equal to zero like for the objective. The emission polarization is distorted less in the center of the mirror so by using a slit we can greatly enhance the polarization contrast in CL-spectroscopy. This approach has been employed previously to probe the polarization response of surface plasmon polariton (SPP) whispering gallery resonators [157]. Takeuchi *et al.* have taken a similar approach where they scan a pinhole over the mirror center to accurately determine the dispersion patterns of SPPs in two-dimensional metallic hole arrays [98]. Furthermore there are several

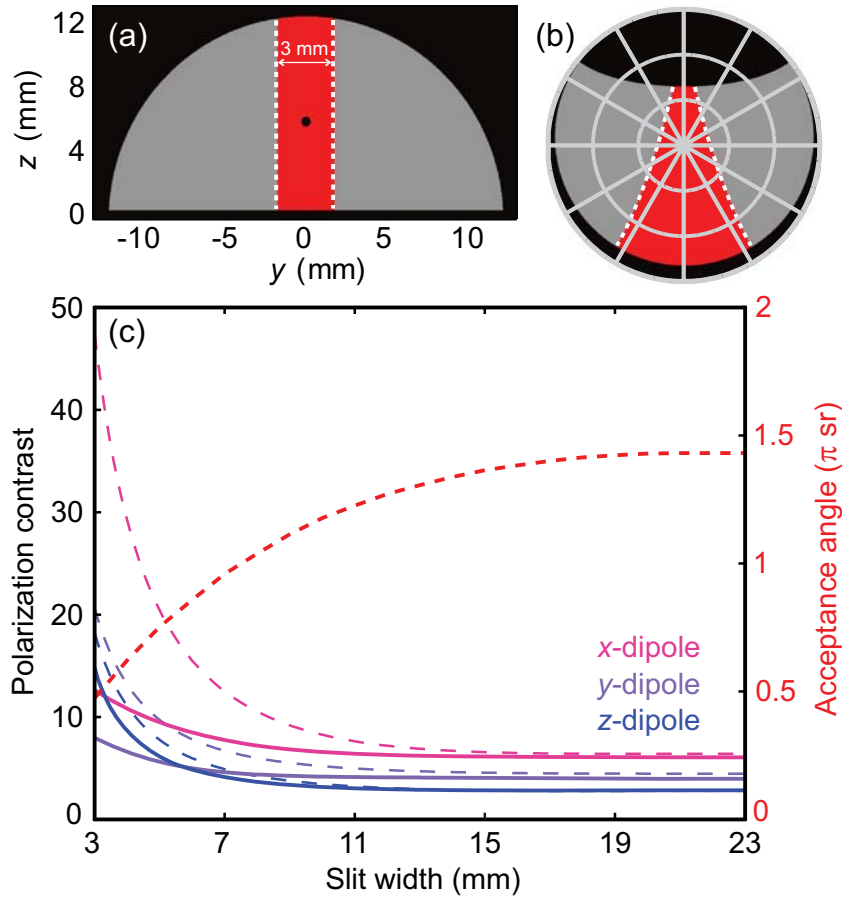


Figure 6.7: (a) Front view of the mirror. The white dashed lines indicate the edge of a rectangular 3 mm slit placed in front of the mirror. The total width of the mirror is 23 mm. The part of the mirror from which light is collected is indicated by the red area and the parts that are blocked are shown in gray. The black dot in the center corresponds to the hole in the mirror (b) Polar plot showing which angles are blocked by the slit. (c) Experimental (solid curves) and calculated (dashed curves) polarization contrast for a z -, y - and x -oriented dipole as function of slit width. The slit was introduced numerically by appropriately clipping the experimental and calculated polarization-filtered angular patterns shown in Fig. 6.4. The red dashed line shows the amount of collected solid angle as function of slit width.

groups that have performed polarization-sensitive CL-spectroscopy on semiconductor and metallic nanostructures where polarization measurements were performed without a slit [87, 158–160].

Here we work out in detail what the effects are of introducing a slit in the beam path. Figure 6.7(a,b) shows what part of the mirror is blocked by a 3 mm slit (the total width of the mirror is 23 mm). Note that the rectangular slit gives an asymmetric shape in the polar plot due to the curvature of the paraboloid. In Fig. 6.7(c) we show how the polarization contrast depends on the slit width for the three different dipole orientations both for theory (dashed curves) and experiment (solid curves). We have numerically introduced a slit by appropriately clipping both the

experimental and calculated polarization-filtered patterns shown in Fig. 6.4 such that all the angles that would be blocked by the slit are set to zero. This was done for slit widths between 3 and 23 mm. For the z -dipole the experiment matches quite closely to the calculated curve and the polarization contrast is enhanced six times for a 3 mm wide slit. The small discrepancy between experiment and theory is mainly caused by imperfections in the detection system like the polarizer for instance, which does not fully block cross-polarized light. For the x - and y -dipole the experiment deviates substantially from the theoretical curve which we attribute to the fact that the ridge is not a perfect dipole emitter. Nevertheless the polarization contrast is enhanced by a factor of two for both dipole orientations (assuming a 3 mm slit) which is still useful for determining the dipole orientation in such structures. This technique could be employed in the future for probing the polarization properties for more complex structures where the orientation of the dipole moment is unknown *a priori*.

Although the polarization contrast is greatly enhanced by using a slit, the acceptance angle decreases (see red dashed curve in Fig. 6.7(c)) lowering the signal-to-noise (SNR) ratio. Furthermore the slit blocks certain emission angles and as a result it acts as a ‘momentum filter’. Therefore one should be cautious in interpreting experimental results when dealing with highly directional antenna structures rather than omnidirectional dipolar emitters. Also it is difficult to distinguish between an x - or z -oriented dipole by the polarization response alone. The angular patterns are very different though (see Fig. 6.2) and can be used to differentiate between the two. Using this knowledge one can now pick the optimum slit width depending on the SNR, directionality of the structure under investigation, and the required polarization contrast. One could even envision using custom slit or pin-hole shapes optimized for a particular angular region of interest.

6.5 Emission polarization reconstruction

In Section 6.3 we have shown how to calculate the polarization-filtered angular pattern if the emission polarization is known. We can also perform the reverse operation by extracting the emission polarization from the experimental data. For a particular emission angle we can plot the CL intensity as function of β . In Fig. 6.8(a) we have plotted the CL-intensity as function of β for $\phi = 180^\circ$ and $\theta = 35^\circ$ for all the three dipole orientations. As was explained in Section 6.3, the intensity is maximum for the z/x -oriented dipole and minimum for the y -oriented dipole when $\beta = 0^\circ$. For linearly polarized light the intensity varies as $\cos^2(\beta - \beta')$, where $\beta' = \tan^{-1}(E_y/E_z)$ represents the angle of the electric field with respect to the z -axis.

In some parts of the mirror the emission becomes slightly elliptical, as explained before. For elliptically polarized light the intensity does not go to zero. In that case the maximum value of the oscillation corresponds to the square of the semi-major axis of the polarization ellipse and the minimum corresponds to the square of the semi-minor axis. The maximum degree of

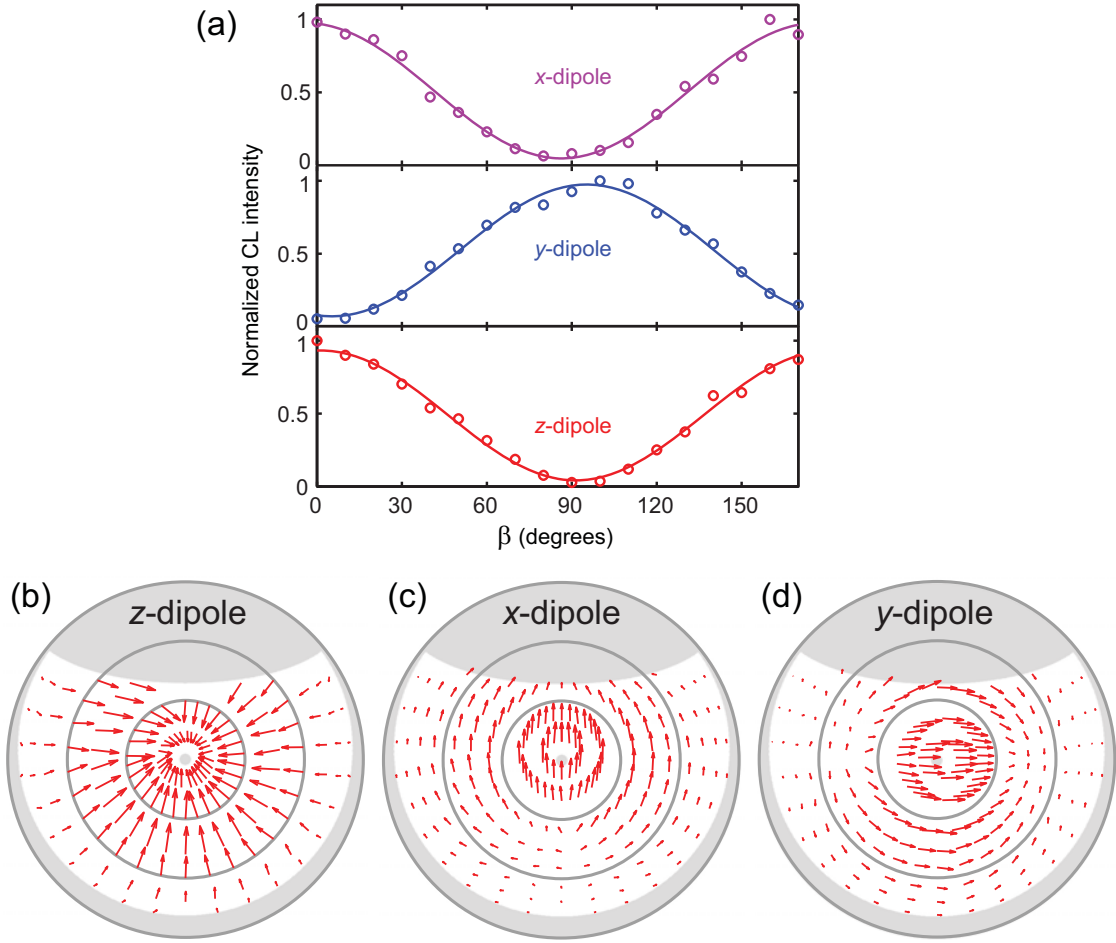


Figure 6.8: (a) Normalized cathodoluminescence intensity as function of polarizer angle (β) for $\theta = 35^\circ$ and $\phi = 180^\circ$ for the three dipole orientations. The open circles represent the experimental data and the solid curves are the numerical fits. (b) Vector field plot showing the orientation of the electric field projected onto the xy -plane (top view of the vector field) for different emission angles (the gray concentric circles correspond to $\theta = 30^\circ, 60^\circ$, and 90° respectively) reconstructed from the experimental data for the z -dipole, (c) x -dipole, and (d) y -dipole. The light gray colored area corresponds to angles that are not collected by the mirror.

ellipticity (DoE) is 0.22 where we define DoE as the ratio between the semi-minor and semi-major axis of the polarization ellipse. For most emission angles the offset in the intensity oscillation caused by this ellipticity is negligibly small and difficult to measure due to uncertainties in the measurement caused by noise and aberrations/imperfections in the optics. Note that it is not possible to extract the complex field amplitudes from the shape of the polarization ellipse alone. To obtain all four independent Stokes parameters interferometric measurements or the addition of a circular polarizer in the beam path would be required [149]. In this reconstruction we will assume for simplicity that the collected emission is linearly polarized and neglect the phase pickup upon reflection from the mirror. We do

divide the p- and s-components of the electric field by $|r_p|$ and $|r_s|$ respectively, to correct for the reflection losses from the mirror.

From the maximum value of the fitted \cos^2 function we can deduce the magnitude of the electric field and from the position of the maximum we can deduce the relative magnitude of E_z and E_y (the electric field orientation). Now we can do the inverse of what was done in Section 6.3 by sending rays back into the mirror (in the negative x -direction) with the electric field orientation that was found from the fitting. This yields the amplitude and orientation of the electric field in 3D-space for each emission angle. It can be difficult to visualize vectors in 3D space, but to distinguish between the different dipole orientations we do not necessarily need E_z .

In Fig. 6.8(b-d) we show the experimentally retrieved emission polarization for z -, x - and y -oriented dipoles respectively. We only plot E_x and E_y as function of emission angle in a vector field plot where the direction of the arrows shows the orientation of the electric field in the xy -plane and the length of the arrows represents $(E_x^2 + E_y^2)^{1/2}$. The base of the arrow corresponds to the emission angle in the polar plot. Note that in all plots the direction of the arrows can be rotated by 180° because the electric field changes sign every half optical cycle. In Fig. 6.8(b) the electric field vectors all are approximately pointing towards the center, thereby confirming that the emission from the TR-dipole (z -dipole) is radially polarized as is expected from theory (see Fig. 6.2(c)) [63]. The electric field amplitude becomes smaller near $\theta = 0^\circ$ as expected from the toroidal far-field pattern. However, the emission intensity should be maximum around $\theta = 60^\circ$ which is not the case here. This is due to the fact that the emission polarization has a large E_z component for the more grazing angles which is not visible in the plot (the plot is a top view of the vector field). In Figs. 6.8(c, d) the electric field is clearly aligned with the dipole moment (along x in Fig. 6.8(c) and along y in Fig. 6.8(d) respectively) and the patterns look similar to those of a point dipole [94, 149]. Thus, although this reconstruction neglects the phase change upon reflection we can clearly infer the orientation of the excited dipole moment without knowledge about the polarization direction of the source.

6.6 Conclusions

In conclusion, we have demonstrated a novel method to perform polarization-sensitive cathodoluminescence Fourier microscopy. As proof of principle we measured polarization-filtered angular emission patterns for three orthogonal dipolar sources and compared them with calculations where we assumed that we were driving a point dipole on the gold surface which was oriented along x , y , or z . The calculated polarization-filtered angular patterns show good agreement with experiments suggesting that the effect of the mirror on the polarization is well-captured by our model. Furthermore we calculate that introducing a slit in the beam path greatly enhances the polarization contrast which is useful

for polarization-sensitive spatially-resolved mapping of the local density of optical states. Finally, we show that we can effectively reconstruct the emission polarization for each of the dipole orientations, assuming that the emission is linearly polarized and that the effect of the mirror on the relative phase between s- and p-components is negligible. The addition of polarization sensitivity makes the cathodoluminescence microscopy technique an even more powerful and versatile tool for probing the near- and far-field properties of nanophotonic structures. By including phase-sensitive detection in future experiments we could extract the full polarization state of the emission as function of wavelength, emission angle, and excitation position. This could lead to new insights in the polarization properties of more complex antenna and metamaterial designs.

7

A planar parabolic antenna

One of the simplest and most common structures used for directing light in macroscale applications is the parabolic reflector. Parabolic reflectors are ubiquitous in many technologies, from satellite dishes to hand-held flashlights. Today, there is a growing interest in the use of ultracompact metallic structures for manipulating light on the wavelength scale. Significant progress has been made in scaling radiowave antennas to the nanoscale for operation in the visible range, but similar scaling of parabolic reflectors employing ray-optics concepts has not yet been accomplished because of the difficulty in fabricating nanoscale three dimensional surfaces. In this Chapter, we demonstrate that plasmon physics can be employed to realize a resonant elliptical cavity functioning as an essentially planar nanometallic structure that serves as a broadband unidirectional parabolic antenna at optical frequencies.

7.1 Introduction

Controlling the far-field emission pattern of nanoscale objects is one of the central goals of optical antennas [29, 161]. In most cases, the desired pattern is a beam of light in the far field, which can couple a nanoscale source or sink of light to a distant object. Optical beaming could improve performance in a variety of important applications, such as photon sources [162], photodetectors [163], sensors [164], and photovoltaics [165]. Previous antennas have demonstrated beaming

in engineered directions over narrow frequency ranges [39, 114, 135, 166–168], or broadband beaming in structures several times larger than the wavelength [169]; however a broadband device with a small footprint and high directivity has not yet been demonstrated. Parabolic reflectors are ubiquitous macroscopic structures that efficiently couple electromagnetic energy from a focal point to a beam and work over a very large range of frequencies. It would seem natural that parabolic structures would also be useful for small-scale optical antennas; however, fabricating complex three-dimensional surfaces is not generally possible with traditional nanofabrication tools. By using a gold surface as a two-dimensional medium for propagation of surface waves, namely, surface plasmon polaritons (SPPs), it is possible to reduce the dimensionality of a parabolic reflector while maintaining its optical beaming behavior. We demonstrate that a two-dimensional cross section of a paraboloid cut into a gold surface, an elliptical cavity, presents the broadband unidirectional emission expected of the full three-dimensional structure and is much more amenable to fabrication. When reduced in size to the wavelength-scale, these structures retain their beaming functionality and also present a set of well-defined optical resonances that enhance emission for particular wavelengths.

Parabolic reflectors are well-known in geometrical optics; they couple the emission of a point source at the parabola's focus to a plane wave propagating parallel to parabola's axis, and *vice versa*. In a classical three-dimensional parabola the emitted light beam originates from the specular reflection of light over the entire parabola's surface. However, due to the special geometrical properties of a parabola, an array of individual scatterers placed in a parabolic arrangement will also generate a parallel beam of light in the far field. In fact, a point source coupled to any two-dimensional subsection of a paraboloidal surface will generate a wave preferentially propagating parallel to the paraboloid's axis. One special case of such a subsection is the elliptical intersection of a paraboloid with a planar surface, with the paraboloid and the planar ellipse sharing a common focus. In such a geometry, a beam of light can be generated by exciting SPPs near one of the two foci inside the planar ellipse followed by coherent scattering of the SPPs to free-space photons via the edges of the area in the form of a collimated beam. The direction of the beam is only determined by the position of the source inside the ellipse and the ellipse's eccentricity. A detailed analytic description of this model is given in the Supporting Information of Ref. [170].

Figures 7.1(a,b) show the sample geometry. A series of concentric elliptical grooves has recently been used to realize a bull's eye type beam director with a controllable beam direction based on a similar concept [171]. In contrast to this work, the elliptical bull's eye structure has a well-defined operation wavelength based on coherent scattering from multiple grooves, whereas here the broad optical resonances of the plasmonic cavity are utilized to achieve high directivities.

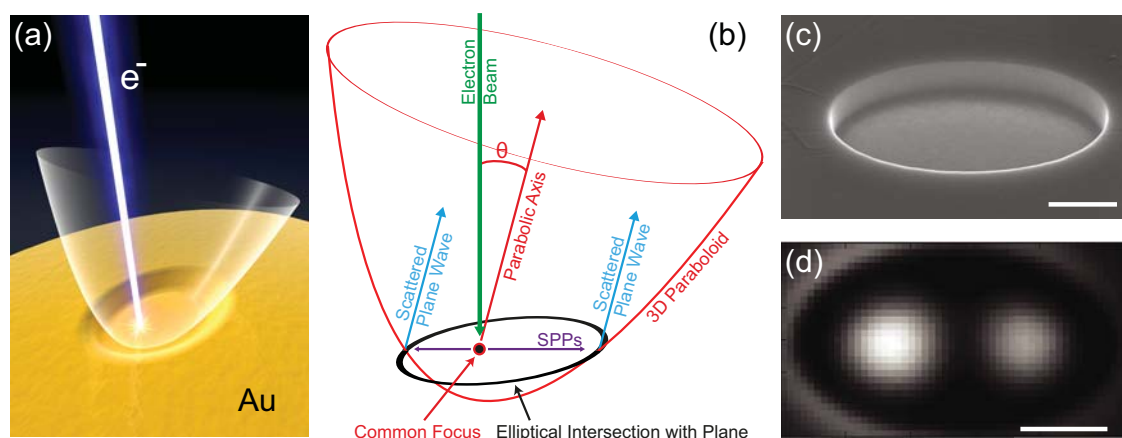


Figure 7.1: (a) 3D Graphical representation of ellips acting as a parabolic antenna (image by Tremani) (b) Schematic of the intersection of a paraboloid with a planar surface, creating an ellipse. (c) SEM image of elliptical arena taken at 52° off the surface normal. The scale bar is 500 nm. (d) 30 keV cathodoluminescence image at a collection wavelength of 720 nm for a 1.0- μm -long, 800-nm-wide elliptical cavity. The scale bar is 250 nm.

7.2 Sample fabrication

The elliptical arenas were fabricated by focused-ion-beam (FIB) milling using an FEI Helios Nanolab Dual Beam instrument into a single crystal pellet of gold which had been previously polished to nanometer-scale roughness. Similar geometries can also be made using template stripping [172]. Patterns were defined as bitmaps and milled top to bottom with a beam current of 1.5 pA. Higher beam currents also provide structures with similar behavior.

7.3 CL imaging of elliptical cavity plasmon modes

A SEM image of a characteristic ellipse is shown in Fig. 7.1(c). Several different elliptical geometries were fabricated with major axis lengths ranging between 500 and 1600 nm, and eccentricities, defined as the ratio between the major axis length and the focus-to-focus distance, between 0 and 1. The depth of the elliptical cavity was also varied; typically a depth of 400 nm was used. The localized optical modes in these structures were determined using our angle-resolved cathodoluminescence imaging spectroscopy (ARCIS) technique (for details on the experimental setup see Chapters 2 and 3). A 30 keV electron beam is raster-scanned over the surface and serves as a broad-band point source of surface plasmon polaritons. The radiation spectrum emitted by the antenna is collected by a half-paraboloidal mirror placed between the microscope's pole piece and the sample, after which the spectrum can be measured with a spectrometer and the angular distribution can be measured with a 2D CCD camera.

Fig. 7.1(d) shows a CL image of a 1000×600 nm elliptical cavity recorded at a wavelength of 720 nm. The pixel size in the images of the smaller cavities is 10×10 nm and 20×20 nm in the largest cavities. The two foci of the elliptical antenna are clearly resolved in the image, demonstrating the subwavelength resolution of the CL technique. As CL is a direct probe of the radiative component of the local density of optical states (LDOS) [63], images such as in Fig. 7.1(d) provide a direct absolute measure of the radiation power of the antenna at any wavelength.

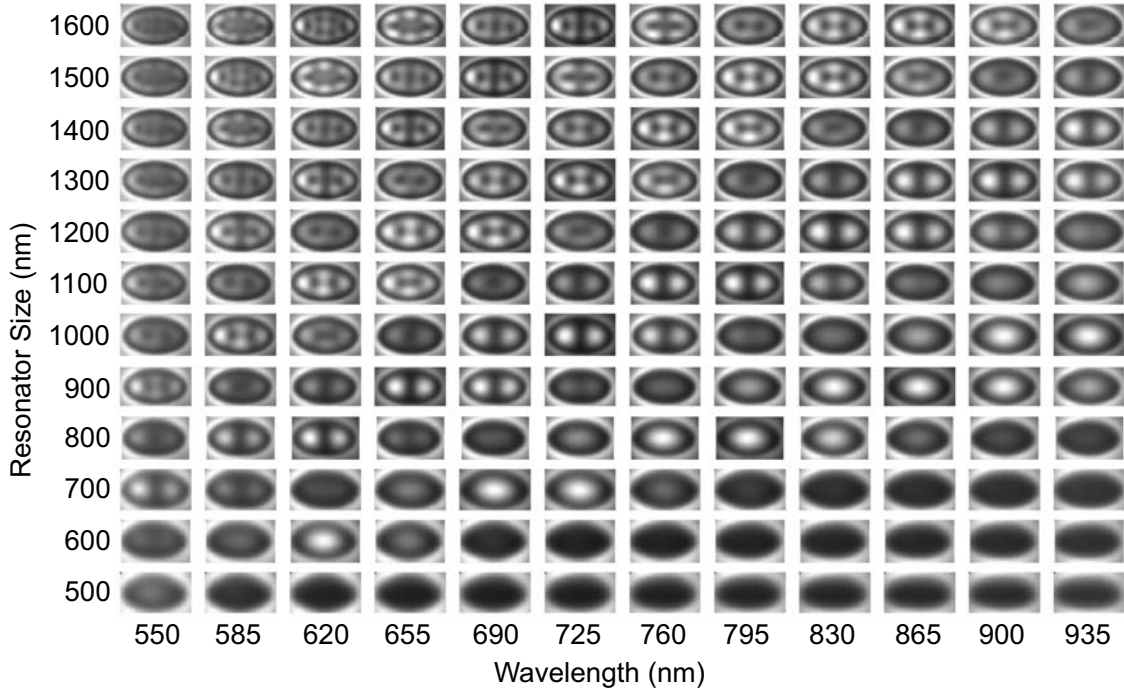


Figure 7.2: Cathodoluminescence images (30 keV electrons) for cavities with eccentricity 0.8 and major axes ranging from 500 to 1600 nm for different collection wavelengths. Cavity modal patterns with increasing mode order ($m = 0, 1, 2, \dots$) are clearly visible. All images are scaled by the major axis length.

Figure 7.2 shows CL images for cavities with an eccentricity of 0.8, with major axes between 500 nm and $1.6 \mu\text{m}$. Data are shown for collection wavelengths in the range 550 – 935 nm. As can be seen, as the ratio of cavity size to wavelength increases, cavity modal intensity distributions of increasing mode order are observed. Modal distributions of a similar type have previously been observed in plasmonic whispering gallery cavities and cylindrical cavities [157, 173], and the modal distributions of photonic elliptical cavities has been explored by near-field scanning optical microscopy [174, 175]. Fig. 7.3 shows the CL spectra averaged over the elliptical cavity area for the 2D scans presented in Fig. 7.2. It can be seen that the resonant modes shift to longer wavelengths as the cavities increase in size. Different resonant modes, observed in Fig. 7.2, appear as different resonant peaks in the spectra. The quality factor for the plasmon resonances in Fig. 7.2 is in the range $Q = 10 - 20$. Larger cavities have lower quality factors due to increased ohmic

losses of the SPPs in the metal. Resonant modes at long wavelengths have lower Q due to a lower reflection coefficient at the cavity end, caused by a larger modal evanescent tail in the normal direction into the air. Similarly, deeper cavities show higher quality factors due to increased reflectivity of the metallic walls, which lowers the radiation losses (see Supplementary Fig. 7.5).

7.4 Resonance model for ellipses

While an exact analysis of the elliptical cavities resonant modes can be made using a Green's function approach or the boundary-element method [174–176], a first-order model that provides very good physical insight predicts resonances occurring when the phase accumulated by SPPs traveling a round trip inside the ellipse is equal to an integer number m times 2π :

$$2Lk_{SPP} + 2\Phi = 2\pi m \quad (7.1)$$

with L the major axis length, k_{SPP} the SPP wave vector, and Φ the phase increment upon reflection at the cavity boundary. This model describes the cavity modes in one-dimensional nanowires where the resonance are determined by the cavity length [32, 136, 143, 177]. All of the experimentally observed peaks can be fit with this model, even though it only considers resonances related to one characteristic length, that of the major axis. This directly follows from the special geometrical properties of ellipses: in an elliptical cavity, in a simple ray optics picture, all rays that emanate from one focus will reflect off the ellipse's edge in the direction of the opposite focus. The distance of this path is the same regardless of the initial direction of the first ray and is equal to the major axis length. Thus the major axis length defines the characteristic resonances for the cavity. The reflections of SPPs in elliptical cavities have been explored previously by leakage radiation microscopy for large cavities with major axis lengths greater than $30 \mu\text{m}$ [178], but this is the first time such a model has been proposed for a resonant SPP cavity on the wavelength scale. We approximate the SPP wave vector by that for an SPP propagating on an infinite plane of gold. The wave vector in the ellipse will be affected by the lateral confinement imposed by the walls of the cavity, which explains the shift observed between the predicted peak positions and those in the experiment. The increased confinement experienced by the SPPs in the elliptical cavity will result in increased wave vector, resulting in shorter SPP wavelengths compared to free space than calculated, thus shifting the observed modes to the left in Fig. 7.3(b), closer to the model prediction. Interestingly we do not see spectral evidence of any whispering gallery type modes. It is possible that such modes, if they exist, are confined to the corners of the structure. If so, they will have a mode index substantially higher than those for the SPPs propagating on the floor of the cavity, and thus may radiate poorly to the far field.

Figure 7.3(b) shows the data from Fig 7.3(a) replotted versus plasmon wavelength and cavity length. The linear resonance redshift with cavity length is clearly

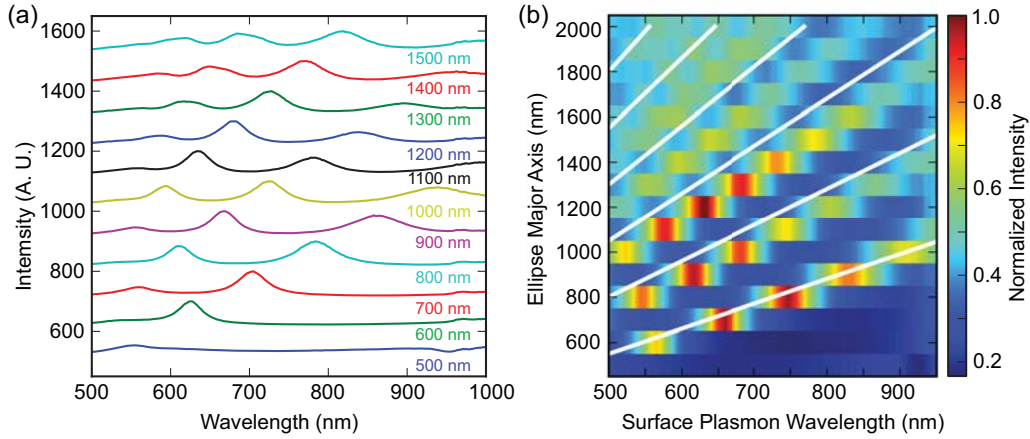


Figure 7.3: (a) Cathodoluminescence spectra for elliptical cavities with eccentricity 0.8 with major axes ranging from 500 to 1600 nm. A redshift for the various resonances increasing cavity size is clearly visible. (b) Same data as in (a) now represented in a map of CL intensity *versus* surface plasmon wavelength and cavity major axis. The white lines indicate the resonant modes calculated using a Fabry-Pérot interference model.

visible (see also Supplementary Fig. 7.6(a)). We fitted Eq. 7.1 through the entire data set for all modes in Fig. 7.3(b), with the phase pickup Φ as the only free parameter, which yields the white dashed lines in Fig. 7.3(b). The model describes the overall trends very well (also see Supplementary Fig. 7.6(b)) and yields $\Phi = -1.2\pi$. The negative value obtained for Φ is in contrast to experiments on strip antennas which have shown a positive phase pickup [142, 143]. The negative phase pickup for an SPP reflecting off the metallic ellipse boundary is similar in nature to the negative phase pickup seen for a plane wave reflection off a metal mirror. This phase shift effectively makes the arena appear smaller than would be expected for a phase pickup $\Phi = 0$. This attenuation in the spatial extent of the modes is also clearly visible in the modal distributions in Fig. 7.2, in which a band of low CL signal is observed on the inside edges of the cavities for all modes and cavity sizes.

Figure 7.4 shows the angular distribution of light emitted by the cavities in terms of the directivity at these angles. The directivity of an antenna is related to an antenna's ability to radiate light in a particular direction:

$$D(\theta, \phi) = \frac{4\pi}{P_{rad}} p(\theta, \phi) \quad (7.2)$$

where the directivity D is given as a function of azimuthal and zenithal angle and is proportional to the emitted power p at these angles normalized by the total radiated power P_{rad} per solid angle. Data are shown for elliptical cavities with eccentricity of 0.8 and major axes of 1.1, 1.3, and 1.5 μm . Figures 7.4(a-c) show the CL intensity maps for the resonances nearest 600 nm for each cavity: at 628 nm, 609 nm, and 589 nm, respectively. Figures 7.4(d-f) show the angular emission patterns collected for e-beam excitation of the antenna in the outermost antinode in the

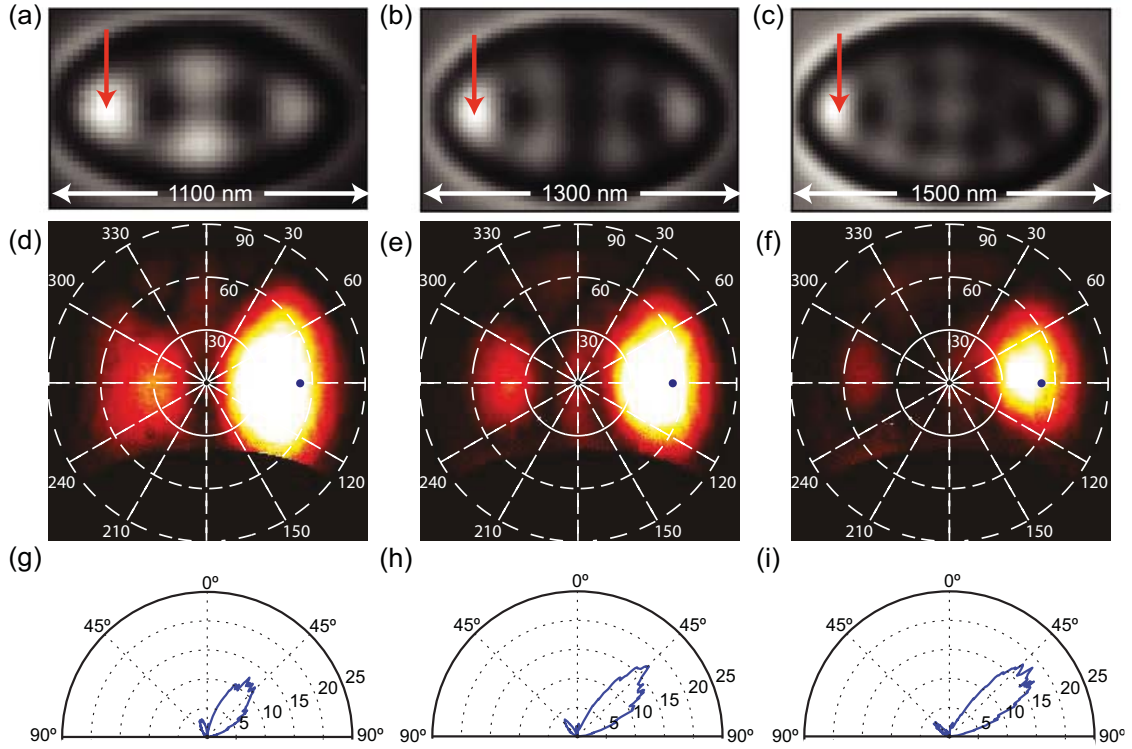


Figure 7.4: (a-c) Cathodoluminescence images of elliptical antennas with eccentricity 0.8 and major axes of 1100, 1300, and 1500 nm taken at resonance wavelengths of 628 nm, 609 nm, and 589 nm, respectively. The images are scaled by the major axis length. (d-f) Normalized angular emission collected using a 40 nm band-pass filter centered at 600 nm for the three cavities taken using electron beam excitation at the modal maxima in (a) (see arrows). Blue dots indicate the paraboloid axis for each structure. (g-i). Line cuts at the azimuthal angle of peak emission with the data normalized as directivity. The maximum directivity in panel (i) is 18.

resonant modal intensity pattern. Clear beaming of light of these resonant modes at an azimuthal angle $\phi = 90^\circ$ and zenithal angle $\theta = 52^\circ$ is observed. Our model predicts the angle to be 53.1° for this eccentricity, in reasonable agreement. The smallest half-width-at-half-maximum (HWHM) is found in the largest cavity: 17° and 24° for the azimuthal and zenithal angles, respectively. Figures 7.4(g-i) show cuts of the angular emission distribution in the zenithal angular emission lobe, with the radial scale plotted as emission directivity, that is, the emission normalized by an isotropic emitter of the same total power. We find that the maximum observed directivity is 18 for the $1.5 \mu\text{m}$ antenna. This value compares favorably to other near wavelength scale devices, such as the nanoscale Yagi-Uda antenna [39], but is clearly lower than structures that are larger in size such as the bull's eye directors [167]. This trade-off is evident in our own observation that larger structures give higher directivities. In the end there will always be a trade-off between absolute size and the maximum achievable directivity related to the diffraction of the

emitted light.

The data in Fig. 7.4 clearly show the strong directivity of the elliptical antenna, a unique feature given its planar geometry. It is the result of the constructive interference in the far-field of surface plasmon polaritons that are coherently scattered off the boundary of the elliptical cavity. The operation wavelength and outcoupling angle can be tuned by varying the ellipses' geometrical size and eccentricity (see Supplementary Fig. 7.7). The main emission near $\theta = 53^\circ$ observed in Fig. 7.4 corresponds well to the optical axis of a paraboloid intersecting with the gold surface, with the focal point at the position of the electron beam impact, as indicated in Fig. 7.4(a). E-beam illumination of the area around the foci which appear bright in the LDOS map (Figs. 7.4(a-c)) leads to a “forward” directed beam in the far field. This work thus provides a demonstration of the coupling of the two-dimensional optical “flatland” with the three-dimensional far field. A central advantage of this type of antenna is that every resonant mode directs energy in the same direction, as can be observed for the three modes in Fig. 7.4. In contrast, many other antenna designs will only broadcast in the “forward” direction for a single designed frequency. In this sense, the antenna is “broadband”. Of course, strong LDOS enhancement is only available when the structure is on resonance, so the most accurate description is that the antenna has several operating bands, each of which broadcasts energy in the forward direction. Since this is a plasmonic cavity with a moderate Q , these bands are not narrow but have a bandwidth of about 50 nm and are tunable by varying the size of the ellipse. Another distinct feature of these elliptical antennas is that the volume from which emitters can couple is relatively large, that is, on the order of a wavelength cubed. This can be contrasted with the Yagi-Uda antenna composed of an array of coupled metal nanoparticles [39, 114]. Such an antenna (which shows a similar angular spread as the elliptical antennas presented here) has an approximately 2 orders-of-magnitude smaller volume from which emitters can efficiently couple to the antenna's radiation field as that is determined by the optical near-field of one metal nanoparticle, typically a shell with a thickness of only ~ 20 nm around the “feed” particle (see Section 7.6.2 in the Supplementary information). In many applications where precise positioning of the local emitter is impossible or difficult, this will be a significant advantage. Furthermore, taking advantage of the fact that SPPs can be excited electrically [41], and the fact that electrical circuitry can be integrated with the planar antenna geometry, this design may pave the way for electrically driven directional optical antenna emitters. Finally we note the application of these elliptical antennas in the receiving mode, for example, in photodetectors and solar cells, in which light with different colors can be selectively collected and converted to electrical current at distinct regions inside the cavity.

7.5 Conclusions

In conclusion, we have demonstrated a novel antenna design, a resonant elliptical cavity, that enables the controlled coupling of optical emitters to the far-field at a well-defined angle. The emission is due to the excitation and coherent scattering of surface plasmon polaritons to the far field at optical resonances with $Q = 10 - 20$. The cavity has strong directivity (18) and has a corresponding optical volume that is more than 100 times larger than that of an optical Yagi-Uda antenna. The direction and wavelength of operation of the antenna can be controlled by simple geometric parameters. This work demonstrates the possibility of integrating “flatland” optics with the far-field, namely, the control of three-dimensional electromagnetic radiation by two-dimensional resonant structures. This could lead to important applications in a large variety of technology areas, including lighting, photodetectors, quantum optical circuitry, and photovoltaics.

7.6 Supplementary information

7.6.1 Supplementary figures

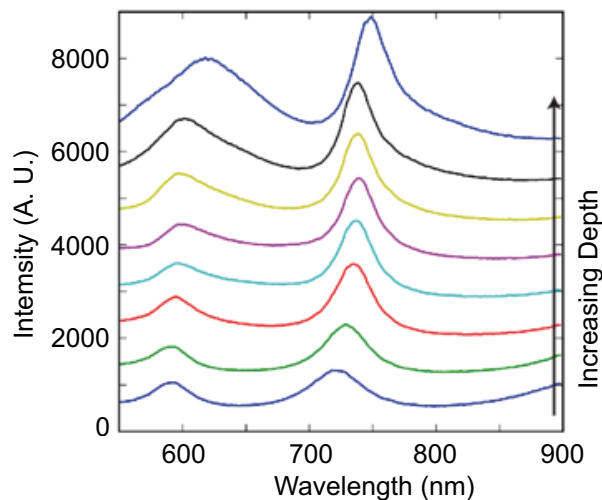


Figure 7.5: Resonator linewidth *versus* depth. Cathodoluminescence spectra collected for arenas with major axis length $1 \mu\text{m}$ and eccentricity 0.8, for structures with depths ranging from 200 nm to $1 \mu\text{m}$. The resonance linewidth increases for increasing depth due to the higher reflectivity of the cavity wall.

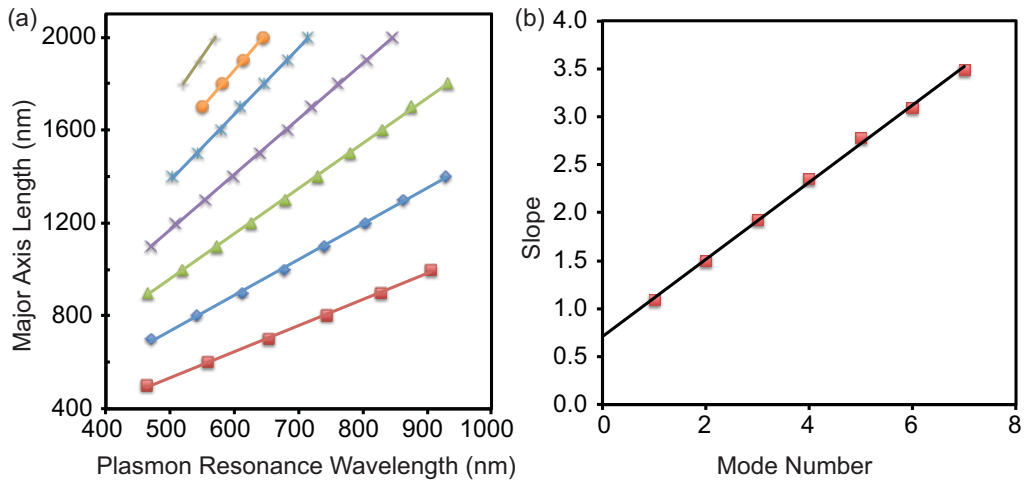


Figure 7.6: Extraction of the phase pickup on reflection. (a) Surface plasmon resonance wavelengths *versus* cavity major axis length for resonators with major axis lengths ranging from 500 nm to 2000 nm, assuming the dispersion relationship for a planar film of gold. A linear relationship between resonator size and the resonant plasmon wavelength is observed, with increasing slope for higher order resonances, in agreement with Eq. 7.1. (b) Slope of the lines in (a) for the subsequent modes. A linear increase of the slope with mode number is observed, in agreement with Eq. 7.1. The intercept with the ordinate of the line fitted through the data is 0.60, corresponding to a phase shift $\Phi = -1.2\pi$.

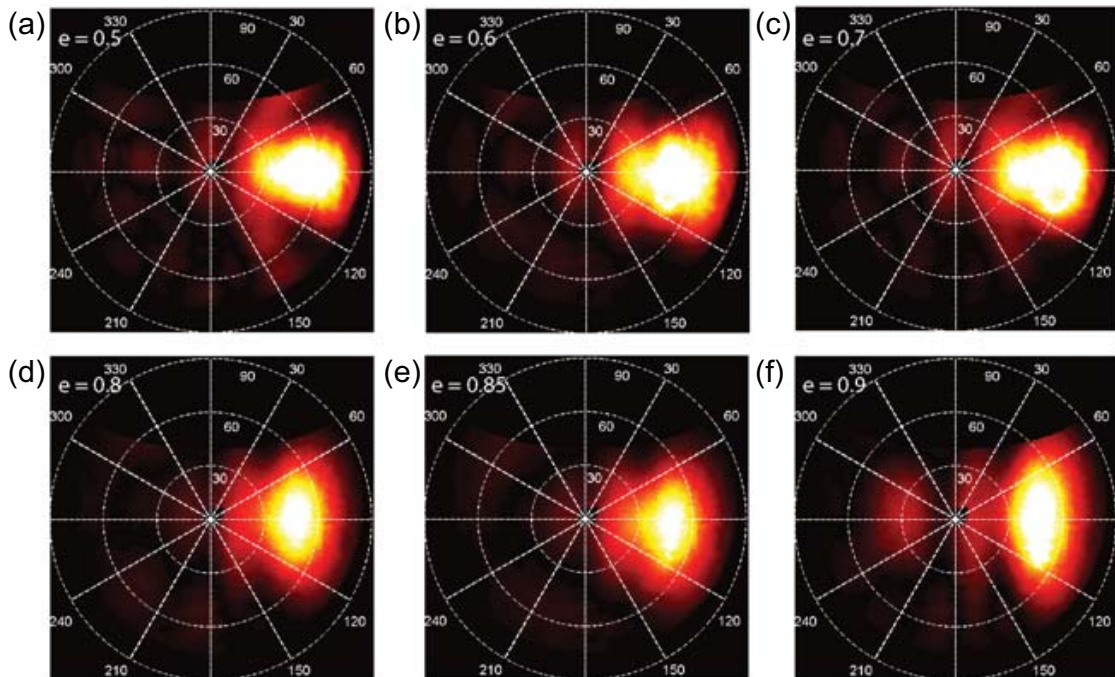


Figure 7.7: Angular radiation patterns as a function of eccentricity. Data are shown for structures with a major axis length of 1 μm and eccentricities (indicated in the panels) in the range 0.5 – 0.9

7.6.2 Calculation of effective coupling volume

In the Chapter it is claimed that the effective coupling volume, *i.e.* the volume in which an emitter will couple well to the antenna modes, is 100 times larger than that quoted recently for a nanoscale Yagi-Uda antenna [39]. In order to calculate this volume, one needs to consider the FWHM of the LDOS antinodes parallel and perpendicular to the long axis, as well as the decay of the SPP mode into the air above the plane of the elliptical cavity. As we assumed for calculating the SPP dispersion in the Fabry-Pérot model, we here assume the dispersion relationship for the SPPs in the structure to be that for a semi-infinite plane of gold. In this case, the decay length of the SPP into the air is given by following the well-known equation:

$$z_{air} = \frac{\lambda_0}{2\pi} \left(\frac{|\epsilon'_{metal}| + \epsilon_{air}}{\epsilon_{air}^2} \right)^{1/2} \quad (7.3)$$

We then make the approximation that the volume is a half ellipsoid with semi-axis lengths given by the x and y HWHM values and the z_{air} given above. For the 1.3 micron ellipse at 600 nm wavelength these values are 106 nm, 86 nm, and 293 nm, for x , y and z , respectively, giving a volume of approximately $5.6 \times 10^6 \text{ nm}^3$. In contrast, other antennas such as the Yagi-Uda require near-field coupling to a local element, which can only occur when the emitter is placed within a few tens of nanometers from the appropriate position. If we assume this corresponds to a sphere of radius 25 nm, the corresponding coupling volume is $3.27 \times 10^4 \text{ nm}^3$, or 171 times smaller than that for the elliptical cavity antenna. In reality, good near-field coupling usually requires even more precise localization of the emitter, so the ratio is actually much larger. However, a conservative claim of 100 times is justified.

8

Directional emission from a single plasmonic scatterer

Directing light emission is key for many applications in photonics and biology. Optical antennas made from nanostructured plasmonic metals are suitable candidates for this purpose but designing antennas with good directional characteristics can be challenging, especially when they consist of multiple elements. In this Chapter we show that strongly directional emission can also be obtained from a simple individual gold nanodisk, utilizing the far-field interference of resonant electric and magnetic modes. Using angle-resolved cathodoluminescence spectroscopy, we find that the spectral and angular response strongly depends on excitation position. For excitation at the nanodisk edge, interference between in-plane and out-of-plane dipole components leads to strong beaming of light. For large nanodisks, higher order multipole components contribute significantly to the scattered field, leading to enhanced directionality. Using a combination of full-wave simulations and analytical point scattering theory we are able to decompose the calculated and measured scattered fields into dipolar and quadrupolar contributions.

8.1 Introduction

Optical nanoantennas have the ability to control the emission and absorption of light at the nanoscale [29]. Nanoantennas composed of metallic nanoparticles that

support localized surface plasmon resonances in the ultraviolet-visible-infrared part of the electromagnetic spectrum have been used to control spontaneous emission [13, 37–40] and surface enhanced Raman scattering [57, 58], and find applications in targeted medicine [55, 56], solar steam generation [50, 51], or photovoltaics [36]. In many of these applications the directionality of the plasmon scattering plays a pivotal role.

The angular scattering profiles of single nanoparticle antennas are usually isotropic around the symmetry axis. To obtain strong directionality in plasmonic nanoantennas multi-element array antennas such as the Yagi-Uda geometry are used. These are composed of a locally driven feed element that is coupled to several parasitic director elements that collectively interfere in the far field [114], giving rise to directional emission [39, 113, 135, 179–181]. However, these array antennas are complex to design and fabricate, and have a relatively large spatial footprint. Strong directionality can also be achieved using just a single element antenna if the interference between electric dipole and higher-order multipole components can be controlled [182–189]. However, efficient excitation of higher-order magnetic and electric multipoles requires strong field gradients on the scale of the nanoparticle which is difficult to obtain using plane wave excitation. Since each multipole component has its own complex vectorial near-field distribution, local excitation of the nanoantenna can enable excitation of the right combination of modes that interfere in such a way as to give strongly directional emission.

In this Chapter we use a tightly focused 30 keV electron beam as local excitation source to drive the resonant electric and magnetic modes in cylindrical Au nanoantennas. The evanescent electromagnetic field about the electron trajectory provides a stable and highly localized (~ 10 nm) broadband source of surface plasmons that does not perturb the dielectric environment enabling spatially-resolved studies of plasmonic modes over a broad spectral range in a single experiment [63, 64, 77, 84, 190–194]. Using angle-resolved cathodoluminescence (CL) imaging spectroscopy (ARCIS) (see Chapters 2 and 3 for details on the experimental setup), we show that the interference between locally excited multipole components in the Au particles can give rise to strongly directional emission in a single element nanoantenna. We demonstrate that the beaming direction is directly controlled by the precise electron beam position on the nanoparticle. From the spectrally-filtered angular emission distributions we detect features in the locally excited plasmon radiation fields that provide key information on the modal composition of the plasmon excitation. By combining full-wave simulations and analytical point scattering theory we are able to decompose the measured far-field radiation patterns into electric dipole, magnetic dipole, and electric quadrupole contributions and show that these all contribute to the antenna's scattering profile.

8.2 Cathodoluminescence spectra

We fabricated cylindrical gold nanoparticles with diameters ranging from 50 – 180 nm in 5 nm steps and a height of 80 nm on a crystalline silicon substrate using a combination of electron beam lithography, thermal evaporation, and liftoff. For the hyperspectral imaging measurements we raster-scan the e-beam in small steps over the disk (5 nm steps for $D \leq 100$ nm and 7.5 nm steps for $D > 100$ nm). Light is collected by a half-parabolic mirror placed between sample and the electron microscope pole piece and directed to a grating spectrometer equipped with a liquid nitrogen cooled CCD camera. At each excitation position we collect a spectrum in the visible/near-infrared spectral region. The integration time was 500 ms per pixel at a beam current of 0.8 nA. By integrating over all scanning pixels we also obtain the average CL spectrum for each nanodisk. The spectra are normalized to the peak intensity and corrected for background radiation from the Si substrate. Figure 8.1(a) shows spatially-averaged spectra for Au nanodisks with $D = 50, 100,$ and 180 nm, respectively. The corresponding scanning electron micrographs of the disks are shown as insets. For the $D = 50$ nm particle we observe a localized surface plasmon resonance (LSPR) peak at $\lambda_0 = 580$ nm. The peak broadens and blueshifts when the diameter is increased to 100 nm. For the largest particle ($D = 180$ nm) the spectrum is broadened further and shows a clear shoulder at $\lambda_0 = 700$ nm suggesting a second LSPR resonance. The gradual blueshift of the main peak and the emergence of a shoulder at longer wavelengths can be seen in more detail in Fig. 8.1(b) where the spatially-averaged CL spectrum is shown for all measured nanodisks with diameters in the range $D = 50 - 180$ nm.

To gain further insight in the nature of the resonant modes we plot the 2D spatial maps at the peak-wavelengths for the three diameters in Fig. 8.1(a) integrated over a 20 nm spectral bandwidth (Fig. 8.1(c-e)). As can be seen for these wavelengths, the 50 and 100 nm disks radiate most efficiently when excited in the center, whereas the 180 nm particle radiates most strongly when excited at the edge. From our previous work, it is known that modes that are efficiently driven by the electron beam in the particle center usually have $m = 0$ (azimuthal) symmetry [157] (also see Chapters 4 and 5) and an out-of-plane oriented electric dipole moment, whereas efficient edge excitation indicates the presence of strong in-plane dipole components ($m = 1$), where m is the azimuthal quantum number. In the first case the vertical component of the electric field is strong in the center while in the second case it is strong at the edge allowing strong coupling to the electron beam at those specific positions. Considering that the nanodisk diameter/height aspect ratio changes from 0.625 (50 nm diameter) to 2.25 (180 nm diameter) respectively, it is to be expected that the in-plane components become more dominant as their scattering efficiency increases for the larger nanodisks.

The evolution of the CL spectrum as function of disk diameter is governed by three effects. First, for the smaller diameters the out-of-plane dipole resonance is dominant and it is known that an increase in particle size transverse to the electric dipole resonance axis leads to a stronger restoring force and thus a blue-shifted

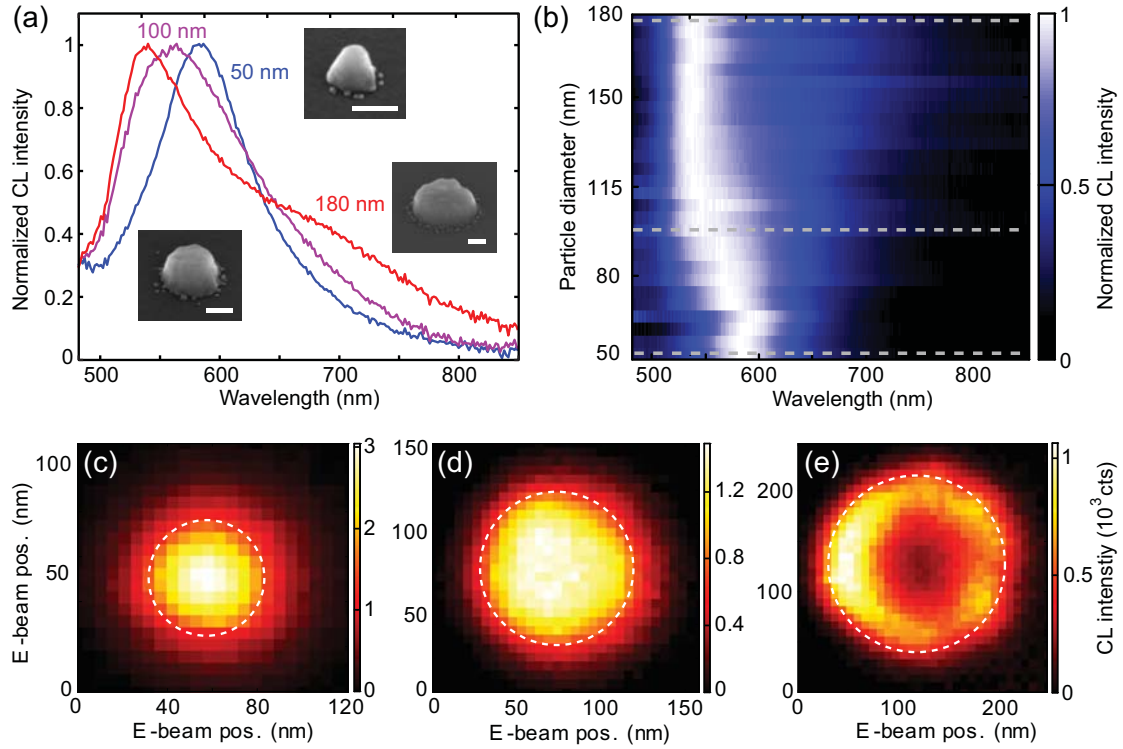


Figure 8.1: (a) Spatially-integrated normalized CL spectra for Au nanodisks with $D = 50$, 100, and 180 nm. Scanning electron micrographs of the corresponding particles are shown as insets in which the scale bars represent 50 nm. (b) Integrated peak-normalized CL spectra for a range of different nanodisk diameters in 5 nm steps. The gray dashed lines indicate diameters for which spectra are shown in (a). CL intensity as function of excitation position for (c) $D = 50$ nm at $\lambda_0 = 580$ nm, (d) $D = 100$ nm at $\lambda_0 = 560$ nm, and (e) $D = 180$ nm at $\lambda_0 = 550$ nm, integrated over a 20 nm bandwidth.

resonance. Second, following the same reasoning the in-plane electric dipole resonance redshifts because the increase in size is now along the dipole axis. Third, higher order resonant modes become more dominant for larger particles, possibly having an effect on the CL spectrum.

8.3 Directional scattering

To gain more insight into the nature of the particle resonances, we measured the far-field angular emission patterns by projecting the beam emanating from the parabolic mirror onto a 2D CCD array. The CCD data are subsequently converted to angular emission distributions (see Fig. 3.1). We collect the angular patterns for free-space (center) wavelengths (λ_0) from 400 to 750 nm using 40 nm band pass filters for $D = 50$, 100, 140 and 180 nm disks. To optimize the signal-to-noise ratio (SNR), we have used 120 s integration time for $\lambda_0 = 400$, 450, 700 and 750 nm and 60 s for $\lambda_0 = 500 - 650$ nm.

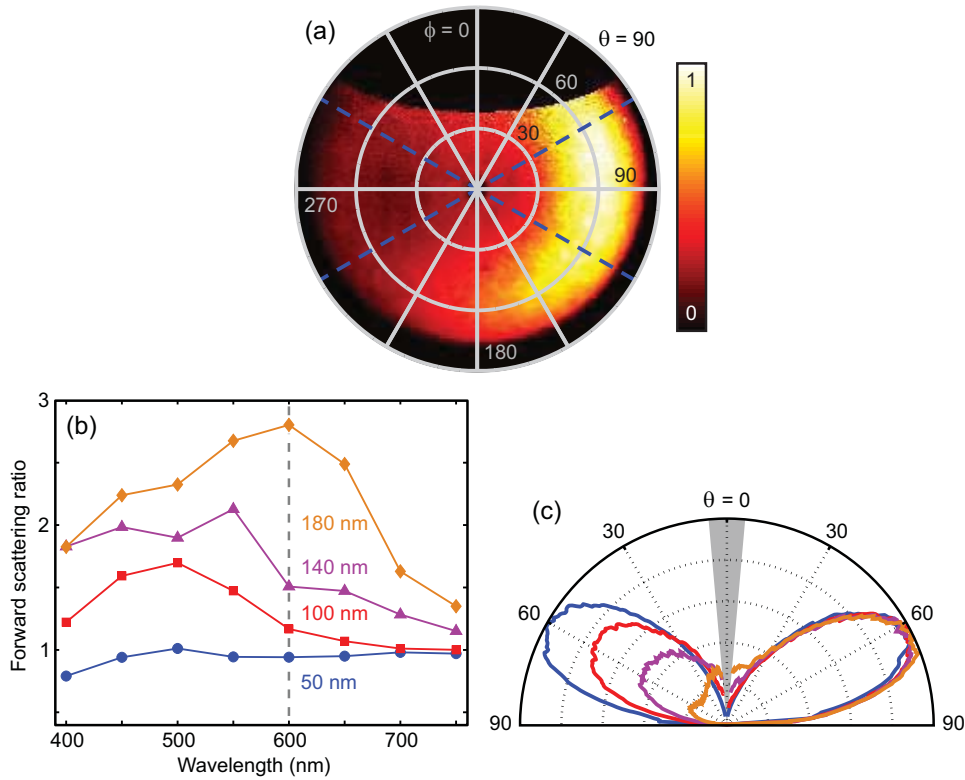


Figure 8.2: (a) Measured angular pattern for a $D = 180$ nm nanodisk at $\lambda_0 = 600$ nm for excitation on the left edge of the nanodisk (b) Forward scattering ratio as function of wavelength for different disk diameters. (c) Cross cuts through radiation patterns for different-diameter disks at $\lambda_0 = 600$ nm (corresponding to the gray dashed line in (b)), plotted with the same color code as in (b). The crosscuts have been integrated over a range of ϕ ($\phi = 60 - 120^\circ$ and $\phi = 270 - 330^\circ$ as indicated by the blue dashed lines in (a)). For visibility all patterns in (c) have been normalized to 1. The gray region is not collected due to the hole in the parabolic mirror

Figure 8.2(a) shows the angular pattern for a $D = 180$ nm particle at $\lambda_0 = 600$ nm for excitation on the left edge of the nanodisk. The pattern clearly shows a strong angular asymmetry. When excited at the edge, the particle preferentially radiates away from the excitation point. Angular patterns for four orthogonal edge positions are shown in Fig. 8.3, demonstrating that the beaming is always directed away from the excitation point. If the nanodisk is excited in the center the overall emission intensity is lower (also see Fig. 8.1(e)) and an azimuthally-symmetric toroidal emission pattern is observed consistent with the radiation pattern of a vertically oriented electric dipole on top of a high-index substrate. A similar beaming effect also occurs for $D = 100$ nm disks which is shown in Fig. 8.4(a-c) for $\lambda_0 = 600$ nm. In contrast, for $D = 50$ nm disks the pattern remains almost toroidal for all excitation positions and very closely matches the angular pattern of a vertical electric dipole (see Fig. 8.4(d-f)).

Figure 8.2(b) shows the magnitude of the angular asymmetry as function of

wavelength, calculated from the integrated “forward” and “backward” half of the angular hemisphere. Data are shown for four different disk diameters. For the $D = 50$ nm disks the measured ratio is close to 1 (except for $\lambda_0 = 400$ nm), indicating that there is no asymmetry in the emission pattern. As the diameter increases, stronger angular beaming is observed and the maximum beaming condition shifts to longer wavelengths. The strongest directionality (forward-to-backward intensity ratio of 2.8) is obtained for the $D = 180$ nm disks at $\lambda_0 = 600$ nm. The increase in directionality for increasing diameter is clearly visible in Fig. 8.2(c) which shows cross-cuts through the angular data at $\lambda_0 = 600$ nm for the same disk diameters as in Fig. 8.2(b). The data in Figs. 8.2 and 8.3 show that directional angular emission can be achieved from a single nanodisk by precisely positioning the local electron beam source. Note that the directionality is reversed with respect to what was shown in Ref. [21]. This is due to the fact that we collect the angular patterns for the upper hemisphere whereas in that work the patterns were measured on the substrate side where the dipole radiation “doughnut” points towards the excitation point.

To study the nature of the different resonant modes that contribute to the radiation patterns we study the angular emission distribution for different wavelengths. Figure 8.5 shows normalized angular patterns for $\lambda_0 = 400 - 600$ nm for the $D = 180$ nm particle disk for edge excitation on the “left” side. The pattern for $\lambda_0 = 400$ nm shows a strong radiation lobe normal to the substrate. The relative contribution of this lobe becomes increasingly weaker for longer wavelength while the sideward lobe gradually becomes more pronounced. At $\lambda_0 = 600$ nm the forward scattering ratio is maximum and most of the radiation is emitted into one strong crescent-shaped lobe pointing away from the excitation position (same data as in Fig. 8.2(a)).

8.4 Multipolar decomposition

Next, we derive a model for the single-disk radiation profiles. If the size of the nanodisk is much smaller than the wavelength it can accurately be described as a point dipole scatterer with a electric dipolar polarizability tensor [195]. For larger sizes higher-order multipole contributions become significant. The coupling efficiency to different moments strongly depends on the type of excitation [196, 197], particle shape, and dielectric environment. In particular for cases where the particles have a non-spherical shape and/or are placed in an asymmetric dielectric environment like on a high-index substrate, quantifying the contributions of the different multipoles is complex. Here we use a 3D surface integral equation (SIE) method to find the relevant multipolar components for our experiment. In this full-wave method the nanodisk is discretized into triangular surface elements [198, 199]. By locally solving Maxwell’s surface integrals for each individual element, the scattered fields for a particular type of driving field, eigenpolarizabilities, and the local density of optical states (LDOS) in the vicinity of a scatterer can be accurately calculated. This method recently has been successfully employed to describe the scattering properties of plasmonic split rings [200].

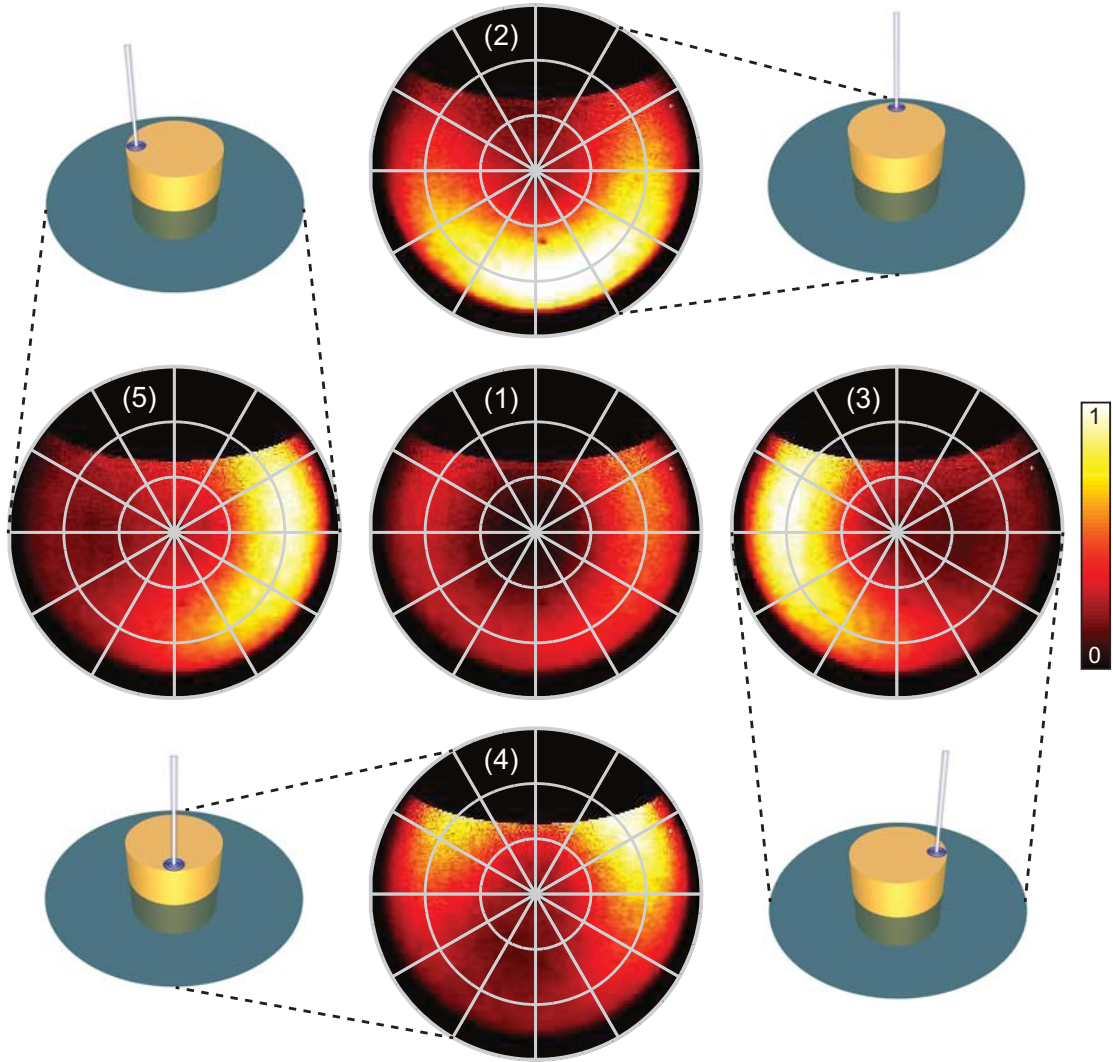


Figure 8.3: Experimental normalized angular cathodoluminescence emission patterns collected from a 180 nm diameter nanodisk at $\lambda_0 = 600$ nm for excitation at the center (1) and near the edge for four orthogonal azimuthal angles: 0° (2), 90° (3), 180° (4), and 270° (5). The edge excitation positions are also indicated by the schematics in the corners. The patterns have been normalized to the maximum intensity value for all five patterns to show the relative brightness for different excitation positions.

To simulate our experiment, we discretize the surfaces of cylindrical particles with 50, 100, and 180 nm diameters into surface elements using a radius of curvature of 5 nm to prevent numerical inaccuracies in the fields. We calculate dipolar and quadrupolar polarizabilities by exciting the structures with orthogonal sets of counter-propagating waves and decomposing the calculated scattered field into vector spherical harmonics. This allows us to represent the nanodisk by a point scatterer of which the scattering properties are described by its superpolarizability tensor (for details see Refs. [199, 201]). To account for the effect of the substrate

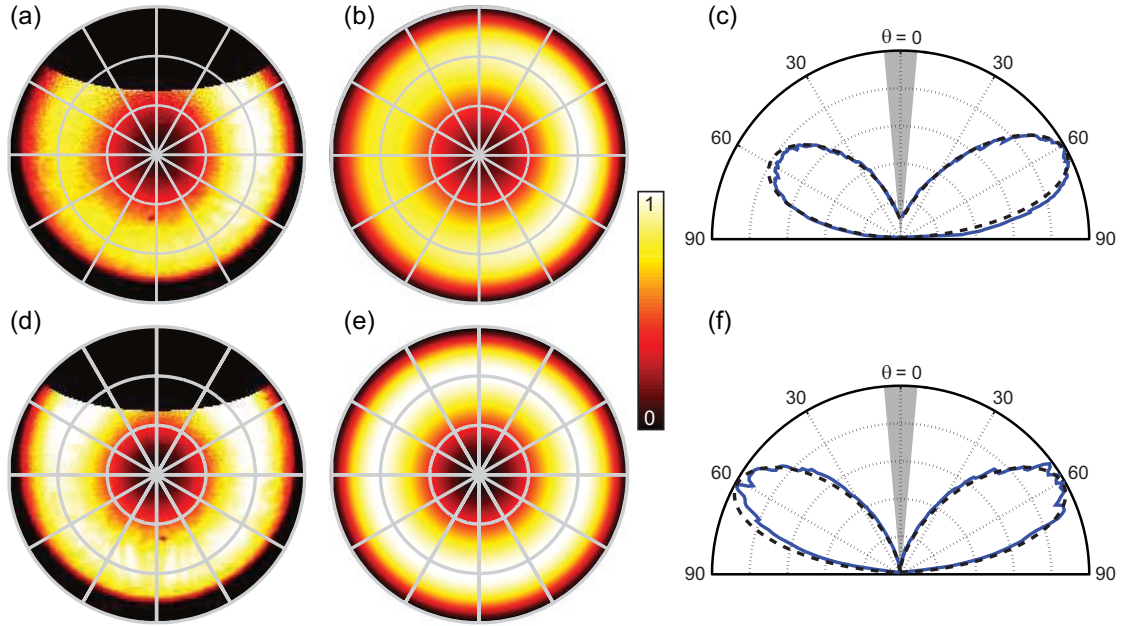


Figure 8.4: (a) Measured angular emission pattern of a $D = 100$ nm disk for left-edge excitation, measured at $\lambda_0 = 600$ nm. Again the nanodisk beams light away from the excitation point. (b) Calculated angular pattern obtained by numerically fitting complex p_z and p_x dipole components (40 nm above the silicon substrate) to the data. (c) Emission intensity as function of zenithal angle θ for the experimental data from (a) (blue curve) and the fitted theoretical pattern in (b) (black dashed curve), integrated from $\phi = 60 - 120^\circ$ and $\phi = 240 - 300^\circ$ as indicated by the blue dashed lines in Fig. 8.2(a). (d) Measured angular emission pattern of a $D = 50$ nm disk for central excitation, measured at $\lambda_0 = 600$ nm. (e) Calculated angular pattern for a vertically oriented electric point dipole source. (f) Zenithal emission profiles for (d) and (e).

a backaction substrate-correction to the superpolarizability tensor is applied to the initial calculation. To drive the disk we place a vertical point dipole at the xy electron beam excitation positions used in the experiment thereby mimicking the electron beam driving. For the z -position of the dipole we study both 40 nm (at the half-height of the disk) and 80 nm (top of the disk). We find that for both excitation dipole heights the relevant components for edge excitation (in the x -direction at $\phi = 90^\circ, 270^\circ$) are electrical dipole moments p_z and p_x , the magnetic component m_y , and quadrupolar moments Q_{xz} (corresponding to the Q_{13} and Q_{31} elements in the quadrupole tensor [149]), and Q_{xy} (corresponding to the Q_{11} and $-Q_{22}$ elements in the tensor which is a quadrupole that is rotated 45° in the xy -plane with respect to the Q_{12}, Q_{21} quadrupole).

The angular patterns and corresponding charge distributions of these individual components are shown in the bottom panel of Fig. 8.5. These are calculated using asymptotic far-field approximations for dipoles and quadrupoles in the presence of a substrate [94, 202, 203]. Both electrical dipole components p_z and p_x show the characteristic toroid shapes centered around the dipole axis. As the fig-

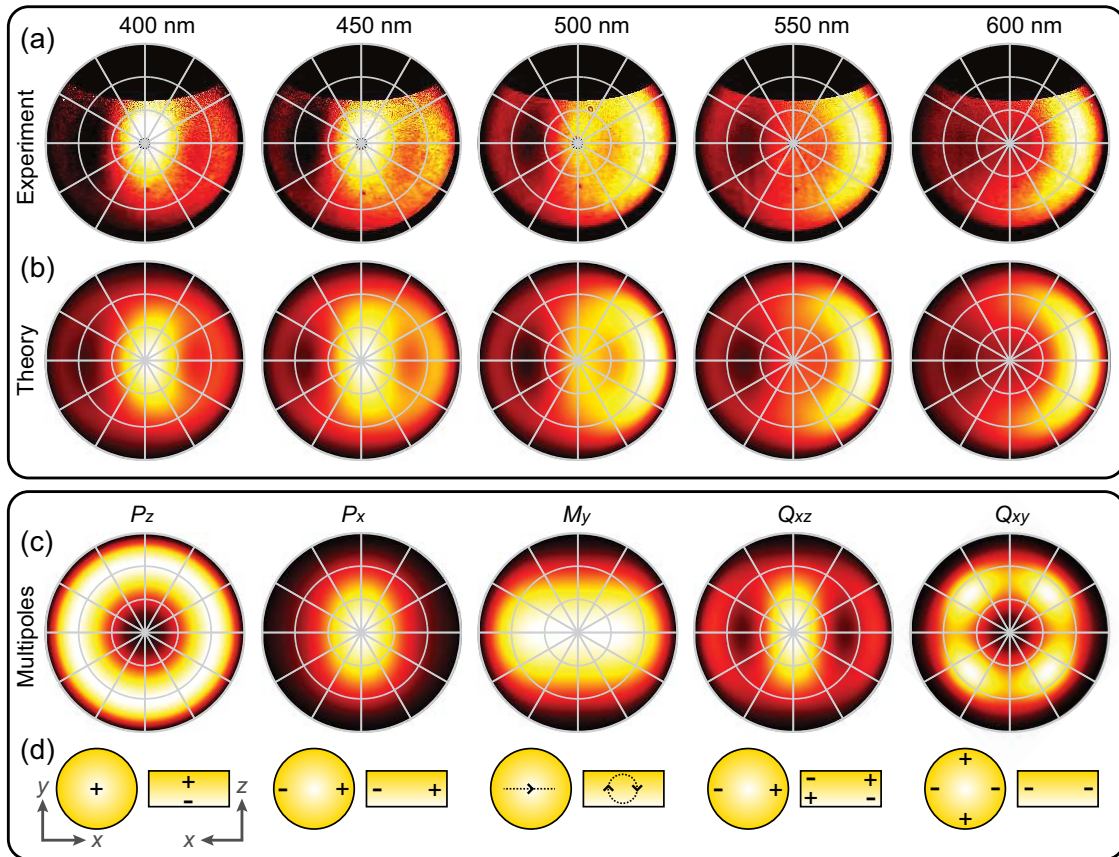


Figure 8.5: Normalized experimental cathodoluminescence radiation patterns (row (a)) and numerically fitted theoretical patterns (row (b)) for a $D = 180$ nm Au disk excited on the “left” side for $\lambda_0 = 400 - 600$ nm. The patterns are a result of the coherent interference of five multipole components. The theoretical radiation patterns for the individual components are plotted in row (c) for $\lambda_0 = 500$ nm for a source placed 40 nm above a silicon substrate. Below each pattern the corresponding charge distribution is shown from two perspectives (row (d)): on the left, a top view of the disk and on the right, a cross section of the disk in the xz -plane.

ure shows the patterns deviate from a perfect toroid because of substrate interference [94]. Both of these dipole components have a significant E_z component at the edge of the nanodisk and thus can be driven by a z -dipole or electron beam at this position. The magnetic dipole component m_y corresponds to an electrical current loop in the xz -plane (indicated by the black dashed line in the schematic for m_y in the bottom panel of Fig. 8.5) which also has a significant E_z component at the edge of the disk. For the Q_{xz} and Q_{xy} quadrupoles the radiation patterns show multiple radiation lobes. These particular quadrupoles would show four radiation lobes in free space of which three are visible in the upper hemisphere for Q_{xz} (because one lobe is oriented directly along the normal into the substrate where it can not be collected by our parabolic mirror) and all four are visible for Q_{xy} because all

λ_0 (nm)	$ p_x $	$ p_z $	$ m_y $	$a Q_{xz} $	$a Q_{xy} $	RMSE
400	1.0	0.24	0.33	0.24	0.13	0.069
450	1.0	0.49	0.32	0.42	0.17	0.072
500	1.0	0.73	0.35	0.47	0.080	0.044
550	1.0	0.17	0.21	0.33	0.012	0.037
600	1.0	0.74	0.30	0.56	0.13	0.038

Table 8.1: Relative absolute magnitudes for relevant components of the multipole expansion for $\lambda_0 = 400 - 600$ nm. In the last column the root-mean-square error of the fit is shown. Note that for the quadrupoles we multiply the magnitude of the tensor elements by $a = k_0/\sqrt{60}$ [201] to directly compare the total radiated power with respect to the dipole moments. The errors are relatively small compared to the maximum intensity in the pattern (normalized to 1) indicating that the fits closely match the experimental data.

lobes lie in the xy -plane. Like for the dipole patterns the quadrupolar patterns are distorted relative to those in a homogeneous dielectric environment due to the presence of the reflective silicon substrate.

Next, using the theoretical far fields of the relevant multipole components we decompose the experimental far-field angular radiation patterns by numerically fitting the complex amplitudes using a least-squares numerical optimization routine [197, 204]. For the smaller disks ($D = 50 - 100$ nm) the patterns are dominated by p_x and p_z due to their size compared to the wavelength so using only those components for the data-fitting yields good results (see Fig. 8.4(c,f)). We find a ratio of $|p_z|/|p_x|$ of 1.9 for $\lambda_0 = 600$ nm for the $D = 100$ nm disk so the p_z component is strongest in that case. Because of their pure dipolar character the resulting asymmetry in the angular pattern is smaller than for the larger disks. For the $D = 50$ nm disk a toroidal “doughnut” shaped pattern is observed, consistent with the emission pattern of a vertically-oriented point dipole source (so a pure p_z contribution) [94, 202]. This is consistent with the spatial profile in Fig. 8.1(c) where we observed an excitation maximum in the center of the nanodisk.

In contrast, for a $D = 180$ nm disk all five dipolar and quadrupolar components mentioned above contribute to the observed radiation profiles. The second row of the top panel in Fig. 8.5 shows the angular patterns obtained from the numerical fits. They agree very well with the measured patterns. This demonstrates that the observed angular patterns indeed can be accurately described as the coherent superposition of the multipoles predicted by the SIE calculations. The absolute values of the different multipole moments are listed in Table 8.1. For all fits the in-plane electrical dipole component p_x is dominant as one might expect for a disk with this diameter and aspect-ratio. Nevertheless in all fits there are significant contributions from the vertical electric dipole, magnetic dipole, and electric quadrupoles.

8.5 Guidelines for strong directionality

Equivalent to Kerker-scattering in dielectric/semiconductor nanoparticles [182–185, 188], strong directionality is expected only when the different multipole components are similar in magnitude as that allows effective interference in the far field. Evidently this condition is not met for the $D = 50$ nm disk, where the pattern is fully dominated by p_z and no beaming is observed. However, when we look at the fitted values for the $D = 180$ nm particle especially at $\lambda_0 = 600$ nm, the p_x component is less dominant and there are significant multipolar contributions, leading to a weaker normal component of the radiation emission and strong asymmetric emission towards the side (Fig. 8.2(a)). For almost all measurements (except for $D = 50$ nm at $\lambda_0 = 400$ nm) the radiation is predominantly emitted away from the excitation point (see Fig. 8.2(b)) so for these nanodisks there are no significant relative phase-flips of the components as function of wavelength that would lead to inversion of the directionality.

Thus, the admixture of multipolar contributions that yields directionality can be controlled on one hand by particle size and shape, *i.e.* by control of the multipole polarizabilities, and on the other hand by changing the particle driving by nano-scale changes in excitation position of a local source like the electron beam such that the structure is excited in an asymmetric way. An alternative way of achieving this driving asymmetry is by using circularly/elliptically polarized light as has been demonstrated recently in Ref. [186].

In some cases it might be desirable to have a more universal unidirectionality, meaning that an antenna is designed in such a way that it emits in the same direction for a large variety of excitation conditions (even for symmetric excitations). This can be achieved by introducing an asymmetry in the nanostructure itself [187, 189]. Also in this case, it has been shown that it is better to have larger structures with more polarizable material in order to promote the higher order multipoles that facilitate a strong directional response. Rather than engineering the structure to constrain the emitted pattern to a given directional distribution, we envision that the strong variability of directionality with excitation position can also be used advantageously. In particular, we propose that the type of position-dependent directionality as shown in this Chapter lends itself perfectly for improving fluorescence correlation spectroscopy (FCS) for instance, where temporal correlations in fluorescence intensity can reveal the diffusion constant of single diffusing fluorophores [46, 47]. By detecting fluorescence intensity of single molecules diffusing over the nanodisks in the Fourier-plane with a quadrant photodiode for instance, one could utilize the antenna directionality to decrease the effective detection volume, thereby boosting the sensitivity.

Finally, in our experiment the antennas are on a high-index substrate that on the one hand helps with the generation of significant multipole moments through backaction on the nanodisks [201] but also leads to large radiation losses into the substrate. These radiation losses could be minimized by for instance using a ground-plane geometry where a mirror underneath the structure ensures that all

of the light is emitted into the upper hemisphere. The concepts shown in this work can directly be applied to such ground-plane antennas which may lead to novel highly-efficient directional antenna designs.

8.6 Conclusions

In conclusion we have measured the directional emission properties of gold nanodisks as function of size and wavelength using angle-resolved cathodoluminescence imaging spectroscopy. For the 50 nm diameter disks the angular pattern is toroidal, corresponding to an out-of-plane dipole resonance. For the larger disks the angular patterns are a coherent superposition of electric dipole, magnetic dipole, and electric quadrupole contributions. For these disks we find that nanoscale in-plane displacements of the electron beam over the nanodisk leads to drastic changes in the angular pattern. We find that off-center excitation leads to an asymmetric radiation pattern where light is preferentially scattered in the forward direction, which is due to the far-field interference of different multipole moments generated in the disk. When the wavelength is large compared to the particle size the emission is dominated by electrical dipole components but when the particle size increases there are clear magnetic dipole and electric quadrupole contributions giving rise to strong directionality without the use of additional parasitic antenna elements. Our work could be utilized in the future to engineer strongly directional single element antennae with a small spatial footprint which could be used in a wide variety of applications.

8.7 Methods

Sample fabrication. We fabricated gold nanodisks on a crystalline silicon substrate using a combination of electron beam lithography, thermal evaporation, and liftoff. We used a 350 nm thick layer of ZEP520A as positive resist for electron beam lithography with a Raith E-line system. After exposure and development, a gold layer was deposited using thermal physical vapor deposition in vacuum. After lift-off in n-methylpyrrolidone (NMP) at 65 °C for 3 hours, we obtained nanodisks on silicon with diameters ranging from 50 – 180 nm and a height of 80 nm.

Optical properties of individual plasmonic holes probed with local electron beam excitation

Just like nanoparticles, nanoscale holes form a basic building block in nanophotonic devices. In this Chapter we study the spectral and angular cathodoluminescence response of individual nanoholes with diameters ranging from 50 to 180 nm. We find that the holes can be excited efficiently at the edge of the hole and that the response becomes stronger in the near-infrared part of the spectrum for larger holes. Using finite-difference time-domain simulations we characterize the resonant modes inside the holes. By using ARCIS we are able to measure the angular response and observe strong beaming towards the side of electron beam excitation, complementary to what was shown for nanoparticles. We find that the angular response can be explained by assuming a coherent superposition of radiating dipole moments, where the contribution of in-plane magnetic and electric dipole components increases for larger diameters.

9.1 Introduction

Nanoscale apertures form a basic building block for plasmonic devices [205]. Similar to nanoparticles, such nanoscale holes and slits have the ability to strongly

confine light due to localized plasmon resonances that are supported by the structure, which for example allows strong enhancement of fluorescence [206]. On the other hand, since a hole is the geometrical inverse of a nanoparticle its transmission and reflection properties are complementary to that of a particle (Babinet's principle) [33, 205, 207–210], although strictly speaking this only holds for 2D structures in a perfectly conducting film [211]. Furthermore, subwavelength holes diffract light in quasi-cylindrical waves (QCWs) and can couple to bound surface plasmon polaritons (SPPs) in plasmonic films which provide extra channels through which holes can be excited and coupled [212–216]. These coupling mechanisms have been utilized in ordered arrays to obtain extraordinary transmission [205, 217] and absorption [218], where the transmission/absorption cross section exceeds the geometrical cross section of the holes. Due to their accessible open geometry and unique transmission and absorption characteristics, plasmonic holes may find applications in CMOS cameras as color filters [52, 53] and nanoscale sensors [42, 47, 48].

Although the collective optical properties of holes in arrays have been studied extensively, characterization of individual holes is difficult owing to their subwavelength size. It has been demonstrated that by using scanning near-field microscopy the fundamental scattering properties can be measured [215, 219]. Alternatively, experimental techniques that employ a fast electron beam as excitation source, like electron energy-loss spectroscopy (EELS) and cathodoluminescence (CL) spectroscopy, have been used to reveal the resonant properties of circular holes [220], rectangular holes [221], nanoslits [209, 210], and inverse split rings [222]. In this Chapter we aim to further elucidate the local optical response of individual deep-subwavelength plasmonic holes, by using Angle-Resolved CL Imaging Spectroscopy (ARCIS).

9.2 Sample fabrication

We deposited a 80 nm thick gold layer on a silicon substrate using thermal evaporation. To reduce the granularity of the film we evaporated a 1 nm thick seed layer of germanium first [223, 224]. Subsequently we used focused-ion-beam (FIB) milling to pattern circular holes in the film, with diameters D ranging from 50 – 180 nm in steps of 5 nm and a depth of 80 nm (we stop the milling process at the silicon interface). To obtain the best patterning resolution we used a low ion-beam current (1.5 pA). Electron micrographs of the resulting structures are shown as insets in Fig. 9.1(a). Inherent to the FIB milling process there is some tapering of the hole due to material redeposition. The lowest-order propagating mode in a circular hole is cut off for wavelengths larger than the cutoff wavelength (λ_{cutoff}). $\lambda_{cutoff} \approx 1.7D$ [205], which for $D = 180$ nm holes, corresponds to λ_0 306 nm. Therefore we expect that the fundamental waveguide mode is cut off in the visible/near-infrared (NIR) regime for the holes that are considered in this experiment. The transmission through a 80 nm thick gold film is $< 5\%$ for this wavelength range as calculated by an

analytical Fresnel code, so any direct transmission through the gold film is strongly attenuated.

9.3 Spectral response measurements

We first measure the local spectral response of the holes (see Chapter 2 for details on experimental setup). To that end we raster scan the electron beam (30 keV acceleration voltage, 0.8 nA current) in 5 nm steps for $D \leq 100$ nm and 10 nm steps for $D > 100$ nm, using an integration time of 1 s per pixel. Figure 9.1(a) shows the spatially averaged spectrum for $D = 50$ nm, $D = 100$ nm, and $D = 180$ nm holes respectively. The spectra are corrected by subtracting the transition radiation (TR) from an unstructured part of the gold film and multiplying with the system response. The system response was calibrated using the same TR radiation. Because

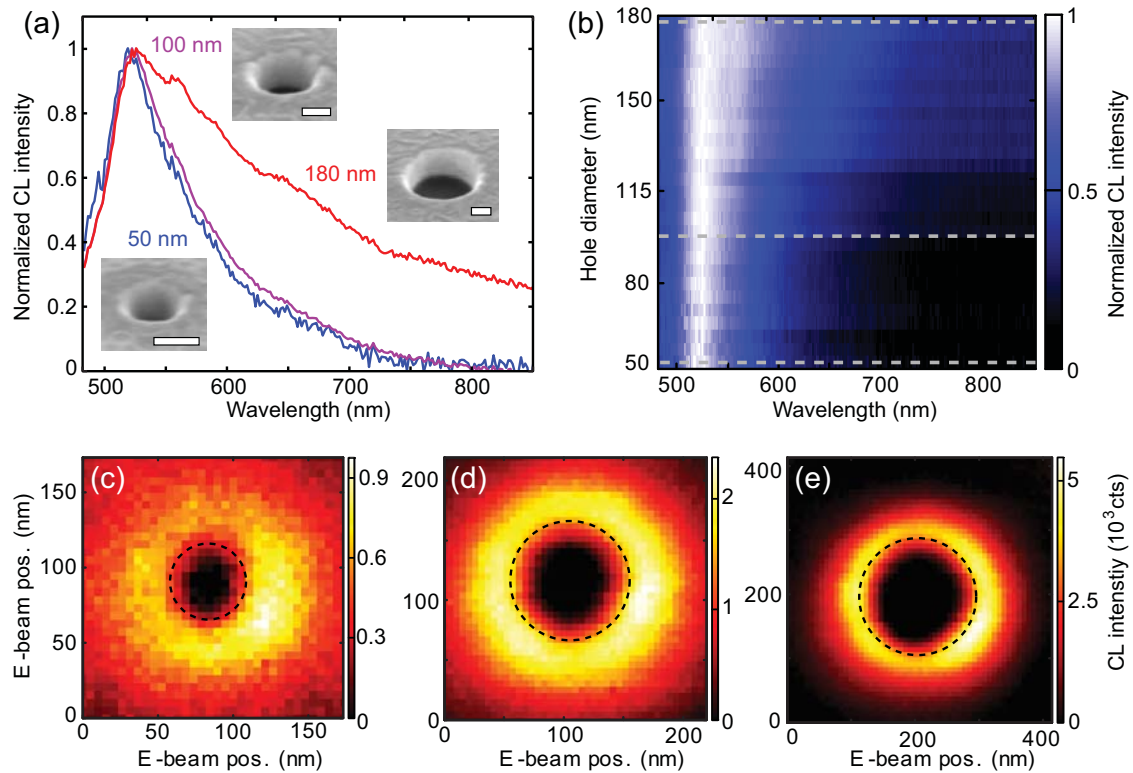


Figure 9.1: (a) Spatially-integrated normalized CL spectra for Au nanoholes with $D = 50$, 100, and 180 nm. Scanning electron micrographs of the corresponding holes are shown as insets in which the scale bars represent 50 nm. The images were taken at a 52° sample tilt. (b) Integrated peak-normalized CL spectra for a range of different nanohole diameters in 5 nm steps. The gray dashed lines indicate diameters for which spectra are shown in (a). CL intensity as function of excitation position for (c) $D = 50$ nm, (d) $D = 100$ nm, and (e) $D = 180$ nm at $\lambda_0 = 520$ nm, integrated over a 20 nm bandwidth. The black dashed circles indicate the edge of the hole.

the signal within the hole is lower than the TR background we get negative intensity values inside the hole, so we mask this area to obtain the integrated spectrum such that it does not artificially perturb the spectrum. For $D = 50$ nm and $D = 100$ nm holes we observe a relatively narrow peak centered around $\lambda_0 = 520$ nm. For $D = 180$ nm the peak wavelength is still around 520 nm but now the peak now is much broader with a long tail extending into the NIR regime. Because this hole is significantly larger in size, a stronger response in the red/NIR part of the spectrum can be expected. Fig. 9.1(b) shows the spatially integrated spectrum for all studied hole diameters in which we can clearly see the gradual broadening of the response for larger diameters.

It is also insightful to study the spatial excitation profiles of the holes. Figures 9.1(c-e) show the spatial distributions at $\lambda_0 = 520$ nm. For all diameters we observe a bright ring around the hole, whereas the hole itself remains dark. For excitation in the center of the hole the evanescent electron fields cannot polarize the metal because the edges are too far away so efficient driving of a p_z component in the center is not possible like is the case for the nanoparticles (see Figs. 8.1 and 8.4). Furthermore, any radiation that is generated at the silicon interface or in the silicon bulk cannot efficiently couple to free-space radiation into the upper angular hemisphere because the waveguide mode in the hole is beyond cutoff for these diameters. Similar spatial excitation profiles were observed in Ref. [220], although those were measured on a free-standing silver film. We note that the larger holes are significantly brighter than the smaller holes. This is quantified in Fig. 9.2(a) where we compare the maximum signal strength at the hole $I_{tot}(\lambda_0)$ with the constant TR background $I_{TR}(\lambda_0)$ by plotting $(I_{tot} - I_{TR})/I_{TR}$ for different diameters and wavelengths. Such a trend is expected as larger holes should scatter more efficiently into the far field.

9.4 CL signal decay away from the hole

To better understand the excitation processes that are involved in the CL experiment we study the decay of the CL signal away from the hole. This is visualized in Fig. 9.2(b) where we plot the CL-intensity (with the TR-background subtracted) as function of the radial distance from the hole center at $\lambda_0 = 520$ nm, extracted from the images shown in Fig. 9.1(c-e). The signal decays rapidly away from the hole edge. The $1/e$ distance corresponds to ~ 35 nm for each hole diameter. Within this spatial region we expect that there is direct coupling to the near-field of the hole resonance. Because of the surrounding gold film, indirect excitation of the holes is also possible through SPPs that are generated by the electron beam away from the hole and subsequently scattered out by the hole.

The interaction with such a circular SPP wave would rapidly decay as function of distance to the hole. We estimate this decay length with a simple intuitive model. First of all, the degree of interaction of the hole with the SPP wave drops as the electron beam moves away further from the hole due to the decreasing 2D acceptance

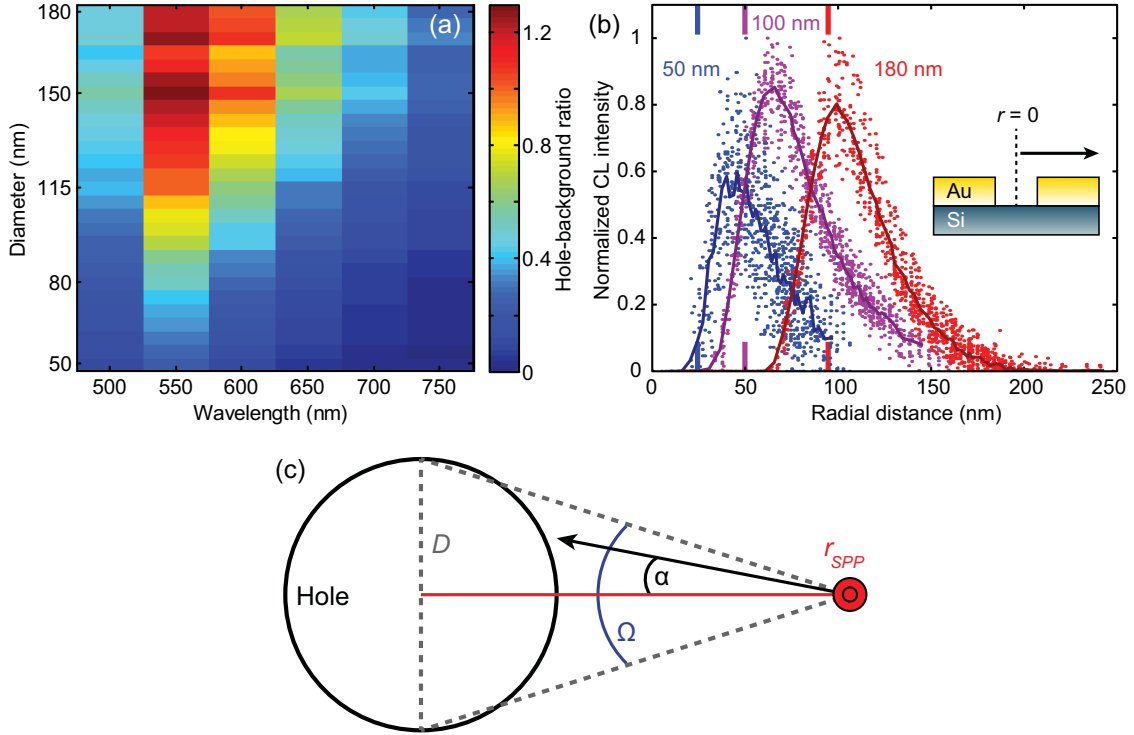


Figure 9.2: (a) Hole-signal to TR background ratio where the color-map represents $(I_{tot} - I_{TR})/I_{TR}$. To compare to the angular measurements and for better signal-to-noise ratio we use 50 nm wavelength bins. (b) Radial dependence of CL signal from the hole at $\lambda_0 = 520$ nm (averaged over a bandwidth of 20 nm) for $D = 50$ nm (blue), $D = 100$ nm (magenta), and $D = 180$ nm (red). Each dot represents a CL pixel to which we assign a radial distance from the hole center. The solid curves represent the average value of 20 binned datapoints. (c) Schematic representation of the interaction of a circular SPP wave with a hole. The geometrical parameters used in the model are indicated in the figure.

angle ($\Omega = \tan^{-1}(\frac{D}{2r_{SPP}})/\pi$) covered by the hole. This effect can give rise to a rapid decrease in signal for increasing r_{SPP} , where r_{SPP} is the position at which the SPP wave is generated (at the beam impact position) relative to the hole center. This is schematically indicated in Fig. 9.2(c). For this calculation we neglect any effects of hole shape and effective scattering cross sections that are either larger or smaller than the hole diameter.

Second, the SPPs also experience Ohmic loss, while propagating towards the hole. In order to quantify the propagation losses we need to know the dispersion characteristics of the SPPs. Using an analytical mode solver we have calculated the dispersion relation for the guided SPP modes in our layered system. We find that the layer supports two plasmon modes, which exhibit very similar dispersion to the single-interface plasmon modes for a vacuum-gold and silicon-gold interface respectively, indicating that there is little coupling between the top and bottom interface of the gold film. The guided plasmon mode on the silicon-gold interface is heavily damped and will couple poorly to free space radiation in the upper angular

hemisphere as it has to couple out through the hole. Hence we expect that the CL response is dominated by SPPs from the top interface. As the propagation length L_{SPP} for this mode is generally larger than 350 nm (calculated from $\text{Im}\{k_{SPP}\}$ using the analytical mode solver calculations), the effect on the overall signal decay is relatively small compared to the acceptance angle losses.

There is some dependence in the SPP propagation decay on the angle α with respect to the axis that is defined by the electron beam position and the hole center (see Fig. 9.2(c)), which leads to $\exp(\frac{-r_{SPP}}{L_{SPP} \cos(\alpha)})$ term for the propagation loss [225]. For small acceptance angles $\alpha \simeq 0$ and the SPP decay reduces to $\exp(\frac{-r_{SPP}}{L_{SPP}})$. For structures that have a more significant transverse spatial extend ($D \gg r_{SPP}$) like gratings the acceptance angle remains constant at a value close to π for any r_{SPP} . Hence, the angle-dependent SPP propagation losses are the dominant decay mechanism in that case which can be used to study plasmon propagation lengths on metal films [225–227].

Taking into account the decrease in acceptance angle and the Ohmic losses, we find 51, 90, and 140 nm decay lengths from the hole edge (for $\lambda_0 = 520$ nm) for $D = 50, 100,$ and 180 nm, respectively. However, in the experiment there is no noticeable diameter dependence in the CL signal decay. Also, the decay occurs over significantly shorter distances suggesting that the direct near-field coupling dominates the CL-experiment.

9.5 Simulation results

To gain more insight into the resonant properties of these holes we perform finite-difference time-domain simulations (FDTD) [228]. In particular, we use a total-field scattered-field source to calculate the scattering spectra for hole diameters between 50 and 180 nm (in 10 nm steps) under plane-wave illumination at normal incidence (the simulation setup is similar to what is described in Fig. 10.9). We use tabulated optical constants for silicon [130] and gold [105]. Figure 9.3(a) shows the normalized upward scattered power spectrum for the same diameters as in Fig. 9.1(a). Similar to the experiment we only consider the upward scattered power. The effective NA of the top monitor is 0.85. We note that the total scattered power spectrum (not shown here) looks very similar to the upward scattered power indicating that upward scattered power is representative for the overall scattering response. In order to calculate the total scattered power the silicon substrate was approximated by a $n = 4$ lossless dielectric such that the light that is scattered down into the substrate is not attenuated by absorption in the silicon before it reaches the power monitor.

Figure 9.3(b) shows the evolution of the spectrum in the range $D = 50 - 180$ nm (calculated in 10 nm steps). The scattering spectrum only changes moderately with diameter, similar to what is observed in the CL experiment. We note that the normalized scattering cross sections Q_{scat} (normalized to the hole area) are quite low ($Q_{scat} = 1.1$ for $D = 180$ nm at the peak wavelength of 575 nm) compared

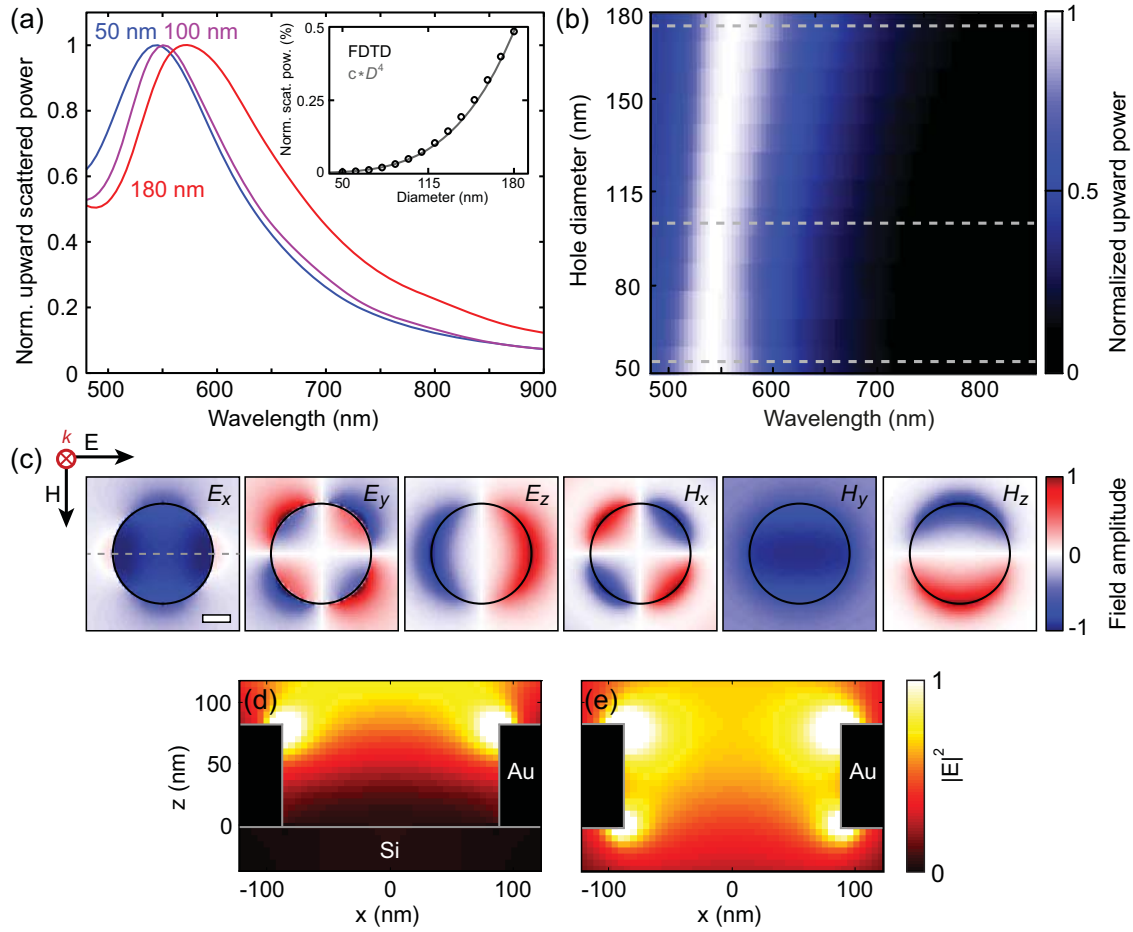


Figure 9.3: (a) Upward scattering for $D = 50, 100$ and 180 nm holes for plane-wave excitation under normal incidence, calculated using a TFSF simulation in FDTD. We only plot the part of the light that is emitted upwards as that is the part that is collected in our CL system. The spectra have been normalized to 1 for visibility as the largest hole scatters much more strongly the smallest one. The inset in shows the amount of upward scattered power relative to the incoming power as function of diameter (black circles), integrated over the full spectral range. Through the data we have fitted a D^4 curve (gray curve) that has been scaled by a constant ($c = 4.7 \times 10^{-10}$). (c) In-plane field (xy) cuts for $D = 180$ nm at $\lambda_0 = 575$ nm showing the real part of $E_x, E_y, E_z, H_x, H_y,$ and H_z respectively. The cuts are taken at half height, 40 nm above the substrate. For reference we have included the incoming plane-wave polarization. The scale bar is 50 nm. Out-of-plane (xz) cuts showing the near field intensity ($|E|^2$) for the same hole with (d) and without (e) silicon substrate at $\lambda_0 = 570$ and 620 nm, respectively. The position of the cut in the xy -plane is indicated by the gray dashed line in the E_x map in (c).

to those for nanoparticles. This could be related to the fact that a hole has less polarizable metal available for a given geometrical cross section. In the inset of Fig 9.3(a) we show the amount of upward scattered power integrated over the full spectrum for different hole diameters, normalized to the incident power in the simulation. We observe a superlinear increase in the amount of scattered power

for larger holes which is proportional to D^4 in this size range. This is consistent with the notion that the emitted power for dipoles is proportional to the square of polarizability which itself generally scales with volume. In this case the effective hole volume increases by D^2 for increasing diameter leading to a D^4 overall power dependence.

By studying the induced near-field distributions one can identify the nature of the resonant peak. Figure 9.3 shows all six electric and magnetic field components for an in-plane cut at half-height (40 nm above the silicon substrate for $D = 180$ nm at $\lambda_0 = 575$ nm). The electric and magnetic fields show a mix of in-plane electric and magnetic dipole contributions. The fields are consistent with a p_x electric dipole moment and m_y magnetic dipole moment, commensurate with the incoming plane-wave electric and magnetic field polarizations. Furthermore, it is clear that there is a significant E_z contribution near the edge of the hole, which is the electromagnetic field component to which the electron beam couples efficiently. The dipole modes we observe here are infinitely degenerate due to the circular symmetry of the hole, which is why we observe a bright ring in the excitation maps in Fig. 9.1(c-e), rather than the E_z profile calculated with FDTD which shows two hotspots along the polarization direction. The $1/e$ decay value for $|E_z|^2$ is ~ 20 nm away from the hole edge where the field is maximum, which is slightly shorter than the experimental values obtained with CL (see Fig. 9.2(b)). Possibly, this is related to the fact that in the FDTD we have a perfectly cylindrical hole, whereas in the experiment the edge is rounded which could smear out the intensity profile. The field maps were also calculated for the other diameters and free-space wavelengths and show similar patterns to Fig. 9.3(c).

Interestingly, we find that when we remove the silicon substrate in the simulations, the holes scatter more strongly ($Q_{scat} = 3$ at the peak wavelength of 630 nm) and also experience a stronger redshift for larger diameters. In the near-fields we still clearly observe the in-plane magnetic and electric dipole fields. It is well-known that a substrate can strongly influence the scattering of dipolar scatterers through the Drexhage-like change in the local density of optical states that it imposes on the position of the scatterer [204, 229, 230]. For a perfectly conducting mirror, the radiative emission from an in-plane electric dipole is suppressed whereas for an in-plane magnetic dipole it is enhanced when close to the mirror. For silicon the situation is different and the emission from both electric and magnetic dipoles is enhanced [230] which is the opposite of what we find in our simulations where the silicon substrate leads to a reduction in the scattering. One possible reason could be that an emitter-mirror configuration does not adequately describe the scattering of a hole due to the surrounding gold layer which potentially could exhibit additional mirror charge effects.

While mirror-like interference effects could have an influence on the hole scattering, the plane-wave driving efficiency of the hole also plays a significant role. When a wave reflects off the silicon substrate, the electric field approximately undergoes a phase shift of approximately π , leading to destructive interference close to the interface [231]. This is corroborated by the near-field distributions for the

cases with and without substrate, which are shown in Fig. 9.3(d,e). This driving interference effect is more pronounced for longer wavelengths as the destructive interference extends over a longer range away from the surface which explains the blue-shifted response of the hole. However, in order to suppress the driving efficiency there must be significant intensity in the reflected wave and this is not the case for small D/λ_0 ratios as the incoming wave is too strongly attenuated. The latter effect dominates for $D = 50$ nm, where the scattering cross sections with and without substrate are similar, whereas for $D = 180$ nm the driving interference does play a significant role.

9.6 Angular response

For sensing applications, the angular emission profile of the hole when coupled to a local emitter can be of significant importance. In this Section we study the angular response of the holes when excited by an electron beam. It has been shown that holes/slits surrounded by grating-like corrugations can be highly directional emitters of free space light [167] or SPPs [232] which can be used to enhance and direct fluorescence originating from the hole for instance [166, 233]. Even unstructured holes/slits can act as directional emitters owing to the fact that they support electrical dipole as well as magnetic dipole modes that can interfere in the far field (Kerker effect) [182, 219, 234]. To study the directionality of holes we measure the angular emission pattern using ARCIS. We collect angular patterns while exciting a single hole at four orthogonal edge positions (left, right, top, and bottom) for center wavelengths $\lambda_0 = 400 - 750$ nm in 50 nm steps using band pass filters (40 nm bandwidth). We do not collect an angular pattern for excitation at the center of the hole as there is practically no CL emission at that position. For the angular patterns we cannot subtract the background radiation pattern from a bare gold substrate which corresponds to a symmetric torus (see Fig. 3.3), as that leads to negative emission values for certain angles.

Figure 9.4 shows angular patterns for a $D = 100$ nm hole measured for top (1), right (2), bottom (3), and left (4) edge excitation as indicated by the schematics below the angular patterns. Similar to the nanoparticles in Chapter 8, the angular pattern co-rotates with the excitation position which means that a different combination of multipole components is excited at each position. Light is scattered towards the direction of the excitation point thus opposite to what was observed for the nanoparticles (see Fig. 8.2), illustrating the complementarity between the two geometries. The backward-to-forward scattering ratio calculated by dividing the integrated backward half of the angular hemisphere by the forward half, is quantified in Fig. 9.5(a) for different diameters and wavelengths. Here backward is defined as towards the excitation position and forward is defined as away from the excitation position. For all measurements we observe dominant backward scattering (ratio being larger than 1) although for smaller diameters the directionality moves more quickly towards 1 for increasing wavelength. This is to be expected as the

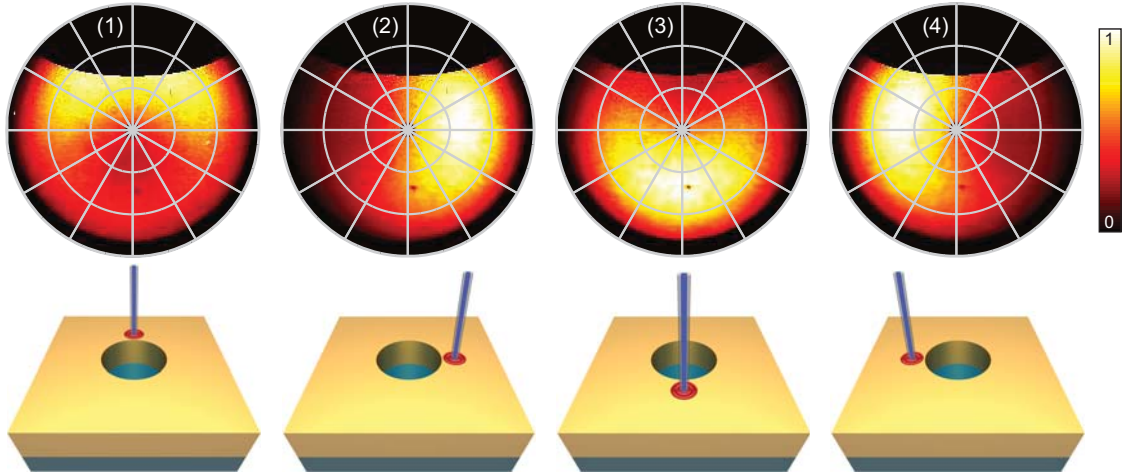


Figure 9.4: Experimental normalized angular cathodoluminescence emission patterns collected from a 100 nm diameter nanohole at $\lambda_0 = 500$ nm for excitation near the edge for four orthogonal azimuthal angles (same coordinate system as in Fig. 8.2): (1) 0° (top), (2) 90° (right), (3) 180° (bottom), and (4) 270° (left). The excitation positions are indicated by the schematics below the patterns. The patterns have been normalized to the maximum intensity value for all four patterns to show the relative brightness for different excitation positions.

smallest holes do not scatter efficiently in the red leaving the azimuthally symmetric TR emission as the dominant source of radiation (see also Fig. 9.2(a) for the ratio between hole scattering and TR signal).

In contrast to what was found for the nanoparticles, varying the diameter does not have a very profound influence on the directionality. This is emphasized in Figs. 9.5(b) where we show angular patterns for $D = 50, 100, 140,$ and 180 nm at $\lambda_0 = 500$ nm for excitation on the left edge of the hole. The patterns look very similar. Figure 9.5(c) shows cross cuts through the patterns in (b), integrated over a range of ϕ to improve the signal-to-noise ratio. For increasing diameter we observe a slow but gradual shift in the pattern towards the normal suggesting that the in-plane components become more dominant.

Based on the FDTD simulations, we know that the hole supports in-plane electric and magnetic dipole modes. From the driving symmetry we expect that for excitation on the left side of the hole we can excite a p_x and m_y component. When we move towards the top of the hole the excited moments would co-rotate and we would have a p_y and m_x component, related to the circular degeneracy of the resonant modes. Although interference between these in-plane dipole components can lead to enhanced out-of-plane upward-or downward scattering [184, 185, 188, 231] it cannot explain the backward-forward asymmetry in our angular measurements. Such an asymmetry requires an out-of-plane dipole component as well. In our experiment we generate TR emission at the edge of the hole which has an effective p_z dipole moment. As is clear from Fig. 9.2(a) the TR contribution is significant and can interfere with the radiation scattered by the hole, similar to

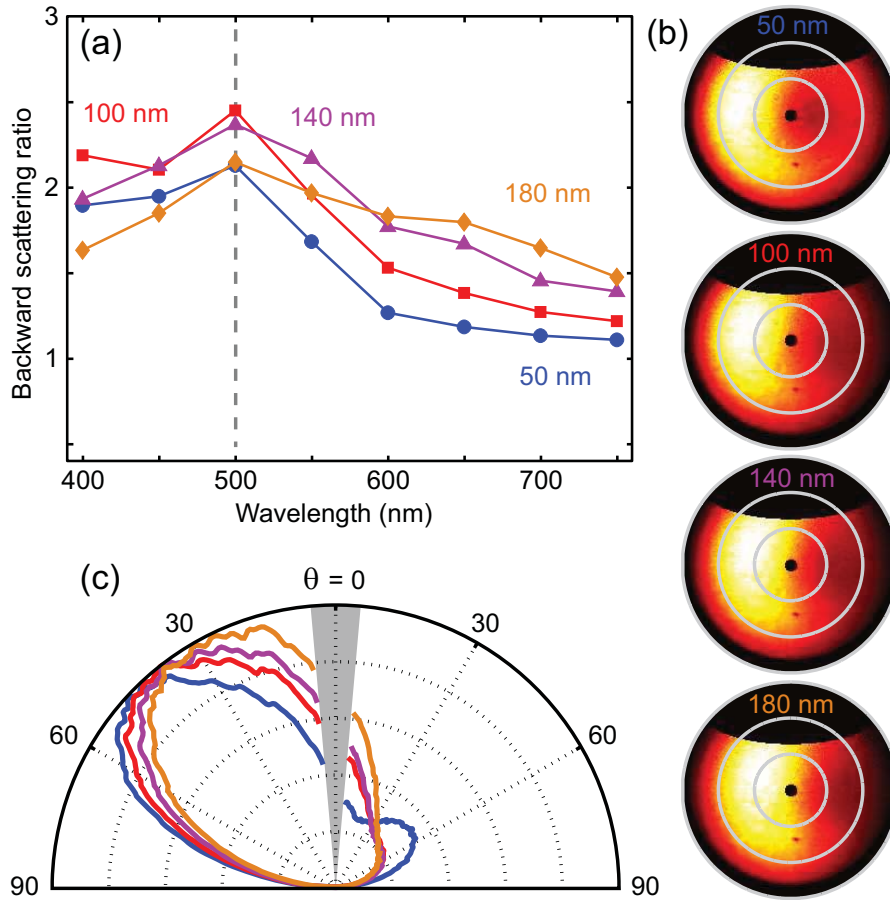


Figure 9.5: (a) Backward-to-forward scattering ratio as function wavelength for different hole diameters. The data was averaged over two excitation positions (left and right) (b) Angular patterns for $D = 50, 100, 140,$ and 180 nm at $\lambda_0 = 500$ nm, as indicated by the gray dashed line in (a). (c) Cross cuts through radiation patterns in (b), plotted with the same color code as in (a). The crosscuts have been integrated over a range of ϕ ($\phi = 60 - 120^\circ$ and $\phi = 240 - 300^\circ$) as indicated in Fig. 8.2(a) by the blue dashed lines. All patterns in (c) have been normalized to 1. No data is collected for the gray region which corresponds to the angular range that is taken by the hole in the parabolic mirror.

what was observed for gratings [103]. Furthermore the hole itself can also support a p_z component [211, 215] which could be driven by the electron beam. These two potential p_z contributions are difficult to separate in this experiment.

Regardless of the origin of the p_z component, we expect that the resulting angular pattern is caused by coherent interference of p_z , p_x , and m_y dipole moments. As a simple estimate for the angular patterns we can take the coherent sum of a p_z moment and in-plane components m_y and p_x where we use the ratios from Fig. 9.2(a) as the ratio between the out-of-plane and in-plane components. To take into account substrate interference we assume that the dipoles are located at a vacuum-gold interface. In our model we place the m_y and p_x components

corresponding to the hole resonance at the center of the hole, whereas the p_z component is positioned at the edge of the hole representing the TR emission at the electron beam impact position (spaced by a distance $D/2$ from the hole center). Finally, we assume a fixed phase relation between all the components and equal m_y , and p_x contributions.

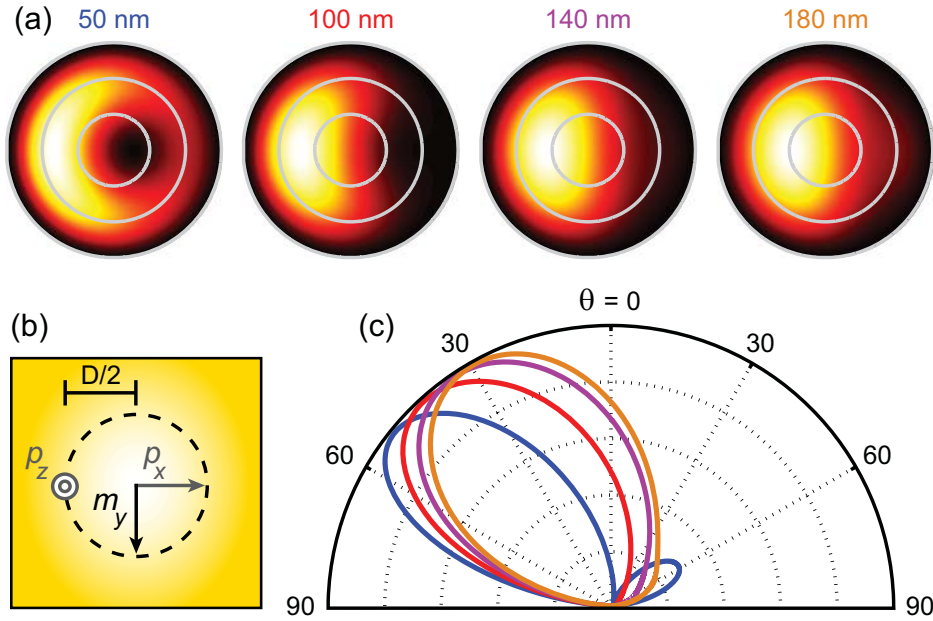


Figure 9.6: (a) Angular patterns for a combination of p_z , p_x , and m_y , where the ratios between in-plane and out-of-plane components for the different hole diameters are taken from Fig. 9.2(a). This combination of dipole moments is expected for excitation on the left edge of the hole. (b) Schematic top view of the dipole orientations with respect to the hole (included as circular dashed line for reference) as used in the model. We position the p_z dipole at the edge of the hole at the electron impact position. (c) Cross cuts through (a) using the same color code and integrated over the same range of ϕ as in Fig 9.5(c).

Figure 9.6 (a) shows the calculated angular radiation patterns for the coherent interference between dipole moments taking the assumptions mentioned above. A top view of the dipole configuration is shown schematically in (b). In (c) we show the cross cuts through the patterns in (a) similar to Fig 9.5(c). Although this model is very simple and is based on several assumptions it already gives remarkably good agreement with the experimental data. Because the in-plane components become stronger for larger diameters, the emission lobe moves towards the normal for larger holes, going from $\theta = 50^\circ$ to $\theta = 30^\circ$, which matches well with the data in Fig. 9.5(c). Furthermore, for the smallest diameter the p_z component is relatively strong which leads to a small forward lobe. This additional lobe is also visible in the CL data (see Fig. 9.5). We note that angular emission profiles of the nanoparticles had significant quadrupolar contributions but for the holes these do not seem to be necessary to explain the data. The fact that the hole response

appears to be mainly dipolar agrees well with our plane-wave simulation results and with results obtained by Rotenberg *et al.* [215, 219], even though the local electron beam driving creates stronger gradients that potentially could enhance higher order moments [201]. The far-field directionality in this experiment is complementary to the directionality that was observed in the near field [219], although in that case the holes were driven through SPPs which cannot efficiently drive an electric dipole moment along the propagation direction due to its transverse-magnetic wave nature. Furthermore there was no TR emission component present in those experiments, as that is unique to electron-beam excitation.

9.7 Conclusions

In conclusion, we have used angle-resolved cathodoluminescence spectroscopy to unravel the local response of individual nanoscale holes patterned in a gold film. We studied the influence of hole diameter on the scattering spectrum and angular radiation profile. In the spectra we find a strong contribution around $\lambda_0 = 520$ nm for all diameters. The response in the red/NIR spectral region increases for larger diameters. By studying the decay of the CL signal away from the hole, we determine that direct coupling to the hole resonance near-fields is the main source of coupling. Using finite-difference time-domain simulations we further elucidate the scattering behavior. We find that the scattering of the holes is suppressed due to the substrate. Furthermore, we deduce from the induced near fields that the emission has both electric and magnetic dipole character. The interference of these in-plane components with an out-of-plane electric dipole moment gives rise to transverse beaming by the holes, complementary to what was found for nanoparticles before. As the diameter increases the in-plane dipole components become more dominant, leading to a shift in the main emission lobe towards the normal. This behavior is well-reproduced by a simple dipole-interference model where we take the spectral measurements as input to determine the ratio between the in-plane and out-of-plane components. These insights could be used in the future to design and characterize novel plasmonic devices based on holes for color filtering and sensing applications.

10

Variable modal excitation efficiency in plasmonic dolmens through nanoscale electron beam positioning

Plasmonic “dolmen” metamolecules support coupled monomer and dimer modes which can interfere to giving rise to distinct resonant scattering phenomena. In this Chapter we study the nanoscale interplay between localized modes in gold dolmens using a combination of cathodoluminescence and electron energy-loss spectroscopy and resolve the degree of radiative character of these modes on the nanoscale. We perform a systematic comparison of dolmens with different sizes and geometries and explain the relevance of different driving positions. By precisely controlling the excitation position we are able to control modal amplitudes which can be used to tailor emission spectra with a great degree of accuracy.

10.1 Introduction

Plasmonic nanostructures have gained significant interest due to their ability to manipulate light on the nanoscale. Plasmonic resonances in nanoparticles can be tuned by their shape, size, and dielectric environment. By combining particles into composite structures one gains additional tunability which can be utilized to engineer *e.g.* highly directional antennas [39, 179]. Furthermore one can combine

particles into “metamolecule” configurations with unique near- and far-field optical properties. Analogous to real molecules, the relative orientation and position of the constituent elements has an important influence on the overall resonant properties. Plasmonic metamolecules can exhibit Fano interference where two modes, typically a high- Q subradiant mode and a low- Q superradiant mode, interfere to yield a Fano lineshape. In some cases this leads to a plasmon-induced transparency (PIT) [112, 235–242]. Such Fano resonances can be engineered to be highly dispersive, which makes them attractive for various types of optical sensing schemes [44, 45, 238, 243, 244].

A particular type of metamolecule which has been studied extensively in the literature is the “dolmen” or “ π ” structure in which a nanorod is capacitively coupled to an orthogonally oriented dimer composed of two vertical nanorods [235–237, 245, 246]. The monomer rod supports a strongly scattering dipole resonance that couples to a subradiant quadrupolar type resonance in the dimer. Depending on the spacing of the elements, *i.e.* the degree of near-field coupling between the elements, and the resonance detuning, the interference between these two modes can lead to a PIT transmission window in the visible/NIR regime, in which the transmission is near-unity. Counterintuitively, the local fields on the dimer are very strong within this transparency window while the extinction is low. This makes the dolmen antennas interesting for coupling to local emitters or for enhancing nonlinear effects. The dolmen scattering behavior can be well understood using a coupled harmonic oscillator model [235, 237]. In fact, this coupling phenomenon is generic and can occur for any type of coupled oscillator system. For instance, a localized surface plasmon resonance (LSPR) coupled to a light-emitting waveguide mode also gives a transparency window in transmission while at the same time the local fields in the waveguide are very strong, allowing fluorescence enhancement within this window [247]. Similarly, it has been shown that there can be enhanced absorption within a window of suppressed scattering for various coupled oscillator systems [248, 249].

Although dolmens have been studied extensively in arrays with plane-wave excitation, to fully exploit their potential, in *e.g.* sensing and spontaneous emission control, it is important to investigate how individual structures respond to a local excitation source. Cathodoluminescence (CL) spectroscopy and electron energy-loss spectroscopy (EELS) provide powerful platforms for studying the local response of composite plasmonic nanostructures owing to the high spatial resolution and broadband spectral characteristics of the electron beam excitation [79, 160, 191, 241, 250–252]. In this Chapter we study the local response of gold plasmonic dolmen structures using EELS and CL. In particular, we study the influence of size and particle separation on the scattering behavior and we investigate how the coupling between the elements manifests itself in the near field. To compare the experimentally studied local response to the plane-wave response, we use finite-difference time-domain (FDTD) simulations. The CL and EELS measurements are performed on the same structures so that we can directly compare the two techniques, enabling a differentiation between “dark”

and “bright” dimer modes for example.

10.2 Dolmen geometry and fabrication

The dolmen structure consists of a horizontal monomer coupled to a vertical dimer. A schematic representation of the experiment and the structure is shown in Fig. 10.1(a). Using a fast electron beam (300 keV for EELS and 30 keV for CL experiments) we can locally excite the dolmen structure. During this excitation process the electrons transfer energy to the structure which can be detected in an electron energy-loss spectrometer (see Section 2.5). This excitation can subsequently couple out as far-field radiation which can be collected by our CL system (see Section 2.2 for details). The EELS and CL measurements were performed in different electron microscopes although simultaneous collection is also possible in principle. The EELS experiments were performed at Stanford University in the group of professor Mark Brongersma with the help of David Schoen.

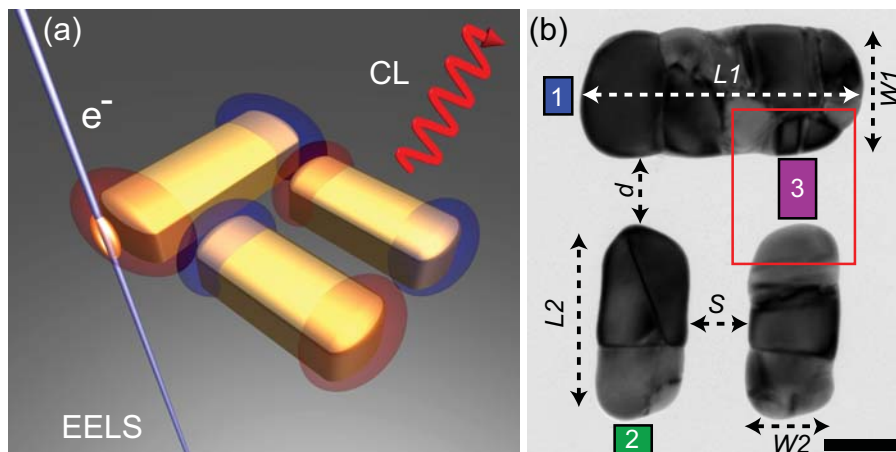


Figure 10.1: (a) Schematic representation of the experiment. Fast electrons excite the structure during which they experience energy loss which can be measured by EELS in a TEM. The excitation can be coupled out as far field radiation (CL) which can be collected by our CL system (b) Bright-field transmission electron micrograph of a gold dolmen structure of size 2 (see Table 10.1). In the image we have indicated the different size parameters. The blue, green, and magenta boxes indicate regions of interest that are referred to throughout the chapter. The red box indicates which part of the image is used for Fig. 10.5(a). The scalar bar represents 50 nm.

In order to perform EELS experiments an electron-transparent substrate is needed. To that end we fabricated gold dolmens on 15 nm thick Si_3N_4 membranes using a combination of electron beam lithography (EBL), thermal evaporation, and lift-off (see Supplementary Section 10.9.1 for details). Although the CL experiments do not require an electron transparent substrate, they do benefit from having such a thin membrane as substrate as this nearly fully eliminates background radiation.

We fabricated three sizes of dolmens (see Table 10.1 for exact dimensions). For the smallest dolmen size we also varied the spacing between the monomer and dimer in order to vary the near-field coupling between the two. Additionally, we have fabricated individual bars and dimers as references for each dolmen size. Figure 10.1(b) shows a bright field (BF) transmission electron micrograph of a dolmen structure of size 2. In the image we have indicated the different in-plane geometrical parameters that define the dolmen geometry. To determine the height of the structures we used atomic force microscopy (AFM) measurements (see Supplementary Fig. 10.8). In Fig. 10.1(b) we have also specified three regions of interest (ROI) to which we will refer throughout this Chapter. Although we have drawn only one box here per ROI we use two (on left and right side) to improve the signal-to-noise ratio in the spectra where we benefit from the fact that the dolmen is mirror symmetric across the vertical axis.

10.3 Single nanorods and dimers

To investigate the response of the dolmen structure we first study its constituent building blocks. To that we end we measured spatially resolved CL and EELS spectra on individual rods and dimers (for details on the experimental parameters see Supplementary Section 10.9.2). We raster-scan the electron beam in small steps over the structure and at each position we measure a EELS/CL spectrum. As the gold layer is quite thick (~ 40 nm, see Supplementary Fig. 10.8), the EELS signal that is measured through the metal does not uniquely represent the optical resonances as other inelastic processes occurring in the dense gold layer also cause energy loss. Hence we only take into account the excitation positions where the beam does not directly hit the structure. Because the evanescent electromagnetic fields extend away from the electron trajectory it can still couple in this “aloof” excitation configuration, while it does not experience collisions in the gold nanostructure. For CL measurements we do not have this restriction because we only measure the far-field emission and do not need to preserve the primary electron beam quality.

Figure 10.2(a) shows the spatially integrated CL and EELS spectrum for a single gold rod with dimensions of size 2. An annular-dark field (ADF) scanning transmission electron microscopy (STEM) image of the structure is shown as inset. We clearly observe two peaks in the spectra which correspond to LSPRs in the structure. To identify these resonances we simulate the scattering (Q_{scat}) and absorption cross section (Q_{abs}) (normalized to the geometrical cross section) for plane-wave excitation with the polarization along and transverse to the long axis of the rod, using total-field scattered-field simulations in FDTD [228] (for details see Supplementary Section 10.9.3). The simulation results are shown in Fig. 10.2(b). For polarization along the long axis we observe a peak in the scattering at $\lambda_0 = 860$ nm while for transverse polarization a peak is observed at $\lambda_0 = 620$ nm. Both resonances have cross sections that significantly exceed the geometrical cross section of the particle, as is often the case for LSPRs. As insets we also plot the real part

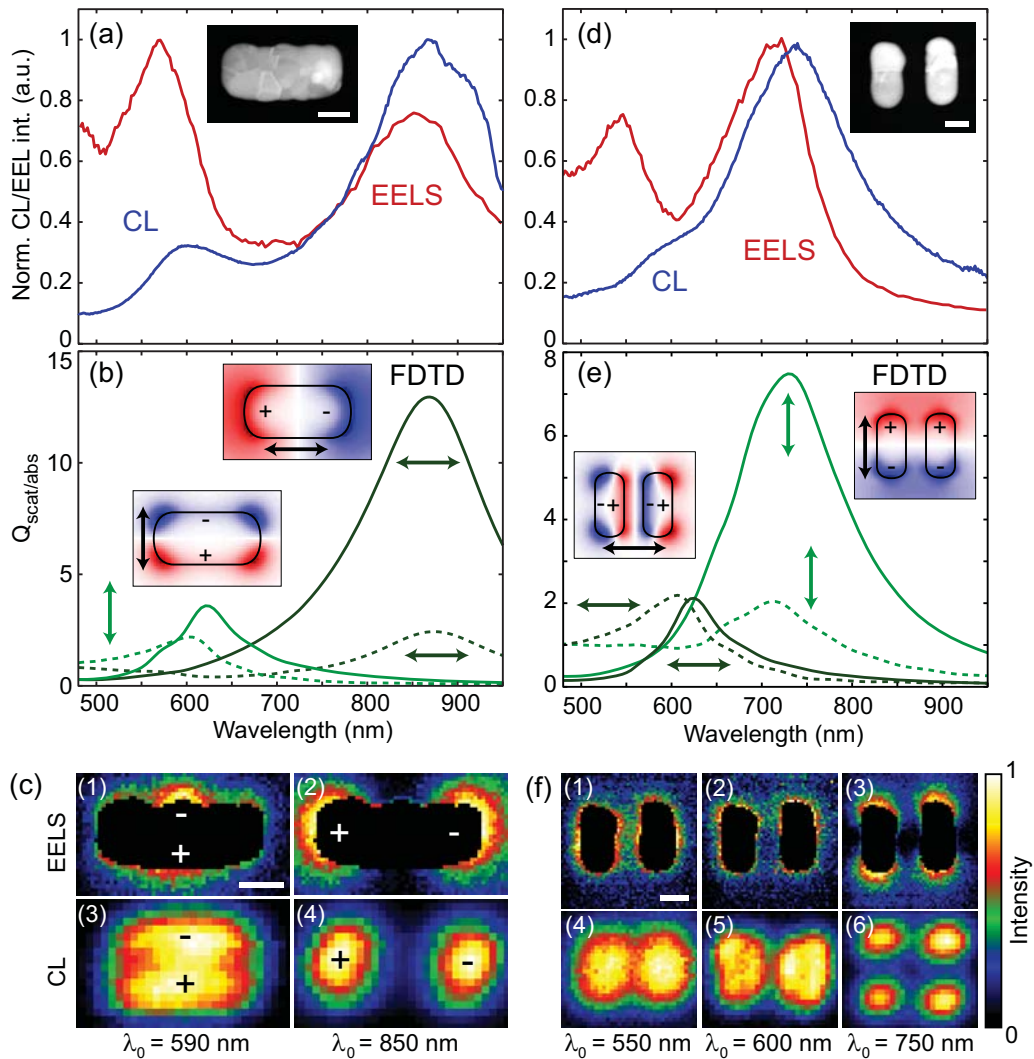


Figure 10.2: Spatially integrated CL and EELS spectrum of (a) a single gold rod and (d) dimer with similar dimensions to the dolmen from Fig. 10.1. ADF STEM images of the structures are shown as insets (b,e) Scattering (solid curves) and absorption (dashed curves) cross section simulations for the single bar and dimer for two orthogonal polarizations as indicated by the arrows, calculated using a TFSF source in FDTD. The cross sections have been normalized by the geometrical cross sections of the structures. As insets we show the corresponding E_z near field distributions, revealing the transverse and longitudinal dipole resonances. (e) EELS and CL spatial excitation distributions for single bar for $\lambda_0 = 550, 600$ and 850 nm corresponding to transverse and longitudinal dipole resonances. (f) EELS and CL spatial excitation distributions for dimer for $\lambda_0 = 550, 600,$ and 750 nm. Scale bars correspond to 50 nm.

of the out-of-plane electric field component (E_z) of the induced near-field (at the middle of the rod, $h = 20$ nm) which clearly reveals that we are driving transverse (blue peak) and longitudinal electric dipole resonances. The transverse resonance is blue-shifted with respect to the longitudinal resonance because the conduction

electrons experience a larger restoring force due to the reduced width.

The simulated scattering cross section spectrum qualitatively matches the integrated CL data, where the resonance wavelengths, linewidths, and relative peak heights are well-reproduced. In contrast, while the EELS spectrum shows similar peak wavelengths and linewidths, the transverse resonance is stronger than the longitudinal resonance, contrary to the CL and FDTD simulations. This can be explained by the following effects. First, the FDTD absorption cross sections for the two resonances are close in magnitude and roughly follow the scattering cross section, but the relative amount of absorption compared to the scattering is larger for the transverse resonance which should lead to an increased peak height in EELS. Furthermore the degree of field confinement is higher for the transverse resonance so any absorbing layer like a contamination layer or the germanium seed layer will increase the absorption more for this resonance compared to the longitudinal mode, leading to a larger difference in EELS and CL. We note that for the transverse resonance the CL and EELS data are slightly blue-shifted compared to the FDTD. It has been suggested that one might expect a red-shift in the EELS measurement, compared to an optical experiment because the near-field should be redshifted compared to the far-field [253]. Thus far it has not been resolved in literature whether CL and EELS measurements are generally blue-shifted or red-shifted with respect to each other or compared to optical data and it highly depends on the experiment and structure what is observed [254, 255]. For comparison with optical simulations, differences in the exact sample geometry and optical constants are a major factor but there are several other effects as well that can influence the experimentally measured spectral positions like charging and carbon deposition as explained in detail in Ref. [255].

By studying the spatial profiles we can verify the nature of the observed resonance peaks. Figure 10.2(c) shows the 2D EELS and CL excitation maps at two resonance wavelengths. As the electron beam preferentially couples to E_z components [63], an electrical dipole resonance will be excited efficiently at the particle extremities along the dipole axis as there is a strong E_z component at those positions (see the field profiles in Fig. 10.2(b) and CL maps in Fig. 5.2(b,d,e)) [256]. Indeed, the EELS and CL maps clearly show such features, consistent with the excitation of transverse and longitudinal resonances.

Next, we perform a similar analysis for the isolated dimer structure. The response of a single dimer rod is not shown here as it is similar to what is shown in Fig. 10.2(a-c) but blueshifted because of the smaller in-plane dimensions. Figure 10.2(d) shows the spatially integrated CL and EELS spectra for the dimer. Again, two peaks are clearly visible in the spectra. The short-wavelength peak is quite weak for CL and appears as a shoulder around $\lambda_0 = 600$ nm whereas for EELS it is much more pronounced and centered around $\lambda_0 = 550$ nm. The FDTD field plots in the inset of (e) shows that plane-wave excitation drives a transverse and longitudinal dipole modes with the rods excited in phase. The blueshift of both peaks compared to the spectra for the individual larger rod is due to the abovementioned size difference. Compared to a single dimer rod however, these collective dimer modes are

redshifted for the transverse mode and blueshifted for the longitudinal mode respectively (not shown here). This can be understood from a hybridization scheme where the transverse mode is energetically favorable (bonding) and the longitudinal mode is energetically unfavorable due to the charge distributions associated with these modes (see hybridization schemes in Fig. 10.10(a,b)) [257, 258].

For the dimer it is less straightforward to directly compare the plane-wave case to the CL and EELS spectra and excitation maps like we could for the single rod. The dimer also supports an antibonding mode for transverse excitation and a bonding mode for longitudinal excitation, where the dipole moments in the rods are in anti-phase (see Supplementary Fig. 10.10(a,b)). These modes are symmetry-forbidden for plane-wave excitation under normal incidence [259–261] but can be accessed with local electron beam excitation [79, 250, 256, 262]. Hence the peaks observed in CL/EELS could be due to four modes rather than two.

Next, we use the spatial profiles in Fig. 10.2(f) to identify which modes are responsible for the peaks observed in the EELS and CL data. For the blue peak in EELS at $\lambda_0 = 550$ nm (excitation map (1)) we observe excitation hotspots along the short axis of the rods and a high excitation probability in the gap region between the two rods, whereas at 600 nm (excitation map (2)) the excitation probability is significantly lower in the gap region. In the bonding mode there is destructive interference of the E_z component in the center of the gap (clearly visible in the FDTD E_z field profile for this mode in Fig. 10.2(e)), so a low excitability is expected at that position whereas for the antibonding mode there is constructive E_z interference leading to a high excitability in the gap region [250, 256, 262]. Therefore we conclude that map (1) is consistent with the transverse antibonding mode and map (2) is consistent with the transverse bonding dimer mode. The position of the peak in CL coincides with the peak in FDTD for the bonding mode and also the spatial profile matches well. The blueshifted antibonding mode most likely does not radiate efficiently and therefore its contribution to CL is small compared to the EELS spectrum. We note that the vertical z -dipole mode in the rods, which peaks around $\lambda_0 = 510$ nm for a single rod without membrane (not shown here), could play a role in explaining the discrepancy between the EELS and CL signal as well, as this resonance has a low albedo due to the high degree of confinement along the z -axis, and thus may appear more strongly in the EELS.

We will now discuss the longitudinal dimer modes which are most relevant for the canonical dolmen PIT behavior. We observe no noticeable peak-splitting in the longitudinal resonance peak around $\lambda_0 = 750$ nm in Fig. 10.2(d) suggesting a relatively weak coupling between the rods for the longitudinal case. This could be due to the fact that the field overlap between the rods is rather small in this configuration, which is corroborated by the EELS and CL maps for this wavelength (maps (3,6) in Fig. 10.2(f)) which shows that there is poor spatial overlap between the excitation hotspots. When the rods are brought close enough ($S < 1$ nm) this splitting can become substantial such that separate peaks are visible as was shown in Ref. [260].

The EELS and CL maps of the dimer for the peak at $\lambda_0 = 750$ nm (maps (3,6) in Fig. 10.2(f)) show that that excitation probability is highest at the rod apices

but such behavior is expected for both the bonding and antibonding longitudinal modes. However, there should be a subtle difference between the two. For the antibonding mode the rods are in phase leading to constructive E_z interference in the gap region near the apices (also clear in FDTD E_z profile for this mode in (e)). As a consequence we expect that we can drive that mode in the gap region as well whereas for the bonding mode that is not be possible because there is no E_z component present. In our case the maps are more consistent with the latter case. Supplementary Fig. 10.11 shows the EELS spectra for excitation within the gap and at the apices. From the spectra it is clear that at the apices the spectrum is slightly redshifted compared to within the gap. This effect is also apparent in the spatial EELS profiles in the range $\lambda_0 = 650$ to 750 nm where the gap region gradually becomes darker for increasing wavelength (see maps (1-3) in Supplementary Fig. 10.11(b)). These observations suggest that the peak at $\lambda_0 = 750$ nm in Fig. 10.2(d) is due to two modes, where the excitation efficiency of the antibonding mode decreases relative to the bonding mode for increasing wavelength.

To verify this hypothesis we perform FDTD simulations where we placed a vertically-oriented electrical point-dipole source at the apex of one of the rods and plotted the resulting E_z field profiles (Fig. 10.11(b)). The driving field of the dipole has not been removed from the image which means that images show a mix of the driving field and the induced field on the dimer. In order to see the induced fields on the dimer the colorscale has been saturated by a factor 300. As is clear from maps 3 and 6 in Fig. 10.2(f) the CL and EELS signal is highest at the apices of the rods for this wavelength, so the spectral contribution from these spots is largest. If a point dipole is placed in one of these hotspots the near-field patterns show that it is predominantly driving one the rods which, through capacitive near-field coupling, induces an opposite dipole moment in the other rod, suggesting that the longitudinal bonding dimer mode is dominant in our experiment. Using the knowledge we have about the individual elements we can now attempt to understand the dolmen response.

10.4 Inter-particle coupling in the dolmen

Figure 10.3(a,b) show spectra measured on a dolmen of size 2 at ROI 1 and 2. At ROI 1 we efficiently drive the longitudinal dipole mode in the top bar. From previous optical experiments, it is known that this monomer mode can couple to the bonding dimer mode [235–237, 245, 246] so possibly we can observe coupling between dimer and monomer at this position. The EELS and CL spectra show three peaks at this excitation position while in the reference monomer in Fig. 10.2(a) we only observe two peaks. At ROI 2 we only observe one main peak at $\lambda_0 = 750$ nm, matching the spectral position of the extra feature for ROI 1, showing that this additional spectral feature is related to coupling with the dimer. Similar to the data for the individual monomer and dimer, the EELS data is more pronounced in the blue compared to the CL data. We know that the dolmen can support a low-energy bonding

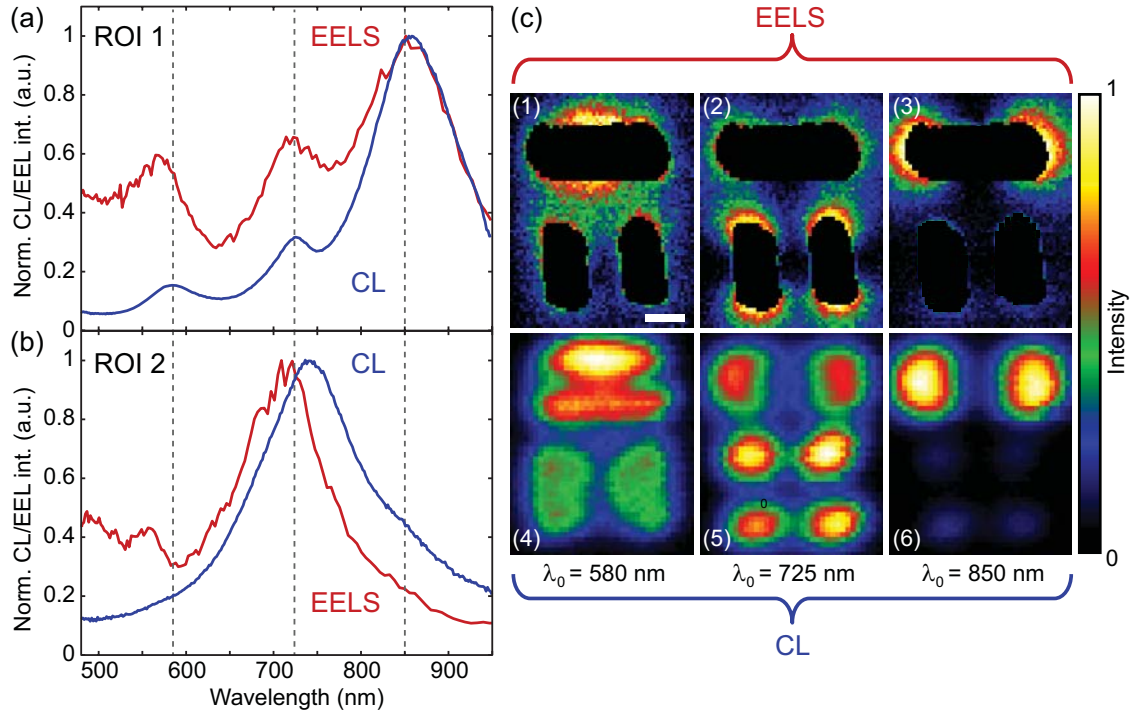


Figure 10.3: (a) CL (blue) and EELS (red) spectrum for excitation position 1 for the dolmen shown in Fig. 10.1c. For this excitation position the top bar is directly driven. (b) CL and EELS spectrum for excitation position 2 where we directly drive on of the dimer rods. (c) 2D EELS (images 1 – 3) and CL (images 4 – 6) for $\lambda_0 = 590$, 725, and 850 nm respectively, integrated over a 30 nm bandwidth. Scale bar is 50 nm.

and a high-energy antibonding mode (see Supplementary Fig. 10.10). Because the dimer mode and monomer mode are detuned and relatively weakly coupled, the hybridized bonding and antibonding modes are close in frequency to those for the bare dimer and monomer states, where the bonding mode has more monomer character and the antibonding mode has more dimer character.

As is explained in Ref. [251] the electron beam excitation is markedly different from plane-wave excitation in the case of such metamolecules. The electron energy-loss probability is determined by the near field acting back on the electron at the impact position [63]. In this case the near field of the entire structure acts back on the excitation positions at ROI 1 and 2. At ROI 1 the monomer is directly excited and the dimer can flip its phase relative to the monomer depending on whether the wavelength is below or above the dimer mode resonance wavelength. In other words, the wavelength with respect to the bonding dimer resonance position determines whether it is excited in-or out-of-phase with the driving field that is mediated by the monomer. Hence, both the bonding and antibonding dolmen mode can be driven at this position and act back on the electron which is the reason why we observe an additional peak in the EELS and CL spectrum. *Vice versa*, at ROI 2 we directly drive the dimer mode and the phase of the monomer can flip

depending on the frequency.

The effects mentioned above are visible in the spatial maps in Fig. 10.3(c) for the three peak positions. For the peak at $\lambda_0 = 850$ nm, the excitation efficiency is highest on the monomer-ends similar to the individual monomer illustrating that is this mode has strong monomer character (maps (3,6)), whereas the mode at $\lambda_0 = 725$ nm (maps (2,5)) has more dimer character. This is consistent with the fact that at these wavelengths the dimer is forced into the bonding and antibonding configuration respectively, due to its in/out-of-phase response with respect to the driving field. The excitation efficiency of the antibonding mode does not decline as one moves towards the top of the monomer. From this we conclude that the dimer excitation is indeed mediated by the monomer and does not occur directly through the evanescent electron fields, for which a rapid signal decay is expected away from the structure as is visible in the reference dimer spatial maps (Fig. 10.2(f), maps (3,6)).

Further proof that the peaks at $\lambda_0 = 850$ and 725 nm correspond to the bonding and antibonding dolmen modes can be given by studying the excitation efficiencies in the gap between monomer and dimer for the two wavelengths. In maps (3,6) the gap between dimer and dolmen is dark due to the destructive E_z near-field interference for the bonding mode, whereas in map (2,5) the gap is significantly brighter, consistent with the antibonding dolmen mode where the interference is constructive. Interestingly, we observe that for $\lambda_0 = 850$ nm the excitability is higher on the bottom of the dimer than on top, suggesting that bonding dolmen mode can be excited more efficiently from this position, although the effect on the spectrum seems to be small.

Because the coupling between dimer and monomer is relatively weak and the peaks both are quite broad spectrally we do not observe a clear Fano feature/PIT window. Also the spectral shift of the hybridized bonding and antibonding dolmen modes, compared to the bare dimer and monomer is not large enough to be clearly resolved, as the experimentally observed spectral shifts are also influenced by small size/shape differences in the dolmen elements, inherent to the EBL fabrication process. We expect that for more strongly coupled systems one could potentially resolve these features [251]. FDTD simulations suggest that smaller spacings would bring the dolmens in this regime where the interference and modesplitting clearly start to manifest themselves in the spectra.

At $\lambda_0 = 590$ nm the transverse dipole resonance in the monomer is dominant, as is clearly visible in maps (1,4). This state can hybridize with the antibonding dimer mode (see Supporting Fig. 10.10(d)) [236]. For our geometry these modes are detuned significantly so we do not observe any extra features in the spectrum related to modal coupling, like we could for the other modes at $\lambda_0 = 725$ nm and $\lambda_0 = 850$ nm.

10.5 Size-dependent optical response

It is well-known that plasmonic resonances redshift for increasing particles size. Here we investigate how the dolmen response scales with size. Figure 10.4(a) shows EELS and CL spectra taken at ROI 1 for the three fabricated dolmen sizes. Clearly, all spectral features move towards the red as the size increases, although the exact detuning between dimer and top bar varies somewhat for each size. For each size we observe coupling from the monomer to the dimer at ROI 1. On the right we also show the EELS and CL excitation maps for the central antibonding dolmen peak for each size at $\lambda_0 = 675, 730,$ and 790 nm for size 1, 2 and 3 respectively. Like the spectra, the spatial profiles remain very similar as the size increases. For the smallest size dolmen the excitation positions on the particles were not masked in the EELS spatial maps because the metal is substantially thinner (see Supplementary Fig. 10.8) and the EELS signal better reflects the optical modes that are excited. For the smallest dolmens the CL data is significantly red-shifted compared to the EELS data. We noticed that during the CL scan the response redshifted while the quality factor remained roughly constant which is an indication that there is local deposition of a carbonaceous contamination layer during electron beam scanning. Such *in-situ* redshifting was not observed in the measurements for other sizes which either means that the contamination level was different on that sample or that the larger structures are simply less sensitive to a thin contamination layer.

Figure 10.4(b) shows the plane-wave scattering and absorption cross section for horizontal polarization along the monomer for each of the dolmen sizes, calculated using FDTD. Also here the features redshift and for each size we observe a modest transparency window (indicated by the gray dashed line). If one decreases the spacing the modal splitting and modulation depth of the window can be substantially increased (not shown here). To show that this transparency window is similar to those discussed in literature we show the induced E_z near-field distribution at the PIT wavelength, for each of the sizes in the first column on the right of Fig. 10.4(b). We clearly see the reduced intensity on the monomer and the antisymmetric charge distribution in the dimer. In the plane-wave case the transverse mode in the dimer is also driven simultaneously unlike in the CL/EELS experiment, which leads to an increased contribution around $\lambda_0 = 600$ nm. To demonstrate that the well-known hybrid dolmen modes can also be driven when locally excited by a point-like source we show the near-field patterns for dipole excitation at ROI 1 as well (see second column in Fig. 10.4(b)). In this case we could not subtract the incident field like we could for the plane wave which distorts the pattern relative to the unperturbed eigenstate. Nevertheless we can clearly recognize the characteristic antisymmetric dimer mode in all dolmen sizes, suggesting that this type of driving excites the same modes as horizontally polarized plane-wave excitation.

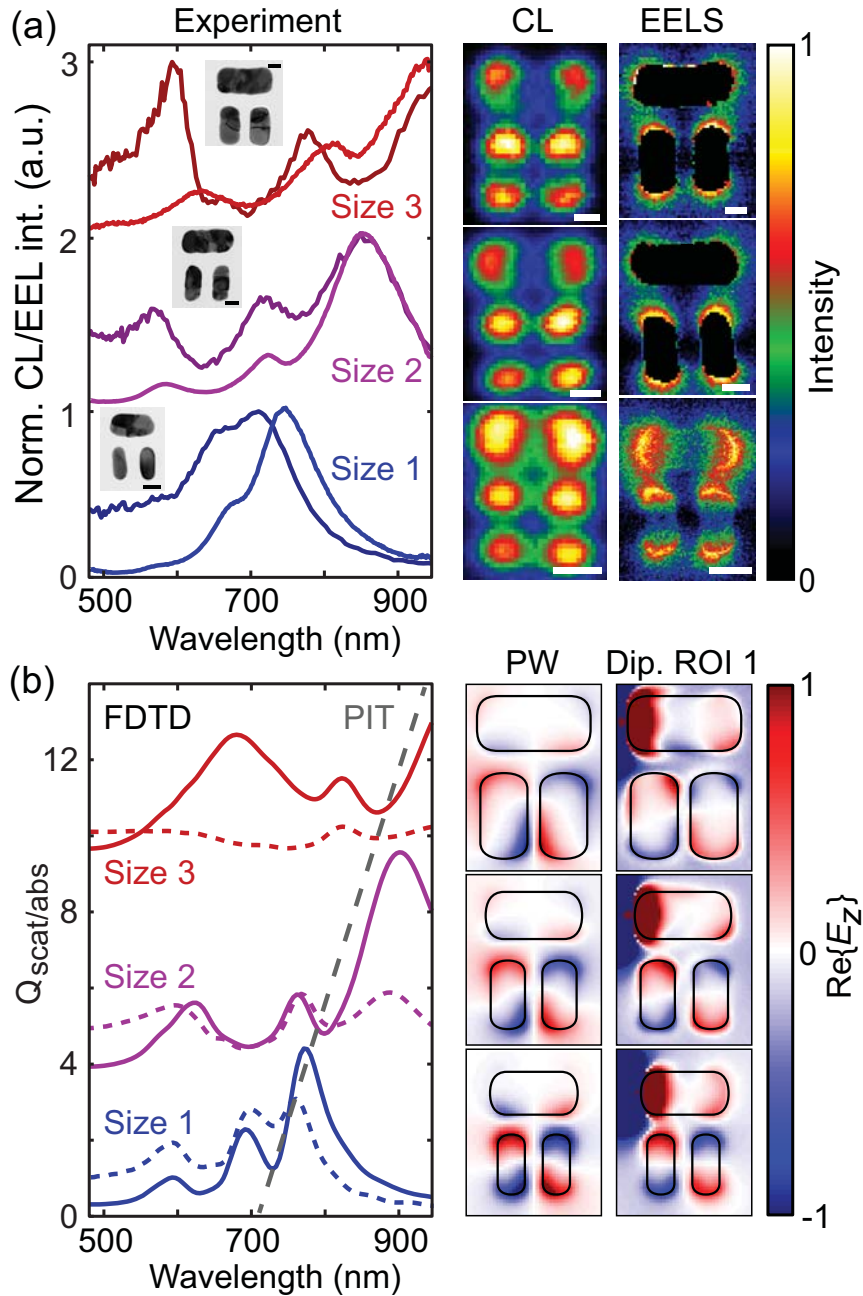


Figure 10.4: (a) EELS (dark curves) and CL spectra (bright curves) at excitation position 1 for all dolmen sizes. The spectra have been vertically offset for clarity. The corresponding BF TEM images are shown as insets. The EELS and CL spatial maps at the central peak, corresponding to the antibonding dolmen mode, are shown on the right (at $\lambda_0 = 675, 730,$ and 790 nm for size 1, 2 and 3 respectively). (b) Normalized scattering (solid curves) and absorption (dashed curves) cross sections of dolmen structures for polarization along the top bar, calculated by FDTD. The spectra have again been vertically offset for clarity. The PIT feature indicated by the gray dashed line shifts with size towards the red. First column on the right shows the E_z near field distribution at the PIT window for plane-wave excitation (PW) ($\lambda_0 = 730, 750,$ and 880 nm for size 1, 2 and 3 respectively). Second column shows the same maps for vertical point dipole excitation 10 nm left of the top bar (ROI 1) at half-height of the rod.

10.6 Variable modal excitation efficiency

Thus far we have focused on ROIs 1 and 2 where just one of the dolmen elements is directly excited by the beam. Next, we investigate the region between the monomer and one of the dimer rods (ROI 3), where simultaneous driving of the dolmen elements is possible. The area of interest is indicated by the multicolored box in the TEM image in Fig. 10.5(a), which itself is a blow-up of the area enclosed by the red box in Fig. 10.1(b)). Figures 10.5(b,c) show the CL and EELS spectra when the electron beam moves from the monomer towards the dimer rod (from top to bottom). The colors in the box in (a) are matched to the curve colors of the spectra in (b,c) and indicate the corresponding electron beam position in this direction. The width of the box (~ 30 nm) represents the lateral averaging range that we used in order to improve the signal-to-noise ratio.

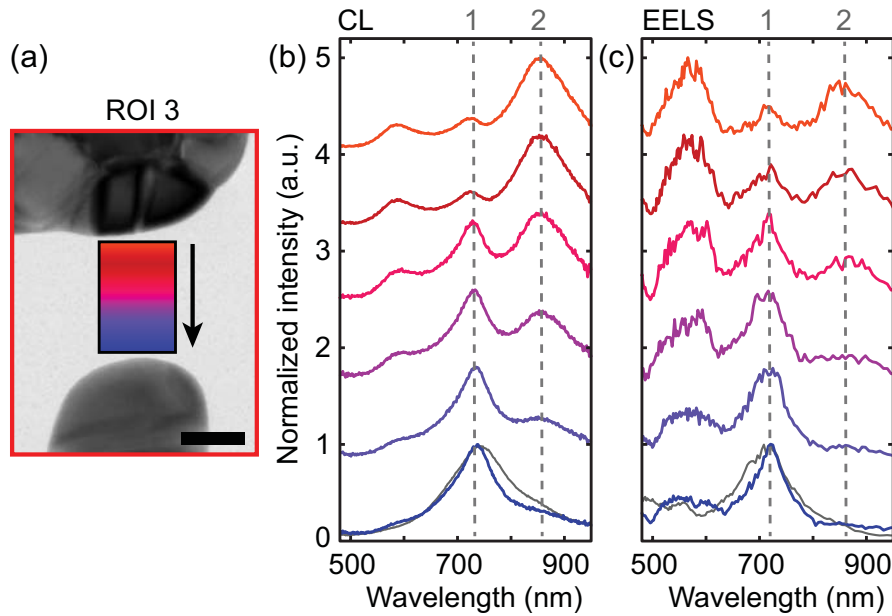


Figure 10.5: (a) BF TEM image corresponding to the area indicated by the red box in Fig. 10.1(b). (b,c) CL and EELS spectra scanning down from the top bar to the dimer (spectra match color code in box). We transversely average along the width of the box for a better signal-to-noise ratio. The gray curves on the bottom correspond to spectra collected at ROI 2. The spectra are vertically offset for clarity. Scale bar is 25 nm.

Clearly the spectra change completely while the electron position is varied by only 40 nm. In the following discussion we neglect the transverse monomer mode which is visible at $\lambda_0 = 590$ nm. Close to the monomer, the peak at $\lambda_0 = 850$ nm (peak 2) corresponding to the bonding dolmen mode is dominant. When moving towards the dimer, the peak at 750 nm (peak 1) corresponding to the antibonding dolmen mode starts to become stronger; close to the dimer it dominates the spectrum. Interestingly, this peak is more narrow than for ROI 2 (see Fig. 10.3) and

the subtle long-wavelength shoulder has disappeared. For comparison we have included the spectra for ROI 2 on the bottom (gray curves) of (b) and (c). We attribute this slightly different spectral shape to the fact that the bonding dolmen mode is inefficiently excited at this position due to destructive E_z near-field interference. This effect is also apparent from the spatial excitation maps 3 and 6 in Fig. 10.3(c) at the bonding mode wavelength ($\lambda_0 = 850$ nm), where a clear dark band is visible between dimer and monomer indicating a low excitation efficiency. For symmetric dimer structures this dark band usually is in the center in the gap as shown by others [79, 250, 262], but for our dolmen the monomer near field is stronger than that of the dimer at this wavelength, and as a result this band of low excitability shifts towards the dimer. This data shows that the spatial precision of electron beam excitation can be used to precisely tune the modal driving efficiency which is not possible for plane-wave excitation at normal incidence.

10.7 Varying intrinsic coupling strength

So far we have investigated the effect of size on the optical response and of changing the degree of modal driving by precisely controlling the excitation position. Next, we control the degree of intrinsic coupling between the dolmen elements. The coupling between monomer and dimer is mediated by the induced near fields in the nanorods which extend ~ 30 nm away from the structure. Hence, the intrinsic coupling strength is mainly determined by the spacing d between monomer and dimer. Figure 10.6(a,b) show CL and EELS spectra at ROI 1 and 2 for dolmens of size 1 with different spacings $d = 30, 40, 50$ and 60 nm. We have also included reference spectra from an individual reference monomer and dimer of this size (" $d = \infty$ "). The spectra are vertically offset for clarity. For each separation distance the corresponding BF TEM image is shown on the right. The coupling between monomer and dimer is reflected by a shoulder in the EELS and CL spectra for ROI 1 around $\lambda_0 = 675$ nm for $d = 30$ nm. For $d = 40$ nm the shoulder is substantially lower and disappears completely for the dolmens with larger particle spacings, indicating that efficient coupling between dimer and monomer requires spacings smaller than 40 nm for this dolmen size.

Note that the main resonance positions also vary slightly from dolmen to dolmen without a clear trend, so we attribute these shifts to small size/shape variations in the dolmen elements. Figure 10.6 (c) show CL and EELS maps close to the antibonding dolmen mode spectral feature ($\lambda_0 = 675$ nm) for $d = 60$ nm (maps (1,2)) and $d = 30$ nm (maps (3,4)). Indeed, these maps show that there is significant field overlap in the case of $d = 30$ nm dolmen, reflecting the efficient near-field coupling, while for $d = 60$ nm dolmen this overlap is much lower thereby preventing effective coupling between dimer and monomer.

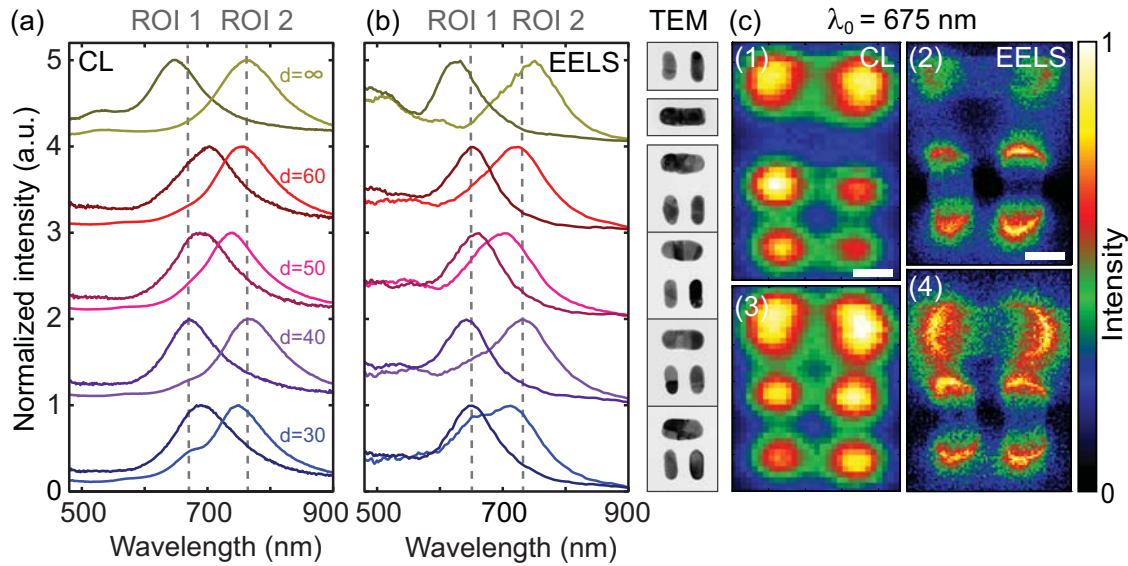


Figure 10.6: Change in coupling as function of distance d between top bar and dimer. (a) CL spectra and (b) EELS spectra for excitation position 1 and 2 for size 1 at spacings $d = 30, 40, 50$ and 60 nm. We also show the reference single bar and dimer spectra ($d = \infty$). The spectra have been vertically offset for clarity. On the right side we show the corresponding BF TEM images of the structures. (c) CL (1,3) and EELS (2,4) maps for $d = 30$ and $d = 60$ nm at $\lambda_0 = 675$ nm.

10.8 Conclusions

In conclusion, we have used cathodoluminescence spectroscopy and electron energy-loss spectroscopy to study the local optical properties of dolmen metamolecules and their individual constituents in great detail. Taking advantage of the high spatial resolution we are able to spatially map the response of the dolmen to the local electron beam source. Additionally, this experiment provides an opportunity to directly compare electron energy-loss and cathodoluminescence signals. We find that the EELS response is stronger for higher energies compared to CL, related to the far-field scattering efficiency of the modes. In both EELS and CL experiments we clearly observe coupling between monomer and dimer in the near field. Furthermore we demonstrate that the dolmen spectral response redshifts for increasing size as is expected for plasmonic structures. The dimer-monomer coupling is a nanoscale near-field effect and we demonstrate that the intrinsic coupling strength can be tuned by changing the spacing. The local electron beam excitation also allows for simultaneous direct excitation of dolmen modes where their relative amplitude can be tuned by precise positioning of the beam. This type of metamolecule excitation allows tailoring of the emission spectrum in ways that cannot be achieved by plane-wave excitation.

10.9 Supplementary information

10.9.1 Sample fabrication on TEM membranes

We fabricated three sizes of gold plasmonic dolmen structures and reference structures on 3×3 mm TEM samples (Ted Pella Inc., USA) with nine $100 \mu\text{m} \times 100 \mu\text{m}$ silicon nitride membranes (15 nm thickness) using a combination of EBL, thermal evaporation, and lift-off. For handling we attached the membrane chips to a 12×12 mm silicon chip. We spin a 145 nm thick layer of polymethyl methacrylate (PMMA) (at 3000 rpm for 45 seconds) onto the silicon support and heat it to 210°C such that it becomes sticky. Subsequently we press the membrane chip into the PMMA (with Si_3N_4 side upward) and let it cool down for 10 minutes after which they are strongly attached (see step 1 in Fig. 10.7).

We then apply a hexamethyldisilazane (HDMS) primer (at 4000 rpm for 30 seconds) and ~ 150 nm of positive ZEP520A resist (at 2000 rpm for 45 sec) using a spincoater (step 2). We bake the sample for 1 minute at 180°C after the HDMS step and 5 minutes after the ZEP520A step. Then we perform EBL in a Raith E-line system with 20 keV electrons using area-exposure at a dose varying between $20 - 250 \mu\text{C}/\text{cm}^2$ (optimal dose between $90 - 130 \mu\text{C}/\text{cm}^2$). The resist was developed by dipping the samples for 90 s in n-Amyl-acetate, 15 s in a 9:1 volume-ratio mixture of methyl isobutyl ketone and isopropyl alcohol, and 15 s in pure isopropyl alcohol (step 3). Subsequently we thermally evaporate 1 nm of germanium which acts both as adhesion layer and seed layer to reduce the metal granularity [223, 224] and a layer of gold (33 and 40 nm) for sample 1 and 2 respectively. We used an evaporation rate of $0.2 \text{ \AA}/\text{s}$ for the germanium and $0.5 \text{ \AA}/\text{s}$ for the gold at a base pressure of $\sim 5 \times 10^{-6}$ mbar.

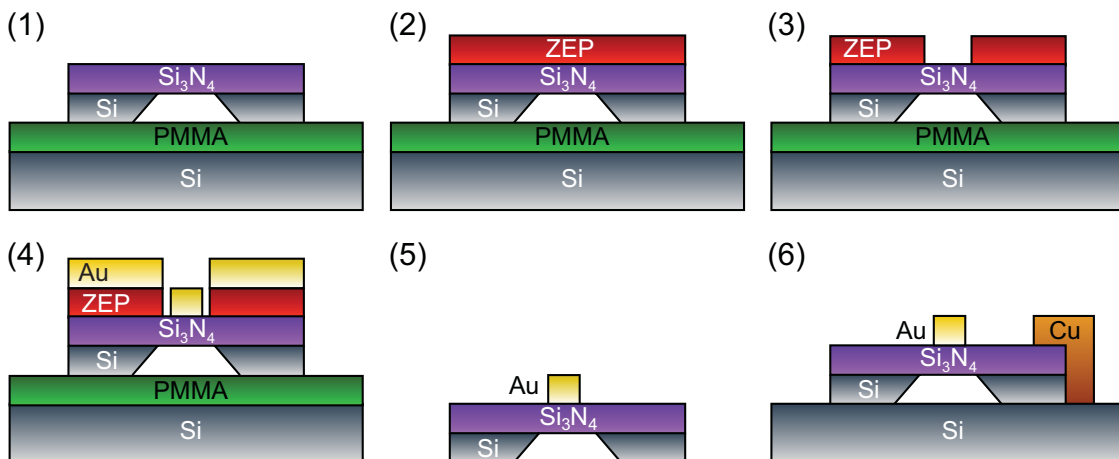


Figure 10.7: Schematic overview of the fabrication steps: (1) Attaching to silicon support using a PMMA resist layer. (2) Spinning of ZEP520A positive resist. (3) EBL and resist development. (4) Thermal evaporation of germanium and gold. (5) Lift-off in NMP. (6) Reattachment to silicon support with copper tape (for CL only).

Next, we lift off the excess metal by placing the sample in n-methylpyrrolidone (NMP) at 65 °C for 3 hours (step 5). In this step the PMMA layer also dissolves thereby detaching the membrane chip from the support. This is necessary for the EELS measurements in the TEM. For the CL measurements we reattach the samples to a support using copper tape (step 6) to be able to clamp the sample in the SEM holder. After these processes we use a soft oxygen reactive-ion-etch (RIE) descum with low forward bias to remove any organic contaminations from the sample without damaging the structures or the membranes.

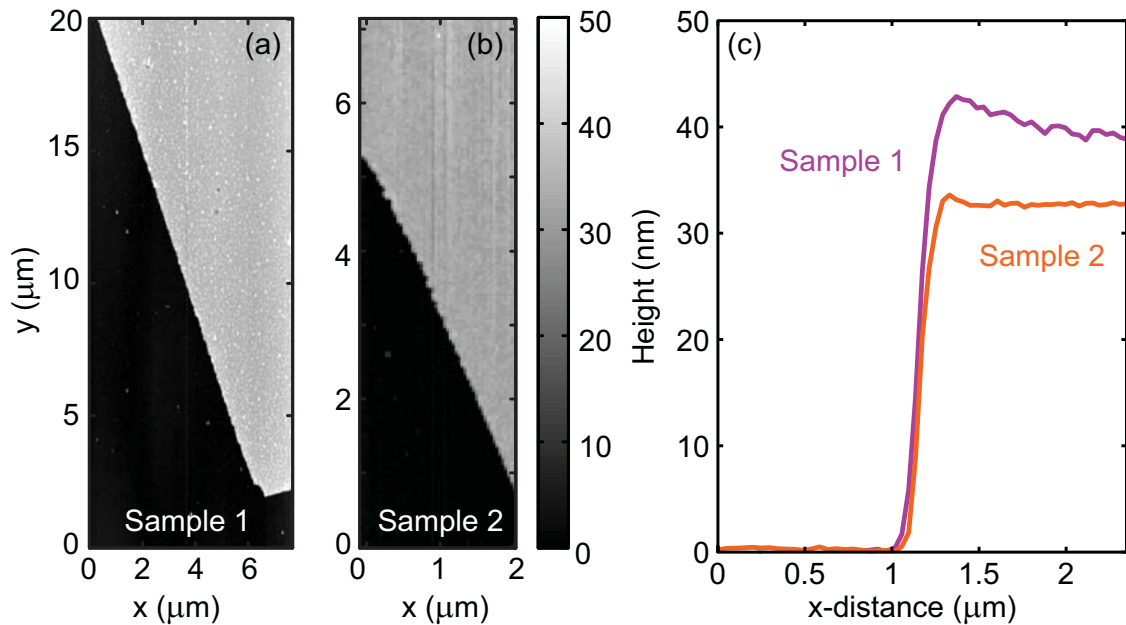


Figure 10.8: 2D AFM scans on reference gold pads on (a) sample 1 (dolmen size 2 and 3) and (b) sample 2 (dolmen size 1) where the grayscale indicates the height in nm. (c) Horizontal cross cuts along x for (a) and (b). We integrate over a 2 μm range in the y -direction and align the edge positions to obtain an average edge profile.

To characterize the metal thickness we use AFM measurements collected in tapping mode (Veeco Dimension 3100 AFM). Figure 10.8 shows AFM data taken on gold pads on sample 1 (dolmen size 2 and 3) and 2 (dolmen size 1). These gold pads are residuals from the electron beam focusing for the EBL process during which these parts of the resist were exposed to electron irradiation. These pads should have the same height as the gold antenna structures as they were created during the same evaporation session. The pads are on the silicon support making it possible to perform the AFM experiments without scanning the structures on the fragile membranes. The sizes of the dolmen structures are given in Table 10.1.

10.9.2 EELS and CL experiments

For more technical information on the CL and EELS setup we refer the reader to Sections 2.2 and 2.5 respectively. The CL measurements were performed in a FEI

Size	$L1$	$W1$	$L2$	$W2$	S	d	h
Size 1	125	60	90	40	30	30 – 60	33
Size 2	185	85	130	60	40	45	40
Size 3	215	100	160	90	30	45	40

Table 10.1: Dimensions of the dolmen structures for the three different sizes. The in-plane dimensions were derived from BF TEM data and the thickness from the AFM measurements. Dimensions are in nanometers.

XL-30 SFEG SEM equipped with a home-built CL-system. The measurements were done at 30 keV acceleration voltage and a beam current of 0.8 nA. The pixel size was 7.5, 8.5, and 10 nm for the three dolmen sizes respectively with an integration time of 0.5 s per pixel. With our CL system we have the capability to measure the angular pattern. However, due to the open geometry of the sample, the emitted light from the antenna can reflect off the bottom of the silicon support, other antennas on the membrane, or on the membrane edges which leads to substantial parasitic interference, thereby obscuring the emission pattern of the individual structure and making the angular measurements too unreliable.

The EELS measurements were taken in STEM mode at 300 kV acceleration voltage and a beam current of ~ 0.2 nA. During the EELS acquisition we simultaneously collect a STEM image using the annular dark field detector. To obtain a good reference we measure the zero-loss peak (ZLP) through a punctured membrane. For the final spectra we use a Richardson-Lucy algorithm to deconvolute the experimental EELS spectra with the ZLP which is considered to represent point spread function (PSF) of the system. The scanning pixel size was 3, 3.75, and 5 nm for the three dolmen sizes respectively with an integration time of 5 ms per pixel. In the EELS camera each pixel corresponds to an energy bandwidth of 0.01 eV. To transform the EELS intensity from per unit of energy to per unit wavelength like the CL data we multiply the data with the appropriate conversion factor: $100 \times hc/e\lambda_0^2$. In order to quantitatively compare the absolute EELS and CL signals one would need to account for the beam currents, integration times, and absolute system responses. Because we do not know all of these numbers we show normalized spectra which does allow direct comparison of the spectral shape. For all measurements shown here the EELS experiments were performed before the CL experiments.

10.9.3 FDTD simulations

To study the scattering properties of the dolmens and reference structures we carry out simulations of their optical scattering and absorption cross sections using finite-difference time-domain software [228]. For this we use a 3D “Total-Field Scattered-Field” (TFSF) source. A broad-band pulse (λ_0 from 400 – 1200 nm) is

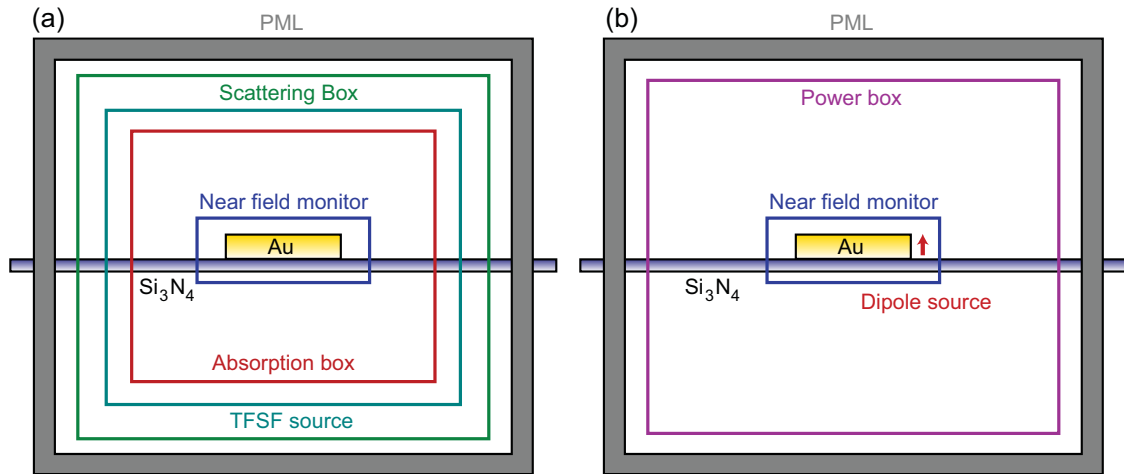


Figure 10.9: (a) Schematic of the FDTD simulation setup for the plane-wave TFSF simulations. The scattering box is used to calculate the scattering cross section whereas the absorption box can be used to calculate the absorption cross section. The near field monitor allows visualization of the induced near-fields on the structure. (b) Schematic of the FDTD setup for the point-dipole simulations. The power box collects the emitted power and the near-field monitor probes the near fields. In this case we cannot separate the driving field from the induced field.

used to simulate white light irradiation, incident on the structure from the top. The lateral dimensions of the structures are taken from TEM images and the thicknesses are taken from the AFM data. The membrane thickness is assumed to be 15 nm as specified by the manufacturer. The optical constants were taken from tabulated data for Au [105] and Si_3N_4 . There are no free parameters in these simulations. In order to directly compare the dolmen simulations with the reference simulations on the monomers and dimers we assume that the references have exactly the same dimensions. In the experiments the particle sizes for the references differ slightly from the dolmen, which could give rise to small discrepancies between the simulated response and the experiments on the references. In the simulations, the particle shape is represented by a rectangular box with hemicylindroid end facets for the first two sizes. For the largest size the end facets are composed of an additional rectangular box sandwiched between two halves of a hemicylindroid. The scattering cross section is obtained by dividing the scattered intensity by the areal footprint of the structure. We simulate for two orthogonal incoming polarizations. To simulate the absorption in the structures we introduce a flux box inside the TFSF source. With a near field box we monitor the local near fields on the structure so that we can identify the responsible modes. Figure 10.9 shows a schematic of the simulation setup.

To mimic electron beam excitation we also simulate the response of the structure to a vertical point dipole source which is placed 10 nm away from structures at half-height of the gold antenna structure. In this case we cannot remove the driving fields from the near-field but nevertheless this procedure gives a good idea of the

induced fields on the structure. This simulation setup is shown in (b). To prevent scattered fields from the simulation boundaries we use perfectly matching layers (PMLs).

10.9.4 Hybridization schemes for dimer and dolmen

To understand the hybrid modes in our dolmen system it is useful to consider simple hybridization schemes [257]. The dimer consists of two nanorods. The longitudinal resonances in these rods can hybridize into a dipolar antibonding mode (which is energetically unfavorable because the charges at the apices repel each other) and bonding quadrupolar mode (see Fig. 10.10(a)). In the figure we show snapshots of the charge distribution at an arbitrary moment in time. Interestingly this antisymmetric charge-distribution is inaccessible for free space light at normal incidence due to its symmetry. We note that this mode has both electric quadrupole and magnetic dipole character [201]. In the context of dolmens it is usually referred to as “quadrupolar” mode whereas for cut-wire pairs it is often called “magnetic” mode.

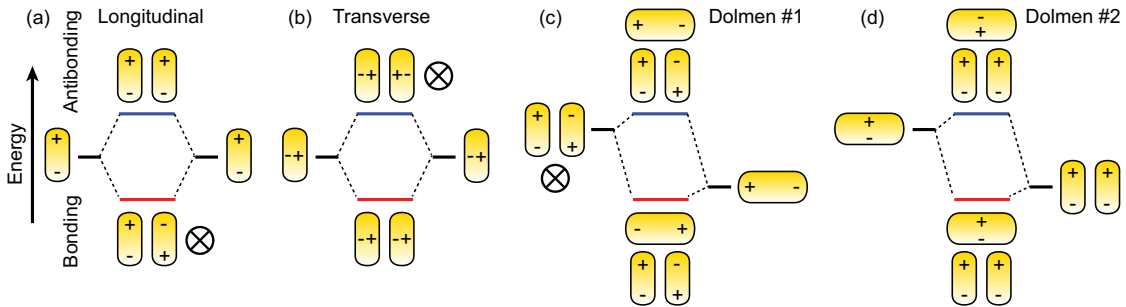


Figure 10.10: Hybridization schemes for (a) longitudinal dimer modes, (b) transverse dimer modes, (c) dolmen modes 1, and (d) dolmen modes 2. Each set of resonances hybridizes to give a set of bonding (lower energy) and antibonding (higher energy) modes. In the case of the dolmen the hybridizing bare-state resonances are also detuned in frequency which leads to asymmetric mode splitting. The \otimes symbol indicates that a mode is symmetry forbidden for plane-wave excitation at normal incidence.

For the transverse case (Fig. 10.10) the bonding mode can be driven efficiently with free-space light whereas the antibonding mode is symmetry forbidden at normal incidence. For off-normal incident light these symmetry-forbidden modes can be excited as that provides sufficient retardation [260]. With the electron beam all these modes can be excited where the excitation rate of each mode is determined by the electron beam position.

For the dolmen there are several hybridizations possible, depending on the size and aspect ratios of the rods. The most relevant for our experiment is the hybridization of the quadrupolar bonding mode in the dimer, which itself already is a hybridized state of two rods, with the longitudinal dipole mode in the horizontal

bar (Fig. 10.10(c)). The spectral measurements and FDTD measurements show that the monomer mode is redshifted compared to the dimer mode so the hybridization is not symmetric like is the case for the dimer. The second hybridization that could occur is between the transverse mode in the monomer and the dipolar antibonding mode in the dimer. In this case the transverse monomer mode is substantially blue-shifted compared to the dimer mode.

10.9.5 Discriminating longitudinal dimer modes

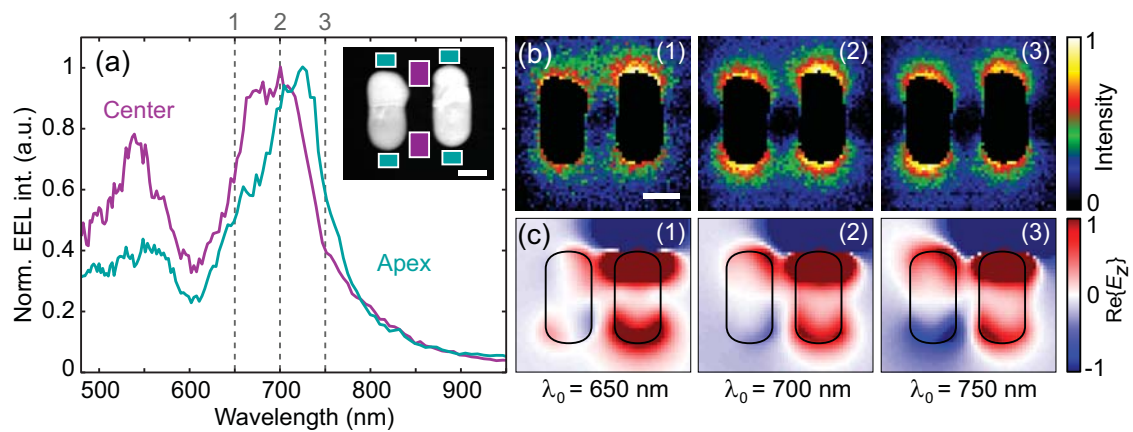


Figure 10.11: EELS spectra taken at the apices (cyan curve) and in the center (magenta curves) of the size 2 dimer. The spectral collection areas are indicated in the STEM image (inset). (b) EELS excitation maps at $\lambda_0 = 650, 700,$ and 750 nm respectively. (c) E_z near-field images of the dimer from FDTD when excited by a vertical point dipole source 10 nm away from the apex. The driving field of the dipole has not been removed from the image so in order to see the induced fields on the dimer the colorscale has been saturated by a factor 300 . Scale bars are 50 nm.

11

Deep-subwavelength imaging of the modal dispersion of light

Numerous optical technologies and quantum optical devices rely on the controlled coupling of a local emitter to its photonic environment, which is governed by the local density of optical states (LDOS). Although precise knowledge of the LDOS is crucial, classical optical techniques fail to measure it in all of its frequency and spatial components. In this Chapter, we use a scanning electron beam as a point source to probe the LDOS. Through angular and spectral detection of the electron-induced light emission, we spatially and spectrally resolve the lightwave vector and determine the LDOS of Bloch modes in a photonic crystal membrane at an unprecedented deep-subwavelength resolution (30 – 40 nm) over a large spectral range. We present a first look inside photonic crystal cavities revealing subwavelength details of the resonant modes. Our results provide direct guidelines for the optimum location of emitters to control their emission, and key fundamental insights into light-matter coupling at the nanoscale.

11.1 Introduction

The LDOS is a key fundamental quantity involved in light-matter interaction, as it provides a direct measure for the probability of spontaneous light emission [263]

and light scattering [264, 265]. Recent advances in nanostructuring of photonic materials have allowed tailoring of the LDOS at the nanoscale, thereby enabling many new applications in lighting, displays, light management in solar cells, quantum optics and information technology. Light-matter coupling, either to the far field or to well-defined optical modes, is maximized when the source is placed at a position where the LDOS is highest. Key demonstrations of this effect are, for example, the enhanced spontaneous emission of quantum dots in the field maximum of a photonic crystal cavity [266, 267] or the directional emission in the proximity of a metallic nanoantenna [39].

Photonic crystals are key geometries that have been studied for many years in this respect, as they provide full control over the dispersion of light by engineering the momentum of light $\mathbf{k}(\omega_0)$. Furthermore, photonic crystal cavities [268] have shown strong confinement of light, leading to nanoscale on-chip lasers, light-emitting diodes and platforms to probe the quantum interaction between light and matter [27]. In a photonic crystal the subwavelength scale modulation of the dielectric constant results in large spatial and frequency variations of the LDOS, corresponding to either strongly inhibited or enhanced light emission at well-defined emitter locations and frequencies. A full understanding of light-matter interaction requires the mapping of the LDOS $\rho(\mathbf{r}, \mathbf{k}, \omega_0)$ in space, momentum and frequency. So far, most methods to determine the LDOS are based on measurements of the modification of the spontaneous emission rate of optical emitters (the Purcell effect). According to Fermi's golden rule the fluorescence decay rate Γ of a single dipole is proportional to the position- and frequency-dependent LDOS $\rho_{\hat{\mathbf{p}}}(\mathbf{r}, \omega_0)$, projected onto the dipole direction $\hat{\mathbf{p}} = \mathbf{p}/|\mathbf{p}|$. Spatially resolved LDOS measurements using this technique require scanning a moveable probe with an optical emitter at its end, such as a fluorescent dye [122], a diamond nanocrystal [269] or a polymer sphere [17], over the optical modal landscape while measuring its fluorescence decay. Pioneering LDOS maps have been recently achieved in this way [17]. Alternatively, in the reciprocal configuration, the photonic structure can be scanned over a fixed dipole emitter. In the last method, the LDOS near metallic nanoantennas [111] and photonic crystals [270][13] has been probed. Conventional passive near-field scanning optical microscopy can also be used to map the LDOS (Refs. [271–273]), but it is restricted to the momentum collected by the tip, and to the spatial resolution of the physical size of the tip aperture of ~ 100 nm. Major disadvantages of the LDOS scanning probe techniques include that they are experimentally challenging, slow and limited by the narrow spectral width, and photobleaching of the light source. Moreover, the fluorescent probe itself potentially affects the LDOS landscape. More importantly, whereas all of the above techniques focus on the spatial dependence of the LDOS, they ignore an equally important aspect of local mode imaging, that is, the determination of the local momentum of light. By collecting the angle-resolved emission spectrum, and thus determining the in-plane wave vector of the emitted light, a wealth of information regarding the photonic band structure and the nature of local modes can be collected [98]. Together, despite numerous experimental efforts, an accurate broadband, non-

invasive technique to determine the LDOS and optical momentum distribution in two-dimensional photonic structures at deep-subwavelength resolution is still elusive.

In this Chapter, we use a scanning electron beam as a point dipole source to probe the LDOS in space, frequency and momentum. Compared with usual fluorescent probes, the created cathodoluminescence probe exhibits a broad spectral range, precise localization down to 30 – 40 nm and no bleaching, therefore allowing us to record high-resolution LDOS maps and reconstruct the optical momentum distribution. Cathodoluminescence originates from the coupling of a high-energy electron's external field to the local modes of a photonic structure. This leads to the generation of cathodoluminescence in the form of transition radiation when the electron crosses an interface or Cherenkov radiation when it moves faster than the speed of light in a medium [63]. The energy and momentum required to excite cathodoluminescence are provided by the kinetic energy and momentum of the electron, and correspond to a very broad excitation spectrum ranging from the ultraviolet to the far-infrared. In practice, the interaction of the electron with the medium can be represented by a transient dipole aligned along the electron trajectory and placed at the electron impact position (transition radiation) or along the electron path (Cherenkov radiation). For a given material, this transient dipole has a constant amplitude but importantly the power dissipated by the electron depends on its local photonic surrounding. This way, it is sensitive to the optical mode density at the impact location [63] and its radiated power is given by $P = (\pi\omega_0^2)/(12\varepsilon_0|\mathbf{p}|^2)\rho_{\hat{\mathbf{p}}}(\mathbf{r},\omega_0)$, where \mathbf{p} is the dipole moment of the induced dipole, ε_0 is the surrounding dielectric constant and $\rho_{\hat{\mathbf{p}}}(\mathbf{r},\omega_0)$ is the radiative part of the projected LDOS. A measurement of the total radiated emission would then directly probe the LDOS $\rho_{\hat{\mathbf{p}}}(\mathbf{r},\omega_0)$. More precisely, at 30 keV electron energy, the observed light emission is a measure of the LDOS component projected onto a single direction along the electron trajectory, which is the direction of the transient dipole [103]. One clear demonstration of this is the fact that angle-resolved measurements of cathodoluminescence on a planar Au surface show a radiation pattern that is identical to that of a z -oriented point dipole placed at the Au surface (see Chapter 3). Moreover, the obtained intensity is a measure of the radiative component of the LDOS, completely unaffected by non-radiative decay channels, in contrast to standard optical probe methods, demonstrating the only technique to our knowledge that probes a pure vectorial component of the radiative LDOS.

11.2 Imaging delocalized photonic crystal modes

So far, cathodoluminescence spectroscopy has mostly been used to investigate optical modes in metallic nanostructures such as nanoparticles and nanodiscs where it excites either local dipolar or higher-order modes [64, 98, 104, 157, 226]. Here, we demonstrate the excitation, by the electron beam, of Bloch modes and localized modes in a two-dimensional dielectric photonic crystal. In the experiment, a 30

keV electron beam is scanned over the surface of a hexagonal photonic crystal composed of holes in a 200-nm-thick Si_3N_4 membrane (refractive index $n \approx 2.0$) supported by a Si wafer. At every electron beam position, the emitted light spectrum is collected using a parabolic mirror placed between the sample and the microscope pole piece (Fig. 11.1(a)) and a two-dimensional map of the photonic crystals LDOS $\rho_{r,\hat{z}}(x, y)$ is recorded. Momentum spectroscopy is carried out by collecting the angular distribution of the emitted light at precise electron beam positions on the photonic crystal (see Chapters 2 and 3 for details on the experimental setup).

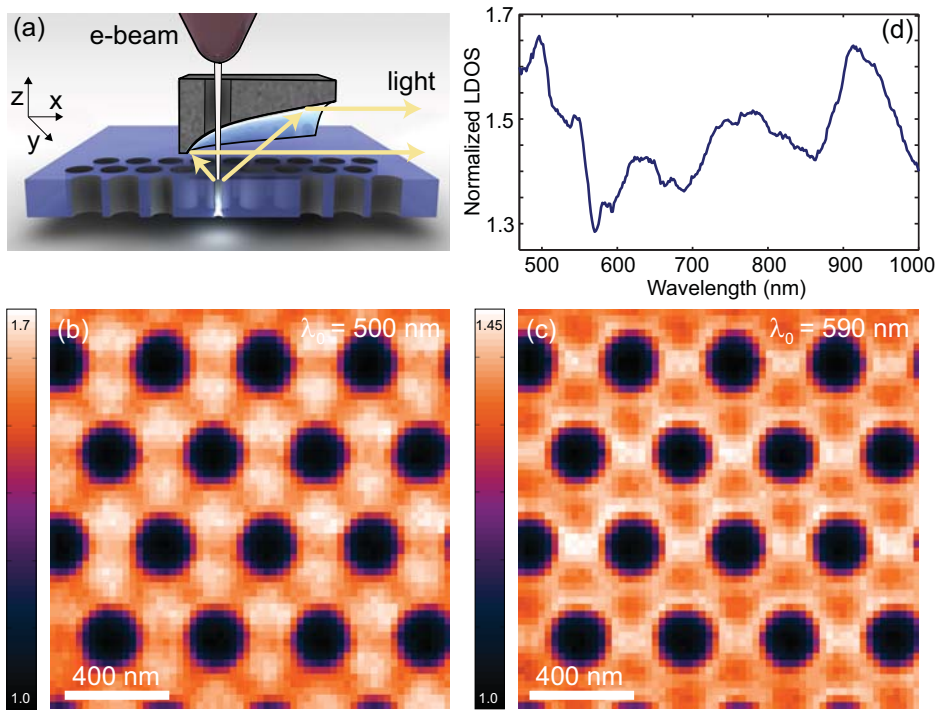


Figure 11.1: High-resolution LDOS mapping on two-dimensional photonic crystals. (a) Sketch of the experimental set-up: an electron beam is incident on the sample surface, generating optical radiation that is collected by the mirror placed above the sample and sent to an optical spectrometer or to an imaging CCD (charge-coupled device) camera. Scanning of the electron beam allows for deep-subwavelength spatial mapping of the LDOS. (b,c) LDOS maps of a photonic crystal Si_3N_4 membrane with a lattice constant $a = 400 \text{ nm}$ and a hole diameter of 230 nm in the high-energy bands at a wavelength of 500 nm ($a/\lambda_0 = 0.8$) and 590 nm ($a/\lambda_0 = 0.68$), respectively. The Bloch modes are visible in their periodic LDOS modulation, they are delocalized over the full crystal and have the same symmetry as the lattice. (d) LDOS spectrum taken in the center between three holes, normalized by the cathodoluminescence emission from an unstructured membrane reference. The Bloch modes modulate the LDOS by 30%. The LDOS maps are the raw data without any background subtraction, corrected only for system response and are integrated over a 9 nm bandwidth.

Figures 11.1(b,c) show LDOS images of the photonic crystal with a lattice constant of $a = 400 \text{ nm}$ and a hole diameter of 230 nm , at collection wavelengths of 500 nm and 590 nm . These wavelengths correspond to frequencies above the first bandgap

for this photonic crystal ($a/\lambda_0 = 0.8$ and 0.68 , respectively, with a being the lattice constant). The periodic pattern of holes is clearly visible as the dark circles at which no emission is excited. The image clearly shows that the modes are fully delocalized over the photonic crystal with the periodicity of the photonic crystal unit cell. The LDOS images are very distinct for the two wavelengths, with LDOS hotspots observed in the triangular regions between the holes for $\lambda_0 = 500$ nm and LDOS maxima around the hole circumferences for $\lambda_0 = 590$ nm. Figure 11.1(d) shows the cathodoluminescence spectrum taken at the symmetry point between three holes. The maximum LDOS variation observed across the images in Figs. 11.1(b,c) is $\sim 30\%$ of the average value.

11.3 Momentum spectroscopy in photonic crystals

Momentum spectroscopy at various wavelengths, by exciting the photonic crystal in the symmetry point between three holes, is presented in Fig. 11.2. Complex angular emission patterns are observed for the photonic crystal with a hexagonal symmetry as expected. As in the spatial maps of Fig. 11.1(b,c), very distinct patterns are observed for the two wavelengths of 500 and 600 nm (collected bandwidth ~ 40 nm), reflecting the different modal distributions. The momentum spectroscopy maps are portions of the isofrequency surfaces, plotting the allowed \mathbf{k} at a given ω_0 : dark areas correspond to forbidden in-plane momenta in the crystal, whereas bright peaks correspond to the in-plane momentum of photonic crystal eigenmodes [265]. Momentum spectroscopy provides key information beyond just the band diagram, as it probes the momentum of light at all angles and not only along the symmetry directions, and could thus be very useful to study negative refraction, self-collimation and light localization in both periodic and aperiodic systems.

11.4 Localized mode in an H1 photonic crystal cavity

Even larger LDOS variations can be achieved with a localized mode in a photonic crystal cavity. Figure 11.3(a) shows a scanning electron microscope (SEM) image of a single-hole defect (H1) cavity in a photonic crystal with a lattice period of $a = 330$ nm and a hole diameter of 230 nm. In Fig. 11.3(b) the LDOS image is taken at a wavelength of $\lambda_0 = 650$ nm ($a/\lambda_0 = 0.51$), corresponding to the cavity resonance frequency inside the photonic bandgap. At this wavelength, the image shows a strongly confined localized mode inside the cavity. The LDOS is imaged with unparalleled resolution, here revealing features of $\sim 70 - 80$ nm width, with a spatial resolution of $30 - 40$ nm (see below). A LDOS hotspot is observed at the cavity center, and further maxima are observed on either side of the six hexagonal spokes extending outwards. Momentum spectroscopy for this cavity is shown in Fig. 11.3(c) by exciting the cavity in the center. A hexagonally shaped angular emission pattern is observed, with a dominant maximum for emission normal to the

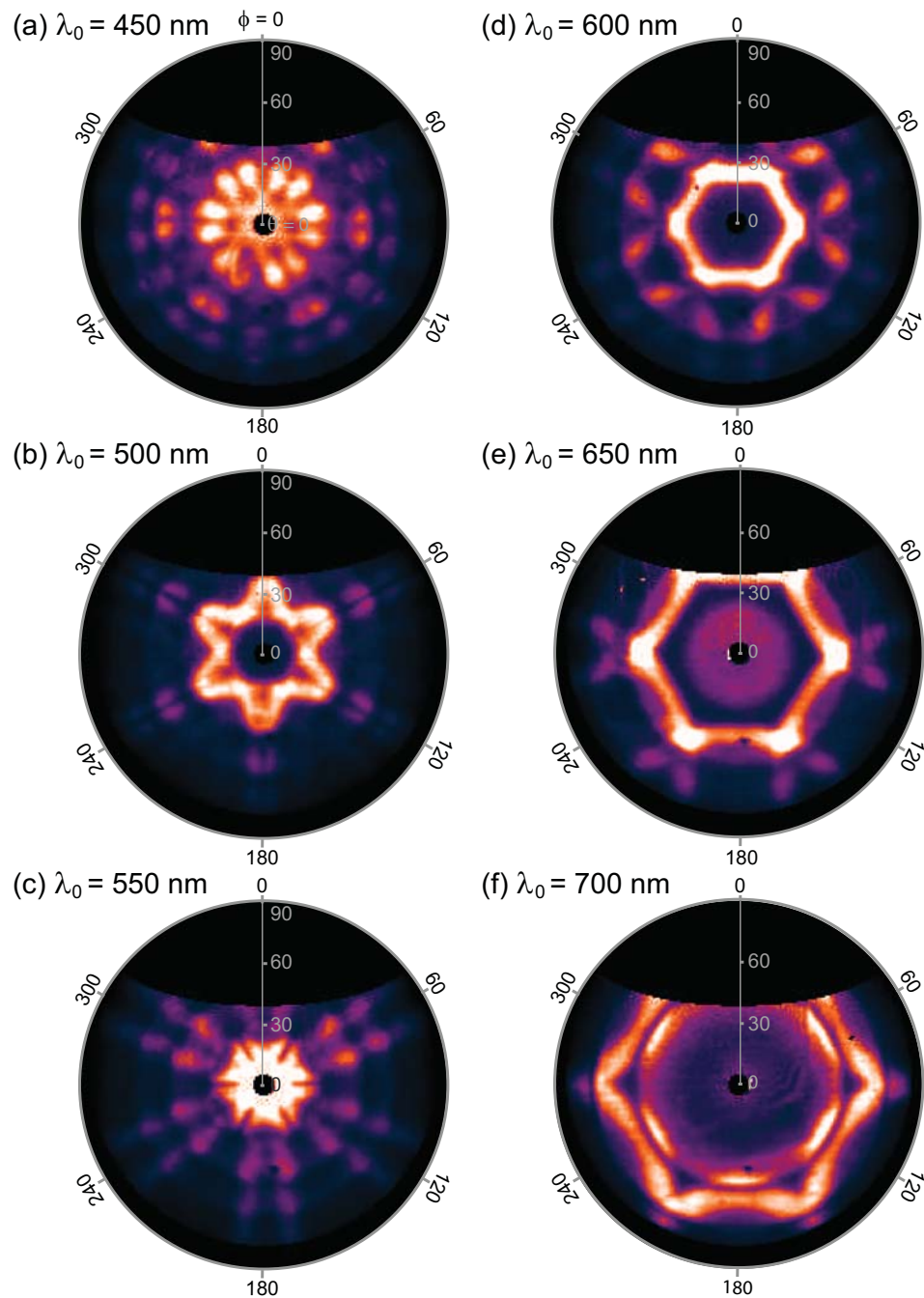


Figure 11.2: Momentum spectroscopy of a two-dimensional photonic crystal. Angular emission patterns from a photonic crystal at different wavelengths (collected bandwidth $\sim 40 \text{ nm}$) by exciting the photonic crystal in the symmetry point between three holes. The images at a wavelength of 500 and 600 nm correspond to the spatial LDOS maps in Figs. 11.1(b,c). Azimuthal (ϕ) and polar (θ) angles are indicated. The hexagonal symmetry is clearly visible as well as an increasing number of polar peaks for higher energies. The black area at the top and the black circle in the center of the images correspond to angular ranges that are not collected by the mirror.

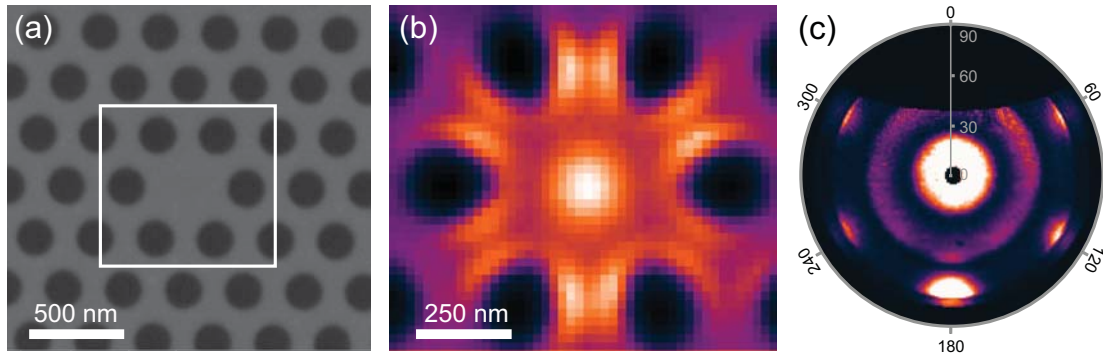


Figure 11.3: LDOS maps and momentum spectrum of a H1 photonic crystal cavity. (a) Secondary electron microscopy image of a photonic crystal membrane with a hole defect (H1 cavity) with a lattice constant $a = 330$ nm and a hole diameter of 230 nm. (b) LDOS image of the cavity (outlined area in (a)) at a wavelength of 650 nm, with a bandwidth of 9 nm. (c) Angular emission pattern when the cavity is excited in its center (collection bandwidth ~ 40 nm). The hexagonal momentum distribution shows a maximum around $k_{\parallel} = 0$ and a hexagonal pattern of lobes.

sample, corresponding to zero in-plane momentum (the black spot in the center for $\theta < 5^\circ$ is due to the hole in the mirror). These are the k components of a localized mode with a large k distribution [274]. k -space engineering, and in particular suppression of the k components close to $k_{\parallel} = 0$ that couple to the light cone, is one of most important techniques to increase the Q value of photonic crystal cavities [275]. Figure 11.3(c) also shows a weaker emission band around a polar angle of $\theta = 45^\circ$. This band is also observed in the angular pattern measured on an unstructured Si_3N_4 membrane (Fig. 11.4(f)) and is attributed to the interference of light emitted from the top and bottom of the membrane, the latter being reflected upwards by the Si substrate 1 μm below the membrane.

11.5 Localized modes in an L3 cavity

Figure 11.4(a,b) shows the LDOS maps for a larger photonic crystal cavity composed of a linear three-hole (L3) defect. Data are taken at two wavelengths corresponding to the two resonant modes observed in the LDOS spectrum of Fig. 11.4(c). The LDOS distributions of the two modes are very distinct and reflect their quasi-orthogonality. At $\lambda_0 = 649$ nm spatially narrow LDOS hotspots are observed around the inner cavity edges near the holes, whereas at 681 nm three LDOS hotspots are observed near the positions of the three missing holes (see Supplementary Fig. 11.6(a) for spectrum near a hole and in the center of the cavity). In the latter hotspots the LDOS is increased by a factor of 2 as compared to an unstructured membrane. This corresponds well to the value calculated from the Purcell formula $\rho_{max}(\lambda_0) = 3/4\pi^2(\lambda_0/n)^3 \times Q/V_{eff} = 1.9$ assuming a mode volume V_{eff} of $0.7 (\lambda_0/n)^3$ and $Q \approx 10$ derived from the linewidth of the

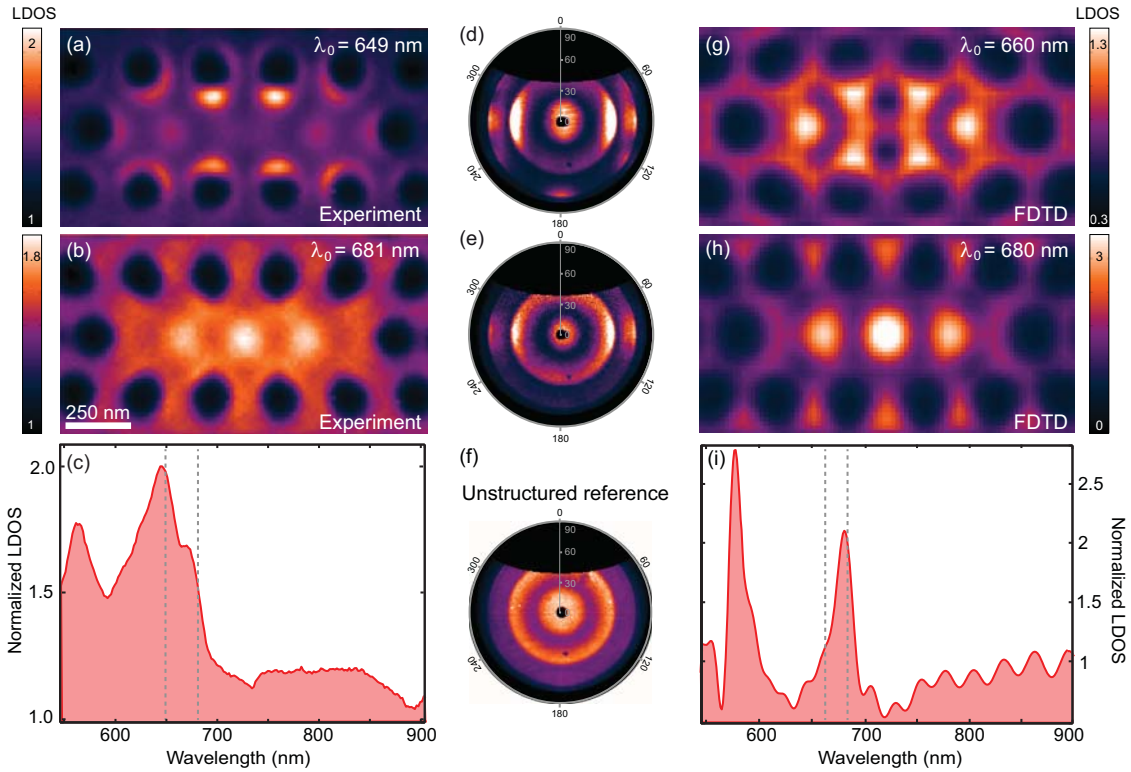


Figure 11.4: Mapping multiple cavity modes of an L3 photonic crystal cavity. (a,b) Measured LDOS maps of an L3 photonic crystal cavity (lattice period $a = 330$ nm, hole diameter $a = 230$ nm) at the frequency of the two cavity modes, 649 and 681 nm, respectively, with a bandwidth of 9 nm. (c) Measured cavity resonance spectrum measured in the centre of the cavity normalized to the spectrum of an unstructured membrane. The cavity modes exhibit an increase of LDOS of a factor of ~ 2 at the resonance location. (d,e) Measured angular emission patterns at the two resonance frequencies. The long axis of the cavity is parallel to the horizontal direction along $\phi = 90^\circ$ and 270° . The cavities exhibit clear directional emission peaks, at 90° and 270° for both wavelengths. (f) The vague circular pattern in the background is attributed to the interference of light emitted from the cavity with light reflected by the silicon substrate, as also observed for a reference unstructured membrane. (g,h) Calculated LDOS maps for the same experimental parameters (see Methods). The theoretical maps exhibit the same symmetry and similar LDOS distribution as in the experiments. (i) The LDOS spectra calculated in the middle of the cavity; two peaks are visible, at around 600 and 680 nm. The vertical dotted lines in (c) and (i) indicate the position of the LDOS maps shown above.

resonances, obtained from the half-profile of the spectral peak at 681 nm in the LDOS spectrum (Fig. 11.4(c)). These low Q values are expected as out-of-plane dipoles experience a much weaker cavity than in-plane ones, for which the bandgap is maximized in a membrane geometry. Further spectral measurements performed at lower electron energy (5 keV) indicate the probing of x , y and z LDOS components, with stronger coupling to in-plane directions, revealing sharper and higher peaks (see Supplementary Fig. 11.6). Numerical calculations, performed by three-dimensional finite-difference time-domain methods, of LDOS spectral maps

are presented in Fig. 11.4(g-i). The experimental spectral peaks in Fig. 11.4(c) are differently shaped than in the theoretical curve in Fig. 11.4(i), which we attribute to a small mismatch between the simulated and measured geometry. The spatial maps in Fig. 11.4(g,h) show the same symmetry and similar LDOS distributions as the measured ones in Fig. 11.4(a,b). Clearly, these high-resolution LDOS maps provide a direct guideline for the optimum locations at which emitters at a certain wavelength would be coupled to the corresponding cavity mode. The momentum spectroscopy maps for the two cavity modes are shown in Fig. 11.4(d,e) for the two resonance frequencies. These data are taken by positioning the electron beam at a LDOS maximum corresponding to each distinct mode. The more complex nature of these cavity modes, compared with the H1 cavity in Fig. 11.3, is directly reflected in the angular emission maps. A strong asymmetry in the emission is observed, with intense lobes at azimuthal angles $\phi = 90^\circ$ and 270° , peaking at a polar angle around $\theta = 53^\circ$. This emission is attributed to the constructive interference of radiation emitted from the linear cavity in the far field, in a way similar to what is observed for standing waves along metallic wire antennas [144] (also see Chapter 5).

11.6 Spatial resolution estimate

The resolution of the LDOS imaging technique is determined by the spot size of the electron beam and the radial extent of the evanescent field around the electron beam trajectory. The first is determined by the electron optics of the electron microscope, and is 1 – 10 nm for a typical SEM. For cathodoluminescence, to increase the signal-to-noise ratio and avoid nanoscale sample drift during the measurement, it is advantageous to use a relatively high beam current (10 nA), in which case the electron beam spot diameter is about 10 nm. The radial extent of the magnetic field around the electron beam trajectory are given by:

$$\mathbf{H}(\mathbf{r}, \omega_0) = -\frac{2e\omega_0}{vc\gamma} K_1\left(\frac{\omega_0 R}{v\gamma}\right) e^{i\omega_0 z/v} \hat{\phi} \quad (11.1)$$

where R is the distance from the electron trajectory, z is the position along the trajectory, e is the electron charge, ω_0 is the frequency, v is the electron velocity, c is the speed of light in vacuum, $\gamma = 1/\sqrt{1 - \epsilon v^2/c^2}$ is the Lorentz contraction factor in which ϵ is the relative permittivity of the medium, $\hat{\phi}$ is the azimuthal unit vector and K_1 is the modified Bessel-function of the second kind. The radial electric field drops off in a similar way to the magnetic field whereas the vertical component drops off as a K_0 Bessel function. Details of the derivation of Eq. 11.1 are given in Ref. [63]. Equation 11.1 is a diverging function for $R = 0$, and thus represents a very high potential spatial resolution. Taking into account the delocalized character of the material response, an upper limit of the resolution is given by the $1/e$ decay distance ($v\gamma/2\omega_0$) of the K_1 function in Eq. 11.1. For a perfectly focused 30 keV electron beam, this corresponds to a $1/e$ distance of 17 nm at a wavelength of 600 nm (Ref. [276]). A corresponding Gaussian function has $\sigma = 11$ nm and a full-width

at half-maximum (FWHM) of 26 nm. For a perfectly focused electron beam, the LDOS resolution at 30 keV thus is < 26 nm. For a typical electron beam spot diameter of 10 nm FWHM, the theoretical spatial resolution then is < 36 nm, depending on the electron beam profile.

To measure the spatial resolution in our set-up we measured the cathodoluminescence intensity along a sharp edge between a Si membrane and air and compared it to the SEM image taken in the same scan. Figure 11.5(a) shows the cathodoluminescence intensity at wavelengths in the range 500 – 900 nm along a line scanned across a 150 nm square hole in a Si membrane, whose SEM image is shown in Fig. 11.5(c). Figure 11.5(b) (open dots) shows a line-scan of the cathodoluminescence intensity at a wavelength of 600 nm. The signal from a single hole is dominated by the transition radiation at the boundary between vacuum and silicon, where the LDOS is increased. In the visible range we do not observe a clear spectral peak signature of a dielectric hole resonance. The cathodoluminescence signal shows a sharp transition at the edge, decreasing from 90% to 10% over a distance of 33 nm. Fitting a Heaviside step function with a Gaussian resolution function on both edges (solid line) we find an average standard deviation (s.d.) in the cathodoluminescence measurement of $\sigma_{CL} = 21$ nm. This measured value thus provides an upper limit of the s.d. of the LDOS resolution. It is determined by the electron beam spot size, the effective width of the edge and the evanescent extent of the field around the electron beam trajectory. The first two terms can be estimated from a line-scan of the secondary electron signal across the edge, which is also shown in Fig. 11.5(b): the corresponding s.d. is $\sigma_{SEM} = 11$ nm. Deconvoluting the two signals we find the electron beam interaction width to be represented by a s.d. of $\sigma = 13$ nm, close to the theoretical value of $\sigma = 11$ nm. This value corresponds to a FWHM of the corresponding Gaussian distribution of 30 nm. Taking into account the electron beam spot diameter of ~ 10 nm the resolution then is 30 – 40 nm, depending on the electron beam profile. The measured value is in excellent agreement with the theoretical resolution of < 36 nm calculated above.

To illustrate that the width of features in cathodoluminescence scans is most often determined by the physical width of the LDOS profile, we measured the cathodoluminescence signal across a narrow free-standing 200-nm-wide, 200-nm-thick Si strip, made using electron-beam lithography and etching of a free-standing Si membrane. This structure acts as a nanoscale Fabry-Pérot cavity with a first-order resonance at 620 nm, determined by the strip width and refractive index. Figure 11.5(d) shows the result of the spectral LDOS measurement. The sharp resonance leads to a strongly enhanced LDOS at the resonance field maxima at the end facets of the cavities, as is clearly seen in Fig. 11.5(d). A line-scan through these sharp features is shown in Fig. 11.5(e) together with a line-scan through the corresponding secondary electron intensity (Fig. 11.5(f)). The FWHM of the cathodoluminescence peaks is 48 nm. Given that the spatial resolution of cathodoluminescence is 30 – 40 nm (see above), this width is also determined by the width of the LDOS profile of the resonant mode on the Si strip. Similarly, the narrowest features in the LDOS measurements on the Si_3N_4 membrane in Fig. 11.4(a), close to the hole

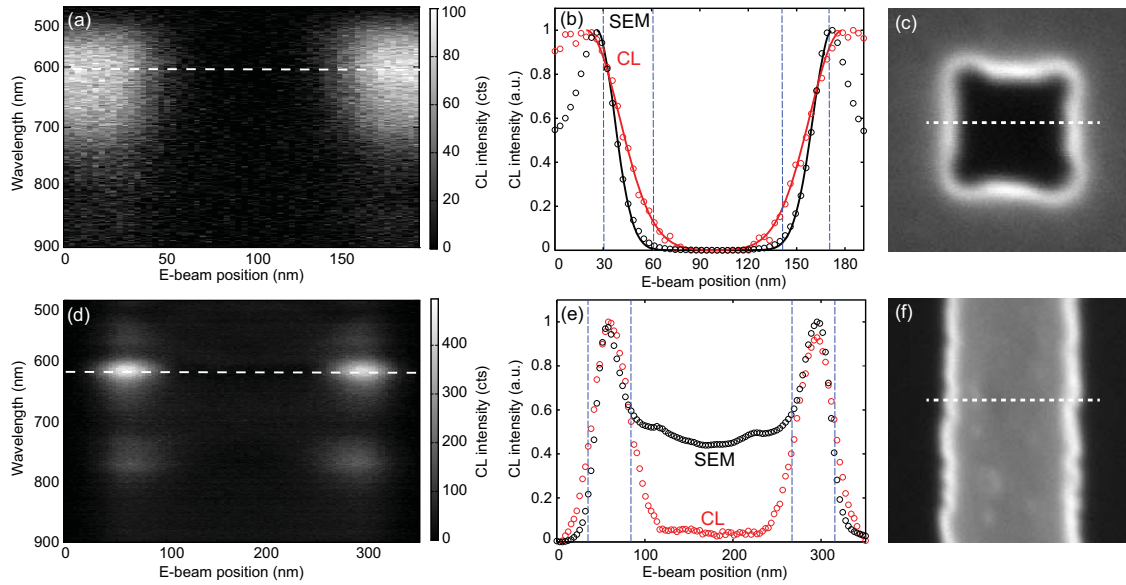


Figure 11.5: Resolution assessment. (a-c) Line-scans over a 150 nm square hole in a silicon membrane. (b) shows the line-cut of the LDOS at the wavelength of 600 nm as compared with the SEM topology line-cut. CL, cathodoluminescence. The LDOS signal drops from 10% to 90% in 33 nm, following the topology, which drops from 10% to 90% in 21 nm. (d-f) Plots of the measurements performed on the opposite geometry of a silicon membrane nanostrip. Such a system supports sharp spectral resonances that are spatially localized at the edges of the strip. These sharp features are compared in e to the SEM topology image. Their width at half-maximum is 48 nm. In (b,e) the open dots are the measured data, and the solid lines are the result of the fit. The blue vertical lines show the 90 – 10% signal drop. In (a,c,d,f) the white dotted line shows the spectral and spatial position of the line-cut. Measurements were made using 3 nm steps in the electron beam position.

edges, have a FWHM of ~ 70 nm, again limited by the physical width of the LDOS profile.

The LDOS imaging we present here, like all spectroscopic techniques, has some limits. LDOS can be probed only in a polarizable medium and not in, for example, the holes of the photonic crystal. The analysis presented here is made for planar samples, for which the electron beam is incident normal to their surface, and so far an extension to three dimensions is lacking. Exotic emission components propagating close to the sample surface could escape the numerical aperture of the detection and therefore their contribution would be underestimated. Last, high-quality LDOS measurements require a (weakly) conducting non-luminescent substrate such as Si or Si_3N_4 to prevent sample charging on electron beam irradiation as well as unwanted optical transitions that could blur the LDOS features.

11.7 Conclusions

We have resolved the LDOS $\rho_{r,\hat{z}}(x, y, \omega_0, \mathbf{k})$ in a two-dimensional photonic crystal in the spatial, spectral and momentum domain using cathodoluminescence imaging spectroscopy. We demonstrate a deep-subwavelength resolution of 30 – 40 nm and background-free detection, in addition to angle-resolved detection capabilities that provide high-resolution momentum imaging. We provide high-resolution images of the propagating modes in the photonic crystal at frequencies above the photonic bandgap. In addition, we directly probe the modal distribution of localized modes inside photonic crystal defect cavities, measured at frequencies inside the bandgap. Momentum spectroscopy reveals the wave vectors for the propagating modes and confirms the nature of the localized modes. This work demonstrates that the angle-resolved cathodoluminescence technique is a very powerful method to resolve the photonic density of states locally in dielectric materials and may enable a wealth of further studies on light propagation and localization in complex photonic systems.

11.8 Methods

Sample. The photonic crystals have been made by structuring a poly (methyl methacrylate) (PMMA) resist by electron-beam lithography followed by reactive ion-etching of the Si_3N_4 membrane. The 200-nm-thick membrane was spaced 1 μm from the silicon substrate by a sacrificial silica layer that has been removed using hydrofluoric acid etching. The samples used for the assessment of the resolution were made in a 200-nm-thick free-standing Si membrane using a combination of electron-beam lithography, reactive ion etching and wet etching (see SEM image in Fig. 11.5(c)).

Numerical simulations. The LDOS of the structure has been calculated by three-dimensional finite-difference time-domain methods, by using the commercial software FDTD Solutions from Lumerical Solutions [228]. LDOS maps are obtained by probing the structure with a z -aligned electrical point dipole at a height of 1 nm above the structure and by recording the emitted power as a function of the dipole position and of its emission frequency. The resulting LDOS maps are normalized by the LDOS simulated for a homogeneous slab.

11.9 Supplementary information

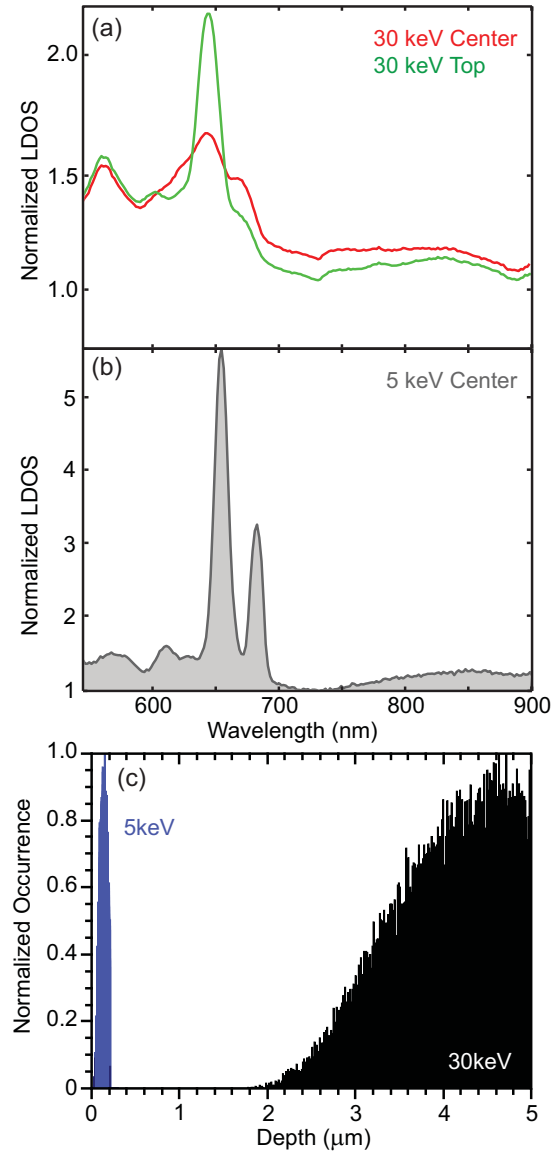


Figure 11.6: Spectral evolution of the LDOS measured in the center of the cavity and on the top part, below one of the holes. (a) LDOS measurement at an electron energy of 30 keV, compared with (b) LDOS measurement at an electron of energy 5 keV. At higher energy the LDOS variations are smoother and weaker, while at low voltage the two resonance are very sharp and twice as high. The strong double-peak profile at 5 keV indicates a partial mixing of xyz LDOS components, which results in larger variations. (c) Simulation of the electron beam propagation depth calculated using the Monte Carlo program Casino [277]. The 30 keV electrons are transmitted through a 200 nm thick membrane while 5 keV are strongly scattered in first few 100 nm.

12

Resonant modes of single silicon nanocavities excited by electron irradiation

High-index dielectric or semiconductor nanoparticles support strong Mie-like geometrical resonances in the visible spectral range. We use angle-resolved cathodoluminescence imaging spectroscopy to excite and detect these resonant modes in single silicon nanocylinders with diameters ranging from 60 to 350 nm. Resonances are observed with peak-wavelengths in the range of 400 – 700 nm, and show a strong red shift with increasing cylinder diameter. The photonic wave function of all modes is determined at deep-subwavelength resolution and shows good correspondence with numerical simulations. An analytical model is developed that describes the resonant Mie-like optical eigenmodes in the silicon cylinders using an effective index of a slab waveguide mode. It shows good overall agreement with the experimental results and enables qualification of all resonances with azimuthal ($m = 0 - 4$) and radial ($q = 1 - 4$) quantum numbers. The single resonant Si nanocylinders show characteristic angular radiation distributions in agreement with the modal symmetry.

12.1 Introduction

nanoparticles and nanowires made from high-index semiconductor or dielectric materials have the ability to strongly confine and scatter light [195, 278–280]. These

properties make them interesting for a large range of applications including solar cells [30, 281–289], lasers [290], and nanoscale photodetectors or sensors [151, 291–294]. Unlike their metallic counterparts, where light is confined to the surface in the form of surface plasmons, in semiconductor/dielectric nanostructures, light is mostly confined within the nanostructure. The resonant eigenmodes of these cavities are often referred to as Mie resonances, after the Lorentz-Mie-Debye solution to Maxwell’s equations, which can be used to describe scattering by wavelength-scale spherical nanoparticles in a uniform dielectric environment [195]. They can also be referred to as geometrical resonances because of their similarity to whispering gallery modes [282, 295].

Silicon is an ideal base material for resonant Mie cavities. Due to its high refractive index, it can strongly confine light, while its indirect electronic band gap leads to relatively low absorption losses. Due to the compatibility with CMOS fabrication processes, resonant Si Mie scatterers can be readily integrated into optoelectronic devices based on silicon. The first applications of silicon Mie scatterers in metamaterials [296–298], optical antennas [30, 31, 296, 299, 300], and anti-reflection coatings [30] are appearing just recently and show the great potential of Mie scatterers as optical building blocks in nanophotonic nanostructures and devices. To fully unleash the potential of these nanoscale Si light scatterers, detailed understanding of their fundamental scattering properties is essential. However, standard optical techniques have been unable to fully resolve the Mie resonant modes due to lack of spatial resolution.

In this Chapter, we study the resonant optical properties of individual silicon cylinders using angle-resolved cathodoluminescence (CL) imaging spectroscopy. With this technique, a 30 keV electron beam acts as a broad-band point source of light that can be employed to probe the optical properties of nanostructures with deep-subwavelength spatial resolution [63]. We determine the spectral and spatial characteristics of the resonant optical eigenmodes for single silicon nanocylinders with different diameters. We compare our results with finite-difference time-domain (FDTD) simulations and an analytical model, and we identify the fundamental and higher-order radial and azimuthal modes of the cavities. In addition, we present experimental data on the angular distribution and polarization of light emission from single resonant Mie cavities.

12.2 Sample fabrication

Figure 12.1(a) shows the geometry of the sample. Single Si nanocylinders were fabricated on a thin SiO₂ layer, supported by a Si substrate. The fabrication starts with a silicon-on-insulator (SOI) wafer with a 100 nm Si layer on a 300 nm SiO₂ layer. Electron beam lithography (EBL) is used to write circular pads as an etch mask in a negative tone resist. Next, anisotropic reactive ion etching (RIE) is used to etch down the top Si layer of the SOI wafer, such that Si nanocylinders are formed on top of the silica layer. Residual resist is removed using an oxygen plasma etch.

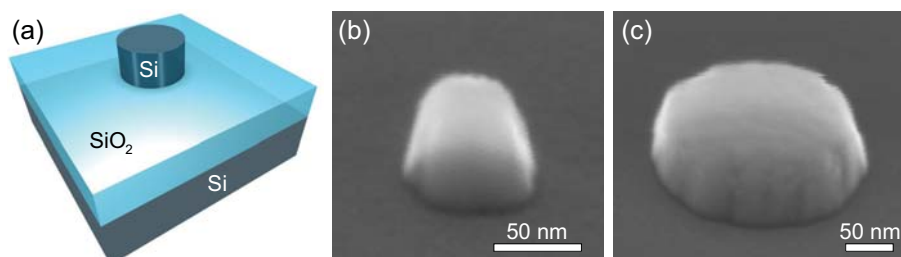


Figure 12.1: (a) Sketch of the sample geometry. Single silicon cylinders are fabricated on a thin silica layer, supported by a silicon substrate. SEM images of fabricated cylinders with base diameters of (b) 80 nm and (c) 200 nm. The cylinders are slightly tapered toward the surface.

The resulting cylinders have diameters ranging from 60 to 325 nm and are 100 nm high. Scanning electron micrographs of a small ($d = 80$ nm) and large ($d = 200$ nm) cylinder are shown in Fig. 12.1(b,c), respectively. From the electron micrographs, it can be seen that the cylinders are slightly tapered due to the non-perfect anisotropy of the Si etch but clearly resemble the intended cylindrical structure.

12.3 Imaging Mie modes in silicon cylinders

To measure the resonant optical properties of single cylinders, we use angle-resolved cathodoluminescence (CL) imaging spectroscopy (see Chapters 2 and 3 for details on setup). The electric field generated by a high-energy electron passing through a dielectric nanoparticle induces a transient vertically oriented polarization that results in the coherent excitation of the resonant modes supported by the Si nanocylinder at a rate that is proportional to the out-of-plane component of the local density of optical states (LDOS) [63, 75]. The excited local modes radiate into the far field; the radiation is collected by a parabolic mirror placed between the sample and the electron column, after which both the spectrum and the angular distribution are analyzed. Since the electron beam can be scanned at very high spatial resolution and the electron range is well beyond the thickness of the Si nanostructures, spatial information about the optical modes inside the nanostructures can be obtained far below the diffraction limit of light.

To probe the resonant optical response we raster-scan a 30 keV electron beam in 10 nm steps over a Si cylinder and collect a CL spectrum for each position. In parallel, we collect the secondary electron (SE) signal to obtain geometrical information about the cylinder (see insets in Fig. 12.2(a,b)). These data are used to define a spatial mask for the CL data, based on a threshold in SE counts, in order to select the pixels in the CL map corresponding to the Si cylinder.

The CL from the Si cylinders is superimposed on a broad background signal peaking at $\lambda_0 = 650$ nm due to CL from intrinsic defects in the SiO₂ matrix, which can vary slightly in intensity over time under electron beam illumination [89]. We

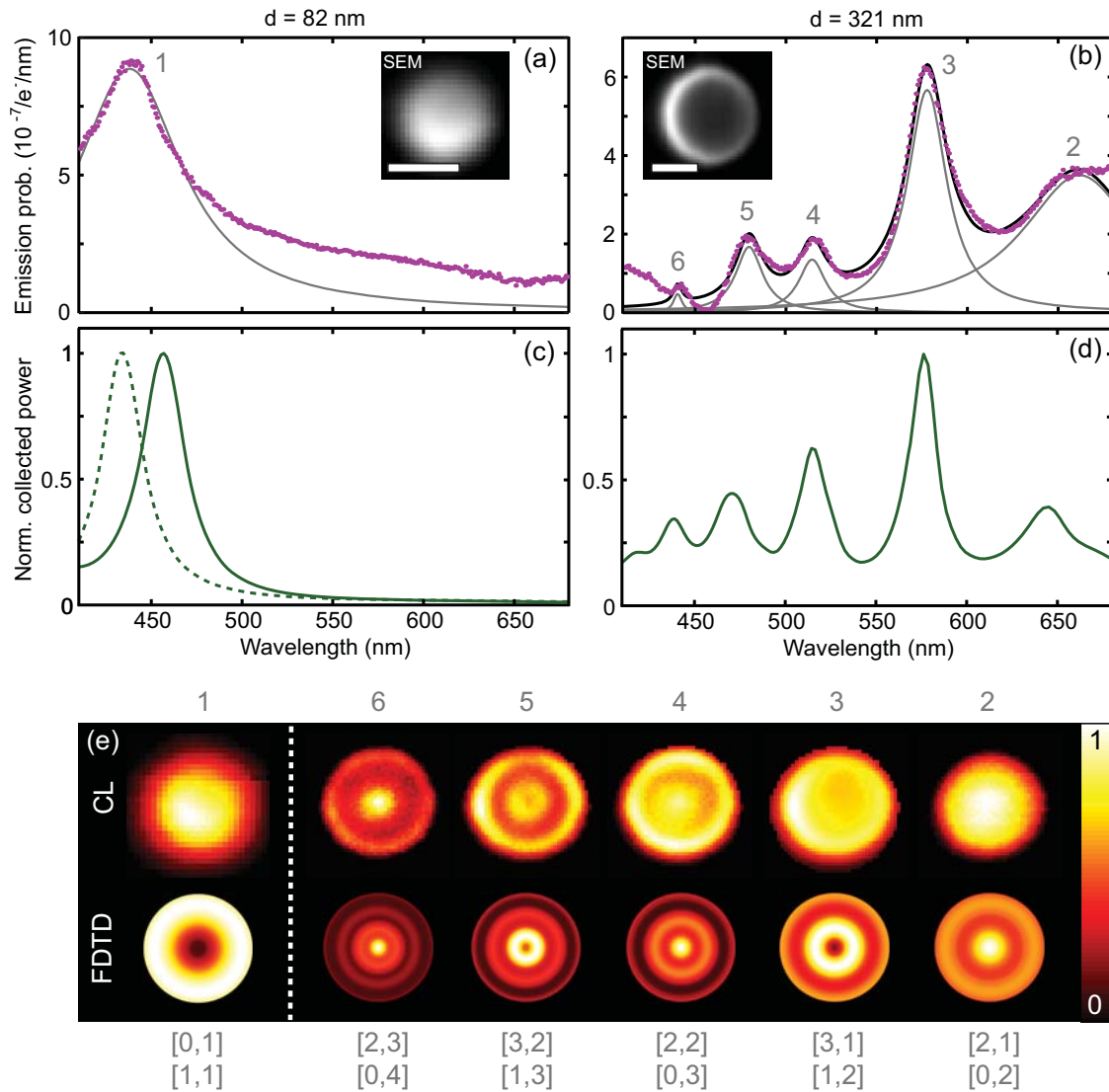


Figure 12.2: (a) Spatially integrated cathodoluminescence spectrum (purple dots) for an 82 nm diameter cylinder. A Lorentzian line shape is fitted to the spectrum (gray curve). The inset shows the secondary electron map collected simultaneously with the CL data collection (scale bar: 50 nm). (b) Similar measurement for a 321 nm diameter particle. The spectrum is fitted with a sum of five Lorentzians (black curve) that are also plotted individually (scale bar SEM image: 150 nm). (c) Normalized FDTD simulation of collected power as function of wavelength for 80 nm (solid green curve) and 70 nm (dashed green curve) cylinders. (d) Same as (c) for a 321 nm cylinder (solid green curve). (e, Top row) Two-dimensional CL intensity maps shown at resonance wavelengths indicated in (a) and (b), displaying the photonic wave functions of the different resonances. (e, Bottom row) Corresponding time-averaged intensity maps calculated using FDTD. The labels $[m, q]$ indicate the corresponding branches in Fig. 12.3(b) from the analytical model.

use a triangular interpolation routine to subtract this variable background from the CL signal from the cylinders (see Methods section). In the experimental geometry, the thickness of the SiO₂ layer was chosen as a compromise between minimizing background from the SiO₂ layer on the one hand and optical isolation of the Si cylinder from the high-index silicon substrate on the other hand.

Figure 12.2(a) shows the spatially integrated CL spectrum for an 82 nm diameter nanocylinder. A clear peak is observed in the spectrum at $\lambda_0 = 439$ nm corresponding to an optical resonance in the nanoparticle. For accurate determination of the peak wavelength, we fit a Lorentzian line shape to the spectrum, using a least-squares fitting routine (solid gray curve). From the width of the Lorentzian, we determine the quality factor of the resonance to be $Q = 6$. The magnitude of Q is determined both by absorption of light by the Si cylinder and radiative loss. Figure 12.2(b) shows the CL spectrum for a 321 nm diameter cylinder, which shows multiple peaks at $\lambda_0 = 440, 480, 515, 578,$ and 662 nm (labeled 2 – 6 in the figure, as will be discussed further on). Due to the larger diameter, this cylinder supports multiple resonant modes of different order within the experimental spectral range. The spectrum is fitted with a sum of five Lorentzians (black curve) which corresponds well to the measured spectrum. The quality factors derived from the individual fits are $Q = 77, 27, 29, 22,$ and 9 for modes with increasing wavelength. Note that the high quality factor of the first peak at $\lambda_0 = 440$ nm has a large uncertainty due to the low intensity with respect to the background signal. To study the spatial characteristics (*i.e.* the “photonic wave functions” of the resonant modes), we determined the two-dimensional excitation distribution at each resonance wavelength. To obtain sufficient signal-to-noise ratio, we integrate the spectra over a 20 nm bandwidth. Figure 12.2(e) (top row) shows these maps for the numbered peak wavelengths indicated in Fig. 12.2(a,b). For the small nanoparticle, the CL emission is observed from the entire nanoparticle, with an antinode (maximum) observed in the center. For the large cylinder, the spatial maps are more complex and consist of multiple rings and dots with alternating minima and maxima in the center, corresponding to resonances with higher radial mode orders, as will be discussed below.

12.4 Numerical modeling

Numerical modeling is performed using finite-difference time-domain (FDTD) simulations [228]. Single Si cylinders (diameter $d = 50 - 350$ nm, height $h = 100$ nm) are placed on a 300 nm thick SiO₂ layer on a Si substrate. In the simulations, the electron source is approximated by a single broad-band vertically oriented electric dipole positioned at 50 nm height inside the cylinder. Radiation from the cylinder into the upper hemisphere is collected using transmission monitors. To simulate a resonant spectrum, the dipole position is varied from the center ($r = 0$) to the outer radius of the cylinder ($r = d/2$), in steps of 5 nm. The collected power spectrum for each radius is then multiplied by $2\pi r$ to account for the cylindrical geometry; all

power spectra are summed, and the result is normalized to its maximum. Optical constants for Si and SiO₂ are taken from Palik [130].

The results for the 80 and 320 nm diameter cylinders are shown in Fig. 12.2(c,d), respectively, where the spatially integrated collected power (green solid lines) is shown as a function of free space wavelength. As in the experiment, the 80 nm cylinder clearly shows one single peak ($Q = 16$), corresponding to the lowest-order resonance, whereas the 320 nm cylinder shows many peaks due to higher-order resonances. Compared with the experiment for the 80 nm cylinder, the simulated peak wavelength is off by 18 nm. We attribute this to the small tapering of the cylinders, resulting in a slightly reduced diameter at the surface, as can be observed in Fig. 12.1(b,c). Indeed, the simulated spectrum for a 70 nm diameter (dashed line) matches the measured spectrum quite well. This indicates that the effective diameter of a particle with an 80 nm diameter base is 70 nm, in good correspondence with the SEM image in Fig. 12.2(a). The simulated spectrum for the 320 nm diameter particle in Figure 2d shows good agreement with the different resonances with the experiment. In agreement with the experiment, the simulated peak at $\lambda_0 = 575$ nm has the highest intensity. The simulated quality factor for the five modes is $Q = 21, 19, 24, 30,$ and 15 , which is in the same range as the experimental values, except for the small lowest-wavelength peak. The observed Q is determined by both absorption in the particle and the radiative coupling to the far field. Absorption losses are larger in the blue spectral range due the higher absorption of silicon in that wavelength range.

Fig. 12.2(e), bottom row, shows the simulated time-averaged photonic wave functions. Analogous to the experiment, the peak intensity is integrated over a 20 nm bandwidth around the peak wavelength for each dipole position, giving the peak intensity as a function of radial position. The data set is then rotated to obtain the two-dimensional photonic wave function maps. Simulations are shown for the 80 and 320 nm diameter cylinders for each resonance. The simulated photonic wave function of the lowest-order mode for the 82 nm cylinder (peak 1) shows a bright ring, while the measurement shows a more uniform distribution peaking in the center. For the 320 nm cylinder, the simulations show good agreement with the measured trends. For lower resonance wavelengths (going from peak 2 to peak 6), more nodes and antinodes are observed in the radial direction, corresponding to higher-order radial modes. For the highest-order mode (peak 6), a bright dot is observed in the center, surrounded by two bright rings. The alternating dark and bright center of the cylinder observed for subsequent resonances is also reproduced in the simulations.

12.5 Mode evolution as a function of particle diameter

From Figs. 12.2 and 12.3, it is clear that the resonant behavior of the cylinders strongly depends on the diameter. To gain more insight into the spectral mode evolution of the resonances for different sizes, we collected the CL spectra from 88

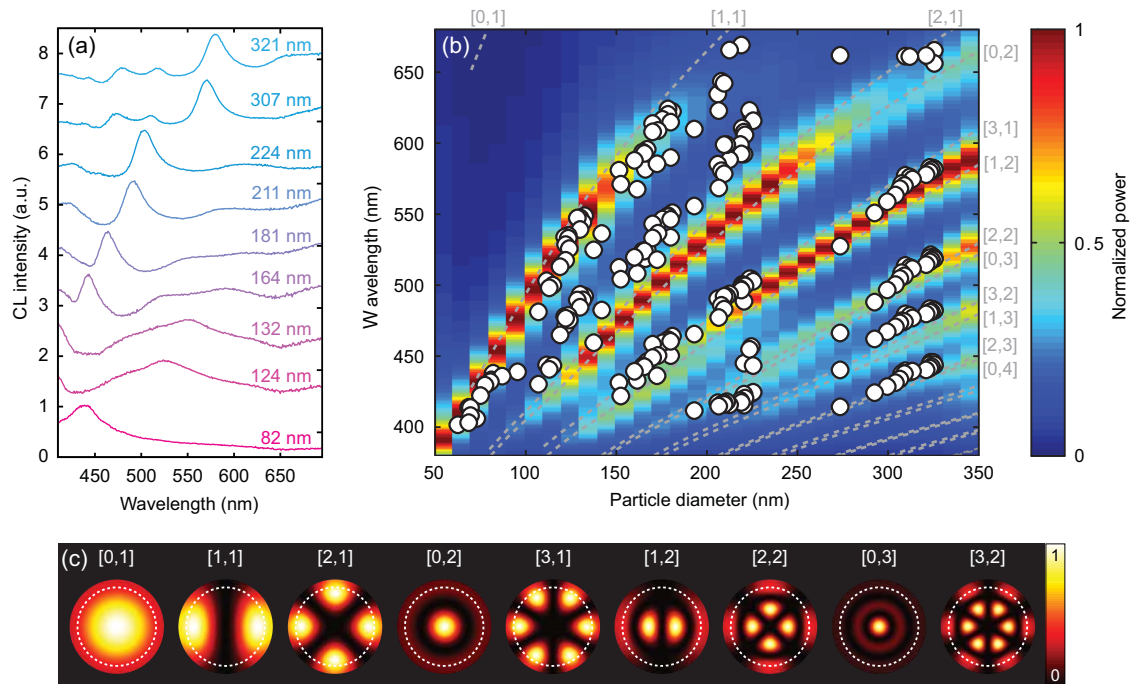


Figure 12.3: (a) Spatially integrated CL spectra for different cylinder diameters. The normalized spectra have been vertically offset for clarity. All resonances show a clear red shift for larger diameters. (b) Resonance peak wavelengths for different cylinder diameters obtained by fitting the CL spectra with Lorentzians (white dots). The color map shows the emitted power as function of particle diameter and wavelength, calculated using FDTD (normalized to its maximum for each particle diameter). The dashed gray curves correspond to the eigenvalues found for different diameter cylinders using the analytical 2D disk resonator model. Each curve is associated with a particular radial and azimuthal quantum number, indicated by the $[m, q]$ notations on the top and side of the figure. (c) Photonic wave functions for a $d = 320$ nm cylinder obtained from the analytical model. The time-averaged amplitude $|E_z(r, j)|^2$ is plotted. The white dashed circles indicate the edge of the particle.

different cylinders with diameters ranging from 60 to 325 nm. Fig. 12.3(a) shows a representative subset of this data set with spectra for different diameters. As the diameter increases, higher-order resonances emerge and all resonances progressively red shift as is expected for geometrical resonances [195].

By using the Lorentzian fitting shown in Fig. 12.2(a,b), we determined the resonance peak wavelength for all measured cylinders. In Figure 12.3(b), these peak wavelengths are shown as a function of diameter. This figure clearly shows how each resonance mode gradually red shifts for increasing diameter. To compare the experimental resonances with the results from numerical modeling, we also plot the collected power as a function of diameter and wavelength in a 2D color plot (Fig. 12.3(b)). Here, every vertical slice in the color plot corresponds to a normalized spectrum, as shown in Fig. 12.2(c,d). The FDTD simulations show multiple branches, each of which corresponds to a particular resonant mode in the

cylinders. Both the number of peaks as well as their peak wavelength show good agreement with the measurements, except the second branch from the top, for which the simulation is blue shifted with respect to the measurements.

12.6 Analytical disc model

To study the nature of these resonances in more detail, we developed an analytical 2D disc resonator model [104, 149, 152, 301, 302]. In this model, we solve for the cylindrical modes of an infinitely long cylinder, which can be analytically calculated using Maxwell's equations. Confinement in the normal direction is then included using a planar waveguide model. This is a reasonable assumption for cylinders with a diameter (much) larger than the thickness. Figure 12.4(a) shows the 2D slab waveguide geometry with the Si/SiO₂/Si layer stack. The 100 nm thin Si slab supports both a fundamental transverse electric (TE₀) and transverse magnetic (TM₀) mode. The incoming electrons mainly couple to vertical electric field (E_z) and in-plane transverse magnetic field components (H_T) [63], which both match the field orientations of the TM mode (see Fig. 12.4(a)), so that only this mode is considered further. We use a numerical method to solve for the dispersion curve of the TM₀ mode and derive from it the mode index n_{eff} at each wavelength. The result is shown in Fig. 12.4b (magenta), along with the refractive index of Si (cyan), SiO₂ (red), and air (black dashed line). For reference, the effective mode index of the TE₀ mode is also shown (blue). Fig. 12.4(b) shows that the effective index of the TM₀ mode gradually decreases from a value close to that of Si at short wavelengths to an index approaching that of SiO₂ for long wavelengths. This can be understood from the increasing overlap of the evanescent tail of the mode profile with the silica and air cladding layer, as the wavelength is increased. We now use this effective index of the Si slab modes as input for the index of the cylinder [104, 301, 302] in the 2D Helmholtz wave equation [149, 152]

$$(\nabla_T + n^2 k_0^2 - \beta^2)\Psi = 0 \quad (12.1)$$

to solve for the radial modes. Here, Ψ is the wave function of the out-of-plane field, ∇_T is the transverse gradient, n is the refractive index in the medium, k_0 is the free space wave vector, and β is the propagation constant in the vertical direction. The solution for Eq. 12.1 is given by

$$\Psi(r, \phi) = \begin{cases} a \frac{J_m(\sqrt{n_c^2 k_0^2 - \beta^2} r)}{J_m(\sqrt{n_c^2 k_0^2 - \beta^2} R)} e^{im\phi} & 0 < r < R \\ b \frac{K_m(\sqrt{\beta^2 - n_s^2 k_0^2} r)}{K_m(\sqrt{\beta^2 - n_s^2 k_0^2} R)} e^{im\phi} & R < r < \infty \end{cases} \quad (12.2)$$

Here, a and b are constants, J_m is the Bessel function of the first kind, K_m is the modified Bessel function of the second kind, m is the azimuthal mode number, n_c is

the effective refractive index of the cylinder, n_s the refractive index of the surrounding medium (vacuum), r the radial position, ϕ the azimuthal angle, and R the radius of the cylinder. We consider the 2D solutions for the TM modes, $\beta = 0$ and $\Psi = E_z$. The transverse field components can easily be derived from Eq. 12.2 [149, 152]. The eigenvalue equation can be obtained from Eq. 12.2 by applying the boundary conditions $E_{z,c}(R) = E_{z,s}(R)$ and

$H_{\phi,c}(R) = H_{\phi,s}(R)$ ($c = \text{cylinder}$, $s = \text{surrounding}$), which can then be solved for different particle radii to give the eigenvalues, corresponding to the resonance wavelengths. For a given azimuthal mode number m (where $m = 0, \pm 1, \pm 2, \dots$ and $m = \pm i$ are degenerate), multiple solutions are found. These correspond to higher-order resonances in the radial direction, with radial mode numbers $q = 1, 2, \dots$

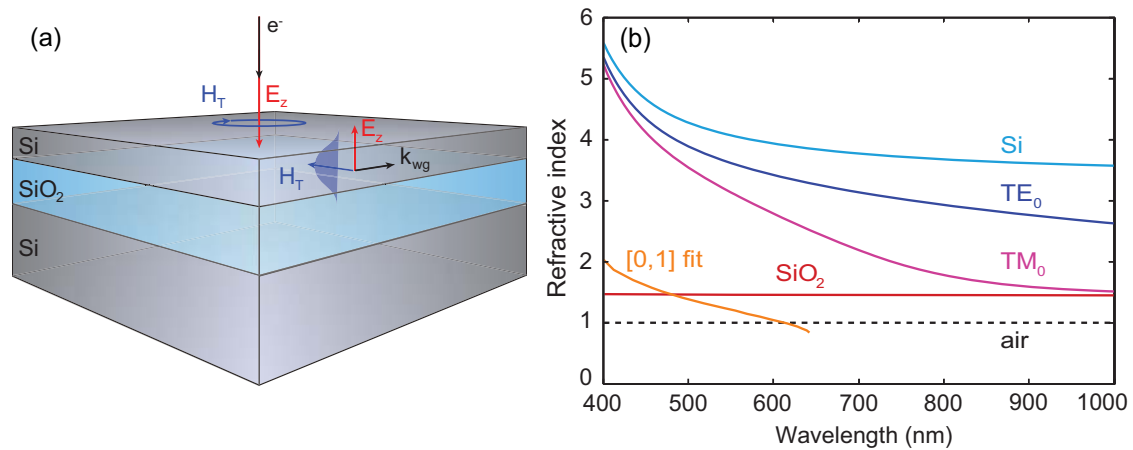


Figure 12.4: (a) Sketch of the layer structure used in the 2D analytical model to calculate the effective mode index of the TM_0 waveguide mode. Also shown are the electromagnetic field components induced by an incoming electron and those of the TM_0 waveguide mode. (b) Real part of the (effective) refractive index of the TM_0 mode (magenta), compared with the index of bulk Si (cyan curve), SiO_2 (red curve), air (dashed black curve), and the TE_0 mode (blue curve). The orange line shows the index obtained when fitting the $m = 0$, $q = 1$ mode to the top resonance branch obtained from numerical modeling. It shows a cutoff above $\lambda_0 = 620$ nm.

Resonant modes calculated using the above model are shown in Fig. 12.3 as gray dashed lines. The quantum numbers $[m, q]$ of each branch are indicated on the top and side of the graph, with the lowest-order mode $[0, 1]$ occurring for the longest wavelengths. The corresponding mode profiles $|E_z(r, \phi)|^2$ are shown in Figure 12.3(c) for the first nine branches, where the dashed white circle indicates the edge of the cylinders. These mode maps also show the azimuthal variations in the photonic wave functions that remain unobserved in the experiment, due to the cylindrical symmetry of the nanoparticle. The model shows good qualitative agreement with the measured data (white dots) and the numerical modeling (colormap); that is, experimental and numerical modal branches each lie close to one or two calculated branches. By comparing the model with the experimental and numerical data, we gain several insights.

First, the increasing number of peaks with increasing diameter observed in Fig. 12.3(a,b) reflects the excitation of higher-order resonances. When increasing the particle diameter at a fixed wavelength, both the azimuthal (m) and the radial (q) mode orders increase stepwise. In particular, for the higher-order resonances, the analytically calculated resonances match well with the numerically calculated ones. For example, the [2,1] and [0,2] branches that could not be resolved experimentally show a close match between the analytical model and numerical simulations.

Second, we can now label the complex photonic wave function maps observed in Fig. 12.2(e) as a superposition of the two photonic wave functions corresponding to the resonances that match the FDTD branches in Fig. 12.3(b). For example, the [3,1] and [1,2] modes in Fig. 12.3(c) together correspond to the map of peak 3 in Fig. 12.2(e), with a dark center and two bright rings. The eigenmodes assigned to the simulated profiles in Fig. 12.2(e) are indicated at the bottom of that figure. The good correspondence between experiment, numerical model, and analytical model is also reflected by the fact that for the 320 nm diameter disk only those with an azimuthal order $m = 0$ show an antinode in the center (peaks 2, 4, and 6).

Third, the analytically calculated modes show strong dispersion (curved resonance branches), in agreement with both the measurements and the FDTD data. This originates from the dispersive effective refractive index n_c of the cylinder due to the strong modal confinement in the vertical dimension. Indeed, the strongly decreasing index as a function of wavelength, as observed in Fig. 12.4b for the TM_0 mode proves to be essential to predict the shape of the measured and FDTD simulated resonance branches. In fact, if the cylinder would be described using the (dispersive) index of bulk Si or using the TE_0 mode, the analytically calculated modal branches in Fig. 12.3(b) would increase superlinearly rather than sublinearly for longer wavelengths as is observed in the experiment and FDTD simulations. This directly proves that the modal dispersion due to the vertical confinement strongly influences the resonant behavior.

While the analytical model thus predicts many of the key features and trends in both the experiments and FDTD simulations, one discrepancy is observed: the calculated lowest-order resonance [0,1], which is visible in the top left corner of Fig. 12.3(b), does not match with any branch observed in the experiment or simulations. This implies that either the lowest-order resonance is not excited in the experiment or that the assumptions of the simple 2D analytical model break down in the range where the wavelength is large compared to the particle diameter. Indeed, the waveguide model assumes an infinitely wide disk.

12.7 Angular patterns

To resolve this issue, we measured the angular emission profiles of individual Si cylinders in the CL system. Here, the light radiated by the cylinders is collected by the parabolic mirror and projected onto a CCD imaging camera; each pixel corre-

sponds to a unique azimuthal/zenithal angle. Using this technique, it is possible to determine the angular emission properties for such a 3D structure on a layered substrate, which is difficult if not impossible to predict either analytically or with numerical methods such as the boundary element method (BEM), FDTD, or finite-element methods (FEM).

Figure 12.5 shows the measured radiation patterns for four different cylinders measured on different resonance branches in Fig. 12.3(b). The pattern strongly depends on the resonance mode order. For the smallest cylinder (Fig. 12.5(a)), which has a resonance lying on the top experimental branch in Fig. 12.3(b), we observe a toroidal “doughnut-like” emission pattern at $\lambda_0 = 400$ nm, which has no light emission along the normal [64, 94, 157]. This pattern corresponds to that of a vertically oriented dipole [0,1] mode, which directly proves that the top measured branch corresponds to the [0,1] branch. Note that the [1,1] mode is not excited in the angular CL experiment as the cylinders are excited in the center, where the [1,1] mode has a node (see Fig. 12.3(c)). We explain the large discrepancy between the experimentally observed top branch and the analytically calculated [0,1] mode by the fact that the analytical waveguide model breaks down when the diameter is small compared to the wavelength. With the experimental data for the top branch in Fig. 12.3(b), identified as the [0,1] mode, we conclude that the [0,1] and [1,1] modal branches are closely spaced and overlap with the top experimental branch, as in the case for all other experimental branches, which also correspond to combinations of two modes (see Fig. 12.3(b)).

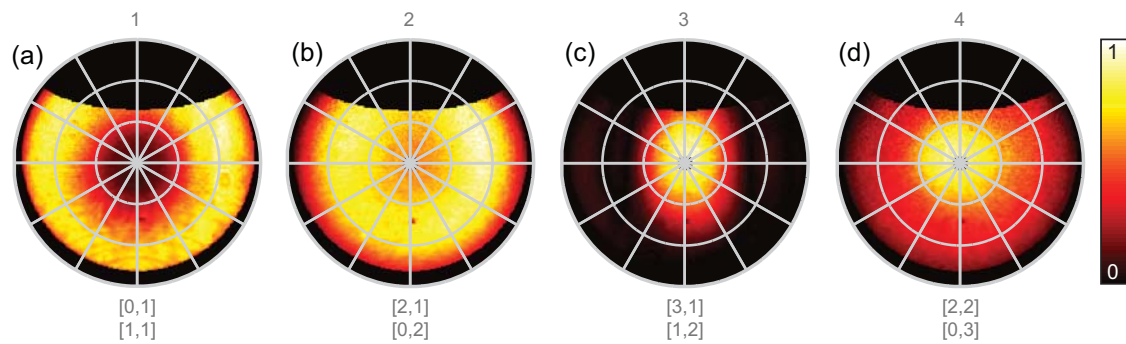


Figure 12.5: Measured angular patterns for the first four modal branches showing the CL emission intensity as function of zenithal angle θ and azimuthal angle φ for (a) $d = 70$ nm, (b) $d = 153$ nm, (c) $d = 176$ nm, and (d) $d = 304$ nm collected at $\lambda_0 = 400, 500, 450,$ and 500 nm, respectively. The specific diameters were chosen to optimally match a band-pass color filter. For all of the images, the cylinders were excited in the center, except for (c), where the cylinder was excited at the edge to optimize the excitation efficiency since this resonance has a node in the center.

The angular profile for the second branch (Fig. 12.5(b)) shows a toroidal shape, as well, consistent with the electron beam selectively exciting the [0,2] mode (the [2,1] mode has a node in the center; see Fig. 12.3(c)), which also has a vertical dipole moment. The modes in the third branch cannot be excited in the center ($m > 0$

for both modes), and therefore, the beam was placed on the edge of the cylinder, exciting a superposition of the [1,2] and [3,1] modes. In this case, clear upward beaming is observed, in agreement with the in-plane character of this mode (see Fig. 12.3(c)). The angular pattern for the fourth branch (Fig. 12.5(d)) appears to be a combination of a toroidal and upward emission. This corresponds to the excitation of the toroidally emitting [0,3] mode and a small contribution of the upward radiating [2,2] quadrupolar mode; while the latter has a node in the center, given the close proximity of its first radial antinode to the center (see Fig. 12.3(c)), it can be excited by the finite-size electron beam.

The large difference in radiation profile between the resonance orders shows that, depending on the angular scattering profile that is desired for specific applications, the cylinder geometry can be tuned to obtain such a scattering profile in the appropriate spectral range. Note that the angular distribution is also influenced by the wavelength-dependent interference with the silicon substrate 300 nm below the nanoparticle [94] (such interference is also present in the angular patterns in Chapter 11).

12.8 Nature of lowest-order mode

To investigate whether the lowest-order [0,1] dipolar resonance is electric or magnetic in nature [31, 296, 298–300], we perform polarization-filtered angular measurements, using a linear polarizer in the beam path. Figure 12.6 shows the angular pattern with the polarizer parallel (a) and transverse (b) to the optical axis of the paraboloid (see blue dashed lines) for the smallest cylinder ($d = 70$ nm) at $\lambda_0 = 400$ nm. In the paraboloid, the emission polarization remains almost unaltered along the center line of the mirror (the line going through $\varphi = 0^\circ$ and 180°). We observe that the light intensity is high along this line when the polarizer is aligned, while it is low when it is transversely oriented. This indicates that the emission is p-polarized, which is consistent with the radiation from an $m = 0$, $q = 1$ electric dipole mode. For a more elaborate description on why these polarization-filtered angular patterns have this specific shape and how the parabolic mirror affects the emission polarization for different electric dipole orientations, we refer the reader to Chapter 6.

Finally, we use the knowledge that the upper experimental/numerical branch corresponds to a [0,1] resonance to fit its appropriate effective index. To do this, we again solve the eigenvalue equation, but now we fix the resonance wavelength to the resonance wavelengths obtained for the top branch from numerical modeling and solve for n_c , given that $m = 0$ and $q = 1$. In this way, we force the [0,1] branch of the model to match the experimental data and use this to obtain the effective index of the cylinder. The resulting index is shown as an orange line in Fig. 12.4(b) and is indeed significantly lower than the TM_0 index that was originally used and gives rise to a significant blue shift of the resonance wavelength. The fitted index steadily decreases with increasing wavelength from $n = 2.0$ at $\lambda_0 = 400$ nm to $n <$

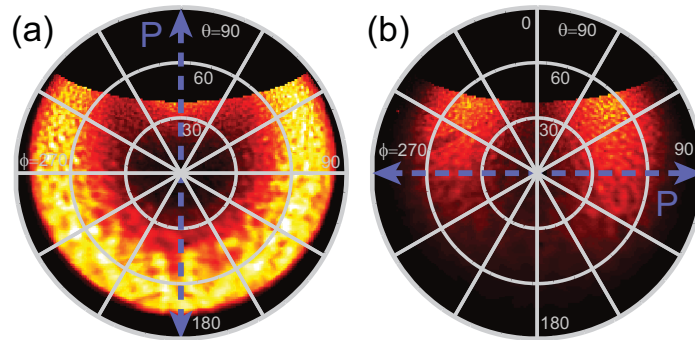


Figure 12.6: Measured polarization-filtered angular patterns for a $d = 70$ nm cylinder measured at $\lambda_0 = 400$ nm with the polarizer positioned (a) vertically (aligned with the optical axis of the paraboloid) and (b) horizontally (transverse to the optical axis). The patterns suggest that this resonance is an electrical dipolar $m = 0$, $q = 1$ resonance.

1 for $\lambda_0 > 620$ nm. This implies that the lowest-order resonance approaches cutoff and becomes a leaky mode that no longer strongly confines light inside the cavity. Close observation of Fig. 12.3(b) shows that both the experimental and simulation data of the top resonance branch fade away around this wavelength, in agreement with this cutoff argument. We note that the decrease in effective mode index for the cutoff mode with increasing wavelength is due to both the reduced confinement and the lower index of bulk silicon at larger wavelengths. The strong reduction in Q for the [0,1] mode with increasing diameter is also clearly visible in Fig. 12.3(a).

12.9 Conclusions

In conclusion, the resonant optical modes of silicon nanocylinders with diameters between 60 and 325 nm can be excited and studied using a 30 keV electron beam. Well-defined fundamental and higher-order azimuthal ($m = 0 - 4$) and radial ($q = 1 - 4$) modes are observed with relatively narrow ($Q = 9 - 77$) emission peaks and complex photonic wave functions. The data agree with finite-difference time-domain simulations and analytical calculations, in which we solve the Helmholtz wave equation using an effective modal index for the corresponding TM_0 waveguide mode to find the in-plane eigenmodes. Characteristic angular emission patterns are observed for each resonant mode, ranging from an upward dipole-like pattern for the lowest-order modes to distributions that show clear beaming in the upward direction for higher-order modes. Using polarization spectroscopy, we identify the lowest-order resonance as an ($m = 0$, $q = 1$) electrical dipole mode; it becomes leaky for long wavelengths.

Our measurements demonstrate that the optical properties of silicon nanocylinders are highly tunable through the visible spectral range. Further tunability may be achieved by varying the nanoparticle shape. With the fundamental

resonant optical properties of single Si Mie resonators now determined, the door is open to studies of more complex geometries of arrays of coupled resonators, in which the directionality and spectra of emitted light can be tuned further. This work also shows that cathodoluminescence spectroscopy, which so far has been used mostly on metallic nanostructures, can be used to study the fundamental resonant properties of single dielectric or semiconductor nanostructures in great detail. In the future, this enables rapid prototyping of semiconductor or dielectric nanostructures, where the spectral and angular emission properties can be fine-tuned for specific applications.

12.10 Methods

Fabrication. Small chips (12 × 12 mm) of SOI wafer (100 nm Si device layer, 300 nm SiO₂ buried oxide layer) are baked for 5 min at 180 °C before spin coating the sample with a thin HMDS adhesion layer (4000 rpm, 30 s). The HMDS layer is baked for 1 min at 180 °C to evaporate the solvents. Next, the sample is spin coated with approximately 65 nm of negative tone resist (ma-N 2401, 2000 rpm, 30 s) and baked for 60 s at 90 °C. Au colloids with a diameter of 50 nm are deposited in the corner of the sample to allow accurate focusing of the electron beam.

Electron beam lithography is performed in a Raith e-LINE system, using a 30 kV acceleration voltage and 7.5 μm aperture, resulting in a beam current of 14 pA. Single dot exposure is used for the smallest cylinders ($d < 240$ nm), whereas area exposure is used for the larger cylinders ($d > 270$ nm). The resist is developed by rinsing in ma-D 332 S for 15 s, followed by rinsing in deionized H₂O to stop the development.

The resulting disks of resist function as an etch mask in the reactive ion etching (RIE) step. A gas mixture of CHF₃ (35 sccm) and SF₆ (5 sccm) is used to anisotropically etch down the Si layer of the SOI wafer (100 nm) in 3.5 min (forward power = 125 W). Subsequently, the residual resist is removed using a 10 min oxygen plasma etch (20 sccm O₂, 50 W forward power).

Cathodoluminescence Experiments. For the spectral images, 0.3 s integration time per pixel was used at a current of 10 nA. The CL data are corrected for system response using a measured transition radiation spectrum from gold and comparing that to theory [63, 103], so that the absolute excitation efficiency is determined per electron per unit bandwidth. For the angle-resolved measurements, we used dwell times between 15 and 30 s depending on wavelength. For the polarization-filtered angular measurements, we used an integration time of 60 s. Spectral sensitivity was achieved by filtering the CL beam with 40 nm band-pass color filters. In all cases, the background CL signal from the substrate was subtracted from the measured data, which includes the transition radiation of the SiO₂ layer and Si substrate. To correctly subtract the variable background from the CL signal, we use a triangular interpolation routine, which interpolates the background intensity between the

four corners (averaged over nine pixels in each corner) of the scan.

FDTD Simulations. The finite-difference time-domain simulations are performed using the commercial software package Lumerical FDTD Solutions [228]. An 800 nm cubed simulation box is used, with perfectly matching layer (PML) boundary conditions on all sides. The simulation box ranges from 150 nm into the Si substrate to 250 nm above the top of the cylinders. A constant current broad band ($\lambda_0 = 300 - 900$ nm) vertically oriented electric dipole, positioned at half the height of the cylinder (50 nm), is used as a source. To simulate the spectrum for a given cylinder diameter, the dipole position is varied from the center to the edge of the cylinder in steps of 5 nm, such that the number of simulations N per cylinder is given by $N = R/5 + 1$, with R being the particle radius in nanometers. Two-dimensional flux box transmission monitors, the top one positioned 100 nm above the top interface of the cylinder, the side ones 360 nm from the center of the cylinder, monitor the power of the light emitted into the upper hemisphere. Note that interference with the Si substrate is taken into account, but that light reflected from the SiO₂-Si interface under large angles may be radiated into the upper hemisphere without being detected. Automatic non-uniform meshing is used, resulting in mesh sizes ranging from 4 to 7 nm in the Si cylinder or air, respectively.

References

- [1] R. Hooke, *Micrographia*, The Royal Society, 1665.
- [2] A. van Leeuwenhoek, *The collected letters of Antoni van Leeuwenhoek*, Swets and Zeitlinger, 1996.
- [3] V. Westphal and S. W. Hell, *Nanoscale resolution in the focal plane of an optical microscope*, Phys. Rev. Lett. **94**, 143903 (2005).
- [4] D. Wildanger, B. R. Patton, H. Schill, L. Marseglia, J. P. Hadden, S. Knauer, A. Schönle, J. G. Rarity, J. L. O'Brien, S. W. Hell, and J. M. Smith, *Solid immersion facilitates fluorescence microscopy with nanometer resolution and sub-Ångström emitter localization*, Adv. Mater. **24**, 309 (2012).
- [5] E. Betzig, G. H. Patterson, R. Sougrat, O. W. Lindwasser, J. S. Olenych, S. Bonifacino, M. W. Davidson, J. Lippincott-Schwartz, and H. F. Hess, *Imaging intracellular fluorescent proteins at nanometer resolution*, Science **313**, 1642 (2006).
- [6] M. Rust, M. Bates, and X. Zhuang, *Sub-diffraction-limit imaging by stochastic optical reconstruction microscopy (STORM)*, Nat. Methods **3**, 793 (2006).
- [7] E. Bauer, *Low energy electron microscopy*, Rep. Prog. Phys. **57**, 895 (1994).
- [8] M. J. Rost, L. Crama, P. Schakel, E. van Tol, G. B. E. M. van Velzen-Williams, C. F. Overgaw, H. ter Horst, H. Dekker, B. Okhuijsen, M. Seynen, A. Vijftigschild, P. Han, A. J. Katan, K. Schoots, R. Schumm, W. van Loo, T. Oosterkamp, and J. W. M. Frenken, *Scanning probe microscopes go video rate and beyond*, Rev. Sci. Instrum. **76**, 053710 (2005).
- [9] M. Ternes, C. P. Lutz, C. F. Hirjibehedin, F. J. Giessibl, and A. J. Heinrich, *The force needed to move an atom on a surface*, Science **319**, 1066 (2008).
- [10] L. Kuipers and J. W. M. Frenken, *Jump to contact, neck formation, and surface melting in the scanning tunneling microscope*, Phys. Rev. Lett. **70**, 3907 (1993).
- [11] E. M. Schroyen Lantman, T. Deckert-Gaudig, A. J. G. Mank, V. Deckert, and B. M. Weckhuysen, *Catalytic processes monitored at the nanoscale with tip-enhanced Raman spectroscopy*, Nat. Nanotechnol. **7**, 583 (2012).
- [12] C. Chen, N. Hayazawa, and S. Kawata, *A 1.7 nm resolution chemical analysis of carbon nanotubes by tip-enhanced Raman imaging in the ambient*, Nat. Commun. **5**, 3312 (2014).
- [13] S. Kühn, U. Hakanson, L. Rogobete, and V. Sandoghdar, *Enhancement of single-molecule fluorescence using a gold nanoparticle as an optical nanoantenna*, Phys. Rev. Lett. **97**, 017402 (2006).

REFERENCES

- [14] M. Burrese, D. van Oosten, T. Kampfrath, H. Schoenmaker, R. Heideman, A. Leinse, and L. Kuipers, *Probing the magnetic field of light at optical frequencies*, *Science* **326**, 550 (2009).
- [15] E. Verhagen, M. Spasenović, A. Polman, and L. Kuipers, *Nanowire plasmon excitation by adiabatic mode transformation*, *Phys. Rev. Lett.* **102**, 203904 (2009).
- [16] J. Dorfmüller, R. Vogelgesang, W. Khunsin, C. Rockstuhl, C. Etrich, and K. Kern, *Plasmonic nanowire antennas: Experiment, simulation, and theory*, *Nano Lett.* **10**, 3596 (2010).
- [17] M. Frimmer, Y. Chen, and A. F. Koenderink, *Scanning emitter lifetime imaging microscopy for spontaneous emission control*, *Phys. Rev. Lett.* **107**, 123602 (2011).
- [18] J. Chen, M. Badioli, P. Alonso-González, S. Thongrattanasiri, F. Huth, J. Osmond, M. Spasenović, A. Centeno, A. Pesquera, P. Godignon, A. Zurutuza Elorza, N. Camara, F. J. García de Abajo, R. Hillenbrand, and F. H. L. Koppens, *Optical nano-imaging of gate-tunable graphene plasmons*, *Nature* **487**, 77 (2012).
- [19] Z. Fei, A. S. Rodin, G. O. Andreev, W. Bao, A. S. McLeod, M. Wagner, L. M. Zhang, Z. Zhao, M. Thiemens, G. Dominguez, M. M. Fogler, A. H. Castro Neto, C. N. Lau, F. Keilmann, and D. N. Basov, *Gate-tuning of graphene plasmons revealed by infrared nano-imaging*, *Nature* **487**, 82 (2012).
- [20] P. Bharadwaj, A. Bouhelier, and L. Novotny, *Electrical excitation of surface plasmons*, *Phys. Rev. Lett.* **106**, 226802 (2011).
- [21] E. Le Moal, S. Marguet, B. Rogez, S. Mukherjee, P. Dos Santos, E. Boer-Duchemin, G. Comtet, and G. Dujardin, *An electrically excited nanoscale light source with active angular control of the emitted light*, *Nano Lett.* **13**, 4198 (2013).
- [22] M. Aeschlimann, M. Bauer, D. Bayer, T. Brixner, F. J. García de Abajo, W. Pfeiffer, M. Rohmer, C. Spindler, and F. Steeb, *Adaptive subwavelength control of nano-optical fields*, *Nature* **446**, 301 (2007).
- [23] L. Douillard, F. Charra, Z. Korczak, R. Bachelot, S. Kostcheev, G. Lerondel, P. M. Adam, and P. Royer, *Short range plasmon resonators probed by photoemission electron microscopy*, *Nano Lett.* **8**, 935 (2008).
- [24] Q. Sun, K. Ueno, H. Yu, A. Kubo, Y. Matsuo, and H. Misawa, *Direct imaging of the near field and dynamics of surface plasmon resonance on gold nanostructures using photoemission electron microscopy*, *Light Sci. Appl.* **2**, e118 (2013).
- [25] P. A. Midgley and R. E. Dunin-Borkowski, *Electron tomography and holography in materials science*, *Nat. Mater.* **8**, 271 (2009).
- [26] G. E. Moore, *Cramming more components onto integrated circuits*, *Electronics* **38**, 114 (1965).
- [27] H. J. Kimble, *The quantum internet*, *Nature* **453**, 1023 (2008).
- [28] T. D. Ladd, F. Jelezko, R. Laflamme, Y. Nakamura, C. Monroe, and J. L. O'Brien, *Quantum computers*, *Nature* **464**, 45 (2010).
- [29] L. Novotny and N. van Hulst, *Antennas for light*, *Nat. Photonics* **5**, 83 (2011).
- [30] P. Spinelli, M. A. Verschuuren, and A. Polman, *Broadband omnidirectional antireflection coating based on subwavelength surface mie resonators*, *Nat. Commun.* **3**, 692 (2012).
- [31] A. I. Kuznetsov, A. E. Miroshnichenko, Y. H. Fu, J. B. Zhang, and B. Luk'yanchuk, *Magnetic light*, *Sci. Rep.* **2**, 492 (2012).
- [32] L. Novotny, *Effective wavelength scaling for optical antennas*, *Phys. Rev. Lett.* **98**, 266802 (2007).
- [33] C. Balanis, *Antenna theory: Analyses and design, 3rd edition*, John Wiley and sons,

- 2005.
- [34] N. Engheta, *Circuits with light at nanoscales: Optical nanocircuits inspired by metamaterials*, *Science* **317**, 1698 (2007).
- [35] M. L. Brongersma, *Plasmonics: Engineering optical nanoantennas*, *Nat. Photonics* **2**, 270 (2008).
- [36] H. A. Atwater and A. Polman, *Plasmonics for improved photovoltaic devices*, *Nat. Mater.* **9**, 205 (2010).
- [37] P. Bharadwaj, P. Anger, and L. Novotny, *Nanoplasmonic enhancement of single-molecule fluorescence*, *Nanotechnology* **18**, 044017 (2007).
- [38] A. Kinkhabwala, Z. Yu, S. Fan, Y. Avlasevich, K. Müllen, and W. E. Moerner, *Large single-molecule fluorescence enhancements produced by a bowtie nanoantenna*, *Nat. Photonics* **3**, 654 (2009).
- [39] A. G. Curto, G. Volpe, T. H. Taminiau, M. Kreuzer, R. Quidant, and N. F. van Hulst, *Unidirectional emission of a quantum dot coupled to a nanoantenna*, *Science* **329**, 930 (2010).
- [40] M. Frimmer and A. F. Koenderink, *Spontaneous emission control in a tunable hybrid photonic system*, *Phys. Rev. Lett.* **110**, 217405 (2013).
- [41] R. J. Walters, R. V. A. van Loon, I. Brunets, J. Schmitz, and A. Polman, *A silicon-based electrical source of surface plasmon polaritons*, *Nat. Mater.* **9**, 21 (2009).
- [42] A. A. Yanik, M. Huang, A. Artar, T. Y. Chang, and H. Altug, *Integrated nanoplasmonic-nanofluidic biosensors with targeted delivery of analytes*, *Appl. Phys. Lett.* **96**, 021101 (2010).
- [43] N. Liu, M. L. Tang, M. Hentschel, G. H., and A. P. Alivisatos, *Nanoantenna-enhanced gas sensing in a single tailored nanofocus*, *Nat. Mater.* **10**, 632 (2011).
- [44] N. Liu, M. Hentschel, T. Weiss, A. P. Alivisatos, and H. Giessen, *Three-dimensional plasmon rulers*, *Science* **332**, 1407 (2011).
- [45] C. Wu, A. B. Khanikaev, R. Adato, N. Arju, A. A. Yanik, H. Altug, and G. Shvets, *Fano-resonant asymmetric metamaterials for ultrasensitive spectroscopy and identification of molecular monolayers*, *Nat. Mater.* **11**, 69 (2012).
- [46] D. Punj, M. Mivelle, M. Satish Babu, T. S. van Zanten, H. Rigneault, N. F. van Hulst, M. F. García-Parajó, and J. Wenger, *A plasmonic 'antenna-in-box' platform for enhanced single-molecule analysis at micromolar concentrations*, *Nat. Nanotechnol.* **8**, 512 (2013).
- [47] L. Langguth, D. Punj, J. Wenger, and A. F. Koenderink, *Plasmonic band structure controls single molecule fluorescence*, *ACS Nano* **7**, 8840 (2013).
- [48] M. P. Jonsson and C. Dekker, *Plasmonic nanopore for electrical profiling of optical intensity landscapes*, *Nano Lett.* **13**, 1029 (2013).
- [49] R. Adato and H. Altug, *In-situ ultra-sensitive infrared absorption spectroscopy of biomolecule interactions in real time with plasmonic nanoantennas*, *Nat. Commun.* **4**, 2154 (2013).
- [50] O. Neumann, A. Urban, J. Day, S. Lal, P. Nordlander, and N. J. Halas, *Solar vapor generation enabled by nanoparticles*, *ACS Nano* **7**, 42 (2013).
- [51] Z. Fang, Y. Zhen, O. Neumann, A. Polman, F. J. García de Abajo, P. Nordlander, and N. J. Halas, *Evolution of light-induced vapor generation at a liquid-immersed metallic nanoparticle*, *Nano Lett.* **13**, 1736 (2013).
- [52] S. Yokogawa, S. P. Burgos, and H. A. Atwater, *Plasmonic color filters for CMOS image sensor applications*, *Nano Lett.* **12**, 4349 (2012).
- [53] S. P. Burgos, S. Yokogawa, and H. A. Atwater, *Color imaging via nearest neighbor*

REFERENCES

- hole coupling in plasmonic color filters integrated onto a complementary metal-oxide semiconductor image sensor*, ACS Nano **7**, 10038 (2013).
- [54] A. M. Gobin, M. H. Lee, N. J. Halas, W. D. James, R. A. Drezek, and J. L. West, *Near-infrared resonant nanoshells for combined optical imaging and photothermal cancer therapy*, Nano Lett. **7**, 1929 (2007).
- [55] R. Huschka, A. Barhoumi, Q. Liu, J. A. Roth, J. Lin, and N. J. Halas, *Gene silencing by gold nanoshell-mediated delivery and laser-triggered release of antisense oligonucleotide and siRNA*, ACS Nano **6**, 7681 (2012).
- [56] B. Kang, M. M. Afifi, L. A. Austin, and M. A. El-Sayed, *Exploiting the nanoparticle plasmon effect: Observing drug delivery dynamics in single cells via Raman/fluorescence imaging spectroscopy*, ACS Nano **7**, 7420 (2013).
- [57] A. Ahmed and R. Gordon, *Single molecule directivity enhanced raman scattering using nanoantennas*, Nano Lett. **12**, 2625 (2012).
- [58] D. Wang, W. Zhu, M. D. Best, J. P. Camden, and K. B. Crozier, *Directional Raman scattering from single molecules in the feed gaps of optical antennas*, Nano Lett. **13**, 2194 (2013).
- [59] J. Renger, R. Quidant, N. F. van Hulst, and L. Novotny, *Surface enhanced nonlinear four-wave mixing*, Phys. Rev. Lett. **104**, 046803 (2010).
- [60] T. Schumacher, K. Kratzer, D. Molnar, M. Hentschel, H. Giessen, and M. Lippitz, *Nanoantenna-enhanced ultrafast nonlinear spectroscopy of a single gold nanoparticle*, Nat. Commun. **2**, 333 (2011).
- [61] M. Castro-López, D. Brinks, R. Sapienza, and N. F. van Hulst, *Aluminum for nonlinear plasmonics: Resonance-driven polarized luminescence of Al, Ag, and Au nanoantennas*, Nano Lett. **11**, 4674 (2011).
- [62] R. Vogelgesang and A. Dmitriev, *Real-space imaging of nanoplasmonic resonances*, Analyst **135**, 1175 (2010).
- [63] F. J. García de Abajo, *Optical excitations in electron microscopy*, Rev. Mod. Phys. **82**, 209 (2010).
- [64] N. Yamamoto, S. Ohtani, and F. J. García de Abajo, *Gap and Mie plasmons in individual silver nanospheres near a silver surface*, Nano Lett. **11**, 91 (2011).
- [65] Z. Mahfoud, A. T. Dijkman, C. Javaux, P. Bassoul, A. L. Baudrion, J. Plain, B. Dubertret, and M. Kociak, *Cathodoluminescence in a scanning transmission electron microscope: A nanometer-scale counterpart of photoluminescence for the study of II-VI quantum dots*, J. Phys. Chem. Lett. **4**, 4090 (2013).
- [66] C. Colliex, *Microscopy: Elementary resolution*, Nature **450**, 622 (2007).
- [67] N. Tanaka, *Present status and future prospects of spherical aberration corrected TEM/STEM for study of nanomaterials*, Sci. Technol. Adv. Mater. **9**, 014111 (2008).
- [68] D. A. Muller, *Structure and bonding at the atomic scale by scanning transmission electron microscopy*, Nat. Mater. **8**, 263 (2009).
- [69] T. Arabatzis, *Cathode rays*, Compendium of quantum physics: Concepts, experiments, history and philosophy, 89 (2009).
- [70] X. Bendaña, A. Polman, and F. J. García de Abajo, *Single-photon generation by electron beams*, Nano Lett. **11**, 5099 (2011).
- [71] B. Barwick, D. J. Flannigan, and A. H. Zewail, *Photon-induced near-field electron microscopy*, Nature **462**, 902 (2009).
- [72] A. Yurtsever, R. M. van der Veen, and A. H. Zewail, *Subparticle ultrafast spectrum imaging in 4D electron microscopy*, Science **335**, 59 (2012).
- [73] F. O. Kirchner, A. Gliserin, F. Krausz, and P. Baum, *Laser streaking of free electrons at 25*

- keV, *Nat. Photonics* (2013).
- [74] A. Asenjo-Garcia and F. J. García de Abajo, *Plasmon electron energy-gain spectroscopy*, *New J. Phys.* **15**, 103021 (2013).
- [75] F. J. García de Abajo and M. Kociak, *Probing the photonic local density of states with electron energy loss spectroscopy*, *Phys. Rev. Lett.* **100**, 106804 (2008).
- [76] U. Hohenester, H. Ditlbacher, and J. R. Krenn, *Electron-energy-loss spectra of plasmonic nanoparticles*, *Phys. Rev. Lett.* **103**, 106801 (2009).
- [77] A. I. Denisyuk, G. Adamo, K. F. MacDonald, J. Edgar, M. D. Arnold, V. Myroshnychenko, J. Ford, F. J. García de Abajo, and N. I. Zheludev, *Transmitting hertzian optical nanoantenna with free-electron feed*, *Nano Lett.* **10**, 3250 (2010).
- [78] N. Mirsaleh-Kohan, V. Iberi, P. D. Simmons, N. W. Bigelow, A. Vaschillo, M. M. Rowland, M. D. Best, S. J. Pennycook, D. J. Masiello, B. S. Guiton, and J. P. Camden, *Single-molecule surface-enhanced Raman scattering: Can STEM/EELS image electromagnetic hot spots?*, *J. Phys. Chem. Lett.* **3**, 2303 (2012).
- [79] N. W. Bigelow, A. Vaschillo, V. Iberi, J. P. Camden, and D. J. Masiello, *Characterization of the electron- and photon-driven plasmonic excitations of metal nanorods*, *ACS Nano* **6**, 7497 (2012).
- [80] A. H. Zewail, *Four-dimensional electron microscopy*, *Science* **328**, 187 (2010).
- [81] O. H. Kwon and A. H. Zewail, *4D electron tomography*, *Science* **328**, 1668 (2010).
- [82] A. Yurtsever and A. H. Zewail, *Direct visualization of near-fields in nanoplasmonics and nanophotonics*, *Nano Lett.* **12**, 3334 (2012).
- [83] A. Hörl, A. Trügler, and U. Hohenester, *Tomography of particle plasmon fields from electron energy loss spectroscopy*, *Phys. Rev. Lett.* **111**, 086801 (2013).
- [84] O. Nicoletti, F. de la Peña, R. K. Leary, D. J. Holland, C. Ducati, and P. A. Midgley, *Three-dimensional imaging of localized surface plasmon resonances of metal nanoparticles*, *Nature* **502**, 80 (2013).
- [85] A. C. Atre, B. J. M. Brenny, T. Coenen, A. Polman, and J. . A. Dionne, *Nanoscale optical tomography with cathodoluminescence spectroscopy*, In preparation .
- [86] B. G. Yacobi and D. B. Holt, *Cathodoluminescence scanning electron microscopy of semiconductors*, *J. Appl. Phys.* **59**, R1 (1986).
- [87] N. Yamamoto, S. Bhunia, and Y. Wantanabe, *Polarized cathodoluminescence study of InP nanowire by transmission electron microscopy*, *Appl. Phys. Lett.* **88**, 154106 (2006).
- [88] L. F. Zagonel, L. Rigutti, M. Tchernycheva, G. Jacopin, R. Songmuang, and M. Kociak, *Visualizing highly localized luminescence in GaN/AlN heterostructures in nanowires*, *Nanotechnology* **23**, 455205 (2012).
- [89] M. A. Stevens-Kalceff, *Cathodoluminescence microcharacterization of the defect structure of irradiated hydrated and anhydrous fused silicon dioxide*, *Phys. Rev. B* **57**, 5674 (1998).
- [90] L. H. G. Tizei and M. Kociak, *Spatially resolved quantum nano-optics of single photons using an electron microscope*, *Phys. Rev. Lett.* **110**, 153604 (2013).
- [91] M. Pagel, V. Barbin, P. Blanc, and D. Ohnenstetter, *Cathodoluminescence in geosciences*, Springer, 2000.
- [92] E. F. Schubert, *Light emitting diodes, 2nd edition*, Cambridge University press, 2006.
- [93] B. J. M. Brenny, T. Coenen, and A. Polman, *Differentiating radiation processes in silicon using angle-resolved cathodoluminescence spectroscopy*, in preparation (2014).
- [94] L. Novotny and B. Hecht, *Principles of nano-optics*, Cambridge University press, 2006.
- [95] M. Lieb, J. Zavislan, and L. Novotny, *Single-molecule orientations determined by direct emission pattern imaging*, *J. Opt. Soc. Am. B* **21**, 1210 (2004).

REFERENCES

- [96] E. J. R. Vesseur, *Electron beam imaging and spectroscopy of plasmonic nanoantenna resonances*, PhD thesis, Utrecht University, 2011.
- [97] T. Suzuki and N. Yamamoto, *Cathodoluminescent spectroscopic imaging of surface plasmon polaritons in a 1-dimensional plasmonic crystal*, *Opt. Express* **17**, 23664 (2009).
- [98] K. Takeuchi and N. Yamamoto, *Visualization of surface plasmon polariton waves in two-dimensional plasmonic crystal by cathodoluminescence*, *Opt. Express* **19**, 12365 (2011).
- [99] M. Bosman, V. J. Keast, J. L. García-Muñoz, A. J. D'Alfonso, S. D. Findlay, and L. J. Allen, *Two-dimensional mapping of chemical information at atomic resolution*, *Phys. Rev. Lett.* **99**, 086102 (2007).
- [100] Z. Wang, M. Saito, K. P. McKenna, L. Gu, S. Tsukimoto, A. L. Shluger, and Y. Ikuhara, *Atom-resolved imaging of ordered defect superstructures at individual grain boundaries*, *Nature* **479**, 380 (2011).
- [101] K. Kimoto, T. Asaka, T. Nagai, M. Saito, Y. Matsui, and K. Ishizuka, *Element-selective imaging of atomic columns in a crystal using STEM and EELS*, *Nature* **450**, 702 (2007).
- [102] E. J. R. Vesseur, F. J. García de Abajo, and A. Polman, *Modal decomposition of surface-plasmon whispering gallery resonators*, *Nano Lett.* **9**, 3147 (2009).
- [103] M. Kuttge, E. J. R. Vesseur, A. F. Koenderink, H. J. Lezec, H. A. Atwater, F. J. García de Abajo, and A. Polman, *Local density of states, spectrum, and far-field interference of surface plasmon polaritons probed by cathodoluminescence*, *Phys. Rev. B* **79**, 113405 (2009).
- [104] M. Kuttge, F. J. García de Abajo, and A. Polman, *Ultrasmall mode volume plasmonic nanodisk resonators*, *Nano Lett.* **10**, 1537 (2010).
- [105] P. B. Johnson and R. W. Christy, *Optical constants of the noble metals*, *Phys. Rev. B* **6**, 4370 (1972).
- [106] J. A. Schuller, E. S. Barnard, W. Cai, Y. C. Jun, J. White, and M. L. Brongersma, *Plasmonics for extreme light concentration and manipulation*, *Nat. Mater.* **9**, 193 (2010).
- [107] S. Lal, S. Link, and N. J. Halas, *Nano-optics from sensing to waveguiding*, *Nat. Photonics* **1**, 641 (2007).
- [108] M. Celebrano, P. Kukura, A. Renn, and V. Sandoghdar, *Single-molecule imaging by optical absorption*, *Nat. Photonics* **5**, 95 (2011).
- [109] M. Stobinska, G. Alber, and G. Leuchs, *Perfect excitation of a matter qubit by a single photon in free space*, *Eur. Phys. Lett.* **86**, 14007 (2009).
- [110] P. Anger, P. Bharadwaj, and L. Novotny, *Enhancement and quenching of single-molecule fluorescence*, *Phys. Rev. Lett.* **96**, 113002 (2006).
- [111] T. H. Taminiou, F. D. Stefani, F. B. Segerink, and N. F. van Hulst, *Optical antennas direct single-molecule emission*, *Nat. Photonics* **2**, 234 (2008).
- [112] M. Hentschel, D. Dregely, R. Vogelgesang, H. Giessen, and N. Liu, *Plasmonic oligomers: The role of individual particles in collective behavior*, *ACS Nano* **5**, 2042 (2011).
- [113] A. F. Koenderink, *Plasmon nanoparticle array waveguides for single photon and single plasmon Sources*, *Nano Lett.* **9**, 4228 (2009).
- [114] R. de Waele, A. F. Koenderink, and A. Polman, *Tunable nanoscale localization of energy on plasmon particle arrays*, *Nano Lett.* **7**, 2004 (2007).
- [115] J. Li, A. Salandrino, and E. N. *Shaping light beams in the nanometer scale: A Yagi-Uda nanoantenna in the optical domain*, *Phys. Rev. B* **76**, 245403 (2007).
- [116] H. Hofmann, T. Kosako, and Y. Kadoya, *Design parameters for a nano-optical Yagi-Uda*

- antenna*, New J. Phys. **9**, 217 (2007).
- [117] M. Quinten, A. Leitner, J. R. Krenn, and F. R. Aussenegg, *Electromagnetic energy transport via linear chains of silver nanoparticles*, Opt. Lett. **23**, 1331 (1998).
- [118] M. L. Brongersma, J. W. Hartman, and H. A. Atwater, *Electromagnetic energy transfer and switching in nanoparticle chain arrays below the diffraction limit*, Phys. Rev. B **62**, R16356 (2000).
- [119] S. Schietinger, M. Barth, T. Aichele, and O. Benson, *Plasmon-enhanced single photon emission from a nanoassembled metal-diamond hybrid structure at room temperature*, Nano Lett. **9**, 1694 (2009).
- [120] D. Ratchford, F. Shafiei, S. Kim, S. Gray, and X. Li, *Manipulating coupling between a single semiconductor quantum dot and single gold nanoparticle*, Nano Lett. **11**, 1049 (2011).
- [121] A. Cuche, A. Drezet, Y. Sonnefraud, O. Faklaris, F. Treussart, J. F. Roch, and S. Huant, *Near-field optical microscopy with a nanodiamond-based single-photon tip*, Opt. Express **17**, 19969 (2009).
- [122] J. Michaelis, C. Hettich, J. Mlynek, and V. Sandoghdar, *Optical microscopy using a single-molecule light source*, Nature **405**, 325 (2000).
- [123] P. Spinelli, C. van Lare, E. Verhagen, and A. Polman, *Controlling Fano lineshapes in plasmon-mediated light coupling into a substrate*, Opt. Express **19**, A303 (2011).
- [124] A. F. Koenderink and A. Polman, *Complex response and polariton-like dispersion splitting in periodic metal nanoparticle chains*, Phys. Rev. B **74**, 033402 (2006).
- [125] P. de Vries, D. V. van Coevorden, and A. Lagendijk, *Point scatterers for classical waves*, Rev. Mod. Phys. **70**, 447 (1998).
- [126] M. Paulus, P. Gay-Balmaz, and O. J. F. Martin, *Accurate and efficient computation of the Green's tensor for stratified media*, Phys. Rev. E **62**, 5797 (2000).
- [127] A. Wokaun, J. Gordon, and P. F. Liao, *Radiation damping in surface-enhanced Raman scattering*, Phys. Rev. Lett. **48**, 957 (1982).
- [128] B. C. Buchler, T. Kalkbrenner, C. Hettich, and V. Sandoghdar, *Measuring the quantum efficiency of the optical emission of single radiating dipoles using a scanning mirror*, Phys. Rev. Lett. **95**, 063003 (2005).
- [129] W. L. Vos, A. F. Koenderink, and I. S. Nikolaev, *Strong dependence of the optical emission rates of a two-level quantum emitter in any nanophotonic environment on the orientation of the transition dipole moment*, Phys. Rev. A **80**, 053802 (2009).
- [130] E. D. Palik, *Handbook of optical constants*, Academic Press, New York, 1985.
- [131] M. W. Knight, H. Sobhani, P. Nordlander, and N. J. Halas, *Photodetection with active optical antennas*, Science **332**, 702 (2011).
- [132] J. Li, A. Salandrino, and N. Engheta, *Optical spectrometer at the nanoscale using optical Yagi-Uda nanoantennas*, Phys. Rev. B **79**, 195104 (2009).
- [133] J. N. Anker, W. P. Hall, O. Lyandres, N. C. Shah, J. Zhao, and R. P. van Duyne, *Biosensing with plasmonic nanosensors*, Nat. Mater. **7**, 442 (2008).
- [134] S. Kim, J. Jin, Y. Kim, I. Park, Y. Kim, and S. Kim, *High-harmonic generation by resonant plasmon field enhancement*, Nature **453**, 757 (2008).
- [135] D. Dregely, R. Taubert, J. Dorfmueller, R. Vogelgesang, K. Kern, and H. Giessen, *3D optical Yagi-Uda nanoantenna-array*, Nat. Commun. **2**, 267 (2011).
- [136] E. J. R. Vesseur, R. de Waele, H. J. Lezec, H. A. Atwater, F. J. Garcia de Abajo, and A. Polman, *Surface plasmon polariton modes in a single-crystal Au nanoresonator fabricated using focused-ion-beam milling*, Appl. Phys. Lett. **92**, 83110 (2008).
- [137] E. J. R. Vesseur, R. de Waele, M. Kuttge, and A. Polman, *Direct observation of plasmonic*

REFERENCES

- modes in Au nanowires using high-resolution cathodoluminescence spectroscopy*, Nano Lett. **7**, 2843 (2007).
- [138] R. Gómez-Medina, N. Yamamoto, M. Nakano, and F. J. García de Abajo, *Mapping plasmons in nanoantennas via cathodoluminescence*, New J. Phys. **10**, 105009 (2008).
- [139] D. Rossouw, V. J. Couillard, E. Kumacheva, and G. A. Botton, *Multipolar plasmonic resonances in silver nanowire antennas imaged with a subnanometer electron probe*, Nano Lett. **11**, 1499 (2011).
- [140] O. Nicoletti, M. Wubs, N. A. Asger Mortensen, W. Sigle, P. A. van Aken, and P. A. Midgley, *Surface plasmon modes of a single silver nanorod: an electron energy loss study*, Opt. Express **19**, 15371 (2011).
- [141] E. S. Barnard, A. R. Pala, and M. L. Brongersma, *Photocurrent mapping of near-field optical antenna resonances*, Nat. Nanotechnol. **6**, 588 (2011).
- [142] E. S. Barnard, T. Coenen, E. J. R. Vesseur, A. Polman, and M. L. Brongersma, *Imaging of hidden modes in ultra-thin plasmonic strip antennas by cathodoluminescence*, Nano Lett. **11**, 4265 (2011).
- [143] E. S. Barnard, J. S. White, A. Chandran, and M. L. Brongersma, *Spectral properties of plasmonic resonator antennas*, Opt. Express **16**, 16529 (2008).
- [144] T. H. Taminiau, F. D. Stefani, and N. F. van Hulst, *Optical nanorod antennas modeled as cavities for dipolar emitters: Evolution of sub- and super-radiant modes*, Nano Lett. **11**, 1020 (2011).
- [145] F. J. García de Abajo and A. Howie, *Relativistic electron energy loss and electron-induced photon emission in inhomogeneous dielectrics*, Phys. Rev. Lett. **80**, 5180 (1998).
- [146] F. J. García de Abajo and A. Howie, *Retarded field calculation of electron energy loss in inhomogeneous dielectrics*, Phys. Rev. B **65**, 115418 (2002).
- [147] S. B. Hasan, R. Filter, A. Ahmed, R. Vogelgesang, R. Gordon, C. Rockstuhl, and F. Lederer, *Relating localized nanoparticle resonances to an associated antenna problem*, Phys. Rev. B **84**, 195405 (2011).
- [148] H. Ditlbacher, A. Hohenau, D. Wagner, U. Kreibig, M. Rogers, F. Hofer, F. R. Aussenegg, and J. R. Krenn, *Silver nanowires as surface plasmon resonators*, Phys. Rev. Lett. **95**, 257403 (2005).
- [149] J. D. Jackson, *Classical electrodynamics, 3rd edition*, John Wiley and Sons, 1999.
- [150] N. J. Halas, S. Lal, W. Chang, S. Link, and P. Nordlander, *Plasmons in strongly coupled metallic nanostructures*, Chemical Reviews **111**, 3913 (2011).
- [151] L. Cao, J. S. White, J. Park, J. A. Schuller, B. M. Clemens, and M. L. Brongersma, *Engineering light absorption in semiconductor nanowire devices*, Nat. Mater. **8**, 643 (2009).
- [152] A. W. Snyder and J. D. Love, *Optical waveguide theory*, Chapman and Hall, London, 1983.
- [153] K. J. Klein Koerkamp, S. Enoch, F. B. Segerink, N. F. van Hulst, and L. Kuipers, *Strong influence of hole shape on extraordinary transmission through periodic arrays of subwavelength holes*, Phys. Rev. Lett. **92**, 183901 (2004).
- [154] O. L. Muskens, V. Giannini, J. A. Sánchez-Gil, and J. Gómez Rivas, *Optical scattering resonances of single and coupled dimer plasmonic nanoantennas*, Opt. Express **15**, 17736 (2007).
- [155] I. Sersic, C. Tuambilangana, and A. F. Koenderink, *Fourier microscopy of single plasmonic scatterers*, New J. Phys. **13**, 083019 (2011).
- [156] K. G. Lee, X. Chen, H. Eghlidi, P. Kukura, A. Lettow, R. Renn, V. Sandoghdar, and S. Göttinger, *A planar dielectric antenna for directional single-photon emission and*

- near-unity collection efficiency*, Nat. Photonics **5**, 166 (2011).
- [157] E. J. R. Vesseur and A. Polman, *Plasmonic whispering gallery cavities as optical antennas*, Nano Lett. **11**, 5524 (2011).
- [158] H. T. Lin, D. H. Rich, A. Konkar, P. Chen, and A. Madhukar, *Carrier relaxation and recombination in GaAs/AlGaAs quantum heterostructures and nanostructures probed with time-resolved cathodoluminescence*, J. Appl. Phys. **1997**, 3186 (81).
- [159] D. H. Rich, Y. Tang, A. Konkar, P. Chen, and A. Madhukar, *Polarized cathodoluminescence study of selectively grown self-assembled InAs/GaAs quantum dots*, J. Appl. Phys. **84**, 6337 (1998).
- [160] J. B. Lassiter, H. Sobhani, M. W. Knight, W. S. Mielczarek, P. Nordlander, and N. J. Halas, *Designing and deconstructing the Fano lineshape in plasmonic nanoclusters*, Nano Lett. **12**, 1058 (2012).
- [161] P. Bharadwaj, B. Deustsch, and L. Novotny, *Optical antennas*, Opt. Photonics **1**, 438 (2009).
- [162] N. Yu, J. Fan, Q. J. Wang, C. Pflügl, L. Diehl, T. Edamura, M. Yamanishi, H. Kan, and F. Capasso, *Small-divergence semiconductor lasers by plasmonic collimation*, Nat. Photonics **2**, 564 (2008).
- [163] L. Tang, S. E. Kocabas, S. Latif, A. K. Okyay, D. S. Ly-Gagnon, K. C. Saraswat, and D. A. B. Miller, *Nanometre-scale germanium photodetector enhanced by a near-infrared dipole antenna*, Nat. Photonics **2**, 226 (2008).
- [164] T. H. Taminiau, R. J. Moerland, F. B. Segerink, L. Kuipers, and N. F. van Hulst, *$\lambda/4$ resonance of an optical monopole antenna probed by single molecule fluorescence*, Nano Lett. **7**, 28 (2007).
- [165] J. H. Atwater, P. Spinelli, E. Kosten, J. Parsons, C. van Lare, J. van de Groep, F. J. García de Abajo, A. Polman, and H. A. Atwater, *Microphotonic parabolic light directors fabricated by two-photon lithography*, Appl. Phys. Lett. **99**, 151113 (2011).
- [166] Y. C. Jun, K. C. Y. Huang, and M. L. Brongersma, *Plasmonic beaming and active control over fluorescent emission*, Nat. Commun. **2**, 283 (2011).
- [167] H. J. Lezec, A. Degiron, E. Devaux, R. A. Linke, L. Martín-Moreno, F. J. Garcia-Vidal, and T. W. Ebbesen, *Beaming light from a subwavelength aperture*, Science **297**, 820 (2002).
- [168] S. Han and D. Norris, *Beaming thermal emission from hot metallic bull's eyes*, Opt. Express **18**, 4829 (2010).
- [169] T. Shegai, V. D. Miljković, K. Bao, H. Xu, P. Nordlander, P. Johansson, and M. Käll, *Unidirectional broadband light emission from supported plasmonic nanowires*, Nano Lett. **11**, 706 (2011).
- [170] D. T. Schoen, T. Coenen, F. J. García de Abajo, M. L. Brongersma, and P. A., *The planar parabolic optical antenna*, Nano Lett. **13**, 188 (2013).
- [171] J. P. Tetienne, R. Blanchard, N. Yu, P. Genevet, M. A. Kats, J. A. Fan, T. Edamura, S. Furuta, M. Yamanishi, and F. Capasso, *Dipolar modeling and experimental demonstration of multi-beam plasmonic collimators*, New J. Phys. **13**, 053057 (2011).
- [172] P. Nagpal, N. C. Lindquist, S. H. Oh, and D. J. Norris, *Ultrasoother patterned metals for plasmonics and metamaterials*, Science **325**, 594 (2009).
- [173] X. Zhu, J. Zhang, J. Xu, H. Li, X. Wu, Z. Liao, Q. Zhao, and D. P. Yu, *Dispersion control in plasmonic open nanocavities*, ACS Nano **5**, 6546 (2011).
- [174] C. Chicanne, T. David, R. Quidant, J. Weeber, Y. Lacroute, E. Bourillot, A. Dereux, G. Colas des Francs, and C. Girard, *Imaging the local density of states of optical corrals*, Phys. Rev. Lett. **88**, 97402 (2002).
- [175] Y. Babayan, J. McMahon, S. Li, S. Gray, G. Schatz, and T. Odom, *Confining standing*

REFERENCES

- waves in optical corrals*, ACS Nano **3**, 615 (2009).
- [176] G. Colas des Francs, C. Girard, J. Weeber, C. Chicane, T. David, A. Dereux, and D. Peyrade, *Optical analogy to electronic quantum corrals*, Phys. Rev. Lett. **86**, 4950 (2001).
- [177] T. Søndergaard and S. I. Bozhevolnyi, *Strip and gap plasmon polariton optical resonators*, Phys. Status Solidi B **245**, 9 (2008).
- [178] A. Drezet, A. L. Stepanov, H. Ditlbacher, A. Hohenau, B. Steinberger, F. R. Aussenegg, A. Leitner, and J. R. Krenn, *Surface plasmon propagation in an elliptical corral*, Appl. Phys. Lett. **86**, 074104 (2005).
- [179] T. Kosako, Y. Kadoya, and H. F. Hofmann, *Directional control of light by a nano-optical Yagi-Uda antenna*, Nat. Photonics **4**, 312 (2010).
- [180] T. Shegai, S. Chen, V. D. Miljković, G. Zentgraf, T. Zengin, P. Johansson, and M. Käll, *A bimetallic nanoantenna for directional colour routing*, Nat. Commun. **2**, 481 (2011).
- [181] F. Bernal Arango, A. Kwadrin, and A. F. Koenderink, *Plasmonic antennas hybridized with dielectric waveguides*, ACS Nano **6**, 10156 (2012).
- [182] M. Kerker, D. S. Wang, and C. L. Giles, *Electromagnetic scattering by magnetic spheres*, J. Opt. Soc. Am. **73**, 765 (1983).
- [183] B. Rolly, B. Stout, and N. Bonod, *Boosting the directivity of optical antennas with magnetic and electric dipolar resonant particles*, Opt. Express **20**, 20376 (2012).
- [184] S. Person, M. Jain, Z. Lapin, J. J. Sáenz, G. Wicks, and L. Novotny, *Demonstration of zero optical backscattering from single nanoparticles*, Nano Lett. **13**, 1806 (2013).
- [185] Y. H. Fu, A. I. Kuznetsov, A. E. Miroshnichenko, Y. F. Yu, and B. Luk'yanchuk, *Directional visible light scattering by silicon nanoparticles*, Nat. Commun. **4**, 1527 (2013).
- [186] F. J. Rodríguez-Fortuño, G. Marino, P. Ginzburg, D. O'Connor, A. Martínez, G. A. Wurtz, and A. V. Zayats, *Near-field interference for the unidirectional excitation of electromagnetic guided modes*, Science **340**, 328 (2013).
- [187] D. Vercruyssen, Y. Sonnefraud, N. Verellen, F. B. Fuchs, G. Di Martino, L. Lagae, V. V. Moschchalkov, S. A. Maier, and P. van Dorpe, *Unidirectional side scattering of light by a single-element nanoantenna*, Nano Lett. **13**, 3843 (2013).
- [188] I. Staude, A. E. Miroshnichenko, M. Decker, N. T. Fofang, S. Liu, E. Gonzales, J. Dominguez, T. S. Luk, D. N. Neshev, I. Brener, and Y. Kivshar, *Tailoring directional scattering through magnetic and electric resonances in subwavelength silicon nanodisks*, ACS Nano **7**, 7824 (2013).
- [189] I. M. Hancu, A. G. Curto, M. Castro-López, Kuttge, and N. F. van Hulst, *Multipolar interference for directed light emission*, Nano Lett. **14**, 166 (2014).
- [190] J. Nelayah, M. Kociak, O. Stéphan, F. J. García de Abajo, M. Tencé, L. Henrard, D. Taverna, I. Pastoriza-Santos, L. M. Liz-Marzán, and C. Colliex, *Mapping surface plasmons on a single metallic nanoparticle*, Nat. Phys. **3**, 348 (2007).
- [191] A. L. Koh, A. Fernández-Domínguez, D. McComb, S. Maier, and J. Yang, *High-resolution mapping of electron-beam-excited plasmon modes in lithographically defined gold nanostructures*, Nano Lett. **11**, 1323 (2011).
- [192] M. W. Knight, L. Liu, Y. Wang, L. Brown, S. Mukherjee, N. S. King, H. O. Everitt, P. Nordlander, and N. J. Halas, *Aluminum plasmonic nanoantennas*, Nano Lett. **12**, 6000 (2012).
- [193] F. P. Schmidt, H. Ditlbacher, U. Hohenester, A. Hohenau, F. Hofer, and J. R. Krenn, *Dark plasmonic breathing modes in silver nanodisks*, Nano Lett. **12**, 5780 (2012).
- [194] J. A. Scholl, A. L. Koh, and J. A. Dionne, *Quantum plasmon resonances of individual metallic nanoparticles*, Nature **483**, 421 (2012).

-
- [195] C. Bohren and D. Huffman, *Absorption and scattering of light by small particles*, Wiley-Interscience, 1983.
- [196] H. Mertens and A. Polman, *Strong luminescence quantum-efficiency enhancement near prolate metal nanoparticles: Dipolar versus higher-order modes*, J. Appl. Phys. **105**, 044302 (2009).
- [197] A. G. Curto, T. H. Taminiau, G. Volpe, M. P. Kreuzer, R. Quidant, and N. F. van Hulst, *Multipolar radiation of quantum emitters with nanowire optical antennas*, Nat. Commun. **4**, 1750 (2013).
- [198] A. M. Kern and O. J. F. Martin, *Surface integral formulation for 3D simulations of plasmonic and high permittivity nanostructures*, J. Opt. Soc. Am. A **26**, 732 (2009).
- [199] F. Bernal Arango and A. F. Koenderink, *Polarizability tensor retrieval for magnetic and plasmonic antenna design*, New J. Phys. **15**, 073023 (2013).
- [200] I. Sersic, M. A. van de Haar, F. Bernal Arango, and A. F. Koenderink, *Ubiquity of optical activity in planar metamaterial scatterers*, Phys. Rev. Lett. **108**, 223903 (2012).
- [201] F. Bernal Arango, T. Coenen, and A. F. Koenderink, *Underpinning hybridization intuition for complex antennas by magnetoelectric quadrupolar polarizability retrieval*, In preparation (2014).
- [202] W. Lukosz and R. E. Kunz, *Light emission by magnetic and electric dipoles close to a plane interface*, J. Opt. Soc. Am. **67**, 1607 (1977).
- [203] M. Ribarič and L. Šušteršič, *Expansions in terms of moments of time-dependent, moving charges and currents*, SIAM J. Appl. Math. **55**, 593 (1995).
- [204] T. H. Taminiau, S. Karaveli, N. F. van Hulst, and R. Zia, *Quantifying the magnetic nature of light emission*, Nat. Commun. **3**, 1984 (2012).
- [205] F. J. Garcia-Vidal, L. Martin-Moreno, T. W. Ebbesen, and L. Kuipers, *Light passing through subwavelength apertures*, Rev. Mod. Phys. **82**, 729 (2010).
- [206] H. Rigneault, J. Capoulade, J. Dintinger, J. Wenger, N. Bonod, E. Popov, T. W. Ebbesen, and P. Lenne, *Enhancement of single-molecule fluorescence detection in subwavelength apertures*, Phys. Rev. Lett. **95**, 117401 (2005).
- [207] F. Falcone, T. Lopetegui, M. A. G. Laso, J. D. Baena, J. Bonache, M. Beruete, R. Marques, and F. Martin, *Babinet principle applied to the design of metasurfaces and metamaterials*, Phys. Rev. Lett. **93**, 197401 (2004).
- [208] T. Zentgraf, T. P. Meyrath, A. Seidel, S. Kaiser, and H. Giessen, *Babinet's principle for optical frequency metamaterials and nanoantennas*, Phys. Rev. B **76**, 033407 (2007).
- [209] B. Ögüt, R. Vogelgesang, W. Sigle, N. Talebi, C. T. Koch, and P. A. van Aken, *Hybridized metal slit eigenmodes as an illustration of Babinet's principle*, ACS Nano **5**, 6701 (2011).
- [210] D. Rossouw and G. A. Botton, *Resonant optical excitations in complementary plasmonic nanostructures*, Opt. Express **20**, 6968 (2012).
- [211] F. J. García de Abajo, *Colloquium: Light scattering by particle and hole arrays*, Rev. Mod. Phys. **79**, 1267 (2007).
- [212] G. Gay, O. Alloschery, B. Viaris de Lesegno, C. O'Dwyer, J. Weiner, and H. J. Lezec, *The optical response of nanostructured surfaces and the composite diffracted evanescent wavemodel*, Nat. Phys. **2**, 262 (2006).
- [213] H. Liu and P. Lalanne, *Microscopic theory of the extraordinary optical transmission*, Nature **452**, 728 (2008).
- [214] J. Parsons, E. Hendry, C. P. Burrows, B. Auguie, J. R. Sambles, and W. L. Barnes, *Localized surface-plasmon resonances in periodic nondiffracting metallic nanoparticle and nanohole arrays*, Phys. Rev. B **79**, 073412 (2009).
- [215] N. Rotenberg, M. Spasenović, T. L. Krijger, B. le Feber, F. J. García de Abajo, and

REFERENCES

- L. Kuipers, *Plasmon scattering from single subwavelength holes*, Phys. Rev. Lett. **108**, 127402 (2012).
- [216] F. van Beijnum, C. Rétif, C. B. Smiet, H. Liu, P. Lalanne, and M. P. van Exter, *Quasi-cylindrical wave contribution in experiments on extraordinary optical transmission*, Nature **492**, 411 (2012).
- [217] T. W. Ebbesen, H. J. Lezec, H. F. Ghaemi, T. Thio, and P. A. Wolff, *Extraordinary optical transmission through sub-wavelength hole arrays*, Nature **391**, 667 (1998).
- [218] J. Braun, B. Gompf, G. Kobiela, and M. Dressel, *How holes can obscure the view: Suppressed transmission through an ultrathin metal film by a subwavelength hole array*, Phys. Rev. Lett. **103**, 203901 (2009).
- [219] N. Rotenberg, T. L. Krijger, B. le Feber, F. J. García de Abajo, and L. Kuipers, *Magnetic and electric response of single subwavelength holes*, Phys. Rev. B **88**, 241408 (2013).
- [220] W. Sigle, J. Nelayah, and C. T. Koch, *Electron energy losses in Ag nanoholes - from localized surface plasmon resonances to rings of fire*, Opt. Lett. **34**, 2150 (2009).
- [221] J. C. Prangma, D. van Oosten, and L. Kuipers, *Local investigation of the optical properties of subwavelength rectangular holes with a focused beam of electrons*, Phil. Trans. R. Soc. A **369**, 3456 (2011).
- [222] F. von Cube, J. Irsen, S. Niegemann, C. Matyssek, W. Hergert, K. Busch, and S. Linden, *Spatio-spectral characterization of photonic meta-atoms with electron energy-loss spectroscopy*, Opt. Mater. Express **5**, 1009 (2011).
- [223] V. J. Logeeswaran, N. P. Kobayashi, M. S. Islam, W. Wu, P. Chaturvedi, N. X. Fang, S. Y. Wang, and R. S. Williams, *Ultrasoother silver thin films deposited with a germanium nucleation layer*, Nano Lett. **9**, 178 (2009).
- [224] H. Liu, B. Wang, E. S. P. Leong, P. Yang, Y. Zong, G. Si, J. Teng, and S. A. Maier, *Enhanced surface plasmon resonance on a smooth silver film with a seed growth layer*, ACS Nano **4**, 3139 (2010).
- [225] J. van Wijngaarden, E. Verhagen, A. Polman, C. Ross, H. J. Lezec, and H. A. Atwater, *Direct imaging of propagation and damping of near-resonance surface plasmon polaritons using cathodoluminescence spectroscopy*, Appl. Phys. Lett. **88**, 221111 (2006).
- [226] M. V. Bashevoy, F. Jonsson, K. F. MacDonald, Y. Chen, and N. I. Zheludev, *Hyperspectral imaging of plasmonic nanostructures with nanoscale resolution*, Opt. Express **15**, 11313 (2007).
- [227] M. Kuttge, E. J. R. Vesseur, J. Verhoeven, H. J. Lezec, H. A. Atwater, and A. Polman, *Loss mechanisms of surface plasmon polaritons on gold probed by cathodoluminescence imaging spectroscopy*, Appl. Phys. Lett. **93**, 113110 (2008).
- [228] FDTD solutions; Lumerical Solutions Inc.; www.lumerical.com.
- [229] S. Karaveli and R. Zia, *Strong enhancement of magnetic dipole emission in a multilevel electronic system*, Opt. Lett. **35**, 3318 (2010).
- [230] A. Kwadrin and A. F. Koenderink, *Probing the electrodynamic local density of states with magnetoelectric point scatterers*, Phys. Rev. B **87**, 125123 (2013).
- [231] J. van de Groep and A. Polman, *Designing dielectric resonators on substrates: Combining magnetic and electric resonances*, Opt. Express **21**, 26285 (2013).
- [232] F. López-Tejiera, S. G. Rodrigo, L. Martín-Moreno, F. J. García-Vidal, E. Devaux, T. W. Ebbesen, J. R. Krenn, I. P. Radko, S. I. Bozhevolnyi, M. U. González, J. C. Weeber, and A. Dereux, *Efficient unidirectional nanoslit couplers for surface plasmons*, Nat. Phys. **3**, 324 (2007).
- [233] H. Aouani, O. Mahboub, N. Bonod, E. Devaux, E. Popov, H. Rigneault, T. W.

- Ebbesen, and J. Wenger, *Bright unidirectional fluorescence emission of molecules in a nanoaperture with plasmonic corrugations*, Nano Lett. **11**, 637 (2011).
- [234] S. Y. Lee, I. M. Lee, J. Park, S. Oh, W. Lee, K. Y. Kim, and B. Lee, *Role of magnetic induction currents in nanoslit excitation of surface plasmon polaritons*, Phys. Rev. Lett. **108**, 213907 (2012).
- [235] S. Zhang, D. A. Genov, Y. Wang, M. Liu, and X. Zhang, *Plasmon-induced transparency in metamaterials*, Phys. Rev. Lett. **101**, 047401 (2008).
- [236] N. Verellen, Y. Sonnefraud, H. Sobhani, F. Hao, V. V. Moshchalkov, P. Van Dorpe, P. Nordlander, and S. A. Maier, *Fano resonances in individual coherent plasmonic nanocavities*, Nano Lett. **9**, 1663 (2009).
- [237] N. Liu, L. Langguth, T. Weiss, J. Kästel, M. Fleischhauer, T. Pfau, and H. Giessen, *Plasmonic analogue of electromagnetically induced transparency at the Drude damping limit*, Nat. Mater. **8**, 758 (2009).
- [238] N. Liu, T. Weiss, M. Mesch, L. Langguth, U. Eigenthaler, M. Hirscher, C. Sönnichsen, and H. Giessen, *Planar metamaterial analogue of electromagnetically induced transparency for plasmonic sensing*, Nano Lett. **10**, 1103 (2010).
- [239] S. N. Sheikholeslami, A. García-Extarri, and J. A. Dionne, *Controlling the interplay of electric and magnetic modes via Fano-like plasmon resonances*, Nano Lett. **11**, 3927 (2011).
- [240] W. S. Chang, J. B. Lassiter, P. Swanglap, H. Sobhani, S. Khatua, P. Nordlander, N. J. Halas, and S. Link, *A plasmonic Fano switch*, Nano Lett. **12**, 4977 (2012).
- [241] M. Frimmer, T. Coenen, and A. F. Koenderink, *Signature of a Fano-resonance in a plasmonic meta-molecule's local density of optical states*, Phys. Rev. Lett. **108**, 077404 (2012).
- [242] R. Hokari, Y. Kanamori, and K. Hane, *Comparison of electromagnetically induced transparency between silver, gold, and aluminum metamaterials at visible wavelengths*, Opt. Express **22**, 3526 (2014).
- [243] Z. Zheyu Fang, Y. Wang, Z. Liu, A. Schlather, P. M. Ajayan, F. H. L. Koppens, P. Nordlander, and N. J. Halas, *Plasmon-induced doping of graphene*, ACS Nano **6**, 10222 (2012).
- [244] B. Gallinet and O. J. F. Martin, *Refractive index sensing with subradiant modes: A framework to reduce losses in plasmonic nanostructures*, ACS Nano **7**, 6978 (2013).
- [245] Z. Ye, S. Zhang, Y. Wang, Y. Park, T. Zentgraf, G. Bartal, X. Yin, and X. Zhang, *Mapping the near-field dynamics in plasmon-induced transparency*, Phys. Rev. B **86**, 155148 (2012).
- [246] C. Forestiere, L. Dal Negro, and G. Miano, *Theory of coupled plasmon modes and Fano-like resonances in subwavelength metal structures*, Phys. Rev. B **88**, 155411 (2013).
- [247] S. R. K. Rodriguez, S. Murai, M. A. Verschuuren, and J. Gómez Rivas, *Light-emitting waveguide-plasmon polaritons*, Phys. Rev. Lett. **109**, 166803 (2012).
- [248] S. R. K. Rodriguez, O. T. A. Janssen, G. Lozano, A. Omari, Z. Hens, and J. Gómez Rivas, *Near-field resonance at far-field-induced transparency in diffractive arrays of plasmonic nanorods*, Opt. Lett. **38**, 1238 (2013).
- [249] S. Weitemeyer, M. Husnik, and M. Wegener, *Observation of unusual absorption and scattering cross-section line shapes of individual optical double-wire antennas*, Appl. Phys. Lett. **104**, 031111 (2014).
- [250] I. Alber, W. Sigle, S. Müller, R. Neumann, O. Picht, M. Rauber, P. A. van Aken, and M. A. Toimil-Molares, *Visualization of multipolar longitudinal and transversal surface plasmon modes in nanowire dimers*, ACS Nano **5**, 9845 (2011).

REFERENCES

- [251] N. W. Bigelow, J. P. Vaschillo, Camden, and D. J. Masiello, *Signatures of Fano interferences in the electron energy loss spectroscopy and cathodoluminescence of symmetry-broken nanorod dimers*, ACS Nano **7**, 4511 (2013).
- [252] J. A. Scholl, A. García-Etxarri, A. L. Koh, and J. A. Dionne, *Observation of quantum tunneling between two plasmonic nanoparticles*, Nano Lett. **13**, 564 (2013).
- [253] J. Zuloaga and P. Nordlander, *On the energy shift between near-field and far-field peak intensities in localized plasmon systems*, Nano Lett. **11**, 1280 (2011).
- [254] V. Myroshnychenko, J. Nelayah, G. Adamo, N. Geuquet, J. Rodríguez-Fernández, I. Pastoriza-Santos, K. F. MacDonald, L. Henrard, L. M. Liz-Marzán, N. I. Zheludev, M. Kociak, and F. J. García de Abajo, *Plasmon spectroscopy and imaging of individual gold nanodecahedra: a combined optical microscopy, cathodoluminescence, and electron energy-loss spectroscopy study*, Nano Lett. **12**, 4172 (2012).
- [255] M. Husnik, F. von Cube, S. Irsen, S. Linden, S. J. Niegemann, K. Busch, and M. Wegener, *Comparison of electron energy-loss and quantitative optical spectroscopy on individual optical gold antennas*, Nanophotonics **2**, 241 (2013).
- [256] M. W. Chu, V. Myroshnychenko, C. H. Chen, J. P. Deng, C. Y. Mou, and F. J. García de Abajo, *Probing bright and dark surface-plasmon modes in individual and coupled noble metal nanoparticles using an electron beam*, Nano Lett. **9**, 399 (2009).
- [257] E. Prodan, C. Radloff, N. J. Halas, and P. Nordlander, *A hybridization model for the plasmon response of complex nanostructures*, Science **302**, 419 (2003).
- [258] P. Nordlander, C. Oubre, E. Prodan, K. Li, and M. I. Stockman, *Plasmon hybridization in nanoparticle dimers*, Nano Lett. **4**, 899 (2004).
- [259] S. C. Yang, H. Kobori, C. L. He, M. E. Lin, H. Y. Chen, C. Li, M. Kanehara, T. Teranishi, and S. Gwo, *Plasmon hybridization in individual gold nanocrystal dimers: Direct observation of bright and dark modes*, Nano Lett. **10**, 632 (2010).
- [260] J. Kern, S. Großmann, N. V. Tarakina, T. Háckel, M. Emmerling, M. Kamp, J. S. Huang, P. Biagioni, J. C. Prangsma, and B. Hecht, *Atomic-scale confinement of resonant optical fields*, Nano Lett. **12**, 5504 (2012).
- [261] P. Pablo Alonso-González, P. Albella, F. Golmar, L. Arzubíaga, F. Casanova, L. E. Hueso, J. Aizpurua, and R. Hillenbrand, *Visualizing the near-field coupling and interference of bonding and anti-bonding modes in infrared dimer nanoantennas*, Opt. Express **21**, 1270 (2013).
- [262] A. L. Koh, K. Bao, I. Khan, W. E. Smith, G. Kothleitner, P. Nordlander, S. A. Maier, and D. W. McComb, *Electron energy-loss spectroscopy (EELS) of surface plasmons in single silver nanoparticles and dimers: influence of beam damage and mapping of dark modes*, ACS Nano **3**, 3015 (2009).
- [263] E. M. Purcell, *Spontaneous emission probabilities at radio frequencies*, Phys. Rev. **69**, 681 (1946).
- [264] S. John, *Strong localization of photons in certain disordered dielectric superlattices*, Phys. Rev. Lett. **58**, 2486 (1987).
- [265] P. D. García, R. Sapienza, L. Froufe-Pérez, and C. López, *Strong dispersive effects in the light-scattering mean free path in photonic gaps*, Phys. Rev. B **79**, 241109(R) (2009).
- [266] A. Badolato, K. Hennesy, M. Atatüre, J. Dreiser, E. Hu, P. M. Petroff, and A. Imamoglu, *Deterministic coupling of single quantum dots to single nanocavity modes*, Science **308**, 1158 (2005).
- [267] D. Englund, D. Fattal, E. Waks, G. Solomon, B. Zhang, T. Nakaoka, Y. Arakawa, Y. Yamamoto, and J. Vučković, *Controlling the spontaneous emission rate of single quantum dots in a 2D photonic crystal*, Phys. Rev. Lett. **95**, 013904 (2005).

- [268] Y. Akahane, T. Asano, B. Song, and S. Noda, *High-Q photonic nanocavity in a 52 two-dimensional photonic crystal*, Nature **425**, 944 (2003).
- [269] S. Kühn, C. Hettich, C. Schmitt, J. P. Poizat, and V. Sandoghdar, *Diamond colour centres as a nanoscopic light source for scanning near-field optical microscopy*, J. Microsc. **202**, 2 (2001).
- [270] D. Englund, B. Shields, K. Rivoire, F. Hatami, J. Vučković, H. Park, and M. D. Lukin, *Deterministic coupling of a single nitrogen vacancy center to a photonic crystal cavity*, Nano Lett. **10**, 3922 (2010).
- [271] G. Colas des Francs, C. Girard, J. Weeber, and A. Dereux, *Relationship between scanning near-field optical images and local density of photonic states*, Chem. Phys. Lett. **345**, 512 (2001).
- [272] S. Vignolini, F. Intonti, F. Riboli, D. S. Wiersma, L. Balet, L. H. Li, M. Francardi, A. Gerardino, A. Fiore, and M. Gurioli, *Polarization-sensitive near-field investigation of photonic crystal microcavities*, Appl. Phys. Lett. **94**, 163102 (2009).
- [273] Y. De Wilde, F. Formanek, R. Carminati, B. Gralak, P. A. Lemoine, K. Joulain, J. P. Mulet, Y. Chen, and J. J. Greffet, *Thermal radiation scanning tunnelling microscopy*, Nature **444**, 740 (2006).
- [274] M. Notomi, *Manipulating light with strongly modulated photonic crystals*, Rep. Prog. Phys. **73**, 096501 (2010).
- [275] J. Vučković, M. Lončar, H. Mabuchi, and A. Scherer, *Optimization of the Q factor in photonic crystal microcavities*, IEEE J. Quantum Electron. **38**, 850 (2002).
- [276] M. Kuttge, *Cathodoluminescence plasmon microscopy*, PhD thesis, AMOLF, 2009.
- [277] P. Hovington, D. Drouin, and R. Gauvin, *CASINO: A new Monte Carlo code in C language for electron beam interaction*, Scanning **19**, 1 (1997).
- [278] A. J. Schuller and M. L. Brongersma, *General properties of dielectric optical antennas*, Opt. Express **17**, 24084 (2009).
- [279] R. Sainidou, J. Renger, T. V. Teperik, M. U. González, R. Quidant, and F. J. García de Abajo, *Extraordinary all-dielectric light enhancement over large volumes*, Nano Lett. **10**, 4450 (2010).
- [280] G. Grzela, D. Hourlier, and J. Gómez Rivas, *Polarization-dependent light extinction in ensembles of polydisperse vertical semiconductor nanowires: A Mie scattering effective medium*, Phys. Rev. B **86**, 045305 (2012).
- [281] M. D. Kelzenberg, S. W. Boettcher, J. A. Petykiewicz, D. B. Turner-Evans, M. C. Putnam, E. L. Warren, and J. M. Spurgeon, *Enhanced absorption and carrier collection in Si wire arrays for photovoltaic applications*, Nat. Mater. **9**, 239 (2010).
- [282] J. Grandidier, D. M. Callahan, J. N. Munday, and H. A. Atwater, *Light absorption enhancement in thin-film solar cells using whispering gallery modes in dielectric nanospheres*, Adv. Mater. **23**, 1272 (2011).
- [283] A. Raman, Z. Yu, and S. Fan, *Dielectric nanostructures for broadband light trapping in organic solar cells*, Opt. Express **19**, 19015 (2011).
- [284] S. Mann, R. R. Grote, R. M. Osgood, and J. A. Schuller, *Dielectric particle and void resonators for thin film solar cell textures*, Opt. Express **19**, 25729 (2011).
- [285] S. Kim, R. W. Day, J. F. Cahoon, T. J. Kempa, K. Song, H. Park, and C. M. Lieber, *Tuning light absorption in core/shell silicon nanowire photovoltaic devices through morphological design*, Nano Lett. **12**, 4971 (2012).
- [286] Y. Yu, V. E. Ferry, A. P. Alivisatos, and L. Cao, *Dielectric core-shell optical antennas for strong solar absorption enhancement*, Nano Lett. **12**, 3674 (2012).
- [287] Y. Yao, J. Yao, V. K. Narasimhan, Z. Ruan, C. Xie, S. Fan, and Y. Cui, *Broadband light*

- management using low-Q whispering gallery modes in spherical nanoshells*, Nat. Commun. **3**, 664 (2012).
- [288] A. P. Vasudev, A. J. Schuller, and M. L. Brongersma, *Nanophotonic light trapping with patterned transparent conductive oxides*, Opt. Express **20**, A385 (2012).
- [289] J. Tang, Z. Huo, S. Brittman, H. Gao, and P. Yang, *Solution-processed core-shell nanowires for efficient photovoltaic cells*, Nat. Nanotechnol. **6**, 568 (2011).
- [290] K. L. van de Molen, P. Zijlstra, A. Lagendijk, and A. P. Mosk, *Laser threshold of Mie resonances*, Opt. Lett. **31**, 1432 (2006).
- [291] L. Cao, J. Park, P. Fan, B. Clemens, and M. L. Brongersma, *Resonant germanium nanoantenna photodetectors*, Nano Lett. **10**, 1229 (2010).
- [292] A. Alù and N. Engheta, *Cloaking a sensor*, Phys. Rev. Lett. **102**, 233901 (2009).
- [293] P. Fan, U. K. Chettiar, L. Cao, F. Afshinmanesh, N. Engheta, and M. L. Brongersma, *An invisible metal-semiconductor photodetector*, Nat. Photonics **6**, 380 (2012).
- [294] R. Yan, J. Park, Y. Choi, C. Heo, S. Yang, L. P. Lee, and P. Yang, *Nanowire-based single-cell endoscopy*, Nat. Nanotechnol. **7**, 191 (2011).
- [295] T. J. Kippenberg and K. J. Vahala, *Cavity opto-mechanics in: Practical applications of microresonators in optics and photonics*, CRC Press: Boca Raton (2009).
- [296] A. García-Etxarri, R. Gómez-Medina, L. S. Froufe-Pérez, C. López, L. Chantada, F. Scheffold, J. Aizpurua, M. Nieto-Vesperinas, and J. J. Sáenz, *Strong magnetic response of submicron silicon particles in the infrared*, Opt. Express **19**, 4815 (2011).
- [297] Q. Zhao, L. Kang, B. Du, H. Zhao, Q. Xie, X. Huang, B. Li, J. Zhou, and L. Li, *Experimental demonstration of isotropic negative permeability in a three-dimensional dielectric composite*, Phys. Rev. Lett. **101**, 027402 (2009).
- [298] Q. Zhao, J. Zhou, F. Zhang, and D. Lippens, *Mie resonance-based dielectric metamaterials*, Mater. Today **12**, 60 (2009).
- [299] A. B. Evlyukhin, S. M. Novikov, U. Zywiets, R. L. Eriksen, C. Reinhardt, S. I. Bozhevolnyi, and B. N. Chichkov, *Demonstration of magnetic dipole resonances of dielectric nanospheres in the visible region*, Nano Lett. **12**, 3749 (2012).
- [300] M. A. Schmidt, R. Esteban, J. J. Sáenz, I. Suárez-Lacalle, S. Mackowski, and J. Aizpurua, *Dielectric antennas: A suitable platform for controlling magnetic dipolar emission*, Opt. Express **20**, 13636 (2012).
- [301] R. E. Slusher, A. F. J. Levi, U. Mohideen, S. L. McCall, S. J. Pearton, and R. A. Logan, *Threshold characteristics of semiconductor microdisk lasers*, Appl. Phys. Lett. **63**, 1310 (1993).
- [302] Y. Yu and L. Cao, *Coupled leaky mode theory for light absorption in 2D, 1D and 0D semiconductor nanostructures*, Opt. Express **20**, 13847 (2012).

Summary

The field of microscopy is an important cornerstone of physical and biological sciences. The development of high-resolution microscopy/nanoscopy techniques has enabled a revolution in science and technology, greatly improving our understanding of the microscopic world around us, and forming the basis for the development of advanced nanotechnology. Similar to electrical integrated circuits there currently is a drive to miniaturize optical components with the aim to generate, detect, guide, or switch light on the nanoscale. To support this emerging field of nanophotonics, experimental techniques that can characterize optical properties on this length scale are required. In this thesis we present a novel experimental nanoscopy technique that can be used as a nanoscale characterization tool for optical properties: Angle-Resolved Cathodoluminescence (CL) Imaging Spectroscopy (ARCIS).

This technique combines electron microscopy with optical microscopy, giving it an excitation resolution greatly exceeding that of optical microscopy, while retaining optical sensitivity. Using ARCIS both the emission spectrum and the angular emission profile of optical nanostructures can be measured with great accuracy. Chapter 2 explains the operating principles of the technique. We discuss the various forms of electron-material interaction and electron-induced radiation, and give a detailed technical description of the setup. We also briefly discuss electron energy-loss spectroscopy (EELS) which is a complementary technique to ARCIS. In Chapter 3 we describe the calculation procedures for retrieving the angular emission pattern of a nanostructure using ARCIS. The technique is calibrated by studying the angle-resolved radiation pattern of a known source of radiation: transition radiation from a single-crystalline gold substrate.

In the body of the thesis we have applied the ARCIS technique to a variety of metallic and dielectric nanostructures to demonstrate its general applicability to nanophotonics. Most of these structures act as nanoantennas which are the elementary building blocks in nanophotonics. Nanoantennas form an interface between the near field and the far field and can exhibit complex angular patterns and scattering spectra which can be accurately probed by ARCIS. Throughout this thesis we have employed state-of-the-art nanofabrication techniques such as electron

beam lithography and focused-ion-beam milling which allow precise engineering of optical structures on the nanoscale.

In Chapter 4 we use ARCIS to study the optical properties an array of five gold nanoparticles which acts as a subwavelength optical Yagi-Uda antenna. We demonstrate that the antenna array is strongly directional and that the directionality can be controlled by selectively driving one of the antenna elements. The angular response of the array antenna is modeled using a coupled dipole model which takes into account interparticle coupling and interaction with the reflective substrate.

In Chapter 5 we focus on the optical properties of gold plasmonic ridge antennas of different length which act as traveling wave antennas. The reflective end facets of the ridge antenna cause standing wave modes which can be visualized with ARCIS. From the data we extract a dispersion relation for the guided ridge plasmon mode. We also study the angular pattern and find that for small ridges the angular pattern can be described by a single dipole. For longer antennas we find a more complex fringe pattern, resulting from the interference of the two radiating end facets of the ridge antennas.

Chapter 6 introduces polarization-sensitive Fourier microscopy as a further extension of the ARCIS technique. We analyze the angular and polarization distributions for transition radiation from a gold surface and from a gold ridge antenna and compare these with the theoretical distributions. We find that we can accurately predict the experimentally measured polarization-filtered angular profile when the theoretical polarization and angular pattern of emission are known. Furthermore, we demonstrate that it is also possible to reconstruct the emission polarization without *a priori* knowledge of the source, enabling accurate determination of the electrical dipole moment orientation.

In Chapter 7 we use ARCIS to characterize elliptical arena cavities that are milled into a gold substrate. We image the plasmon modes inside the cavities and find that the resonance spectrum is solely determined by the major axis length and the reflection phase pickup at the cavity boundaries. We demonstrate that these elliptical cavities act as parabolic antennas and hence can show a remarkably strong directionality which can be tuned with size, ellipse eccentricity, wavelength, and the electron beam excitation position.

Chapter 8 describes how a single plasmonic nanoparticle can act as directional scatterer. Using ARCIS, we find that the angular response of the nanoparticle strongly depends on excitation position and that this can be used to beam light in a well-defined direction. The beaming is caused by interference between in-plane and out-of-plane electric and magnetic multipole components. The directionality is enhanced for larger particles, which is caused by higher-order multipole contributions to the scattering. Using a combination of full-wave simulations and analytical point-scattering theory we determine the relative contribution of different multipoles.

In Chapter 9 we study the spectral and angular properties of nanoscale holes in a gold film. We study the decay of the CL signal away from the hole to distinguish

between direct near-field coupling and indirect surface plasmon polariton excitation. Furthermore, we find a striking complementarity in the directionality of the emission compared to that of the nanoparticles studied in Chapter 8. The data are compared to full-wave simulations and a simple analytical model. The data suggest that the observed directionality is caused by the Kerker effect where magnetic and electric dipole components interfere in the far-field.

In Chapter 10 we use EELS and CL measurements to gain more insight into the near-field coupling in composite plasmonic “dolmen” antennas. We demonstrate that the degree of coupling to different modes of the system can be controlled by precisely positioning the electron beam. Furthermore, we study the effect of size, particle spacing, and excitation position on the spectra. The EELS and CL measurements were performed on the same structures enabling a direct comparison between the two. We find that in some cases EELS and CL yield very similar information, while in other cases they are distinct, related to differences in the modal scattering efficiencies.

Chapters 4-10 discuss the optical properties of plasmonic metal nanostructures. In Chapters 11 and 12 we move to dielectric/semiconductor nanostructures which form an important class of structures within nanophotonics as well. In Chapter 11 we study the optical modes in 2D silicon nitride photonic crystal membranes using ARCIS. We use CL to image delocalized modes in hexagonal 2D crystals and localized modes in photonic crystal cavities. Using momentum spectroscopy we visualize the spatially-resolved dispersion in the crystal.

Finally, in Chapter 12 we study the resonant behavior of silicon nanodiscs using ARCIS. We measure resonance spectra and determine the corresponding field profiles for different disc diameters. We find that larger discs support multiple Mie resonances with complex modal profiles. Using the angular emission profiles we resolve the electric and magnetic nature of the disc resonances, and elucidate their directional properties.

Overall, this thesis introduces Angle-resolved Cathodoluminescence Imaging Spectroscopy as a novel microscopy technique to resolve optical properties at the nanoscale. By combining elements from electron and optical microscopy we are able to resolve optical phenomena that are impossible to elucidate with other techniques.

List of publications

This thesis is based on the following publications:

- *Angle-resolved Cathodoluminescence Spectroscopy*, T. Coenen, E. J. R. Vesseur, and A. Polman, Appl. Phys. Lett. **99**, 143103 (2011). (**Chapter 3**)
- *Directional emission from plasmonic Yagi-Uda antennas probed by angle-resolved cathodoluminescence*, T. Coenen, E. J. R. Vesseur, A. Polman, and A. F. Koenderink, Nano Lett. **11**, 3779-3784 (2011). (**Chapter 4**)
- *Deep-subwavelength spatial characterization of angular emission from single-crystal Au plasmonic ridge nanoantennas*, T. Coenen, E. J. R. Vesseur, and A. Polman, ACS Nano **6**, 1742-1750 (2012). (**Chapter 5**)
- *Polarization-sensitive cathodoluminescence Fourier microscopy*, T. Coenen and A. Polman, Opt. Express **20**, 18679-18691 (2012). (**Chapter 6**)
- *The planar parabolic antenna*, D. T. Schoen, T. Coenen, F. J. García de Abajo, M. L. Brongersma, and A. Polman, Nano Lett. **13**, 188-193 (2013). (**Chapter 7**)
- *Directional emission from a single plasmonic scatterer*, T. Coenen, F. Bernal Arango, A. F. Koenderink, and A. Polman, Nat. Commun. **5**, 3250 (2014). (**Chapter 8**)
- *Optical properties of individual plasmonic holes probed with local electron beam excitation*, T. Coenen and A. Polman, in preparation. (**Chapter 9**)
- *Variable modal excitation efficiency in plasmonic dolmens through nanoscale electron beam positioning*, T. Coenen, D. T. Schoen, B. J. M. Brenny, S. R. K. Rodriguez, S. Mann, A. Polman, and M. L. Brongersma, in preparation. (**Chapter 10**)
- *Deep-subwavelength imaging of the modal dispersion of light*, R. Sapienza, T. Coenen, J. Renger, M. Kuttge, N. F. van Hulst and A. Polman, Nat. Mater. **11**, 781-787 (2012). (**Chapter 11**)
- *Resonant Mie modes of single silicon nanocavities excited by electron irradiation*, T. Coenen*, J. van de Groep*, and A. Polman, ACS Nano **7**, 1689-1698 (2013). (*equal author contribution) (**Chapter 12**)

Patent application:

- *Generation of a single guided excitation in a waveguide*, A. Polman, E. J. R. Vesseur, T. Coenen, and F. J. García de Abajo, European Patent Application 2012042057 (2012).

Other publications by the author:

- *Imaging the hidden modes of ultrathin plasmonic strip antennas by cathodoluminescence*, E. S. Barnard, T. Coenen, E. J. R. Vesseur, A. Polman, and M. L. Brongersma, *Nano Lett.* **11**, 4265-4269 (2011).
- *Plasmonic light trapping in thin-film Si solar cells*, T. Coenen, M. Frimmer, A. Polman, and A. F. Koenderink, *Ned. Tijdschrift v. Natuurkunde (Journal of the Dutch Physical Society)* **78**, 62-66 (2011).
- *Signature of a Fano-resonance in a plasmonic meta-molecule's local density of optical states*, M. Frimmer, T. Coenen, and A. F. Koenderink, *Phys. Rev. Lett.* **108**, 077404 (2012).
- *Plasmonic excitation and manipulation with an electron beam*, E. J. R. Vesseur, J. Aizpurua, T. Coenen, A. Reyes-Coronado, P. E. Batson, and A. Polman, *MRS Bulletin* **37**, 752-760 (2012).
- *Dispersive ground plane core-shell type optical monopole antennas fabricated with electron beam induced deposition*, H. Acar, T. Coenen, A. Polman, and L. Kuipers, *ACS Nano* **6**, 8226-8232 (2012).
- *Experimental verification of $n = 0$ structures for visible light*, E. J. R. Vesseur, T. Coenen, H. Caglayan, N. Engheta, and A. Polman, *Phys. Rev. Lett.* **110**, 013902 (2013).
- *Underpinning hybridization intuition for complex antennas by magnetoelectric quadrupolar polarizability retrieval*, F. Bernal Arango, T. Coenen, and A. F. Koenderink, in preparation.
- *Nanoscale optical tomography with cathodoluminescence spectroscopy*, A. C. Atre, B. J. M. Brenny, T. Coenen, A. Polman, and J. A. Dionne, in preparation.
- *Differentiating radiation processes in silicon using angle-resolved cathodoluminescence spectroscopy*, B. J. M. Brenny, T. Coenen, and A. Polman, in preparation.
- *Investigation of resonant modes in plasmonic patch antennas*, A. Mohtashami, T. Coenen, A. Polman, and A. F. Koenderink. in preparation.



The work described in this thesis was performed at the FOM-Institute AMOLF, Science Park 104, 1098 XG Amsterdam, The Netherlands.